UNIVERSITY OF SOUTHAMPTON
FACULTY OF ENGINEERING, SCIENCE AND MATHEMATICS
Optoelectronics Research Centre

Investigation of code reconfigurable fibre Bragg gratings for Optical Code Division Multiple Access (OCDMA) and Optical Packet Switching (OPS) Networks

by
Chun Tian

Thesis submitted for the degree of Doctor of Philosophy

March 2009

UNIVERSITY OF SOUTHAMPTON

ABSTRACT

FACULTY OF ENGINEERING, SCIENCE AND MATHEMATICS

OPTOELECTRONICS RESEARCH CENTRE

Doctor of Philosophy

INVESTIGATION OF CODE RECONFIGURABLE FIBRE BRAGG GRATINGS FOR OPTICAL CODE DIVISION MULTIPLE ACCESS (OCDMA) AND OPTICAL PACKET SWITCHING (OPS) NETWORKS

by Chun Tian

This thesis documents my work in the telecommunication system laboratory at the Optoelectronics Research Centre, towards the implementation of code-reconfigurable OCDMA and all-optical packet switching nodes based on fibre Bragg grating (FBG) technology. My research work involves characterizing the performance of various gratings, specifically high reflectivity, short chip duration, long code sequences, multiple phase level and tunable superstructured fiber Bragg gratings (SSFBGs), by using the recently proposed Frequency-Resolved Optical Gating technique based on Electro-Absorption Modulator (EAM-FROG). This technology can obtain the complex code profile along the grating, making it a powerful method to understand the thermally-induced code-reconfigurable grating. Efforts have been made to improve the grating design to achieve better system performance. Three different types of FBGs optical encoder/decoder, e.g. conventional discrete phase-shift SSFBGs, code-reconfigurable gratings, and novel continuous phase-shift SSFBGs, have been investigated comparatively, as well as their performance in various optical coding/decoding systems. This thesis also discusses the possibility of reducing multiple access interference (MAI) using a Two-Photon Absorption (TPA) process. The advanced grating devices enable the improvement of system performance. A dynamically reconfigurable optical packet processing system and a 16-channel reconfigurable OCDMA/DWDM system with 50GHz DWDM intervals has been demonstrated.

These results highlight the feasibility of FBG-based optical coding/decoding techniques, with improved system flexibility and sustainability.

Contents

List of Figures

List of Tables

Declaration of Authorship

I, Chun Tian, declare that the thesis entitled "Investigation of code reconfigurable fibre Bragg gratings for Optical Code Division Multiple Access (OCDMA) and Optical Packet Switching (OPS) Networks" and the work presented in the thesis are both my own, and have been generated by me as the result of my own original research. I confirm that:

- this work was done wholly or mainly while in candidature for a research degree at this University;

- where any part of this thesis has previously been submitted for a degree or any other qualification at this University or any other institution, this has been clearly stated;

- where I have consulted the published work of others, this is always clearly attributed;

- where I have quoted from the work of others, the source is always given. With the exception of such quotations, this thesis is entirely my own work;

- I have acknowledged all main sources of help;

- where the thesis is based on work done by myself jointly with others, I have made clear exactly what was done by others and what I have contributed myself;

- I have published as part of Ph.D. work some of the research material contained within this thesis as journal and conference papers (see List of Publications).

Signed: ……..

Date:…….

Acknowledgements

I would like to take this opportunity to thank those people who have helped me throughout my study life towards a PhD at the University of Southampton.

I sincerely thank my supervisor Prof. David Richardson, for his excellent and invaluable guidance and support during the course of my research work. I feel so grateful to have been his student.

A very special thank you to Dr. Periklis Petropoulos, who has also been patiently guiding and helping me throughout my PhD life, despite his busy schedule.

I would like to thank Dr Morten Ibsen, for providing many fiber gratings and constructive suggestions.

I would like to express my gratitude to Dr. Benn Thomson. It was him who provided the introduction and hands-on help in the lab during the start of my PhD.

My colleagues in the telecommunication lab, Anoma, Paulo, Francesca and Michaël, who are all Doctors now. I appreciate the time spent with you guys in the lab and in the life. Thank you for all your helpful support and discussion. I am also grateful for the close collaborations with Dr. Zhaowei Zhang.

Thank you to Dr. Eleanor Tarbox, Mrs. Eveline Smith, Mrs. Jenifer Morley, Mr. Chris Nash, Mr. Simon Butler and Mr. Timothy McIntyre for their kind help during my study.

Finally, I would like to thank my parents, my wife, and my baby son Kairui, your love keeps me going ahead.

Acronyms

AC	Alternating current
AON	All-Optical Networks
ASE	Amplified spontaneous emission
BER	Bit error rate
CDMA	Code Division Multiple Access
DC	Direct current
DS-OCDMA	Direct sequence Optical Code Division Multiple Access
DWDM	Dense wavelength division multiplexing
EAM	Electro-Absorption Modulator
EDFA	Erbium-doped fiber amplifier
EDFL	Erbium-doped fiber ring laser
FBG	Fibre Bragg grating
FDM	Frequency Division Multiplexing
FE-OCDMA	Frequency encoding Optical Code Division Multiple Access
FH-OCDMA	Frequency hopping Optical Code Division Multiple Access
FROG	Frequency-Resolved Optical Gating
FWHM	Full width at half maximum
LAN	Local area networks
MAI	Multiple access interference
MAN	Metro area networks
NOLM	Nonlinear optical loop mirror
NRZ	Non-Return to Zero
OCDMA	Optical Code Division Multiple Access
OHL	Optical hard limiter
OOC	Optical orthogonal codes
OPS	Optical Packet Switching
OSA	Optical spectrum analyzer
PER	Packet error rate
PPLN	Periodically poled Lithium Niobate
QoS	Quality of Service
RF	Radio frequency

SC	Super-continuum
SHG	Second-harmonic-generation
SNR	Signal to noise ratio
SPM	Self-phase-modulation
SSFBG	Superstructured fiber Bragg grating
TDM	Time Division Multiplexing
TPA	Two-Photon Absorption
WDM	Wavelength division multiplexing

Chapter 1
Overview

For most of us it is hard to imagine life without the telephone, mobile, even internet nowadays. The latest global internet user population has exceeded 1.46 billion by June 2008, which is more than 300% growth since 2000[1-1]. The current boom in broadband services has placed significant demands on telecommunications network. While the optical network plays a key role, one promising developing trend of the telecommunication network is towards the "all-optical network"[1-2, 3], which utilises the huge capacity of optical fiber and ultra fast optical processing to provide high speed and transparent signals and thus eliminate the 'electronic bottleneck'[1-4]. Besides the constant interest in capacity and speed, the contemporary metro network is evolving to provide 'triple-play' services, which combine voice calls, internet and TV, or video-on-demand services over a single scalable network[1-5]. The subscriber-oriented network requires flexible data rates, dynamic configuration, variable Quality of Service (QoS) etc. Many efforts have been made to fulfil the requirements imposed by the developing services on the telecommunication networks. Basically, there are three main multiplexing technologies available to improve the optical network capacity. The first one is Optical Time Division Multiplexing (OTDM), which interleaves lower bit rate data streams into a single high speed stream in the optical domain; each user occupies a designated time slot. The second one is Frequency Division Multiplexing (FDM), which specifies an individual frequency band for each user. In the context of optical networks this scheme is usually termed as Wavelength Division Multiplexing (WDM) to denote the large scale of channel spacing between the different channels. The last one is Optical Code Division Multiple Access (OCDMA), which is a spread spectrum technique allowing user signals to share the same frequency spectrum and temporal slots, but where each user's information data

can be distinguished with a specified code. With the great success of CDMA technology in wireless communication systems, OCDMA has generated wide research attention. The unique features presented by OCDMA include service transparency, asynchronous operation, flexible bandwidth management, higher system security, and the potential for network scalability. These features are especially attractive for future metropolitan and access networks.

There are wide research areas in the OCDMA system. Besides the optical codes and network architecture, a key issue to implement OCDMA is all-optical code generation and recognition, which can also be used in other applications e.g. optical labeling for packet switching systems. Among various optical coding/decoding schemes, the approach based on fibre Bragg gratings (FBGs) is a promising technology with distinguished advantages. The feasibility of using superstructured fiber Bragg gratings (SSFBGs) to process the optical codes has been previously demonstrated in our lab. Following up the previous work, this thesis investigates the characteristics and performance of different types of improved FBGs, including discrete phase-shift and continuous phase-shift SSFBGs and code-reconfigurable gratings and their applications in both OCDMA systems and packet switching systems. The results highlight the potential of the SSFBG-based optical coding/decoding approach.

Chapter 2 overviews the principles of OCDMA and classifies the reported technologies. Several approaches for the optical coding/decoding are outlined. Then I focus on the optical coding/decoding using FBGs. The theoretical background of FBGs is introduced. The gratings writing technique and gratings characteristics are also described.

Chapter 3 introduces the characterization of the gratings using Electro-Absorption Modulator based Frequency-Resolved Optical Gating (EAM-FROG). Firstly several existing grating characterization techniques are reviewed. Then I investigate the performance of using second-harmonic generation (SHG) FROG and EAM-FROG. Several different types of gratings have been characterized by using the EAM-FROG technique. The grating's modulation profile, both amplitude and phase, can be obtained accurately.

Chapter 4 comparatively investigated the performance of the OCDMA systems based on different types of 15-chip gratings, which include conventional discrete phase-shift SSFBGs, thermally code-reconfigurable gratings, and novel continuous

phase-shift SSFBGs. The performance of different combinations of these gratings as the encoder and decoder has been investigated.

Chapter 5 introduces various approaches to reduce the interference from multiple access interference (MAI) which degrades the performance of OCDMA systems. We proposed a scheme of nonlinear thresholding based on the Two-Photon Absorption (TPA) process, which can perform nonlinear thresholding and opto-electronic detection in one step. The feasibility of the scheme is experimentally demonstrated in this chapter.

Chapter 6 reports our experiments to demonstrate a reconfigurable all-optical packet processing system using the 15-chip code-reconfigurable gratings to perform the header generation and recognition functions. These experiments combine the unique advantages of FBG-based coding/decoding technology with the common bit-serial time-domain labeling techniques. The relative factors that affect the system performance have also been discussed in this chapter.

Based on the inherent wavelength selectivity of the gratings, Chapter 7 introduces the demonstration of a reconfigurable 16-channel OCDMA/DWDM system with the wavelength interval down to 50GHz by incorporating the code-reconfigurable gratings, and the continuous phase-shift SSFBGs into the system. This demonstration features 31-chip codes, high spectral efficiency, low cost, and reconfigurability. Error-free operation has been achieved for all the channels.

The thesis is summarised in Chapter 8, with a few discussions on future directions of this research area.

References

[1-1] "INTERNET USAGE STATISTICS ": http://www.internetworldstats.com/stats.htm.

[1-2] S. Ken-Ichi and S. Okamoto, "Photonic transport technologies to create robust backbone networks," *IEEE Communications Magazine*, vol. 37, pp. 78-87, 1999.

[1-3] "All-Optical Communication Systems: Architecture, Control, and Network Issues III," Dallas, TX, USA, 1997.

[1-4] "Special Issue on factors Affecting Data Transmission Quality," *IEEE J. Lightwave Technol.*, vol. 6, 1988.

[1-5] D. Gallant, "Optical network foundation for triple play services roll-out," Anaheim, CA, United States, 2006.

Chapter 2

Introduction to Optical Code Division Multiple Access (OCDMA)

This chapter overviews the principles of OCDMA and introduces the reported technologies. Several approaches for the optical coding/decoding are outlined. Then I focus on the optical coding/decoding using fiber Bragg gratings (FBGs). The theoretical background of FBGs and the grating writing technique, which is used in our laboratories, are also introduced in this chapter.

2.1 Overview of OCDMA technology

One of the basic concepts in data communication is the idea of allowing several transmitters to send information simultaneously over a single communication channel. Code Division Multiple Access (CDMA) is a telecommunication multiplexing scheme that sits alongside Time Division Multiplexing (TDM) and Frequency Division Multiplexing (FDM). Figure 2.1 illustrates the concept of TDM, FDM and CDM schemes in the time and frequency domain. TDM multiplexes the multiple signals over one communication medium by interleaving the signals in sequential time slots. For FDM, the carrier bandwidth is divided into sub-channels of different frequency widths, each carrying a signal at the same time in parallel. For both TDM and FDM, each individual signal channel is distinguishable either in the time domain or in the frequency domain. By contrast, the signal channels in CDM are overlapped in both the time domain and the frequency domain. Each channel has been encoded

with a unique code and can only by recognised from the overlapped signals with the correct code.

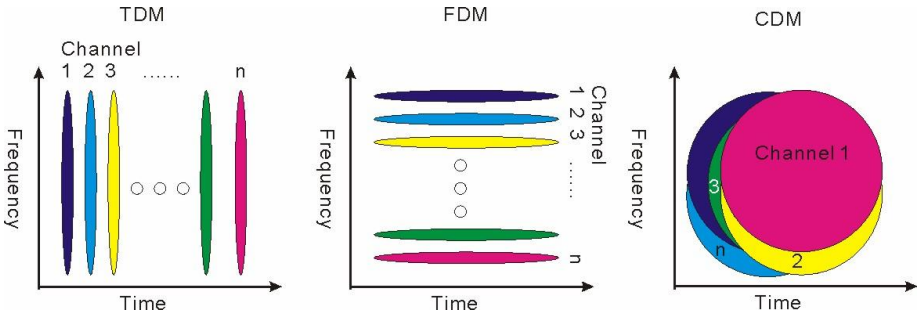

Figure 2.1 Concept of TDM, FDM and CDM schemes.

Generally, CDMA is a spread spectrum technique which first achieved huge success in wireless communications. It spreads the spectrum of a narrowband signal over a much wider frequency spectrum according to some designated codes. The spread spectrum is much wider than required to transmit data at the same rate using conventional, e.g. Non-Return to Zero (NRZ), modulation formats. Due to the spreading, the transmitted signal has a noise-like characteristic and can not be distinguished unless the receiver knows the designated codes[2-1]. The received signal is correlated by the authorized receiver with a local code, which is a copy of the code used for transmitting.

The research work of implementing CDMA principles directly in the optical domain, known as OCDMA, has been a hot area recently. In OCDMA systems each channel is optically encoded with the specific code. Only the authorized receiver with the correct code can restore the encoded information in the presence of the interference from other users. Unlike the common wireless receiver, which mixes a local copy of the code used to spread the transmitted signal with the received spread spectrum signal, it is difficult to obtain a coherent local carrier to perform the strict synchronous operation in the optical domain. Thus the matched filtering technique is preferred in OCDMA. A matched filter is obtained by correlating a known signal, or template, with an unknown signal to detect the presence of the template in the unknown signal. This is equivalent to convolving the unknown signal with a time-reversed version of the template. The matched filter is the optimal linear filter for maximizing the signal to noise ratio (SNR) in the presence of additive stochastic noise. Convolution of the received code with the impulse response of the correct filter results in a distinct autocorrelation peak that can be readily recognized. On the other hand,

the cross-correlation between all other codes in operation on the system can only generate a low-level, noise-like output. Figure 2.2 illustrates the operation of an OCDMA system.

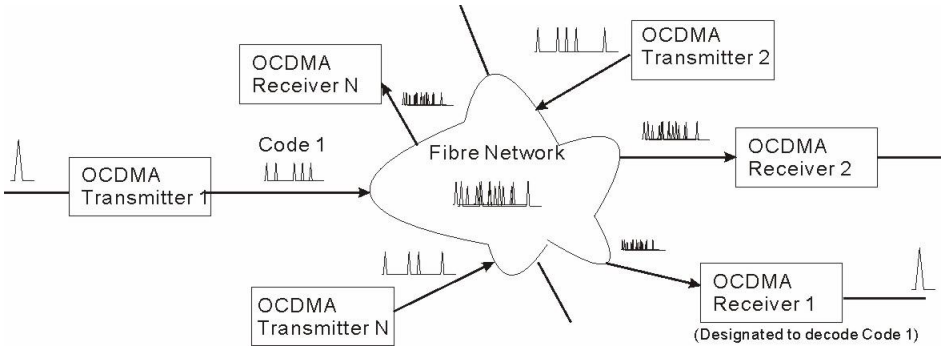

Figure 2.2 Operation of OCDMA system. The encoded signals are overlapped randomly with other users' signal and transmitted through the network, the receiving user can restore the designated information from the overlapped signal by using the matched code.

Compared to the other two multiplexing approaches, OTDM and WDM, OCDMA has some distinguishing features. The TDM scheme is a strictly synchronous approach, which must carefully synchronize the transmission times of all the users to ensure that they are received in the correct timeslot and do not cause interference. Due to time-serial nature of TDM technology, the allocation of dedicated time slots makes it difficult to adjust the bandwidth of each user flexibly. In order to break through the limit of electronic circuit speed, another key issue of the TDM is the deployment of optical logic gate, which is still under development. Although Wavelength Division Multiplexing (WDM) can be seen as asynchronous, it is generally transmission-oriented. It is difficult to achieve the flexible channel granularity required by the bursty packet-based services. Thus it may waste the wavelength resources. By contrast, OCDMA allows asynchronous operation. OCDMA is a subscriber-oriented scheme, and simultaneous multiple access can be achieved without a complex network protocol. It is more suitable for modern data communications. The spread spectrum technique also offers advantages in terms of system security. OCDMA also allows for flexible and efficient bandwidth management. It is also promising for efficient distribution of subscriber channels in metro/local area networks (MAN/LAN) as well as in access network applications. It is

believed that the advantages of All-Optical Networks (AON) will only be fully realized with the application of OCDMA.

In 1986, P. Prucnal et al. reported the first OCDMA demonstration which used tapped delay lines and prime sequence codes[2-2]. Since then, various approaches to implement OCDMA have been proposed and demonstrated. According to the types of optical source and the detection techniques, OCDMA techniques can be classified into incoherent and coherent categories. Incoherent OCDMA detects the optical signal directly without the use of coherent interference. Due to its incoherent nature, the optical source is cheaper and the system is less sensitive to environmental changes and polarization problems. However, incoherent coding is limited to unipolar codes (0/1 sequences), which can't yield perfect orthogonality between the codes. This leads to limited system performance. The first demonstration mentioned above is an incoherent system.

Later on, a coherent OCDMA system was demonstrated using a spectral phase mask and binary M sequence codes[2-3]. The coherent scheme, which can share the development in wireless CDMA, exhibits significant advantages such as spectral and phase coding, and better correlation performance.

Similar to wireless CDMA, the coding parameters in the optical domain can be amplitude, phase or both. According to whether the optical encoding/decoding process is performed in either the frequency domain, time domain or both, coherent OCDMA approaches can be classified as frequency-encoded FE-OCDMA, direct sequence DS-OCDMA, and frequency-hopping FH-OCDMA.

In DS-OCDMA, each data bit to be transmitted is turned into a time-serial sequence of individual pulses, referred to chips, according to a specific code. Coded bits are then broadcast onto the network and the designated users can recognize the coded data bits only with a receiver matched to the specific code[2-4]. DS-OCDMA involves coding in the time domain, either amplitude coding or phase-coding. For the incoherent processing, unipolar pseudo-orthogonal codes, such as optical orthogonal codes (OOCs) [2-5, 6] and prime codes [2-7]are employed. For the coherent processing, it may utilize bipolar orthogonal codes, such as M-sequences [2-8] and Gold codes [2-9], and even higher phase level codes, e.g. quaternary Family A sequences[2-10]. The research has proved that, compared to the incoherent scheme, the coherent orthogonal codes can produce a near-zero cross-correlation performance,

which is critical to reduce multiple-access interference and accommodate more in-channel users [2-8].

In FE-OCDMA, a broad-spectrum signal is sliced into a series of discrete frequency components. The amplitude and/or phase of these frequency components represent a specific code. As a result, the encoded signal has the feature of a long duration and low intensity in the time domain. [2-11, 12]. Bipolar orthogonal codes, such as M-sequences and Walsh codes, are also used in FE-OCDMA.

In FH-OCDMA, although a data bit also consists of a series of discrete frequencies, the code is presented by the serial sequence of these frequencies. In other words, the frequency of an encoded signal hops around in a dedicated way at a much higher rate than the information data rate. [2-13, 14]

FE-OCDMA and DS-OCDMA employ one-dimensional (1-D) codes which are applied in the frequency domain and time domain respectively. The codes used in FH-OCDMA are called two-dimensional (2-D) codes. Other 2-D codes include time-space codes [2-15] and wavelength-time [2-16, 17] codes. Three-dimensional (3-D) codes involving simultaneously coding in the time, space and wavelength domain have also been proposed [2-18, 19]. The advantages of multi-dimensional codes include fewer restrictions on the ultra short pulses and shorter code lengths to achieve a similar correlation performance as the coherent scheme, with the compromise of spectral bandwidth and system complexity.

Besides the code theory and system structure, an important research area in OCDMA is the optical coding/decoding process. Various coding/decoding schemes have been proposed and demonstrated. Generally, they are based on optical delay line (ODL)[2-2, 20], planar lightwave circuit (PLC)[2-21, 22], arrayed waveguide grating (AWG)[2-23, 24], phase masks[2-25, 26], and fiber Bragg grating (FBG)[2-27, 28]. Among these schemes, the FBG-based technique displays unique features such as compactness, fiber compatibility, potential for low cost and simplicity to fabricate long codes with accurate amplitude/phase controlling capability.

Figure 2.3 illustrates the DS-OCDMA encoder/decoder functions using SSFBGs. When the grating reflectivity strength is within the low reflectivity limit, the optical signal is able to penetrate the full grating. The frequency response of the grating is simply defined by the Fourier transform of the spatial refractive-index modulation profile of the grating. The impulse response of the grating thus directly follows the superstructure profile imposed upon the grating. When the short input pulse is

reflected from the encoding SSFBG, the generated encoded signal will be composed of a specific sequences of short pulses which represents the same profile as the superstructure profile along the grating. Thus the encoded signal can be generated in this way to present designated individual users with the system. Code recognition is achieved by a matched filtering process, using a decoding grating which has the conjugate impulse response to the encoding grating. The conjugate impulse response is easily obtained by spatially reversing the superstructure profile relative to that of the encoding grating. This is achieved by using a grating which has exactly the same refractive-index profile as the encoding grating, but injecting the light from the other end. In the matched case, the decoding grating has a time-reversed profile compared to the encoding grating, the matched filtering process results in a distinguished autocorrelation pulse which is readily detected. The encoded information can thus be correctly recovered from the overlapped, noise-like encoded signals. While in the unmatched case, which means an incorrect decoding grating is used, the output will present a low intensity cross-correlation of the two codes, which means that no information can be obtained from the encoded signals.

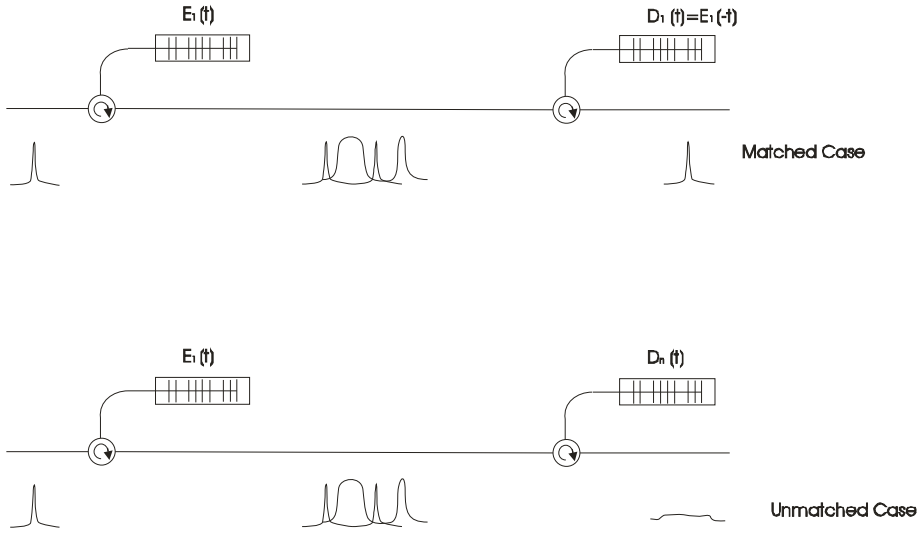

Figure 2.3 An example of SSFBG-based OCDMA encoder/decoder process.

2.2 DS-OCDMA based on SSFBG technology

With the fiber Bragg grating (FBG) fabrication technique at ORC, University of Southampton, we are able to implement optical coding/decoding for DS-OCDMA using superstructured fiber Bragg grating (SSFBG)-based techniques.

A Fiber Bragg Grating (FBG) is a periodic, or almost periodic, structure consisting of a variation of the refractive index along the length of a fiber. It acts as a band-rejection filter, reflecting any wavelength that satisfies the Bragg condition and passing all wavelengths that are not resonant with the grating. The advantages of FBGs in systems applications include low insertion loss, all fibre compatibility, relative ease of manufacture and low cost; but a major feature is that by changing the grating parameters such as induced index change, length, apodization, period chirp, fringe tilt, we can achieve the desired grating spectral characteristics[2-29]. The FBG has a range of applications in the optical communications area, such as wavelength selection, laser stabilization, dispersion compensation, pulse shaping, etc[2-30].

A Super Structure Fiber Bragg Grating (SSFBG) is defined as a fiber grating having a rapidly varying refractive index modulation of uniform amplitude and pitch, onto which an additional, slowly varying refractive index modulation profile has been imposed along its length. The uniform rapid refractive index modulation defines the central wavelength of the grating's reflection band. The additive refractive index modulation can either be amplitude-modulated (unipolar coding) or be phase-modulated (bipolar or higher order coding).The variation in modulation profile defines the phase and amplitude response of the reflectivity profile. Figure 2.3 illustrates the relative refractive index modulation of the SSFBGs, which contain a 7-chip code. Figure 2.4(a) is an amplitude-modulated (unipolar coded) grating, Figure 2.4(b) is a phase-modulated (bipolar coded) grating. It has been shown that current SSFBG technology is capable of fabricating long codes, short chip duration and multiple phase levels which can hardly be achieved by using other technologies e.g. PLC's [2-31].

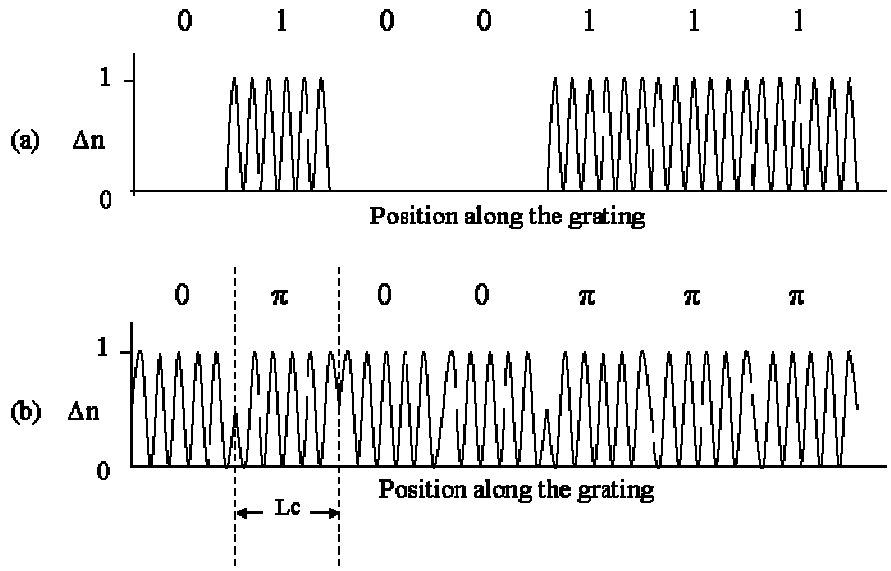

Figure 2.4 Examples of the refractive index modulation profiles along the SSFBGs. (a) a 7-chip unipolar code, (b) a 7-chip bipolar code.

The code sequence of a grating is made up of a number of chips (N_c chips). Each chip has a finite length (L_c) along the grating. The corresponding chip duration is $T_c = 2nL_c/c$. Where n is the average refractive index of the grating.

Thus a grating with a N_c chips code will require a grating length of $N_c L_c$ and produces a coded sequence that is $N_c T_c$ in duration.

In this thesis, code length and chip duration is used to describe the SSFBGs used in the following research. For example, a 15-chip, 50ps SSFBG means that the code length is 15, the encoded signal reflected from the grating is 15-chip and the chip duration T_c is 50ps; the resulting duration of the whole encoded signal is ~800ps. The corresponding chip length L_c is ~5mm and the actual total grating length is 8.22cm. The other equivalent parameters to describe the SSFBGs for OCDMA coding/decoding purposes include the chip rate and the effective bit rate. The 50ps chip duration also implies that the maximum chip rate is 20G chip/s. Because during the decoding process, the encoded signal will be reflected from the same length grating to produce autocorrelation or cross-correlation, the resulting output signal will thus double the duration of the input encoded signal. In order to avoid decoded pulses overlapping, the effective bit rate R_e is thus limited. Take the above 15-chip, 50ps SSFBG for example, the encoded signal is ~800ps, after the decoding process the

output signal will be 1.6ns long. The maximum effective bit rate for each user is 625M bit/s if the requirement to avoid decoded pulses overlapping is fulfilled.

In order to achieve a higher effective bit rate, we can either reduce the chip length or reduce the chip number for codes. For example, a 4.62mm long 7-chip grating has a chip length of 0.66mm for each chip. The total reflected pulse sequence duration is ~46.2ps. The maximum effective bit rate is about 10G bit/s, and the chip rate is around 160G chip/s. However, a lower chip number grating will allow fewer simultaneous users. In my research work, I have tried to reduce the chip length of the grating while keeping a reasonable code length.

The impulse response h(t) of a fiber grating is given by the inverse Fourier transform of its frequency response H(ω)

$$h(t) = \int_{-\infty}^{+\infty} H(w) e^{-jwt} dw \tag{2.1}$$

When a short pulse is reflected by a SSFBG, it is transformed into a pulse with a temporal shape given by the convolution of the input pulse and the impulse response of the grating

$$y(t)=x(t)*h(t) \tag{2.2}$$

According to Fourier transform theory, in the frequency domain

$$Y(\omega)=X(\omega)H(\omega) \tag{2.3}$$

Now we consider the SSFBG being used as a matched filter, which has a frequency response G(ω) and associated impulse response g(t). In the frequency domain, the result after the decoder is

$$R(\omega)=Y(\omega)G(\omega)= X(\omega)H(\omega)G(\omega) \tag{2.4}$$

To recover the input pulse X(ω) or x(t), it is required that

$$G(w) = H^{*}(w) \tag{2.5}$$

$$g(t)=h(-t) \tag{2.6}$$

According to the discussion above, the superstructure function of the decoder grating is just the spatially reversed form of the structure used to write the encoder grating.

Coupled mode theory [2-29]is a straightforward, intuitive and accurate tool for modeling the optical properties, such as reflection and transmission spectra, of most

fiber gratings. However it is time-consuming. Another often preferred approach for calculating the reflection and transmission spectra of a grating is the piecewise-uniform approach [2-29], which takes the grating to be composed of a number of uniform pieces. Each section of the grating is identified by a 2×2 matrix. Then all the matrices can be multiplied together to obtain a single 2×2 matrix that describes the whole grating. For SSFBGs, the number of sections needed for the piecewise-uniform calculation is simply determined by the number of actual uniform sections in the grating.

$$\begin{bmatrix} R(z+\Delta z) \\ S(z+\Delta z) \end{bmatrix} = \begin{bmatrix} \cosh(g_B \Delta z) - i\frac{\hat{s}}{g_B}\sinh(g_B \Delta z) & -i\frac{k}{g_B}\sinh(g_B \Delta z) \\ i\frac{k}{g_B}\sinh(g_B \Delta z) & \cosh(g_B \Delta z) - i\frac{\hat{s}}{g_B}\sinh(g_B \Delta z) \end{bmatrix} \cdot \begin{bmatrix} R(z) \\ S(z) \end{bmatrix} \tag{2.7}$$

where R and S are the backward and forward propagating field respectively. $\hat{s}$ is the "DC" coupling coefficient, k is the "AC" coupling coefficient, $g_B = \sqrt{k^2 - \hat{s}^2}$, Δz is the length of the uniform section.

After obtaining the transfer matrix of the grating, field reflection and transmission can be obtained:

$$\begin{aligned} H_R &= \frac{R(0)}{S(0)} \\ H_T &= \frac{S(L)}{S(0)} \end{aligned} \tag{2.8}$$

The reflection amplitude and reflection phase are calculated:

$$\begin{aligned} R &= \left|H_R\right|^2 \\ f_R &= angle(H_R) \end{aligned} \tag{2.9}$$

I have written a code in MATLAB using the transfer matrix method to simulate the properties of SSFBGs in my research work.

The continuous grating writing technique, developed at the University of Southampton, has been shown to be capable of fabricating gratings with complex refractive index profiles[2-32]. This technique uses a simple phase mask with a uniform pitch and operates by precisely controlling the position of the photosensitive

fiber relative to the phase mask, and controlling the exposure to the index modifying UV light used to write the grating. Thus a simple phase mask can be used to write a range of complex grating structures. This technique is to be contrasted with the traditional phase mask technique where the induced refractive index pattern is written into the phase mask itself, and simply imprinted into the fiber. All the gratings used in the following experiments were manufactured by Dr. Morten Ibsen with the continuous grating writing technique.

Preliminary work at the telecommunications laboratory of ORC, University of Southampton, demonstrated the feasibility of SSFBG-based optical coding/decoding techniques[2-8, 2-28, 2-33, 2-34]. In 1998, the first demonstration of OCDMA based on a 7-chip 6.4ps unipolar coded SSFBGs was reported. This was followed by bipolar SSFBGs using the same 7-chip M-sequence codes. The investigation of the performance of the SSFBG approach was extended to longer code sequences, specifically, 63-chip 6.4ps bipolar Gold sequences, and 255-chip 3.2ps quaternary Family A sequences. These results show that the SSFBG-based OCDMA approach offers potential to support a reasonable number of users, which is a key factor in the realistic telecommunication applications. Note that the previous experiments employed SSFBGs which have a weak reflectivity (less than 25%), to ensure that the signal field can penetrate the full length of the grating. This condition allows the use of Fourier transform techniques to analyze the grating response. However, high reflectivity SSFBGs will have less optical insertion loss and thus reduce the performance impairment brought about by the need for additional optical amplification. In order to achieve the operation with short chip duration (6.4ps and 3.2ps) SSFBGs, a mode-locked fiber ring laser had to be used to generate the ultra short input pulses, which inevitably incurs considerable cost and increases sensitivity of the system. In addition, the previous work was mainly focused on the fixed-coded SSFBG, where the designated code had been imprinted on the grating during the grating writing process and could not be readily changed. This feature limits the flexibility of the SSFBGs application in the OCDMA networks. A dynamically code-reconfigurable device which includes both the advantages of the FBG based coding/decoding technique and the flexible reconfigurability is highly desirable. Although the thermally-induced code-reconfigurable device based on a uniform FBG has been proposed at the ORC[2-35], further work needs to be done to fully understand the behavior and performance of the code-reconfigurable device, as well

as its application in the OCDMA and other optical networks, e.g. Optical Packet Switching Network.

My research work focused on the possibility to improve the SSFBGs in terms of higher reflectivity, shorter chip length and higher chip rate, and other advanced grating designs, e.g. the code-reconfigurable device and the continuous phase-shift SSFBG. Meanwhile, the gratings used in my experiments were designed to be compatible with a relative wide input pulse to reduce the system cost. Electro-Absorption Modulator based Frequency-Resolved Optical Gating (EAM-FROG) technology has been implemented to characterize the SSFBGs, especially to understand the behavior of the code-reconfigurable device. All the efforts are focused to realize a more efficient and flexible optical coding/decoding technology at a reasonable cost. Particularly, I investigated the performance from a system point of view.

The range of different gratings fabricated for my experiments are summarized as below:

- In order to establish the feasibility of using the EAM-FROG technique to characterize SSFBGs, some simple SSFBGs with a single discrete phase-shift at the centre of the grating were fabricated. Each grating has a length of 5mm. The four different phase-shift values are uniform (no phase-shift), 0.5π, π, and 1.5π. These phase-shift values are used in the following quaternary phase-shift gratings.
- Having confidence in the EAM-FROG technique, fixed-coded 15-chip 25ps SSFBGs were then fabricated. Each grating is 40mm long, with discrete quaternary phase-shift codes. These gratings were used to perform more complicated EAM-FROG characterization and also used as the optical code/decoder in the investigation of system applications.
- Similarly, we constructed a simple reconfigurable grating device to investigate the behavior of the code-reconfigurable grating. This simple reconfigurable grating is 17mm long and can produce a single variable phase-shift at the middle of the grating. Then a 15-chip 25ps code-reconfigurable grating device was manufactured. This reconfigurable device can produce quaternary phase-shift on demand and is compatible

with the above fixed-coded 15-chip 25ps SSFBGs. A reconfigurable optical packet switching system has been demonstration with this device.

- Followed our study results of the code-reconfigurable grating device, a new type of SSFBG was proposed and demonstrated. It is called continuous phase-shift SSFBG, in contrast to the previous discrete phase-shift SSFBG. Firstly, 15-chip 25ps continuous phase-shift SSFBGs were fabricated with the same code as the previous fixed-coded 15-chip 25ps SSFBGs .
- Based on the above study results, we fabricated 31-chip 25ps continuous phase-shift SSFBGs and the corresponding 31-chip 25ps code-reconfigurable grating device to demonstrate a 16-channel OCDMA/DWDM system.

The research work was performed in collaboration with Mr. Zhaowei Zhang, a PhD student from the Fiber Bragg Grating group.

References

[2-1] R. C. Dixon, *Spread spectrum systems*: Wiley, 1976.

[2-2] P. R. Prucnal, M. A. Santoro, and T. R. Fan, "Spread spectrum fiber-optic local area network using optical processing," *IEEE J. of Lightwave Tech.,* vol. 4, pp. 547-554, 1986.

[2-3] A. M. Weiner, J. P. Heritage, and J. A. Salehi, "Encoding and decoding of femtosecond pulses," *Optics Letters,* vol. 13, pp. 300-2, 1988.

[2-4] J. A. Salehi, "Code Division Multiple-Access Techniques in Optical Fiber Networks," *IEEE Transactions on Information Theory,* vol. 37, p. 824-833, 1989.

[2-5] F. R. K. Chung, J. A. Salehi, and V. K. Wei, "Optical orthogonal codes: design, analysis and applications," *IEEE Transactions on Information Theory,* vol. 35, pp. 595-604, 1989.

[2-6] S. Mashhadi and J. A. Salehi, "Code-division multiple-access techniques in optical fiber networks - part III: optical AND logic gate receiver structure with generalized optical orthogonal codes," *IEEE Transactions on Communications,* vol. 54, pp. 1457-68, 2006.

[2-7] A. A. Shaar and P. A. Davies, "Prime sequences: quasi-optimal sequences for OR channel code division multiplexing," *Electronics Letters,* vol. 19, pp. 888-90, 1983.

[2-8] P. C. Teh, P. Petropoulos, M. Ibsen, and D. J. Richardson, "A comparative study of the performance of seven- and 63-chip optical code-division multiple-access encoders and decoders based on superstructured fiber Bragg gratings," *Journal Of Lightwave Technology,* vol. 19, pp. 1352-1365, Sep 2001.

[2-9] E. H. Dinan and B. Jabbari, "Spreading codes for direct sequence CDMA and wideband CDMA cellular networks," *IEEE Communications Magazine,* vol. 36, pp. 48-54, 1998.

[2-10] S. Boztas, R. Hammons, and P. Y. Kumar, "4-phase sequences with near-optimum correlation properties," *IEEE Transactions on Information Theory,* vol. 38, pp. 1101-1113, 1992.

[2-11] M. Kavehrad and D. Zaccarin, "Optical Code-Division-Multiplexed Systems Based on Spectral Encoding of Noncoherent Sources," *Journal of Lightwave Technology,* vol. 13, pp. 534-545, Mar 1995.

[2-12] S. Ayotte, M. Rochette, J. Magne, L. A. Rusch, and S. LaRochelle, "Experimental verification and capacity prediction of FE-OCDMA using superimposed FBG," *Journal of Lightwave Technology,* vol. 23, pp. 724-31, 2005.

[2-13] H. Fathallah, L. A. Rusch, and S. LaRochelle, "Passive optical fast frequency-hop CDMA communications system," *Journal of Lightwave Technology,* vol. 17, pp. 397-405, Mar 1999.

[2-14] M. Thiruchelvi, M. Meenakshi, and G. Geetha, "Multimedia applications using optical FFH-CDMA communication systems," *Microwave and Optical Technology Letters,* vol. 34, pp. 259-263, Aug 20 2002.

[2-15] K. S. Kim, D. M. Marom, L. B. Milstein, and Y. Fainman, "Hybrid pulse position modulation/ultrashort light pulse code-division multiple-access

systems - Part II: Time-space processor and modified schemes," *IEEE Transactions on Communications,* vol. 51, pp. 1135-1148, 2003.

[2-16] L. Tancevski, I. Andonovic, M. Tur, and J. Budin, "Massive optical LAN's using wavelength hopping/time spreading with increased security," *IEEE Photonics Technology Letters,* vol. 8, pp. 935-937, 1996.

[2-17] W. C. Kwong, G.-C. Yang, and C.-Y. Chang, "Wavelength-hopping time-spreading optical CDMA with bipolar codes," *Journal of Lightwave Technology,* vol. 23, pp. 260-267, 2005.

[2-18] K. Sangin, Y. Kyungsik, and N. Park, "A new family of space/wavelength/time spread three-dimensional optical code for OCDMA networks," *Journal of Lightwave Technology,* vol. 18, pp. 502-11, 2000.

[2-19] M. Chopra, M. Bhardwaj, M. Kulkarni, A. De, and R. K. Sinha, "Design of a hybrid fiber-optic network using 3-D optical code sequences," *Fiber and Integrated Optics,* vol. 21, pp. 253-68, 2002.

[220] D. A. Chapman, P. A. Davies, and J. Monk, "Code-division multiple-access in an optical fiber LAN with amplified bus topology: the SLIM bus," *IEEE Transactions on Communications,* vol. 50, pp. 1405-8, 2002.

[2-21] N. Wada and K. Kitayama, "A 10 Gb/s optical code division multiplexing using 8-chip optical opticalbipolar code and coherent detection," *IEEE J. of Lightwave Tech.,* vol. 17, pp. 1758-1765, 1999.

[2-22] K. Takiguchi, T. Shibata, and H. Takahashi, "Time-spreading/wavelength-hopping OCDMA experiment using PLC encoder/decoder with large spread factor," *Electronics Letters,* vol. 42, pp. 301-2, 2006.

[2-23] H. Tsuda, H. Takenouchi, T. Ishii, K. Okamoto, T. Goh, K. Sato, A. Hirano, T. Kurokawa, and C. Amano, "Spectral encoding and decoding of 10 Gbit/s femtosecond pulses using high resolution arrayed-waveguide grating," *Electronics Letters,* vol. 35, pp. 1186-8, 1999.

[2-24] C. Jing, R. G. Broeke, N. K. Fontaine, C. Ji, Y. Du, N. Chubun, K. Aihara, P. Anh-Vu, F. Olsson, S. Lourdudoss, and S. J. B. Yoo, "Demonstration of spectral phase O-CDMA encoding and decoding in monolithically integrated arrayed-waveguide-grating-based encoder," *IEEE Photonics Technology Letters,* vol. 18, pp. 2602-4, 2006.

[2-25] C. C. Chang, H. P. Sardesai, and A. M. Weiner, "Code-division multiple-access encoding and decoding of femtosecond optical pulses over a 2.5-km fiber link," *IEEE Photonics Technology Letters,* vol. 10, pp. 171-3, 1998.

[2-26] R. P. Scott, C. Wei, V. J. Hernandez, K. Li, B. H. Kolner, J. P. Heritage, and S. J. B. Yoo, "An eight-user time-slotted SPECTS O-CDMA testbed: demonstration and simulations," *Journal of Lightwave Technology,* vol. 23, pp. 3232-40, 2005.

[2-27] N. Wada, H. Sotobayashi, and K. Kitayama, "2.5 Gbit/s time-spread/wavelength-hop optical code division multiplexing using fibre Bragg grating with supercontinuum light source," *Electronics Letters,* vol. 36, pp. 815-17, 2000.

[2-28] P. C. Teh, P. Petropoulos, M. Ibsen, and D. J. Richardson, "Phase encoding and decoding of short pulses at 10 Gb/s using superstructured fiber Bragg gratings," *IEEE Photonics Technology Letters,* vol. 13, pp. 154-156, Feb 2001.

[2-29] T. Erdogan, "Fiber grating spectra," *Lightwave Technology, Journal of,* vol. 15, pp. 1277-1294, 1997.

[2-30] P. P. M. Ibsen, R. feced, P.C.Teh, J.H.Lee, M.K.Durkin, M.N.Zervas, D.J.Richardson, D.N.Payne, R.I.Laming, "Systems applications of fibre Bragg

grating technology," *Optoelectronics and Communications Conference (OECC/IOOC 2001),* 2001.

[2-31] M. I. P.C.Teh, J.H.Lee, P.Petropoulos, D.J.Richardson, "A 4-channel WDM/OCDMA system incorporating 255-chip 320 Gchip/s quaternary phase coding and decoding gratings," *Optical Fiber Communication (OFC 2001),* vol. Postdeadline, 2001.

[2-32] W. H. Loh, M. J. Cole, M. N. Zervas, S. Barcelos, and R. I. Laming, "Complex Grating Structures with Uniform Phase Masks Based on the Moving Fiber-Scanning Beam Technique," *Optics Letters,* vol. 20, pp. 2051-2053, Oct 15 1995.

[2-33] P. C. Teh, M. Ibsen, J. H. Lee, P. Petropoulos, and D. J. Richardson, "A 4-channel WDM/OCDMA system incorporating 255-chip 320 Gchip/s quaternary phase coding and decoding gratings," *Optical Fiber Communication (OFC 2001),* vol. Postdeadline, 2001.

[2-34] P. Petropoulos, N. Wada, P. C. Teh, M. Ibsen, W. Chujo, K. I. Kitayama, and D. J. Richardson, "Demonstration of a 64-chip OCDMA system using superstructured fiber gratings and time-gating detection," *IEEE Photonics Technology Letters ,* vol. 13, pp. 1239-1241, 2001.

[2-35] M. R. Mokhtar, M. Ibsen, P. C. Teh, and D. J. Richardson, "Reconfigurable multilevel phase-shift keying encoder-decoder for all-optical networks," *IEEE Photonics Technology Letters,* vol. 15, pp. 431-433, Mar 2003.

Chapter 3

Characterization of fibre Bragg gratings

In order to assess the quality of our SSFBGs, especially to investigate the thermally-induced phase-shift in the code-reconfigurable device, it is necessary to characterize the gratings completely, in terms of both amplitude and phase, to obtain the grating's modulation profile. During my research, the feasibility of using Frequency-Resolved Optical Gating (FROG) to characterize the spatial effective refractive index profile in Bragg gratings has been investigated. In this chapter, a brief overview was firstly given about the existing grating characterization techniques which are implemented in the spatial domain, spectral domain and the temporal domain. According to FBG theory, the temporal impulse response of the grating approximates to its spatial refractive index profile in the weak grating limit. Thus the problem of characterising weak gratings can be turned into characterising an optical signal incident upon and reflected from the FBGs. In the case of high-speed optical telecommunications, the traditional electronic intensity measurements are not sufficient to investigate the properties of these optical signals. However, the well-known techniques initially developed to measure ultrafast laser pulses such as SHG-FROG, which characterizes the optical signal in terms of a spectrogram, can be used

to reconstruct the intensity and phase profile of the optical signals under test. Among the various FROG techniques, the results obtained by SHG-FROG and EAM-FROG for FBG characterisation has been comparatively investigated. It is initially showed that the SHG-FROG technique, which is successfully used to measure ultrashort pulses, is not suitable for measuring optical signals reflected from FBGs, which have more complicated profiles and much longer pulse durations. the ability of EAM-FROG to characterise FBGs is confirmed by starting with some simple SSFBGs which have a single abrupt phase-shift at the centre of the SSFBGs. I then moved on to characterise complex 15-chip quaternary phase shift SSFBGs. Also using this technique, the thermally-induced phase distribution in our code reconfigurable grating device has been investigated. My study shows that EAM-FROG is able to provide accurate, unique and useful information in terms of grating characterization and performance. The results obtained were used in our further system experiments.

3.1 Grating Characterization

3.1.1 Techniques overview

There are several approaches to characterize gratings: directly or indirectly, in the spatial domain, spectral domain or in the time domain.

In the spatial domain, the variation of refractive index along the fiber grating is measured. Several techniques, such as side-scattering [3-1, 2], heat-scan [3-3], and optical low coherence reflectometry (OLCR) [3-4,5,6], have been reported to perform the spatial characterization. Although these techniques can measure the amplitude of the refractive index profile of FBGs, only the OLCR technique in [3-6] was demonstrated to be able to measure spatial phase shift and chirp of the FBGs.

On the other hand, since in most cases, it is possible to obtain the length of the gratings and the reflectivity response in the spectral domain and the time domain of the gratings, the quality of the grating can be roughly assessed by assuming the grating design profile, simulating the reflectivity response of the assumption and then comparing it with the experimental measurement. This solution thus leads to characterizing the optical response in the spectral domain and the time domain. It is called indirect characterization.

In the spectral domain, the measurements primarily include the reflectivity spectra and time delay response as a function of wavelength. The reflectivity spectra can be measured directly by coupling white light, or the ASE from an optical amplifier, into the FBG, or by scanning a tunable laser source across the FBG operating band, then measuring the reflected optical intensity spectrum using an optical spectrum analyzer (OSA). The principle of measuring the time delay response is to compare the phase difference between the reflected signal and a modulated input signal using a vector-voltmeter. The input signal is a tunable single-frequency source, and is modulated by a chosen RF signal using an electro-optic modulator. By scanning the wavelength of the single-frequency source across the FBG band, it is possible to accurately measure the phase difference between the reflected and reference RF-modulated signals, and thereby to determine the time delay response of the FBG.

The index profile can be reconstructed from the complex Bragg reflection spectra, by integrating the coupled-mode equations to build the relationship between the complex coupling coefficient and the complex reflectivity spectrum [3-7, 8]. Being a linear system, the complex reflection spectrum of a grating is the inverse Fourier transform of its temporal impulse response. When the input pulse is short

enough compared to the chip-length of the grating, the reflection response is a good approximation to its impulse response. As it is mentioned at the beginning, the refractive index profile can be approximately obtained from the temporal impulse response. Based on these principles, the spatial refractive index profile of a FBG can be determined by fully characterizing the temporal reflection response of the grating. The problem thus leads to how to measure the intensity and the phase of a reflected optical pulse accurately.

3.1.2 SHG-FROG

A common technique to measure the length of an ultrashort pulse is second-harmonic-generation (SHG) autocorrelation [3-9]. However it gives no direct information on the pulse shape and phase, and very different pulses can yield the same autocorrelation traces. Thus the pulse shape must be assumed and the resulting pulse length depends sensitively on the shape chosen. Therefore it is not a suitable technique to measure a complex pulse.

A much more powerful autocorrelation-type approach, that can be used to achieve complete characterization, is Frequency-Resolved Optical Gating (FROG), which involves simultaneously both temporal and frequency measurements. FROG records the spectrogram, which is the spectrum of the interaction between the input pulse and the gate as a function of time delay. The temporal and spectral profiles of the input pulse (intensity and phase) can be retrieved from the spectrogram. According to the different geometries used to perform autocorrelation, there are several types of FROG, such as polarization gate (PG), self-diffraction (SD), second-harmonic generation (SHG), third-harmonic generation (THG), and transient grating (TG) [3-10, 11].

Figure 3.1 shows the schematic of SHG-FROG[3-12], the most commonly used FROG technique in the optical telecommunications area. A beamsplitter splits the input into probe and gate beams. The two beams are focused into a SHG crystal. The spectrum of the second harmonic is recorded as a function of delay between the two replicas of the input pulse.

$$I_{FROG}(w,t) = \left| \int_{-\infty}^{+\infty} E(t)G(t-t)\exp(-iwt)dt \right|^2$$

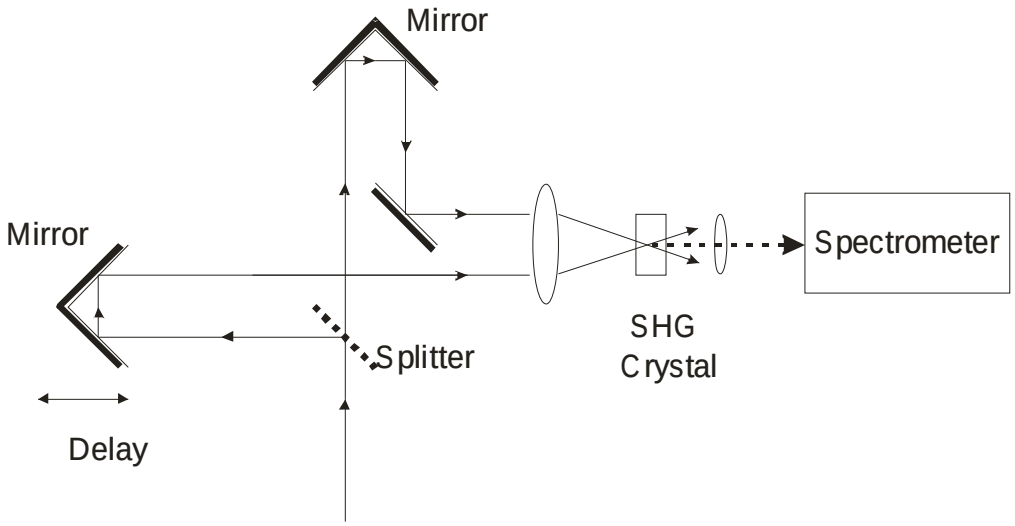

Figure 3.1 Operating principle of SHG-FROG

Figure 3.2(a) gives an example of the spectrogram for a 2ps mode-locked erbium-doped fiber ring laser (EDFL) pulse with a central wavelength of 1551.42nm. The spectrogram was obtained with commercial SHG-FROG equipment in our lab (Southern Photonics HR100 Pulse Analyser). Figure 3.2(b) shows the retrieved profile of the pulse.

Just like the autocorrelation, the SHG-FROG trace is a time symmetric function. As a result, it has an ambiguity in the direction of time. The pulse E(t), and its time-reversed replica E(-t), both yield the same SHG-FROG spectrogram. Another ambiguity in SHG-FROG, is that two separate pulses with a relative phase difference of φ or $\varphi+\pi$ produce the same spectrogram [3-13]. In our case, the reflected pulse from the grating has a complicated structure and a long pulse duration of up to hundreds of picoseconds, which requires better resolution of the spectrogram. Since the SHG bandwidth of the crystal is inversely proportional to its thickness, a thinner crystal has a larger bandwidth, but is less efficient in its SHG effect. Thus there is a trade-off between sensitivity and resolution. Additionally, it is quite difficult to retrieve a satisfactory result if the spectrogram is gated by the complicated long pulse itself.

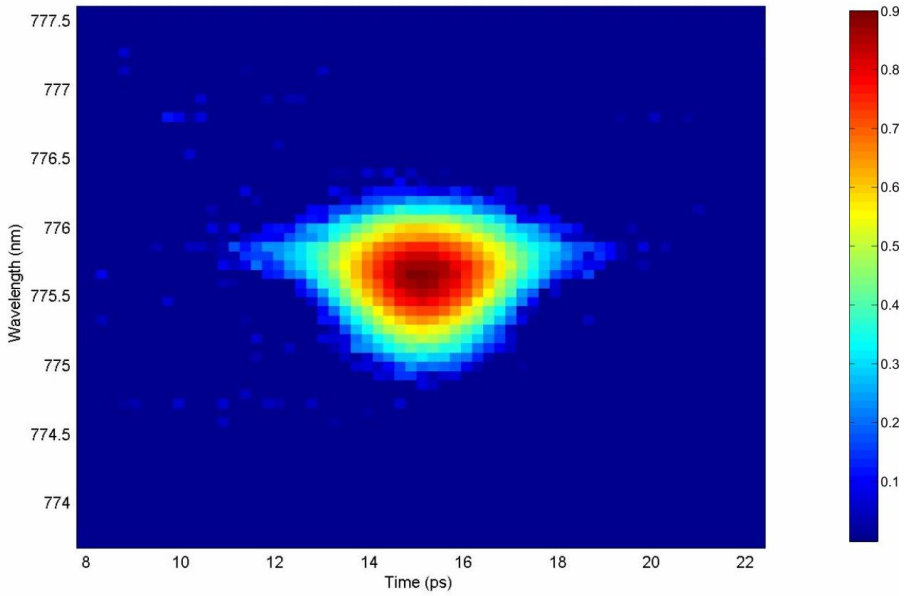

(a) SHG-FROG spectrogram for a 2ps mode-locked EDFL pulse with a central wavelength of 1551.42nm

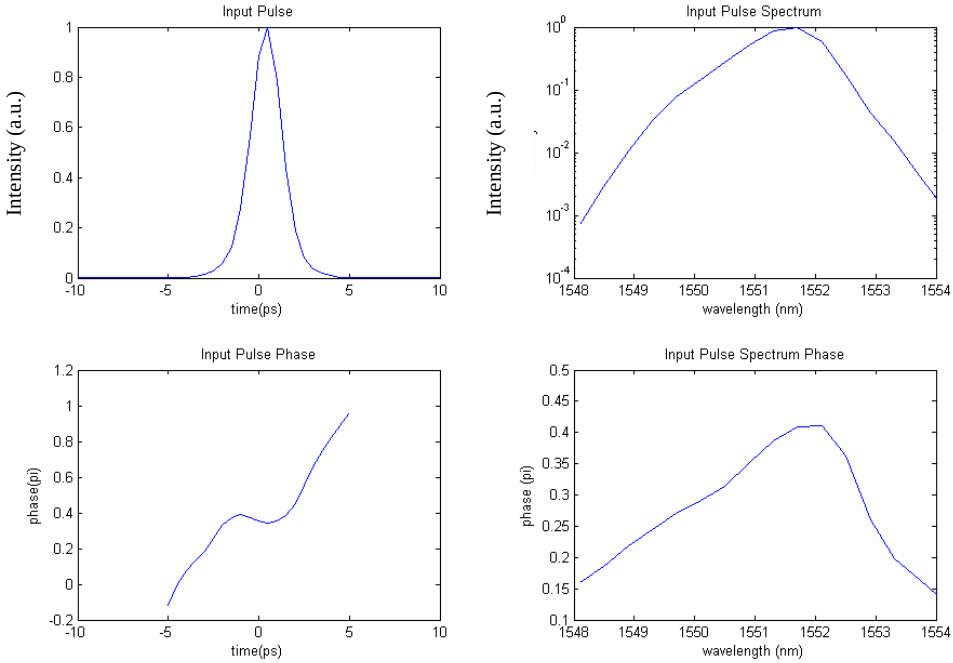

(b) SHG-FROG retrieved profile of the 2ps EFRL pulse

Figure 3.2 An example of SHG-FROG charaterization

3.1.3 EAM-FROG

The development of deconvolution algorithms allow the use of two different pulses, instead of replicas of the same pulse, to produce the spectrogram. Dorrer and Kang demonstrated, in 2002, that it is possible to implement the gating with a

modulator [3-14], instead of relying on nonlinear optics. Dr. Benn Thomson and Mr. Michael Roelens, in our lab, implemented the approach which incorporates an Electro-Absorption Modulator (EAM) and we call it EAM-FROG [3-15, 16]. This approach utilized the commonly available devices and components in the telecommunications labs and thus is particularly suitable for our uses to characterize telecommunication grade signals. Figure 3.3 shows the basic EAM-FROG schematic, in which the input pulse is split into two replicas by a 3dB coupler. One of the replicas is the probe signal, and passes through the EAM. The other replica, which is the gate signal, is delayed with a varying time, amplified by an EDFA to boost the optical power, then converted into electrical current by a photon detector to drive the EAM. The gated signal is then spectrally resolved by an OSA. The time delay is realized with a free space delay stage, which has a maximum delay of 220ps.

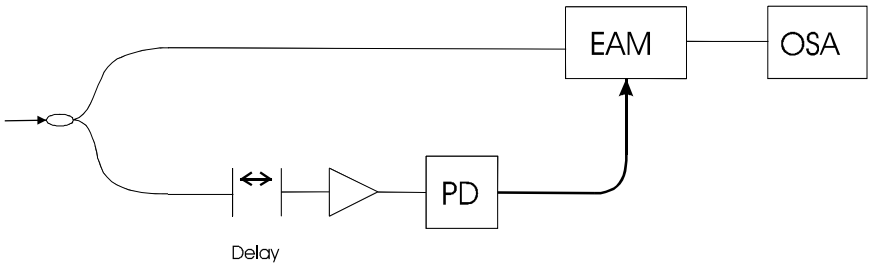

Figure 3.3 The basic EAM-FROG setup

The EAM-FROG setup was modified to meet the needs of characterizing the optical coded pulses generated by the gratings, since the pulses reflected from a grating are more than tens of picoseconds long with a complicated pulse structure. Basically, the gate signal is the short pulse, which is also used as the input pulse for the grating. The probe signal is the complicated pulse reflected from a grating. The schematic is shown in figure 3.4.

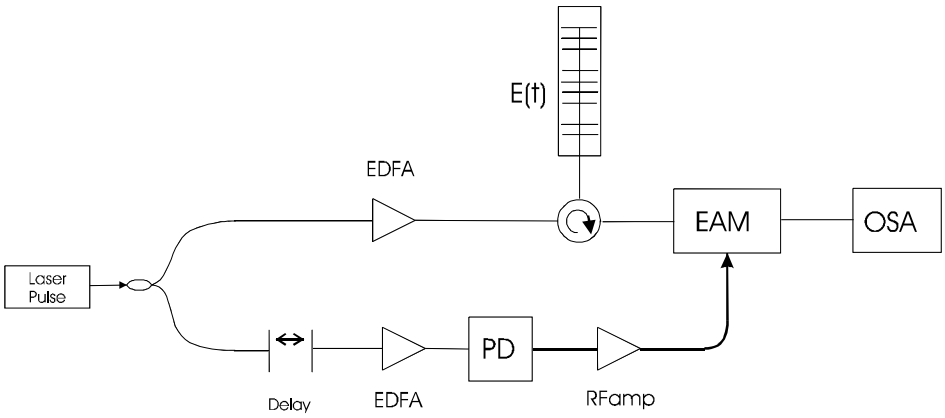

Figure 3.4 EAM-FROG setup using a short pulse to gate a long duration pulse

Furthermore, as the SSFBGs used in the system experiments normally have a length of tens of millimeters, accordingly, the coded optical pulses have a length of hundreds of picoseconds. To characterize a pulse longer than 220ps, it is possible to scan a different part of the pulse (up to 220ps) for each delay stage session, and then stitch the multiple scans together to form a whole spectrogram. This is achieved by controlling the position of the gate signal relative to the probe signal before applying the delay stage. Theoretically this technique allows the measurement of pulses of any length.

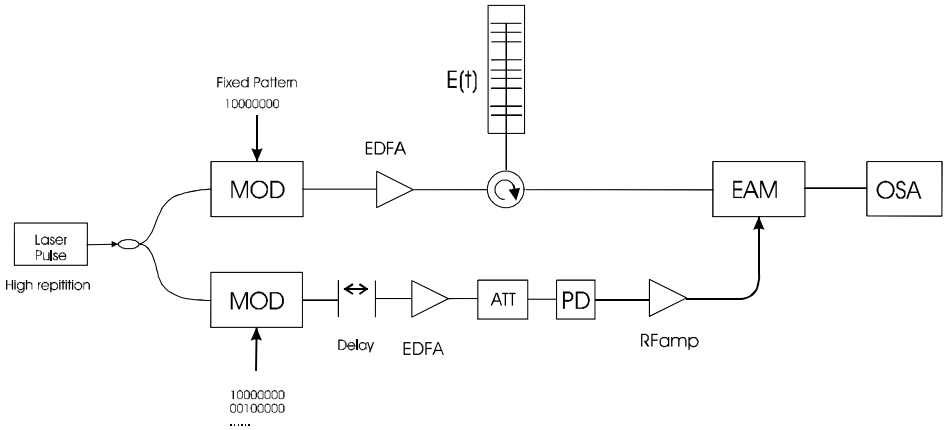

(a) EAM-FROG setup to measure a long pulse that exceeds the delay stage time

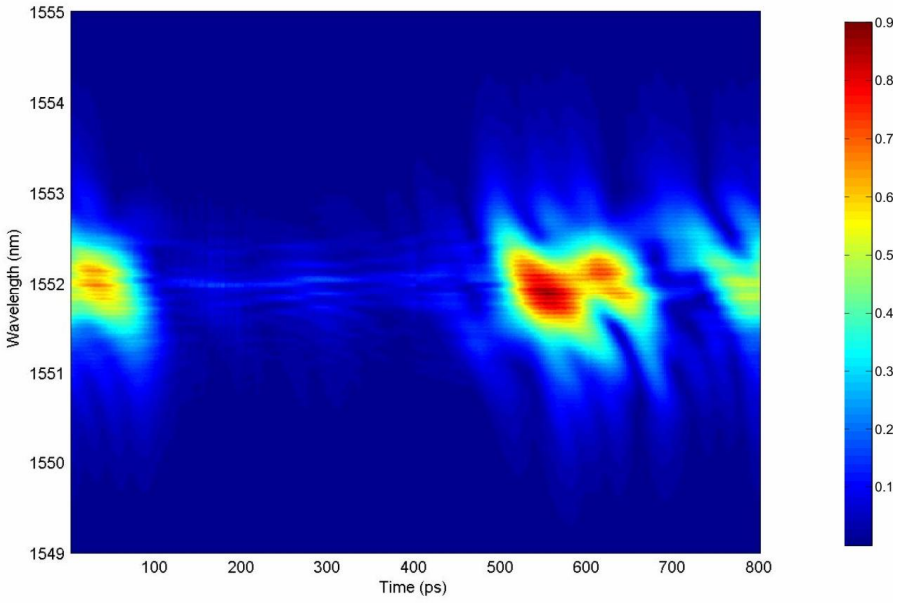

(b) The stitched spectrogram of a 400ps pulse. The spectrogram was sampled every 2ps over a time delay of 800ps; the spectrum resolution is 0.01nm.

Figure 3.5 (a) EAM-FROG setup to measure a long pulse that exceeds the delay stage time; (b) the stitched spectrogram of a 400ps pulse

Figure 3.5 (a) illustrates the improved setup. A high repetition rate pulse source, for example at 10GHz, was used as the input pulse. The input pulse is introduced in Section 3.1.4. If the reflected pulse from the grating is 400ps, it is required to cut the pulse rate down to 1.25GHz to ensure the reflected pulses are well separated. To do this, a $LiNbO_3$ modulator is used. The modulator is driven by a data pattern, which is composed of one '1' every seven '0's, thus only one of the eight consecutive pulses goes through the modulator and the pulse repetition rate is gated down. This scheme was also used in the following system experiments in order to gate down the repetition rate. Another synchronous pattern was applied to modulate the gate pulse. To change the relative position to the signal under test, it is to simply change the position of "1" in the pattern for the probe pulse, to scan a different part of the long duration pulse. Figure 3.5 (b) gives an example of the stitched spectrogram for a 400ps pulse with a period of 800ps. Because the location of the pulse in the 800ps period is unknown, it is necessary to scan the whole 800ps period with four separate scans.

3.1.4 The input short pulse

In my characterization of the gratings using the EAM-FROG technique, three different kinds of short pulses were employed in different cases. The first kind was the 2ps pulses generated by an actively mode-locked EDFL, operating at a repetition rate of 10GHz. However, this pulse source is not stable enough due to its long cavity length. Because the gratings have a narrow reflection bandwidth and are quite sensitive to the drift of the input pulse wavelength, especially for the realistic multi-chip SSFBGs in our OCDMA experiments, the performance of the measurements was affected by this laser pulse. Much more stable pulses than the mode-locked EDFL were generated by a Gain-switched laser and EAM-carved pulse, with a pulse width of 6ps and 25ps respectively.

Note that, although the resolution of the EAM-FROG technique is largely tolerant to the probe pulse width, the temporal resolution of the reflected pulse (and thus the equivalent spatial resolution of the refractive index profile of the grating) is determined by the input pulse width. The 2ps pulses were used to characterize the single phase shift gratings, which have a relative simpler structure and shorter length than the realistic SSFBGs used in my OCDMA and OPS system experiments. While

the 6ps and 25ps pulses were used to characterize the realistic multi-chip gratings. These short pulses were also used in my following experiments where applicable.

3.2 The characterizations of SSFBGs with single discrete phase shift

In order to verify the capability of the EAM-FROG technique, eight simple SSFBGs have been prepared, with no, or only one, discrete phase shift at the centre of the grating. The four kinds of phase shifts are: uniform (no phase shift), 0.5π, π, and 1.5π. These phase values are used in a quaternary phase code system. Two gratings were made for each kind of phase shift, with different reflectivity strength, 50% and 99.9%. Defining by the corresponding transmission loss, we call them 3dB gratings and 30dB gratings respectively. Each grating has a length of 5mm, which corresponds to a reflected pulse width of 50ps. The spectral bandwidth of the uniform gratings is around 0.7nm. For the other gratings with a phase shift, the bandwidth is around 0.3nm.

First of all, SHG-FROG was used to characterize the reflected pulse from the 30dB strong gratings. The 2.2ps pulses generated by the ring laser were used as the input pulses. The retrieved results are shown in Figure 3.6. The ultra short pulses ensure that the reflected pulses have a high resolution to present the code information of the grating.

As it can be seen for the strong reflectivity (30dB) gratings, the output pulses are similar regardless of the different phase shift. And the pulse width is much shorter than the expected 50ps. This is due to the strong reflectivity of the grating. Most of the light is reflected at the starting end and cannot penetrate the whole grating. Thus the input pulse experiences little phase shift and the output pulse looks similar. Although theoretically the strong grating can reduce the insertion loss, it fails to reflect all the coding information on the grating and thus is not suitable for optical coding applications. In the following discussion, the strong grating is ignored and it is concentrated on the 3dB gratings.

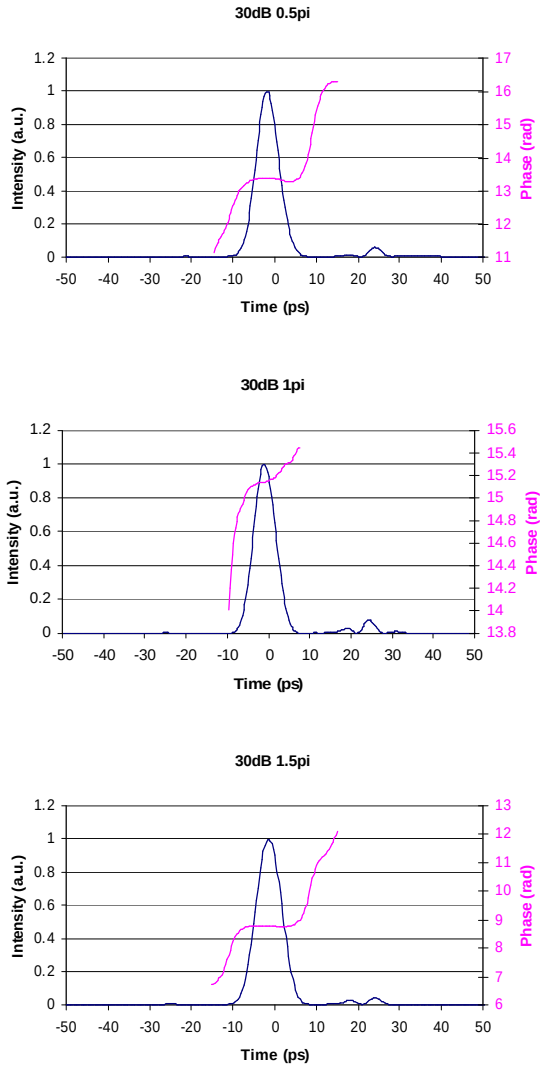

Figure 3.6 SHG-FROG retrieved results for 30dB strong gratings with a single phase shift of 0.5π, π, 1.5π respectively.

The optical reflectivity spectrum of the 3dB gratings was measured using an optical spectrum analyser (OSA). The measured results are plotted in Figure 3.7, together with the simulation results.

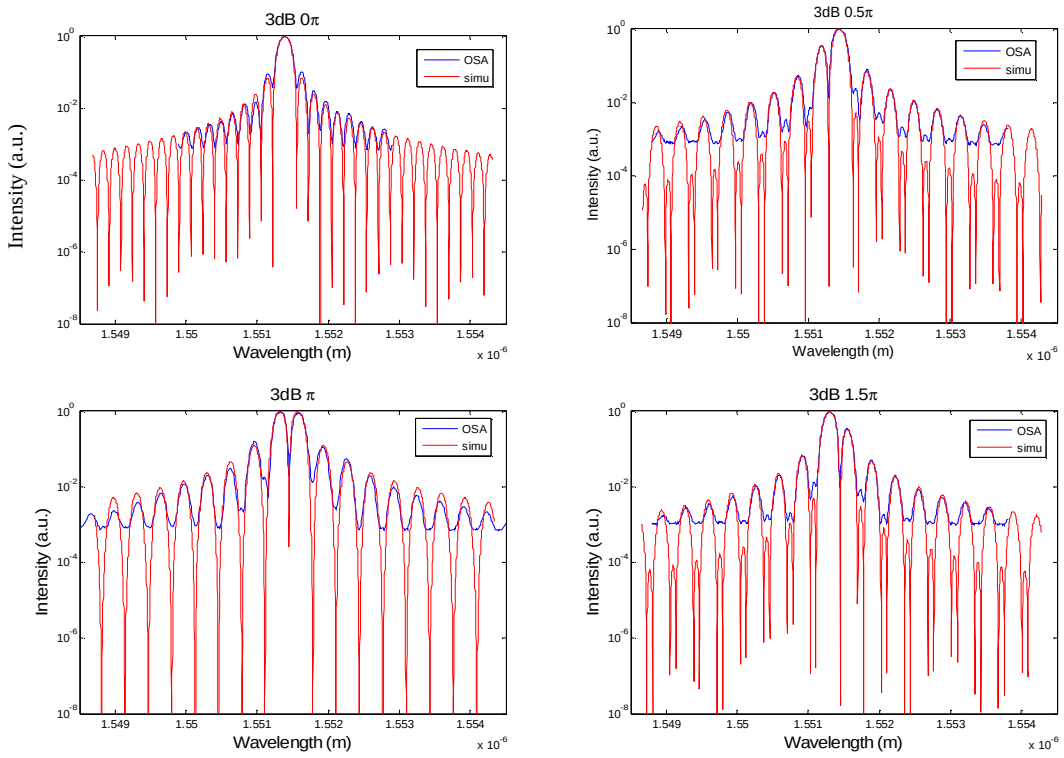

Figure 3.7 The measured and calculated reflectivity spectra of the 3dB grating with a single phase shift of 0π, 0.5π, π, 1.5π respectively.

The measured peak reflectivity of these gratings is about 50%, which meets our design requirement of '3dB transmission'. The measured spectra agreed with the simulated spectra excellently. The results suggest that the gratings meet the design requirement in the spectrum domain. Next, these gratings were characterized in the time domain, using SHG-FROG and EAM-FROG respectively.

The 2.2ps mode-locked EDFL pulses were used as the input signal. The SHG-FROG retrieved results, compared with the simulated results, are shown in Figure 3.8.

For the 3dB gratings, it could be seen that the reflected pulse has a length of about 50ps with a more complicated structure than the hyperbolic-sech profile and that a different grating phase shift causes different output pulse shapes. It shows that the SHG-FROG retrieved result tends to have a shorter pulse width and the retrieved phase roughly agrees with the simulation results. Considering that the pulse being characterized has a pulse width of only 50ps, which is not very long, and a relatively simple pulse structure, it can be claimed that the SHG-FROG technique performs reasonably for this kind of pulses.

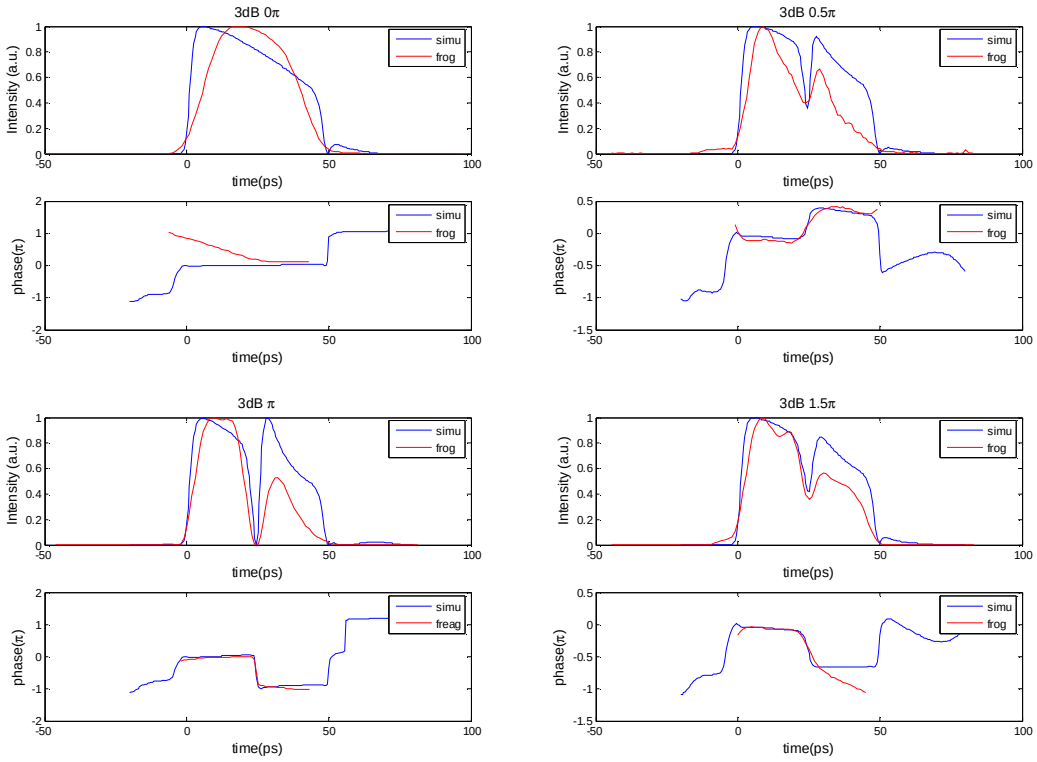

Figure 3.8 SHG-FROG retrievals compared with simulation results for different 3dB gratings

To investigate the capability of the EAM-FROG, I characterized the four 3dB gratings with the EAM-FROG setup as shown in Figure 3.4. The 2.2ps pulse was also used as the input pulse. Figure 3.9 shows a typical measured (a) and retrieved (b) spectrogram of the 2.2ps pulses reflected from the π/2 phase shifted grating.

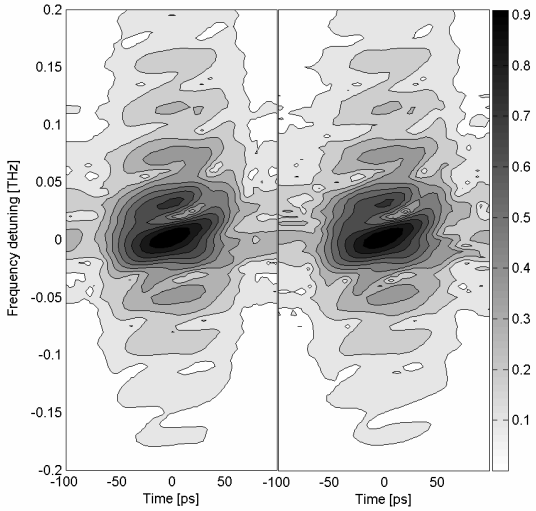

(a) (b)

Figure 3.9 Measured (a) and retrieved (b) spectrogram of the 2.2ps pulses reflected from the π/2 phase shifted grating

As can be seen, excellent agreement between the retrieved and experimental spectrograms is obtained, confirming the quality of the measurement processes.

The EAM-FROG retrieved temporal results are compared with the simulation results in Figure 3.10. Figure 3.11 shows the corresponding pulse spectra. Compared with the results obtained by the SHG-FROG, the EAM-FROG results display some more interesting features. The rising and falling edges of the pulse are now well resolved. The phase retrievals are in excellent agreement with the designed conditions. It also displays clearly that the phase shift has an abrupt change at the centre of the grating. In addition, the satellite pulses following the main pulse, as well as the associated π phase shift at the boundary of these satellite peaks, were also present in the EAM-FROG retrievals. The satellite pulses which originate from the reflection by the sidelobes of the grating's reflection spectrum (as shown in Figure 3.7) and the multiple reflections between the chips of the grating[3-17], have very low intensity. The high accuracy and sensitivity of the EAM-FROG are due to the high resolution of the OSA and the fact that no nonlinear process is involved.

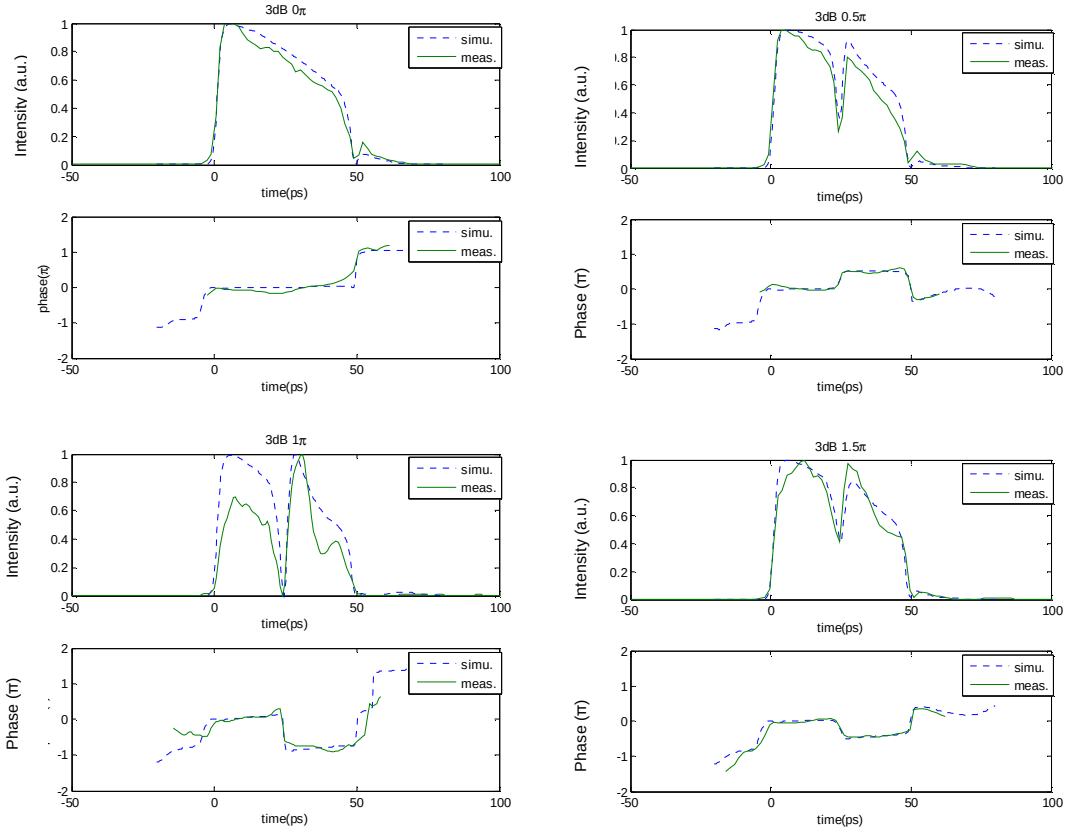

Figure 3.10 EAM-FROG temporal retrievals compared with simulation results

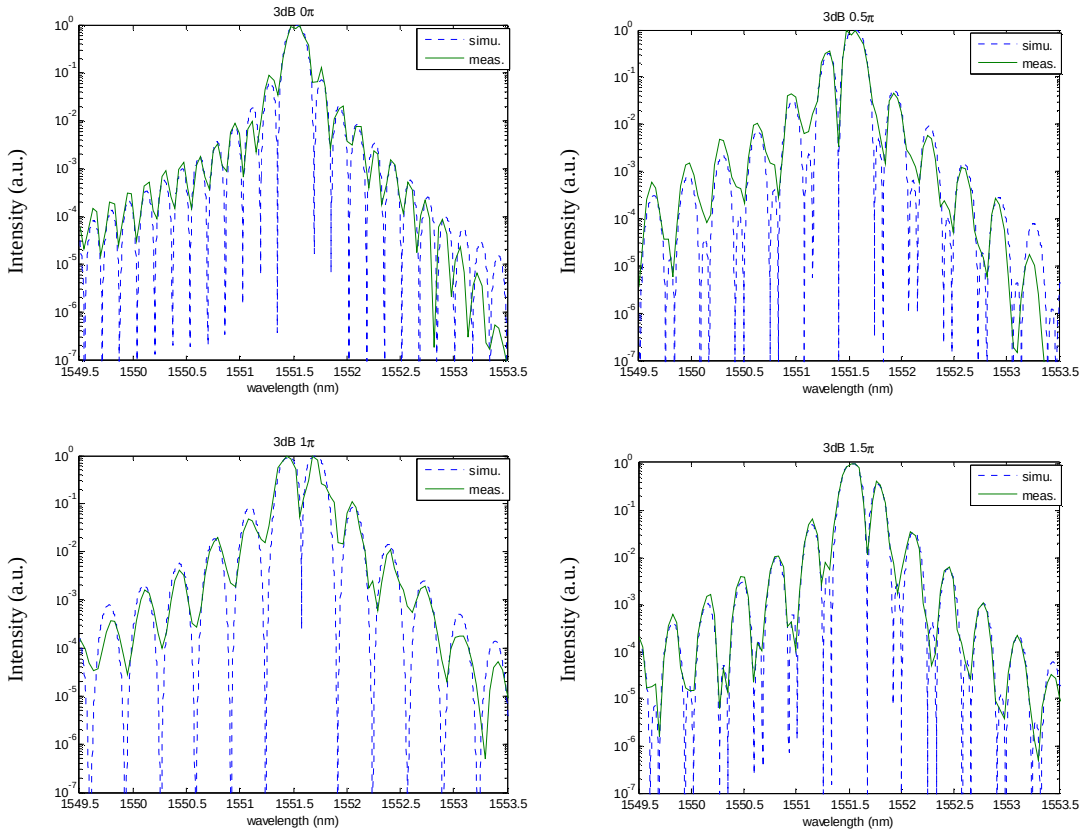

Figure 3.11 EAM-FROG measured spectra compared with simulation results

Note that one disadvantage of the EAM-FROG characterization is that it takes a relatively long time to complete the whole scan, especially when scanning a long pulse. It thus places a high requirement on the stability of the input pulse and the environment, as the grating is sensitive to the input pulse wavelength and any environmental change. Considering that the input pulse generated by the ring laser is not very stable, in terms of its central wavelength, the agreement is still very encouraging. Better results would be expected if the input pulses were more stable.

3.3 15-chip fixed-coded SSFBGs

After successfully characterizing the single discrete phase-shift SSFBGs, it gave confidence to explore the ability of the EAM-FROG technique to investigate more complicated gratings. The gratings used in the applications of OCDMA and optical packet switching have many more chips than one single phase shift. It is a challenge to characterize this kind of encoded pulse, which has a much longer pulse length and a much more complicated pulse structure. For example, a 15-chip, 40mm long grating generates a reflected pulse of 400ps width. The pulse is too long to be characterized

by SHG-FROG. The feasibility of characterizing complex gratings was investigated with our EAM-FROG setup.

Two pairs of SSFBGs, namely Q1, Q1*, Q2, Q2*, have been fabricated for the following OCDMA system experiments. All the gratings have 15 chips with a chip length of 2.5mm, resulting in the total grating length of 37.5mm.

Q1 = [3 1 0 1 1 2 0 3 2 2 2 3 1 1 1]

Q1*=[1 1 1 3 2 2 2 3 0 2 1 1 0 1 3]

Q2 = [3 2 1 1 1 1 2 3 2 3 1 0 0 1 0]

Q2*=[0 1 0 0 1 3 2 3 2 1 1 1 1 2 3]

where one unit means a $\pi/2$ phase shift.

The Bragg wavelength of the SSFBGs is about 1551nm, which can be tuned by stretching the gratings. The measured peak reflectivity strength for these SSFBGs is around 40%.

Two fixed coding gratings labelled as Q1 and Q1* were characterized. Firstly, the measured reflectivity spectra of the fixed-coded SSFBGs were calculated and compared. The results are shown in Figure 3.12. The OSA has a resolution of 0.05nm. The measured results agreed quite well with the calculated spectrum.

The EAM-carved 25ps pulse was used as the input. The repetition period of the input pulse should be longer than the duration of the reflected pulse, which is 400ps in this case. The EAM-FROG setup, as in Figure 3.5, was used to cut the 10GHz EAM carved pulse train down to 1.25GHz, which corresponds to a period of 800ps, to ensure that the pulses reflected by the grating are not overlapped. Given that the maximum delay time of our delay stage is 220ps, four scans were needed to complete the whole scan covering the 800ps period.

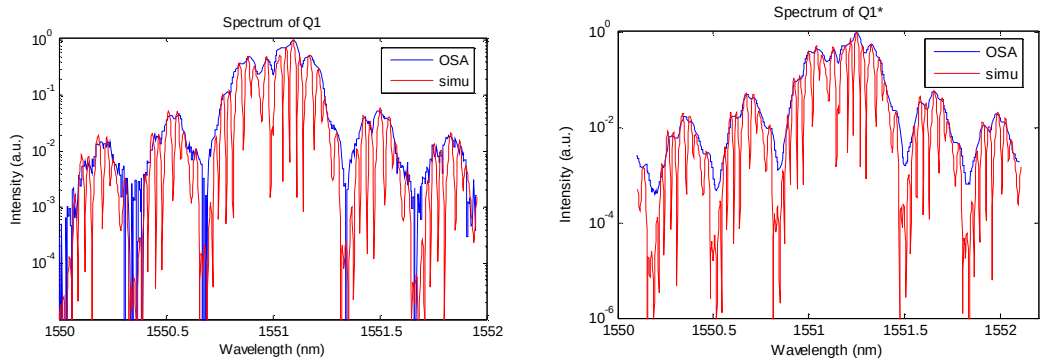

(a) Q1 *(b) Q1**

Figure 3.12 The reflectivity spectra of 15-chip fixed SSFBGs.

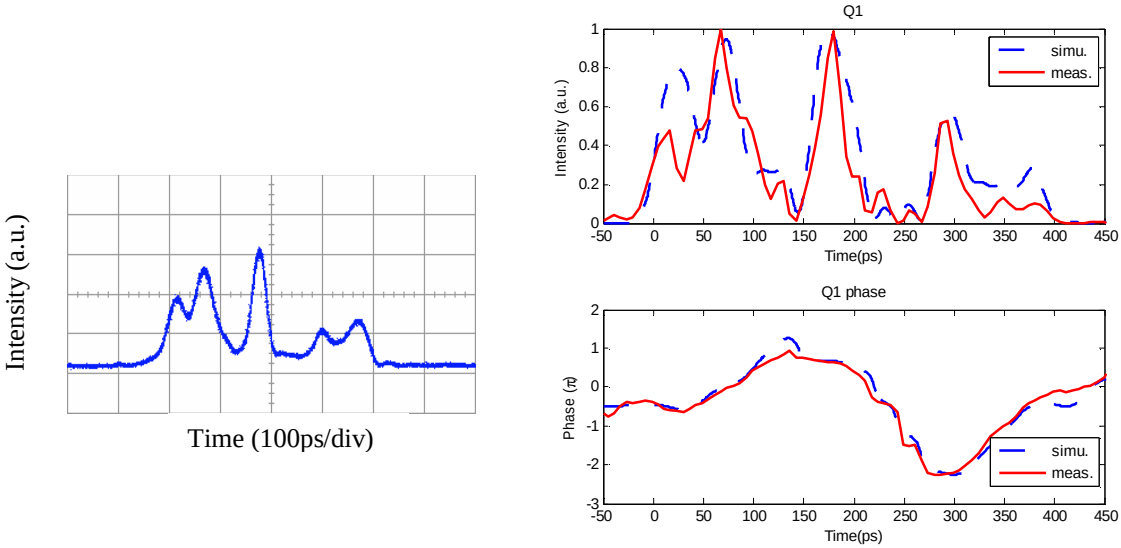

(a) Q1

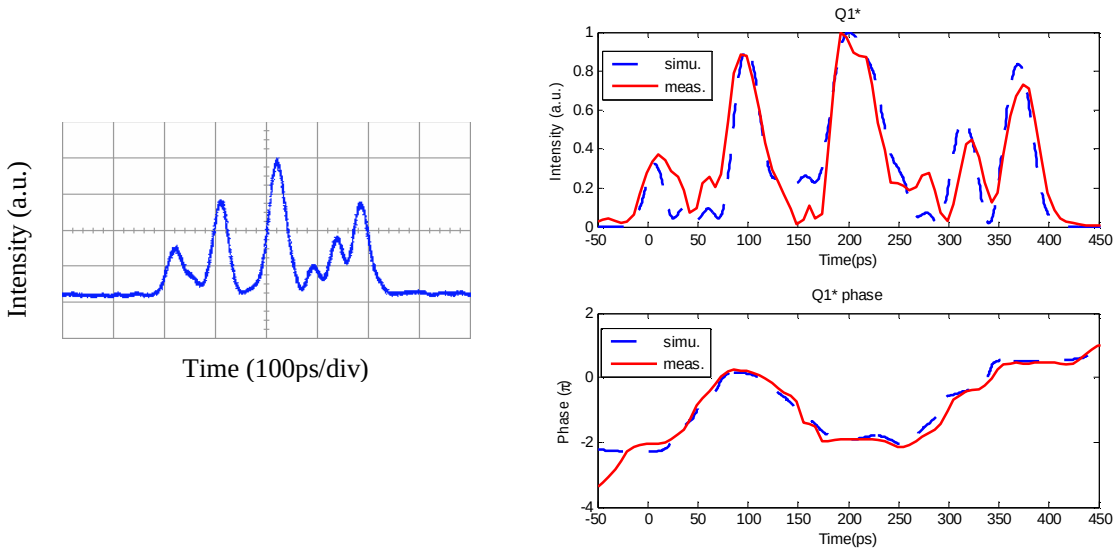

*(b) Q1**

*Figure 3.13 EAM-FROG retrievals compared with simulation results, and the oscilloscope trace for the different SSFBGs labelled as Q1, Q1**

Figure 3.13 shows the simulated and retrieved results as well as the oscilloscope traces. The retrieved intensity profiles are in good agreement with the directly measured results obtained by the oscilloscope. While the retrieved intensity profiles generally match the simulation results, the retrieved phase of gratings Q1and Q1* agreed excellently with the simulated results. This is partly due to the bandwidth

limitation of the oscilloscope and also probably because the actual grating profile is not exactly the same as the simulation condition, and the grating response is quite sensitive to the wavelength and environment changes in terms of temporal intensity. However, the phase shift along the grating is hardly affected.

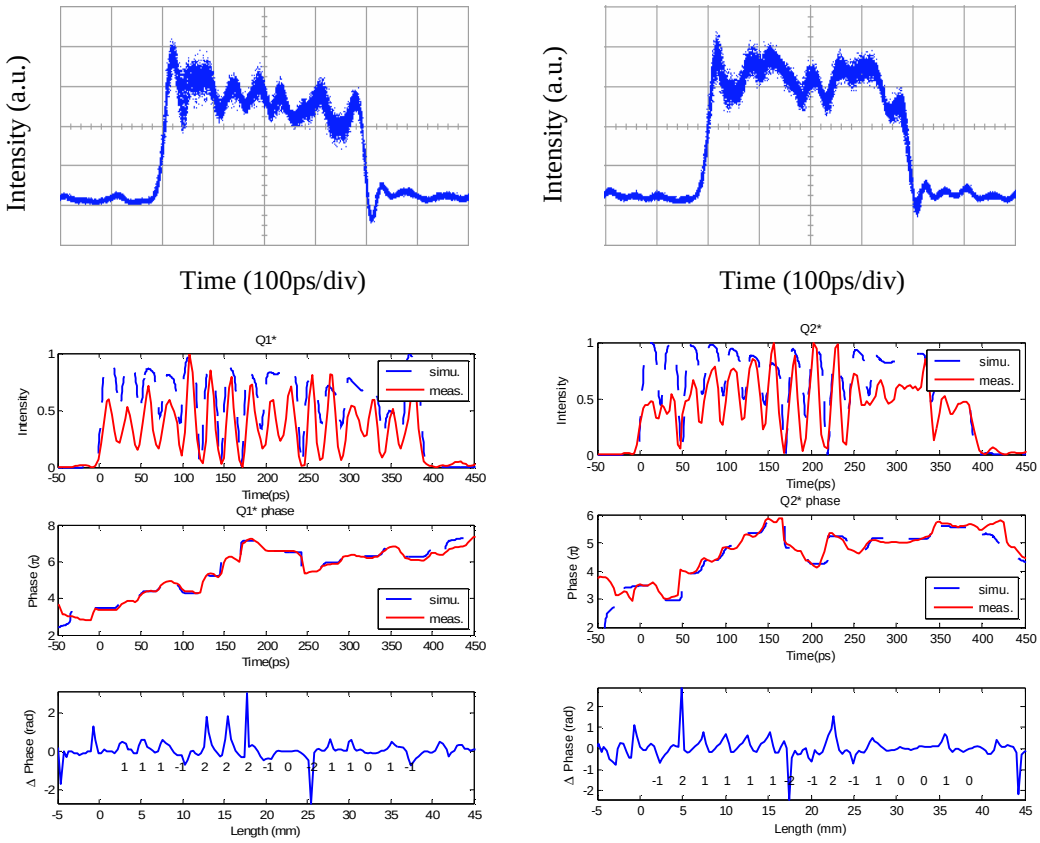

(a) *(b)*

Figure 3.14 EAM-FROG retrievals with 6ps input pulse compared with simulation results, and the oscilloscope trace (100ps/div) for the SSFBGs (a)Q1 and (b)Q2**

As we have shown in the single phase shift simple grating experiments, a shorter input pulse can produce higher resolution of the phase shift in the reflected pulses. I used the 6ps pulses as the input pulse to characterise the gratings Q1* and Q2*. The retrieved results, shown in Figure 3.14, can distinguish the chip slots clearly. Even the 20GHz oscilloscope cannot reach the resolution. The retrieved phase profile displays the abrupt phase shift between the chips and matched the design profile excellently. The deduced local phase distribution shows directly the code written on the SSFBGs. For grating Q1*, the designed code is [1 1 1 3 2 2 2 3 0 2 1 1 0 1 3], where one unit means a $\pi/2$ phase shift. The code is equivilant to [1 1 1 -1 2 2 2 -1 0 2 1 1 0 1 -1]. For

grating Q2*, the designed code is [3 2 1 1 1 1 2 3 2 3 1 0 0 1 0], which is equivilant to [-1 2 1 1 1 1 -2 -1 2 -1 1 0 0 1 0]. Note that, theoretically, the SSFBGs have an abrupt phase shift between the adjacent chips, while the deduced local phase distribution displays a narrow distribution. This is merely because of the spatial resolution defined by the 6ps input pulses.

3.4 The characterization of reconfigurable gratings with a simple tunable phase-shift

Next, this technique was used to investigate the behaviour of the tunable phase shift gratings. Firstly, similarly to the characterization of the fixed-coded SSFBGs, a simple case was characterized, the phase-shift introduced by a single electrical-heating wire. The preliminary result was obtained by using 25ps EAM-carved pulse as the input pulse. The study revealed important features of the tunable phase-shift. Secondly, the 6ps gain-switched laser pulses were used to obtain more detailed and accurate results. Thirdly, thanks to the reconfigurability of the tunable FBG device, it is possible to investigate several simple tunable phase-shift combinations to obtain a better understanding of the tunable device. Finally, the effect of different electrical-heating wire diameters on the thermally-induced phase-shift was investigated. These results highlight the feasibility of the code-reconfigurable FBG device in a more straightforward way and are important for us to design a proper code-reconfigurable FBG device for the following reconfigurable OCDMA and packet-switching system experiments.

3.4.1 25ps EAM-FROG with single tunable phase-shift

A 17mm long tunable grating has been prepared to investigate the thermally-induced phase-shift in the reconfigurable grating. One fine tungsten wire (18μm in diameter) is placed across the centre of the 17mm uniform SSFBG. Figure 3.15 illustrates the structure of the tunable device. By controlling the current flowing through the tungsten wires to heat the grating, we can achieve the desired phase shift in the grating. By comparing the simulation and measurement in the spectral domain, the 0.5π, π, 1.5π phase shift corresponds to a heating current of 52mA, 70mA, and 84mA respectively. The measured reflectivity spectra of the grating at these heating

currents are shown in Figure 3.16. The thermally-induced spectrum change can be observed for different heating currents.

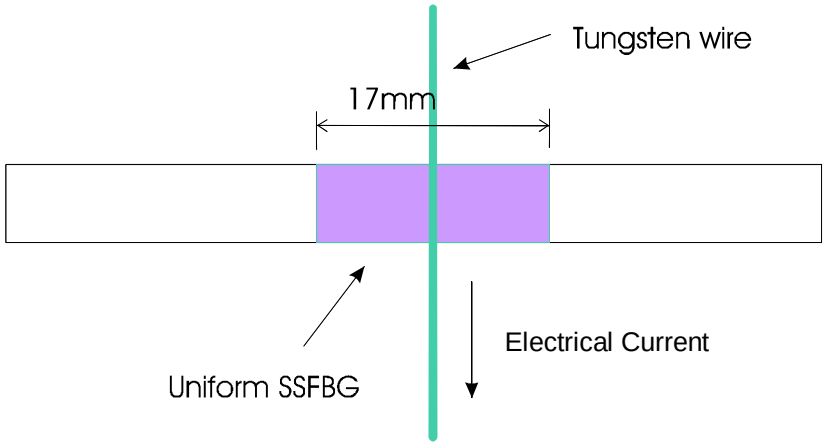

Figure 3.15 Schematic structure of a simple phase tunable SSFBG

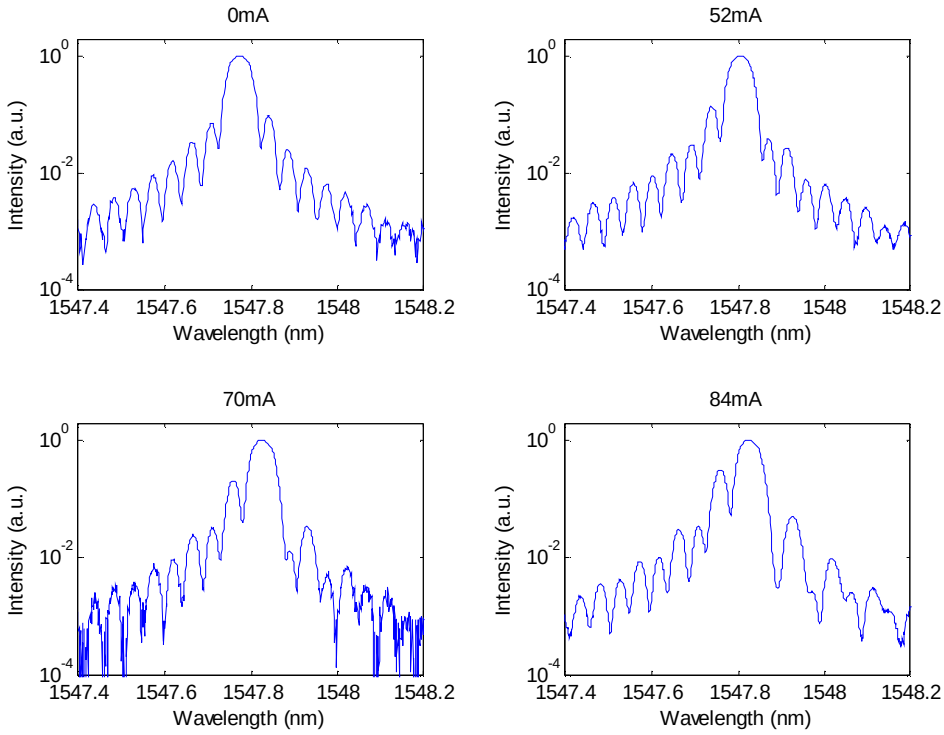

Figure 3.16 Tunable SSFBG spectral reflectivity profile for different heating current

To perform a more stable EAM-FROG characterization, the 25ps EAM carved pulse was used as the input pulses to do some preliminary measurements and then moved on to use 6ps gain-switched laser pulses as the input pulses to verify the results. Both of the two pulses are more stable than the 2.2ps EDFL pulse which we used in the previous experiments. The reflected pulse has a duration of about 170ps. The oscilloscope trace and EAM-FROG retrievals are shown in Figure 3.17. On the

retrieved graphs for each heating current, from top to bottom, the first one is the retrieved pulse intensity, which is directly comparable to the oscilloscope trace on the left side. The second one is the retrieved phase profile of the reflected pulse, which shows the phase-shift along the pulse. The third one is the phase distribution along the grating, which is derived by differentiating the retrieved phase profile (the second graph), and converting the pulse duration into grating length (for 0mA case, there is no phase-shift being introduced along the pulse, thus the phase-distribution is not shown). In Figure 3.17(e), the three different thermally-induced phase distributions in (b,c,d) are superposed together for comparison.

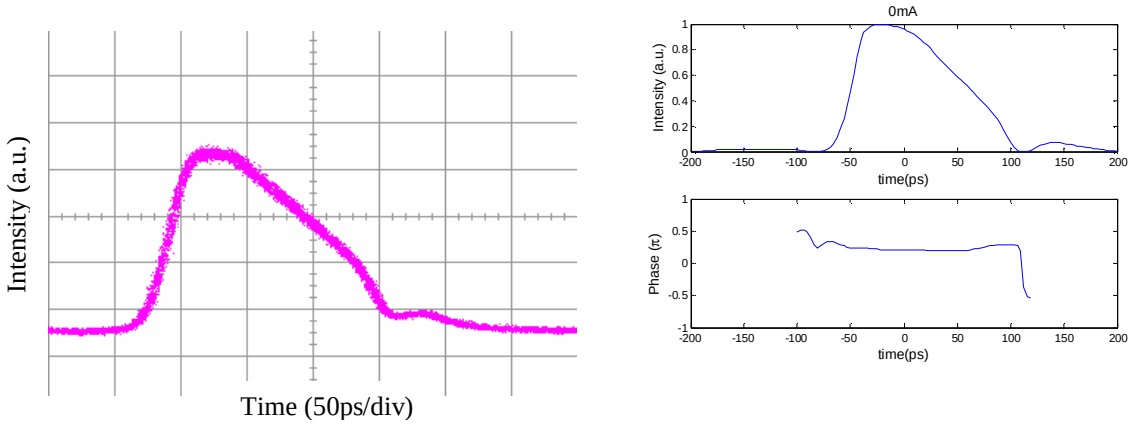

(a) 0mA

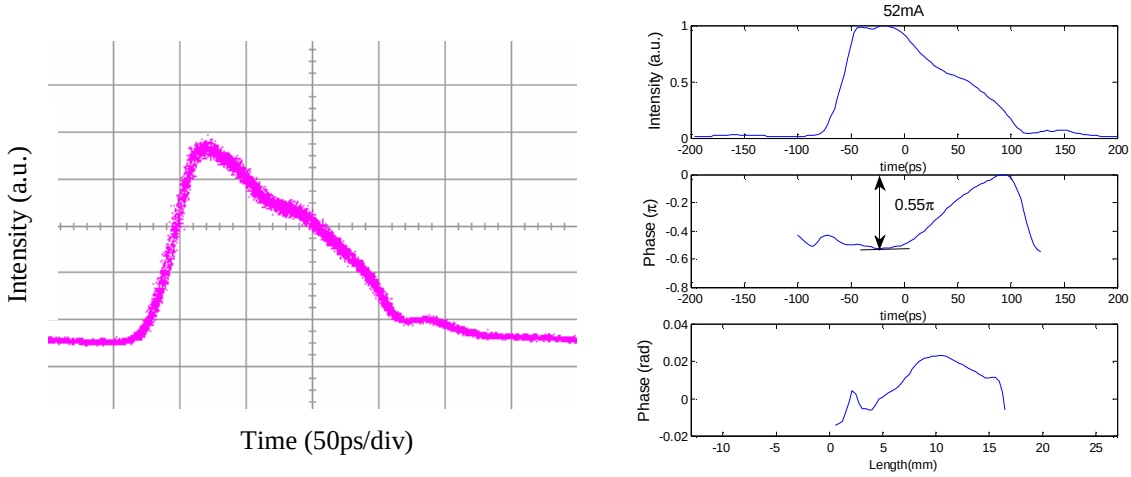

(b) 52mA

Figure 3.17

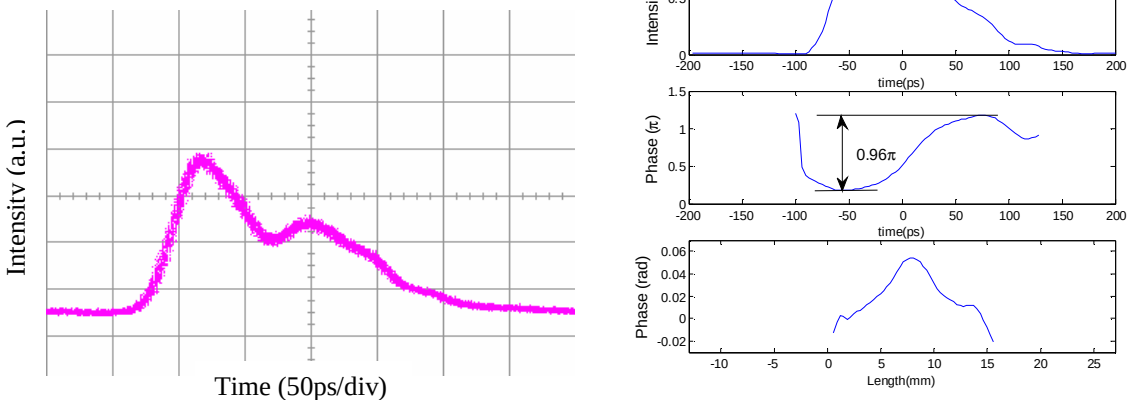

(c) 70mA

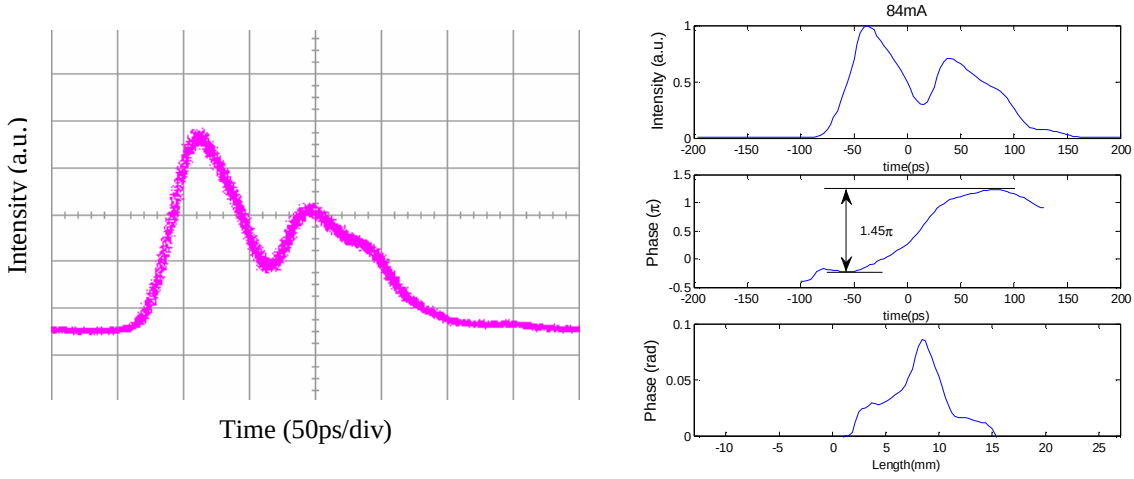

(d) 84mA

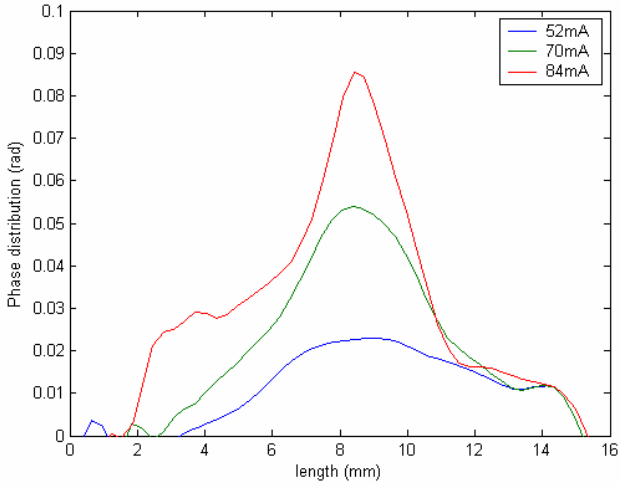

(e) The thermally-induced phase distribution along the grating

Figure 3.17 The oscilloscope trace and EAM-FROG retrieved results for the simple tunable grating, at a heating current of 0mA, 52mA, 70mA, 84mA

From these results we could see that the EAM-FROG retrieved pulse shape is similar to what we observed on the oscilloscope, the retrieved phase shift is in good agreement with the expected value. The measured phase change for the heating currents of 52mA, 70mA, 84mA is 0.55π, 0.96π, 1.45π respectively. Also from the retrieved phase, unlike the discrete grating characterized before which has an abrupt phase shift at the centre, it could be seen that the thermal-induced phase shift has a distribution along the grating, the overall phase change covers a time span of more than 100ps. Although the slow phase change is partly due to the input pulse width, what is more important is the effect due to the thermally-induced refractive index distribution along the grating, because the distribution is much longer than the input pulse width. The FWHM of the phase distribution along the grating for the heating currents of 52mA, 70mA, 84mA is 6.3mm, 4.8 mm and 3.5mm respectively.

Using the parameters obtained above, a simulation for the spectral and temporal response of the grating with the 4 different phase-shift was performed (with 25ps input pulse). The simulation results are shown in Figure 3.18, which agrees well with the experimental results. It confirms that the exact phase-shift is achieved with the three different heating current.

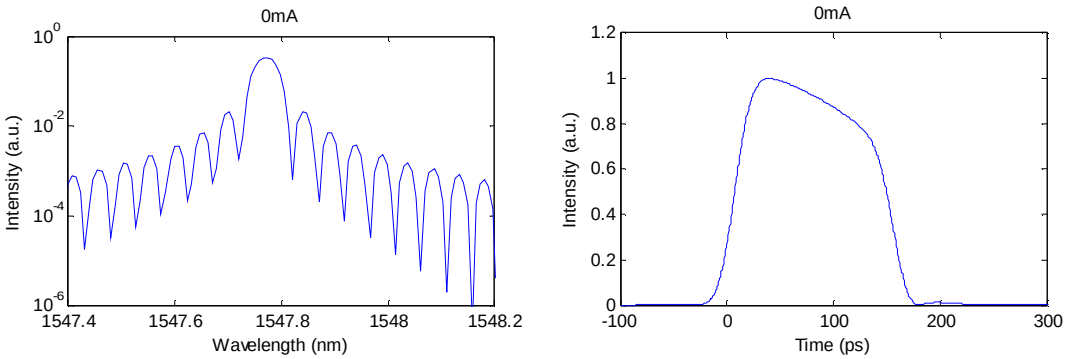

(a) uniform

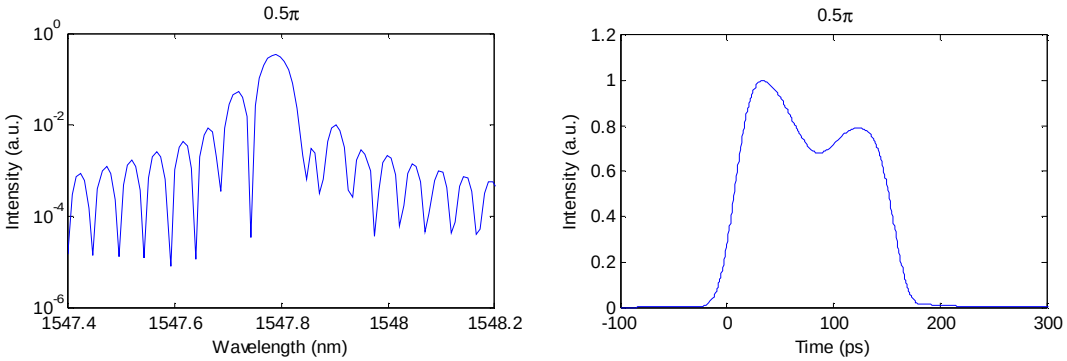

(b) 0.5π

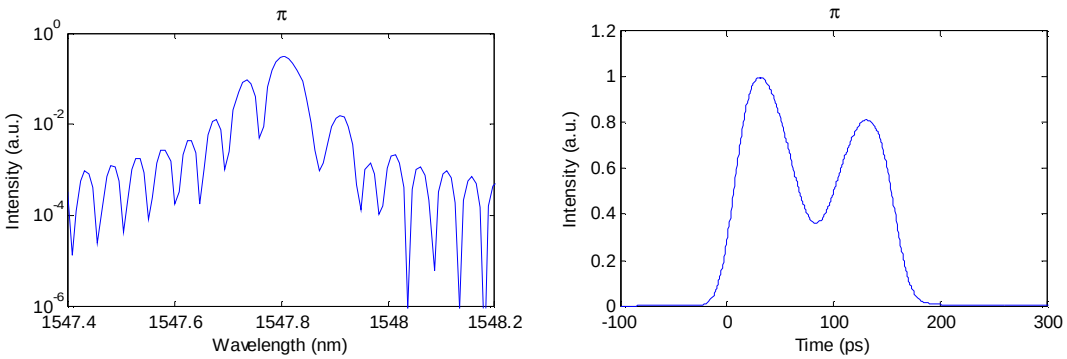

(c) π

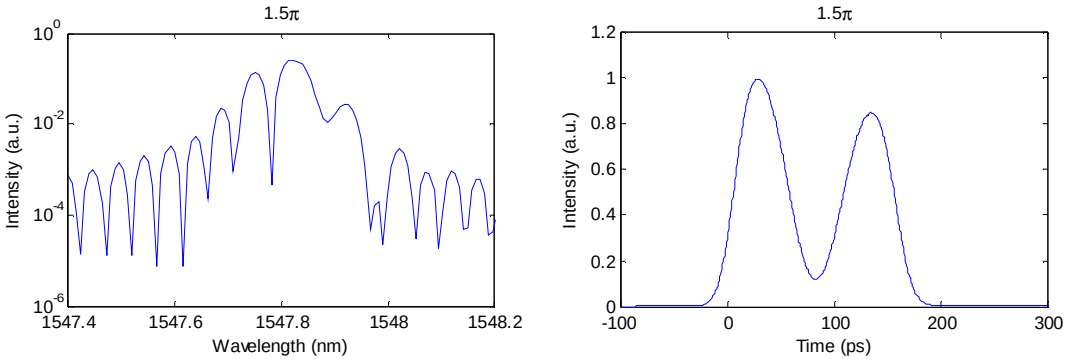

(d) 1.5π

Figure 3.18 The simulated spectral and temporal response (with 25ps input pulse) for 4 different distributed phase-shift along the thermally reconfigurable grating.

3.4.2 6ps EAM-FROG with single tunable phase-shift

As the spatial resolution of the code profile in the reflected pulse (and the corresponding refractive index profile) is determined by the input pulse width, in order to obtain a higher resolution of the thermal induced phase shift, more EAM-FROG measurements with the 6ps input pulse generated by gain-switched laser have been done. The new measurements were based on a 15-chip code-reconfigurable device, by applying heating current on selected tungsten wire(s). The 15-chip code-reconfigurable device was prepared for our reconfigurable OCDMA and Optical Packet Switching system experiments, with fifteen 50μm tungsten wires laid evenly across a 40mm long uniform FBG.

Firstly, a current (0mA, 174mA, 235mA, 285mA respectively) was applied to the 4th tungsten wire from the input end, which is at 10mm from the starting point of the grating (as shown in Figure 3.19), to produce the four different single phase shifts (0π, 0.5π, π, 1.5π)and then to characterize them respectively. The position of the phase shift in the grating means that the phase shift in the reflected pulse happens at around 100ps from the starting point of the pulse.

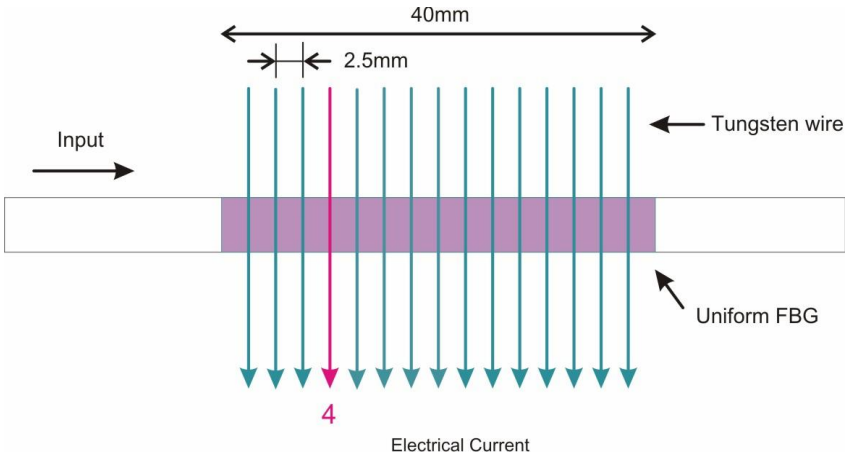

Figure 3.19 illustration of the reconfigurable grating

Figure 3.20 shows the oscilloscope trace and EAM-FROG retrieved results. Again, the retrieved intensity profiles are comparable with the oscilloscope traces. For the heating electrical current of 174mA, 235mA, 285mA, the retrieved phase-shift values are as expected around 0.5π, π, 1.5π respectively. By differentiating the retrieved phase-shift, the phase distribution along the grating was derived. Figure 3.21 summarises the thermally induced phase shift distribution for the three different heating currents.

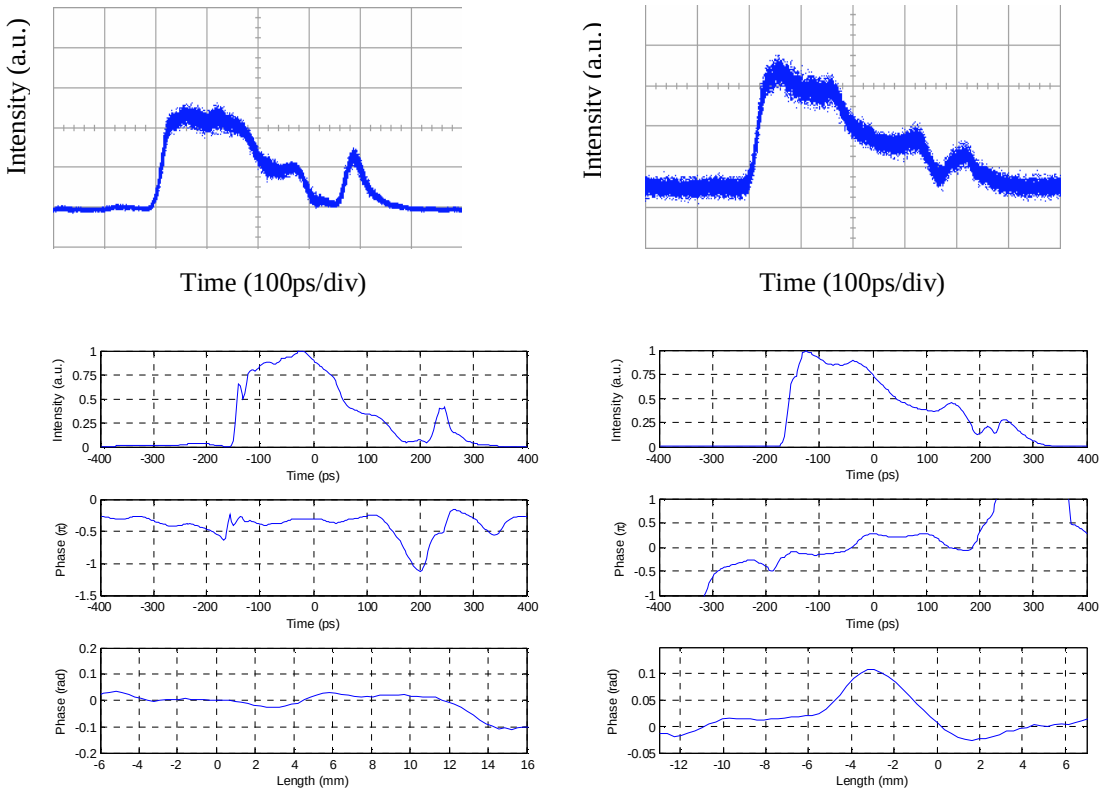

(a) 0mA *(b) 174mA*

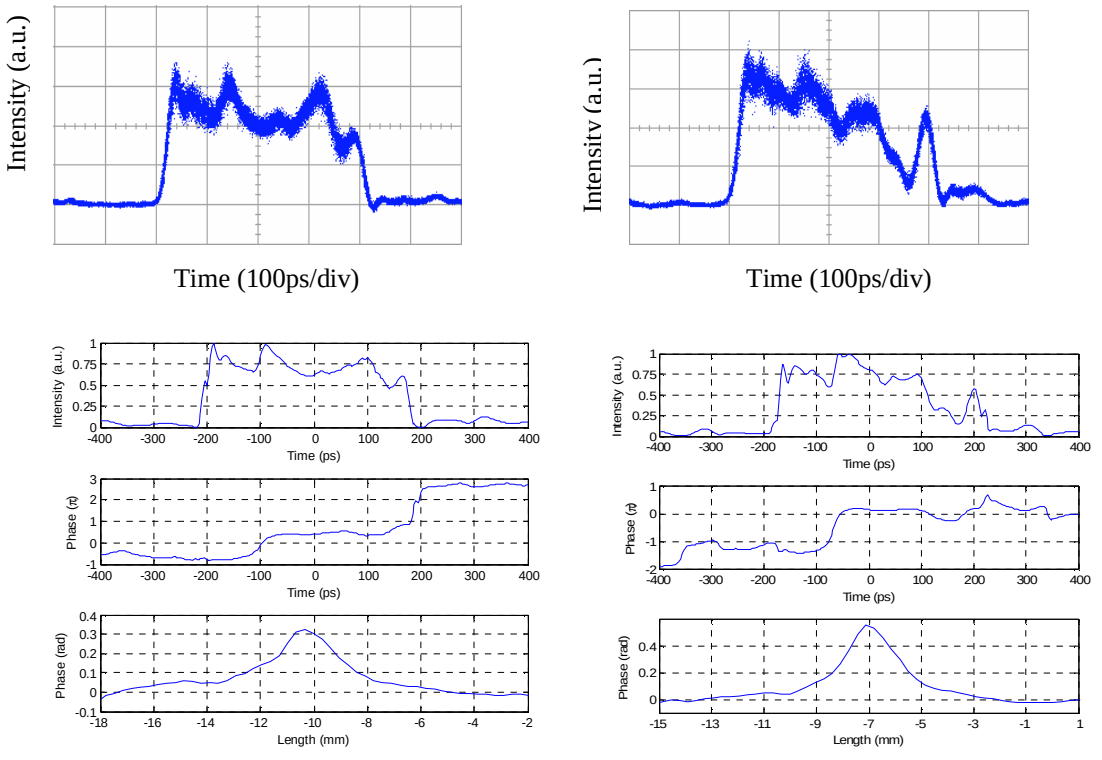

(c) 235mA *(d) 285mA*

Figure 3.20 The oscilloscope trace (100ps/div) and EAM-FROG retrieved results for the simple tunable grating, at a heating current of (a) 0mA, (b)174mA, (c) 235mA, (d)285mA

In Figure 3.21, The FWHM of the phase distribution along the grating is shown for the heating currents of 174mA, 235mA, 285mA is 3.5mm, 2.6mm and 2.3mm respectively. For comparison, the Gaussian distribution was superposed. The excellent shape agreement indicates that the thermally induced phase shift follows the Gaussian distribution. The obtained parameters can be used in our further simulations regarding the code-reconfigurable gratings. Comparing with the results obtained by 25ps input pulses (Figure 3.17), a narrower phase distribution can be seen for the 6ps input pulse. This is believed to be due to the different diameter of the tungsten wires used in the two experiments (18μm wires in the 25ps experiments , 50μm wires in the 6ps experiments). This is confirmed in our further experiment, in section 3.4.4, by characterizing the phase distribution induced by an 18μm tungsten wire with 6ps input pulse.

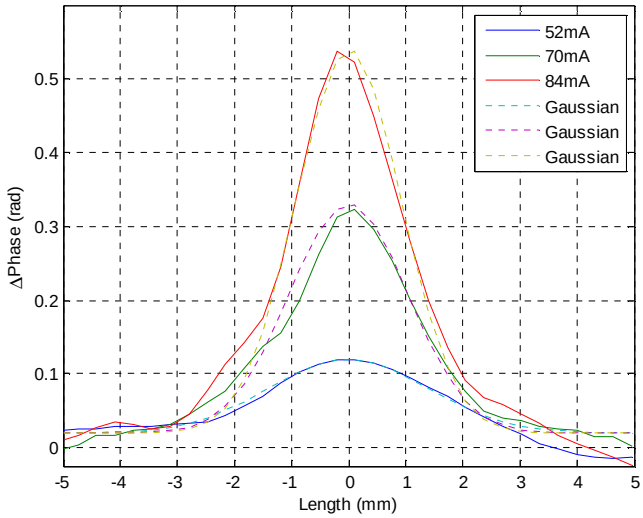

Figure 3.21 The thermally-induced local phase-shift distribution.

3.4.3 6ps EAM-FROG with simple tunable phase-shift combinations

The aim of this research was to develop a code-reconfigurable device that was as compact as possible. So after obtaining the idea of phase-shift distribution for single heating wire, further investigations were carried out on the effect of heating wire combinations. (1) with the applied current on both the 4^{th} and 5^{th} tungsten wires from the input end, which are 2.5mm apart from each other, to produce π phase shift at each position. (2) with the applied current on the 4^{th} and 6^{th} tungsten wires from the input end, which are 5mm apart from each other, to produce π phase shift at each

position. (3) with the applied current on the 6^{th} 7^{th} and 8^{th} tungsten wires from the input end, to produce π phase shift at each position. The characterization results for each configuration are shown in figure 3.22.

For all the three configurations, the good agreement between the retrievals and the oscilloscope traces in the time domain indicated the accuracy of the characterizations. Due to the distributed phase shift induced by each of the tungsten wires, the combined local phase shifts are partly merged together. However, the accumulated phase shift still equals the expected value (for (1) and (2) it is ~ 2π. For (3) it is ~ 3π). Although the spatial resolution is limited by the 6ps input pulse, the separation of the adjacent phase shift at the 2.5mm grid is still resolved. It is shown that 2.5mm is the grid limit for this reconfigurable grating. The simulations done by Mr. Zhaowei Zhang about the reconfigurable grating's performance regarding the distance between the tungsten wires also confirm this point. If the distances between the tungsten wires are narrower than 2.5mm, the correlation performance will be unacceptable.

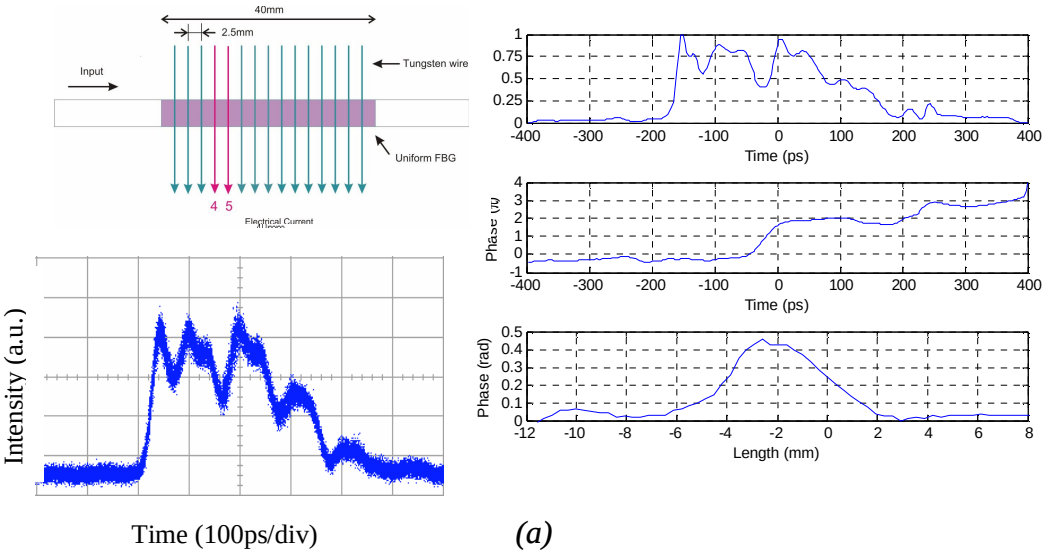

(a)

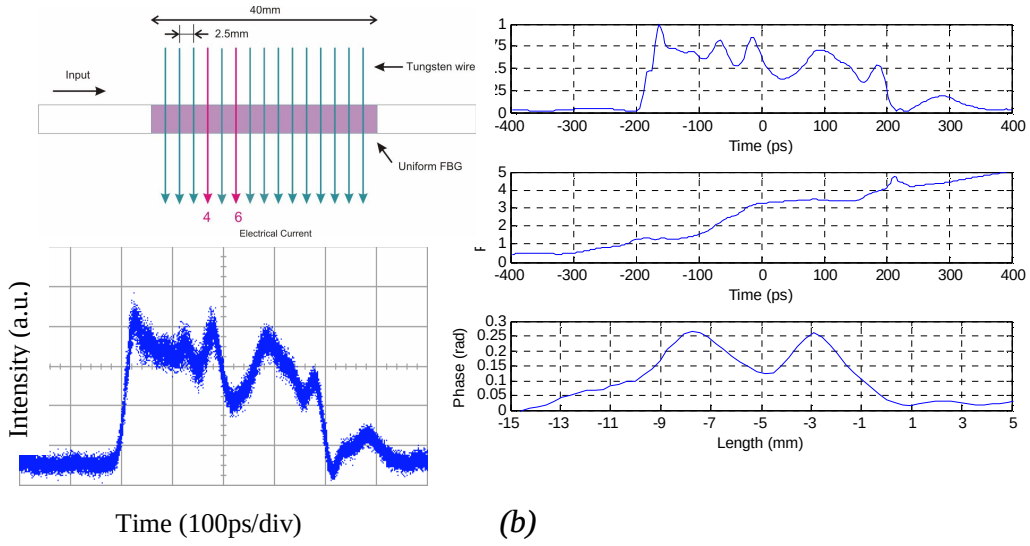

(b)

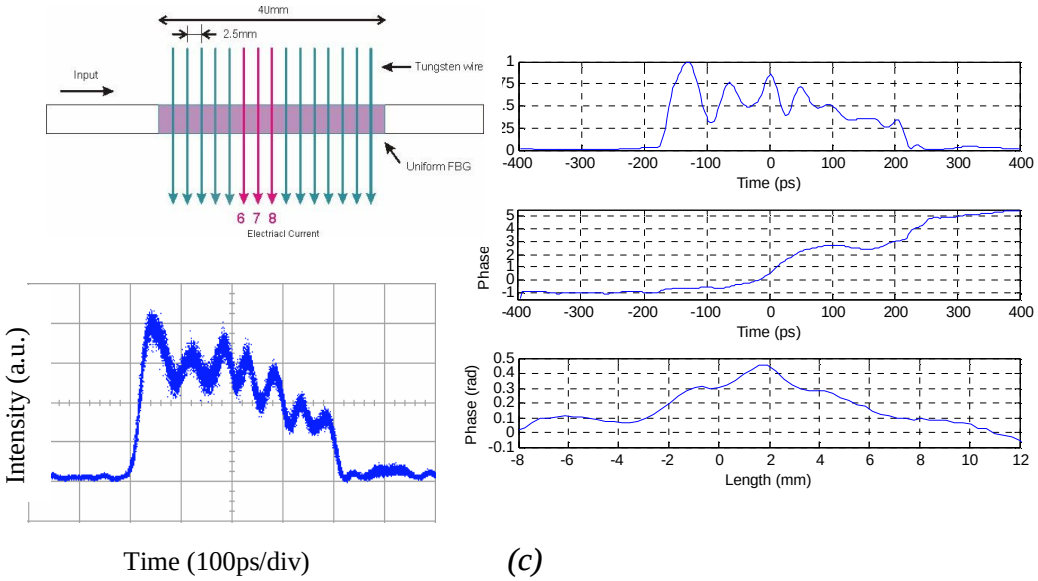

(c)

Figure 3.22 The oscilloscope trace and EAM-FROG retrieved results for some different configuration of the tunable grating,

3.4.4 The effect of tungsten wire diameter

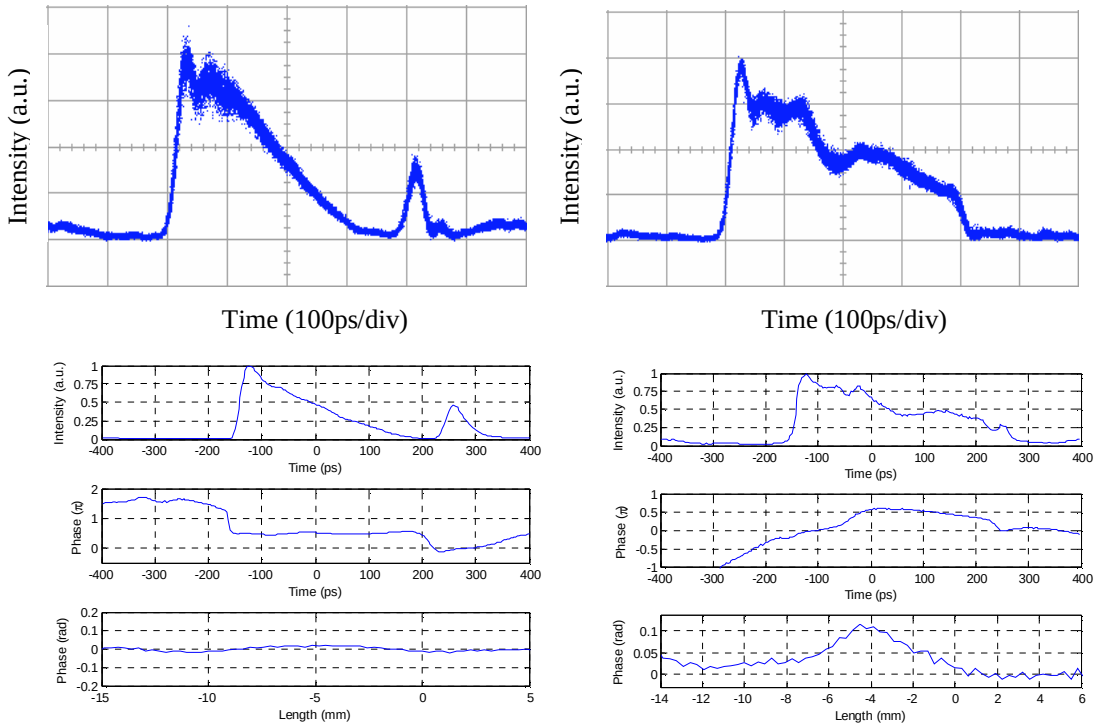

(a) Uniform *(b) 0.5π*

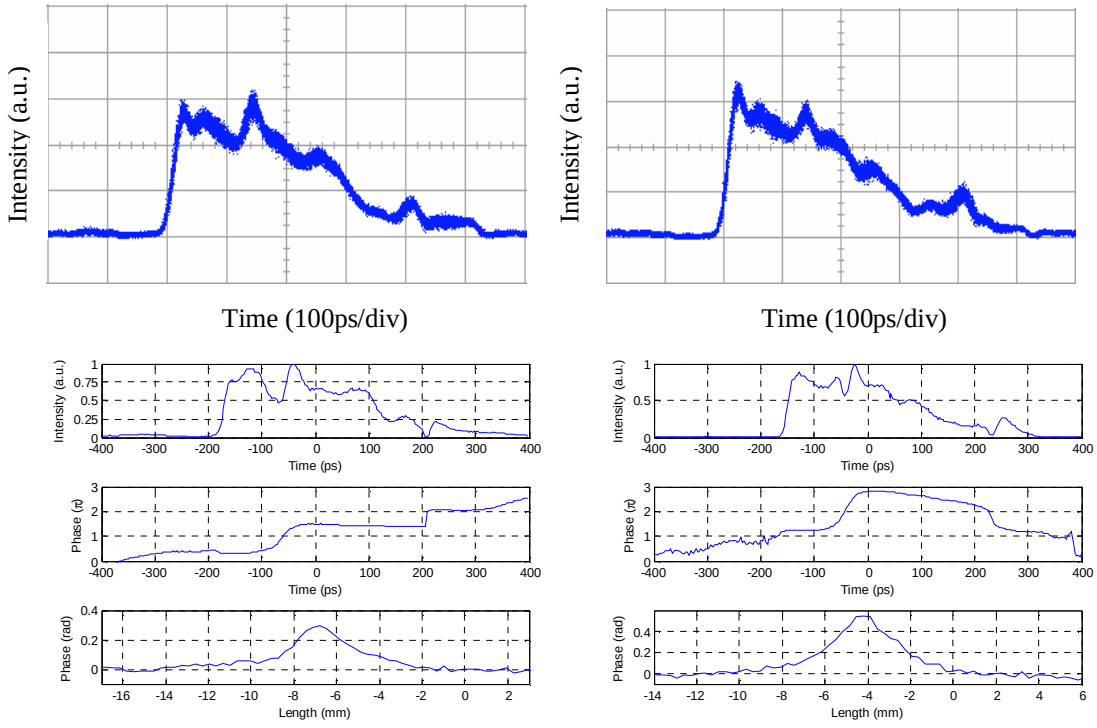

(c) π *(d) 1.5 π*

Figure 3.23 The oscilloscope trace and EAM-FROG retrieved results for the phase shift produced by a 18μm tungsten wire

The 6ps input pulses was used to further investigate the effect of the tungsten wire diameter on the thermally-induced phase-shift, by replacing the 4th 50μm tungsten wire from the starting end with a 18μm tungsten wire. 52mA, 70mA, 84mA current was applied on this tungsten wire to produce a single 0.5π, π, 1.5π phase shift respectively. The EAM-FROG retrieved results are shown in Figure 3.23. The high similarity of the retrieved intensity profiles, compared with the oscilloscope traces, indicate the accuracy of the EAM-FROG retrieved results. Figure 3.24 summarises the thermally induced phase distribution obtained in Figure 3.23. The FWHM of the phase distribution along the grating, for the three heating currents producing phase shifts of 0.5π, π, 1.5π, is 5.5mm, 4.2mm and 3.3mm respectively.

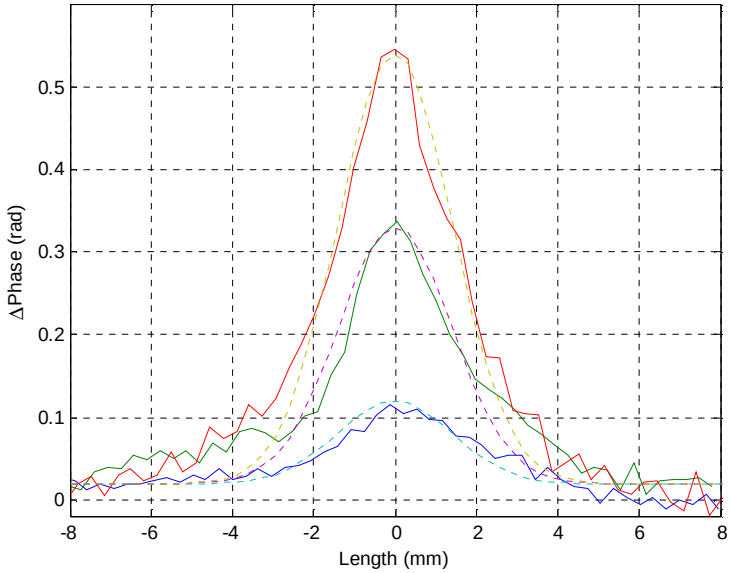

Figure 3.24 The thermally-induced local phase-shift distribution produced by a 18μm tungsten wire.

Table 3.1 summarises the measured FWHM of the thermally-induced phase distribution in three different cases: 18μm tungsten wire with 25ps input pulses; 18μm tungsten wire with 6ps input pulses; and 50μm tungsten wire with 6ps input pulses. When using 18μm tungsten wire, the FWHM values are comparable for both 6ps and 25ps input pulses, being just slightly narrower for 6ps input pulses. This is believed to be due to the narrower input pulse. It is also noticed that, for the thicker 50μm tungsten wire, the spatial FWHM of the thermally-induced phase distribution is apparently narrower than that induced by 18μm tungsten wire. This phenomenon is

against the assumption that narrower tungsten wire would produce narrower phase distribution. However it makes sense given that the thicker tungsten wire can apply heat on the grating more efficiently to produce the phase-shift. The diameter of the tungsten wire is an important factor in designing an appropriate code-reconfigurable grating device.

Table 3.1 Summary of the effect of tungsten wire diameter and input pulse width

Diameter of tungsten wire (μm)	Input pulse width (ps)	0.5π		π		1.5π	
		Current (mA)	FWHM (mm)	Current (mA)	FWHM (mm)	Current (mA)	FWHM (mm)
18	25	52	6.3	70	4.8	84	3.5
18	6	52	5.5	70	4.2	84	3.3
50	6	174	3.5	235	2.6	285	2.3

3.5 The 15-chip code-reconfigurable grating

After characterizing the 15-chip fixed coding SSFBGs, it is impressive with the ability of EAM-FROG to measure a long duration and complex pulse. As the behaviour of the simple grating with a single tunable phase shift has already been investigated, now we try to characterize the 25ps 15-chip phase-tunable SSFBG, which is an important device in my future system experiments to enhance the network flexibility.

The structure of the tunable grating has been described in the previous chapter. The electrical currents flowing through each of the tungsten wire was controlled independently to produce a phase code the same as the code in the fixed grating labelled as Q2*. According to the earlier experiments in section 3.3, 174mA, 234mA, 285mA current were used to produce 0.5π, π, 1.5π phase shift respectively.

Similarly to the characterization of the fixed-coded SSFBGs, both 25ps and 6ps input pulses are tested on the reconfigurable grating by using the same EAM-FROG setup described in section 3.4. Firstly, 25ps input pulses were used to characterize the reconfigurable grating with code Q2*. Figure 3.25 shows the EAM-FROG retrieved results and the oscilloscope traces. Considering the high coincidence of the retrieved and observed intensity profile, the EAM-FROG results are believed to be accurate.

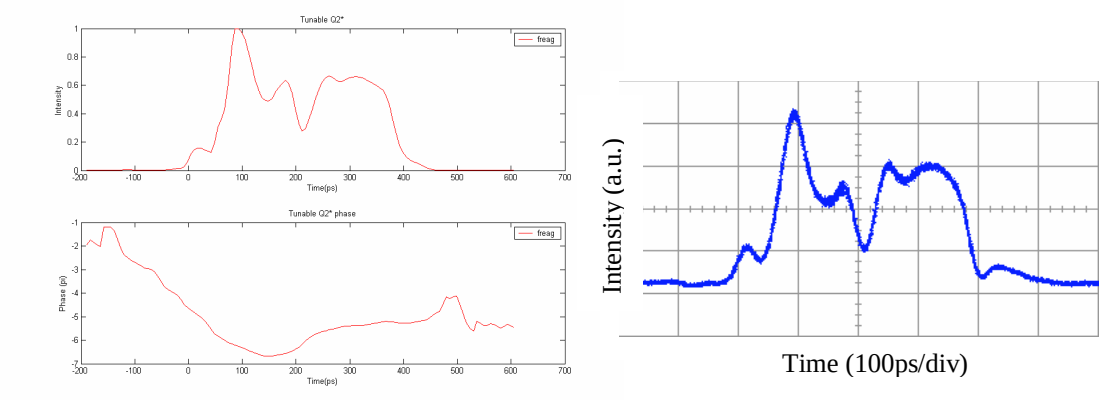

*Figure 3.25 EAM-FROG retrievals with 25ps input pulse and the oscilloscope trace (100ps/div) for the tunable gating with the code as Q2**

Then I used the 6ps input pulse to implement the characterization. The reconfigurable grating was configured with code Q1T and Q2T respectively. Figure 3.26 shows the oscilloscope traces and the EAM-FROG retrievals. Due to the stability of the reconfigurable grating, the retrieved pulse intensity profile deviates slightly from the simulation results, however it still agrees well with the oscilloscope trace.

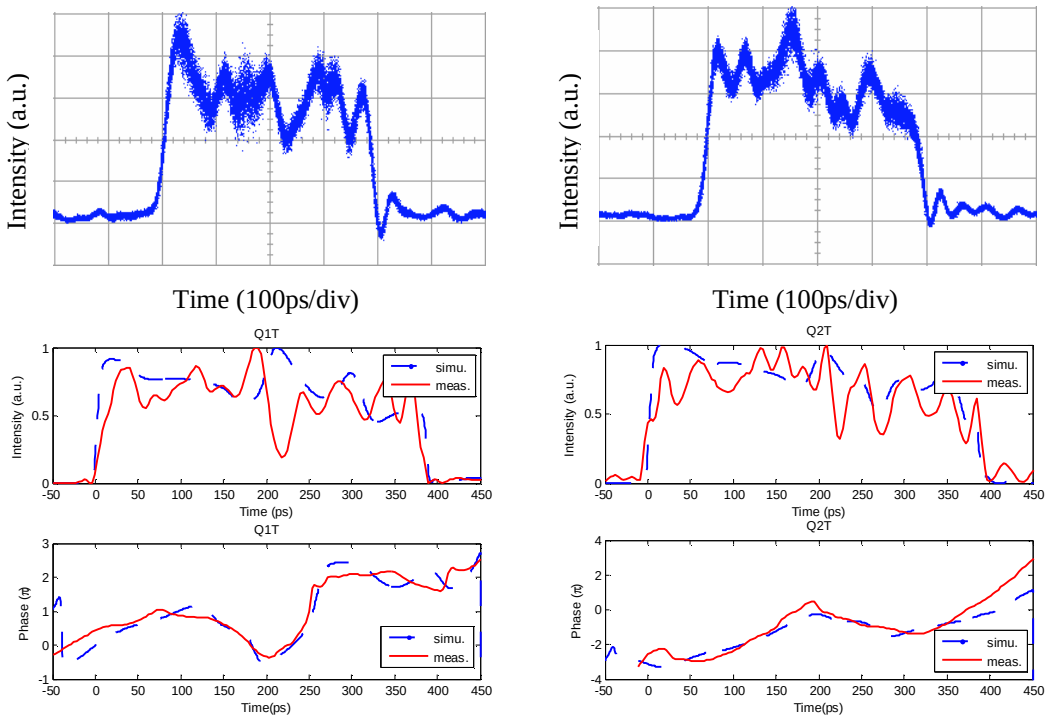

Figure 3.26 EAM-FROG retrievals with 6ps input pulse compared with simulation results, and the oscilloscope trace (100ps/div) for the reconfigurable grating when configured with different codes (a)Q1T and (b)Q2T

The retrieved phase-shift also follows the simulation result. Because the thermally induce phase distribution spreads along the grating, it is difficult to further analyse the individual phase-shift within this multiple code-reconfigurable grating.

3.6 Conclusion

In this chapter, the work on directly characterizing the various fiber Bragg gratings is introduced. While some work can be carried out with SHG-FROG technique for the short pulses, EAM-FROG technique is demonstrated to be a more capable and accurate. The thermally-induced phase-shift in the reconfigurable grating has been investigated. Complex gratings can be characterized with high accuracy. The EAM-FROG technique is proved to be an effective approach to assess the properties of fiber Bragg gratings.

References

[3-1] L. Poladian, B. Ashton, W. E. Padden, A. Michie, and C. Marra, "Characterisation of phase-shifts in gratings fabricated by over-dithering and simple displacement," *Optical Fiber Technology: Materials, Devices and Systems*, vol. 9, pp. 173-88, 2003.

[3-2] L. M. Baskin, M. Sumetsky, P. S. Westbrook, P. I. Reyes, and B. J. Eggleton, "Accurate characterization of fiber Bragg grating index modulation by side-diffraction technique," *IEEE Photonics Technology Letters*, vol. 15, pp. 449-451, 2003.

[3-3] S. Sandgren, B. Sahlgren, A. Asseh, W. Margulis, F. Laurell, R. Stubbe, and A. Lidgard, "Characterisation of Bragg gratings in fibres with the heat-scan technique," *Electronics Letters*, vol. 31, pp. 665-666, 1995.

[3-4] P. Lambelet, P. Y. Fonjallaz, H. G. Limberger, R. P. Salathe, C. Zimmer, and H. H. Gilgen, "Bragg grating characterization by optical low-coherence reflectometry," *IEEE Photonics Technology Letters*, vol. 5, pp. 565-7, 1993.

[3-5] A. F. Obaton, C. Palavicini, Y. JaouenJaouen, E. Kerrinckx, Y. Quiquempois, and M. LievreLievre, "Characterization of fiber Bragg gratings by phase-sensitive optical low-coherence reflectometry," *IEEE Transactions on Instrumentation and Measurement*, vol. 55, pp. 1696-703, 2006.

[3-6] E. I. Petermann, J. Skaar, B. E. Sahlgren, R. A. H. Stubbe, and A. T. Friberg, "Characterization of fiber Bragg gratings by use of optical coherence-domain reflectometry," *Journal of Lightwave Technology*, vol. 17, pp. 2371-8, 1999.

[3-7] E. Brinkmeyer, "Simple Algorithm for Reconstructing Fiber Gratings from Reflectometric Data," *Optics Letters*, vol. 20, pp. 810-812, 1995.

[3-8] D. W. Huang and C. C. Yang, "Reconstruction of fiber grating refractive-index profiles from complex Bragg reflection spectra," *Applied Optics*, vol. 38, pp. 4494-4499, 1999.

[3-9] G. P. Agrawal, *Nonlinear Fiber Optics Third Edition*.

[3-10] R. Trebino, K. W. DeLong, D. N. Fittinghoff, J. N. Sweetser, M. A. Krumbugel, B. A. Richman, and D. J. Kane, "Measuring ultrashort laser pulses in the time-frequency domain using frequency-resolved optical gating," *Review of Scientific Instruments*, vol. 68, pp. 3277-3295, 1997.

[3-11] K. W. DeLong, D. N. Fittinghoff, and R. Trebino, "Practical issues in ultrashort-laser-pulse measurement using frequency-resolved optical gating," *Ieee Journal of Quantum Electronics*, vol. 32, pp. 1253-1264, 1996.

[3-12] D. J. Kane, "Recent progress toward real-time measurement of ultrashort laser pulses," *Ieee Journal of Quantum Electronics*, vol. 35, pp. 421-431, 1999.

[3-13] R. Trebino, K. W. DeLong, D. N. Fittinghoff, J. N. Sweetser, M. A. Krumbugel, B. A. Richman, and D. J. Kane, "Measuring ultrashort laser pulses in the time-frequency domain using frequency-resolved optical gating," *Review of Scientific Instruments*, vol. 68, pp. 3277-95, 1997.

[3-14] C. Dorrer and I. Kang, "Simultaneous temporal characterization of telecommunication optical pulses and modulators by use of spectrograms," *Optics Letters*, vol. 27, pp. 1315-1317, 2002.

[3-15] M.A.F.Roelens, B.C.Thomsen, and D.J.Richardson, "Multi-wavelength EAM based optical sampling for performance monitoring in high bit-rate systems," presented at ECOC 2004, Stockholm, 2004.

[3-16] C. Dorrer and I. Kang, "Real-time implementation of linear spectrograms for the characterization of high bit-rate optical pulse trains," *IEEE Photonics Technology Letters*, vol. 16, pp. 858-860, 2004.

[3-17] L. R. Chen, S. D. Benjamin, P. W. E. Smith, and J. E. Sipe, "Applications of ultrashort pulse propagation in Bragg gratings for wavelength-division multiplexing and code-division multiple access," *IEEE Journal of Quantum Electronics*, vol. 34, pp. 2117-2129, 1998.

Chapter 4

OCDMA systems based on 15-chip gratings

4.1 Overview

The work in the telecommunication system laboratory of the ORC has previously demonstrated the feasibility of optical coding/decoding based on SSFBG technology[4-1, 2]. In this chapter, the performance of OCDMA systems is comparatively investigated, based on a range of 15-chip encoder/decoders, which includes the traditional discrete phase-shift SSFBGs, the thermally code-reconfigurable gratings, and the novel continuous phase-shift SSFBGs. In Section 4.2, the correlation properties of using discrete phase-shift SSFBGs and code-reconfigurable gratings are introduced. The performance of different combinations of these gratings as the encoder and decoder has been investigated, which includes (a) both encoder and decoders are discrete phase-shift SSFBGs, (b) discrete phase-shift SSFBG as the encoder and code-reconfigurable grating as the decoder, (c) both encoder and decoders are code-reconfigurable gratings. In Section 4.3, the unique features of novel continuous phase-shift SSFBGs are described. This chapter is summarized In Section 4.4.

4.2 15-chip Discrete phase-shift SSFBGs

The study started with discrete phase-shift SSFBGs as they are the traditional gratings used in our previous OCDMA demonstrations[4-3]. Two pairs of 15-chip quaternary phase-shift codes, labelled as Q1, Q1*, Q2 and Q2* respectively, are

chosen from Family A sequences [4-4]as the address codes of the OCDMA encoder/decoders.

Q1 = [3 1 0 1 1 2 0 3 2 2 2 3 1 1 1]

Q1*=[1 1 1 3 2 2 2 3 0 2 1 1 0 1 3]

Q2 = [3 2 1 1 1 1 2 3 2 3 1 0 0 1 0]

Q2*=[0 1 0 0 1 3 2 3 2 1 1 1 1 2 3]

where one unit means a π/2 phase shift

The fabricated 15-chip quaternary discrete phase-shift SSFBGs have a chip length of 2.5mm, resulting in a total grating length of 37.5mm. The Bragg wavelength of all the SSFBGs is about 1551nm, which can be tuned by stretching the gratings. The measured peak reflectivity strength for these SSFBGs is around 40%. The phase distributions of the fabricated discrete phase-shift SSFBGs Q1, Q1*, Q2 and Q2* are illustrated in Figure 4.1. In Chapter 3 these SSFBGs have been characterized and they are proven to meet the design parameters.

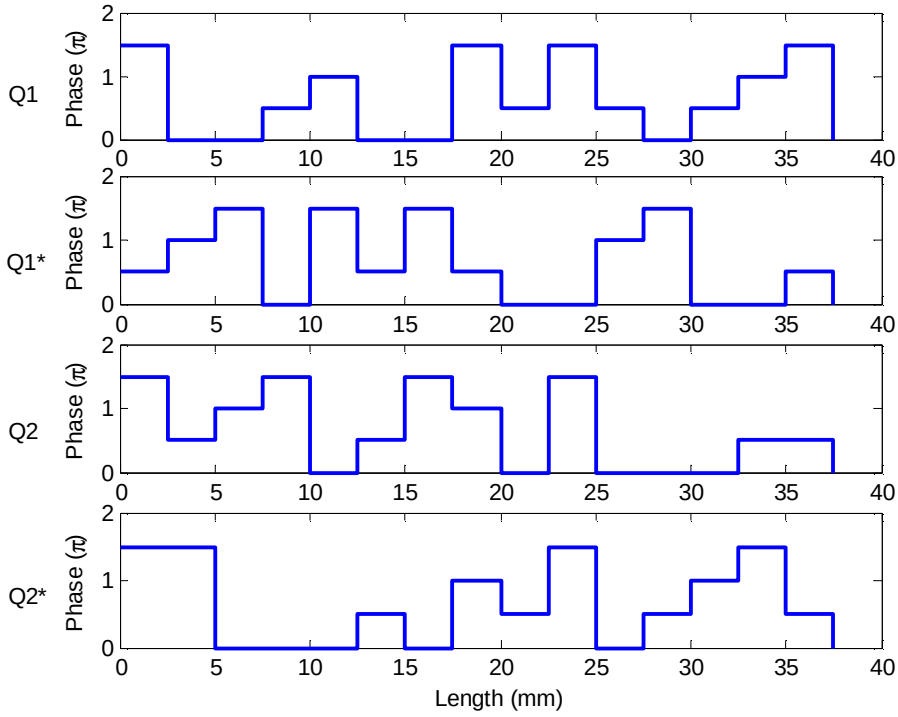

Figure 4.1 The phase profile for the discrete phase-shift SSFBGs Q1, Q1, Q2 and Q2**

Figure 4.2 shows a simple OCDMA coding/decoding system. The modulated short pulse is reflected from the encoding SSFBG through a circulator. The encoded signal is then fed into the decoding SSFBGs to perform code recognition. EDFAs are

incorporated within the system to compensate the optical power loss due to the modulator, circulator and SSFBG insertion loss. As mentioned before, for the matched codes, a distinctive autocorrelation will be produced from the matching process. While for the unmatched codes, low intensity, noise-like cross correlations will be produced. Because the SSFBGs for the experiments were fabricated with a low birefringence photosensitive fibre, they are polarization insensitive. Therefore polarization controllers are no longer required, in contrast to the previous experiments by Teh [4-1,2,3]. The system is thus more robust and easier to use in practice.

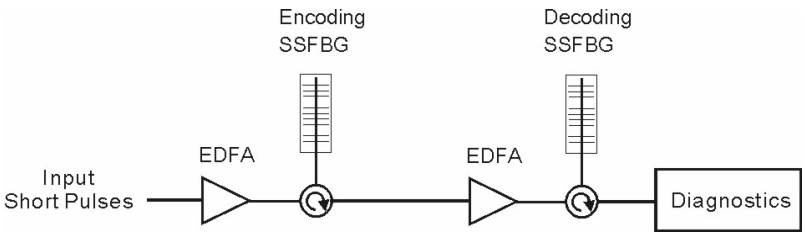

Figure 4.2 A simple OCDMA coding/decoding system

As for the characterization experiments in Chapter 3, two different types of short pulses, EAM-carved 25ps pulses and 6ps pulses from a Gain Switched laser were used as the input pulses to study the performance of the OCDMA systems.

4.2.1 Correlation properties of discrete phase-shift SSFBGs with 25ps input pulse

The preliminary study was carried out with the discrete phase-shift SSFBG encoder and discrete phase-shift SSFBG decoder using the relatively wide 25ps pulses. The reflectivity spectra of the gratings have been measured in Chapter 3. Fig. 3.20 shows the simulated and measured reflectivity spectra of 15-chip quaternary discrete phase-shift SSFBGs. The gratings' temporal response has also been simulated and measured. The simulation of the temporal response is based on a simple Fourier transform. Firstly, the spectral reflectivity responses of the gratings are obtained through the transfer matrix model[4-5]. The grating's temporal response with a short input pulse, is calculated through the inverse Fourier transform of the product of the input pulse spectrum, and the spectral reflectivity responses of the grating. The decoded signal, i.e., the autocorrelation and cross-correlation, are again obtained through the inverse Fourier transform of the product of the input pulse spectrum, the

spectral reflectivity response of the encoding grating, and the spectral reflectivity response of the decoding grating.

Figure 4.3 shows the measured and simulated gratings' temporal response for the four gratings with 25ps input pulses. The 25ps input pulses are spread into ~400ps encoded pulse sequences. Note that the oscilloscope in the experiment has a detection bandwidth of 20GHz, while each chip of the encoded waveform has a duration of ~25ps. Therefore the individual features of the encoded waveform are not well resolved. However, it is clear that the temporal response of the matched gratings, i.e. Q1 and Q1*, Q2 and Q2*, have a time-reversed feature, which is consistent with the time-reversed code profile for the matched gratings.

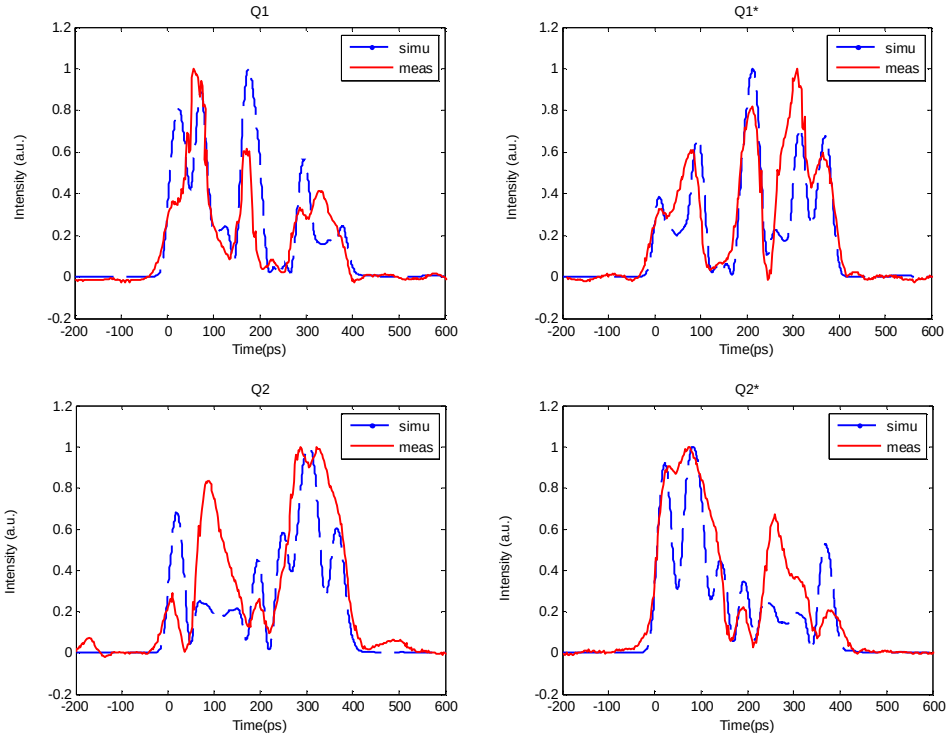

Figure 4.3 Normalised oscilloscope traces compared with the simulation results for the gratings' temporal response.

Figure 4.4 shows the measured and simulated results for the decoding process. For the matched cases, Q1:Q1*, the decoded signal has a distinct well defined autocorrelation peak with low-level pedestals at both sides (Figure 4.4 (a)). Note that the undershooting following the peak pulse is due to the effects of the photodiode. For the unmatched cases, Q1:Q2*, the cross-correlation exhibits a low level, noise-like features (Figure 4.4 (b)). Similar results for autocorrelation Q2:Q2* and cross-

correlation Q2:Q1* are also obtained, as shown in Figure 4.4 (c) and Figure 4.4 (d) respectively. The measured autocorrelation pulse width is about 30ps for both codes, in good agreement with the simulations. The contrast ratio between the cross-correlation and autocorrelation peaks is about 20% for both cases, confirming that good code recognition quality and correlation properties can be obtained with such kinds of grating.

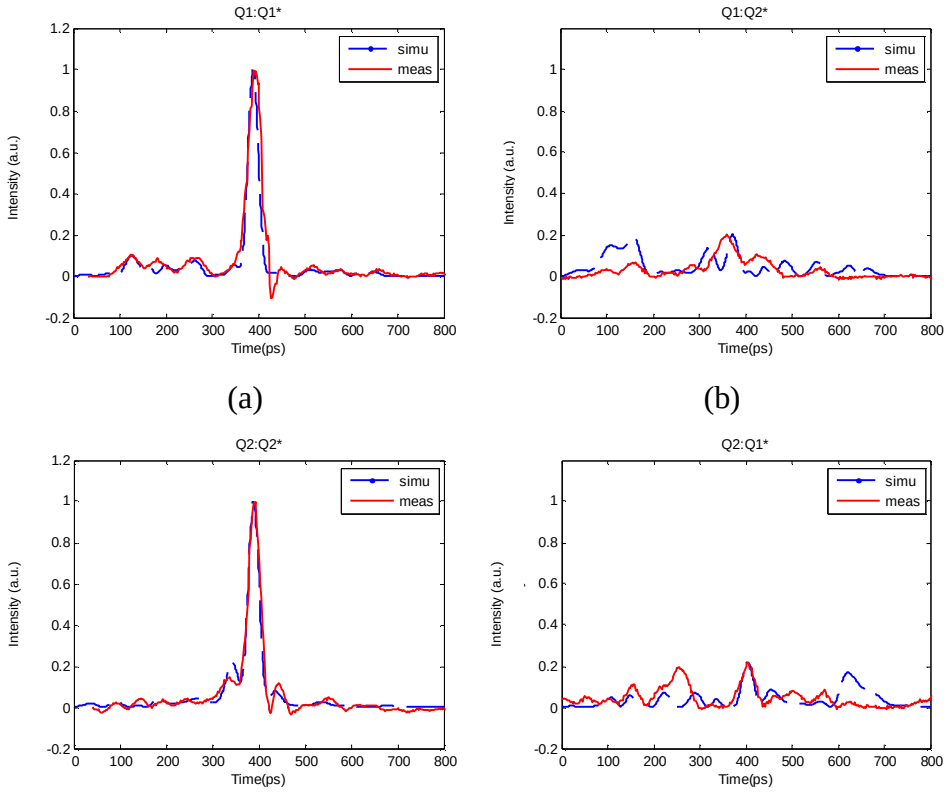

Figure 4.4 Normalised oscilloscope traces compared with the simulation results for (a) autocorrelation of Q1:Q1, (b) cross-correlation of Q1:Q2*, (c) autocorrelation of Q2:Q2*, and (d) cross-correlations of Q2:Q1*.*

Figure 4.5 shows the spectra of the input short pulse and the reflectivity spectra of the encoding and decoding SSFBG when the experimental system is working under the matched status, that is with the best autocorrelation recognition. The spectra display some notable features:

Firstly, each pair of encoding and decoding SSFBGs have the same reflectivity strength, the same spectral shape, and the same spectral position. There is a slight difference in the lower intensity level between the individual SSFBG, e.g. in Figure

4.5(a) the spectrum dip for Q1 is down to about -80dB, while that for Q1* is about -70dBm. This minor difference is due to the connection between the individual SSFBG and circulator, which induces a different reflection loss. However, it does not affect the peak reflectivity strength significantly.

Secondly, the measured 20dB bandwidth of the reflectivity spectra for both Q1 and Q2 are 0.55nm, while the measured 20dB bandwidth of the 25ps input pulse is 0.45nm. It is obvious that the spectrum of the input pulse is only just enough to cover the main lobe of the SSFBG's spectra. Since the sidelobes of the SSFBG's spectra carry duplicate information to the mainlobe, we would claim that the "just-enough" input pulse spectrum is a proper choice to utilise all the coding information and at the same time to occupy the minimum spectral bandwidth. It can also be explained reasonably in the temporal domain, the input pulse should not be wider than the chip duration so that the input pulse can be spread into a pulse sequence by the grating without overlapping of the individual pulses.

Thirdly, the spectra of the input pulse and the encoding/decoding SSFBGs are positioned at the same central wavelength. It is essential to align the encoding and decoding SSFBGs to achieve matched filtering. Although the central wavelength of the input pulse can be offset relative to the central wavelength of the SSFBGs as long as the SSFBGs are well matched, it will degrade the correlation performance in terms of grating insertion loss and spectral efficiency, all of which are critical factors in an optical communication system.

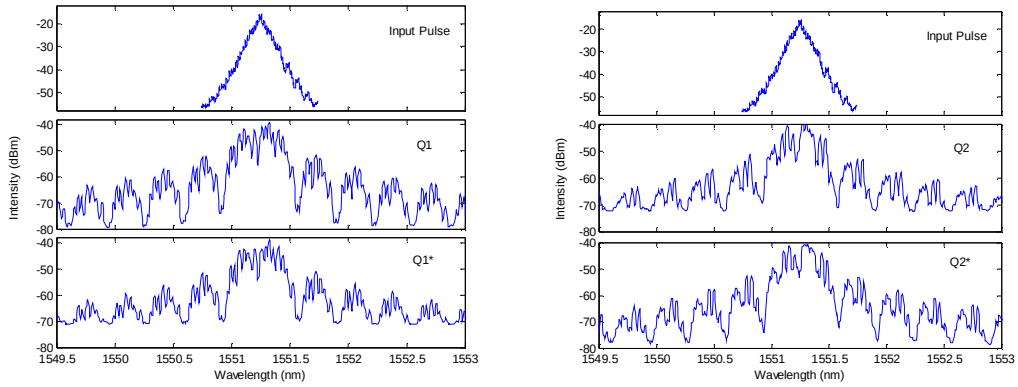

(a) Q1:Q1* (b) Q2:Q2*

Figure 4.5 The spectra of the input short pulse and the reflectivity spectra of the encoding and decoding SSFBG when the experimental system is working under the matched status.

The clearly open eye diagram in Figure 4.6 also confirms the code recognition capability of the SSFBGs. The PRBS 2^7-1 data was modulated at a bit rate of 1.25Gbit/s to avoid overlapping of adjacent decoded correlation pulses. The same data pattern is also used for BER tests.

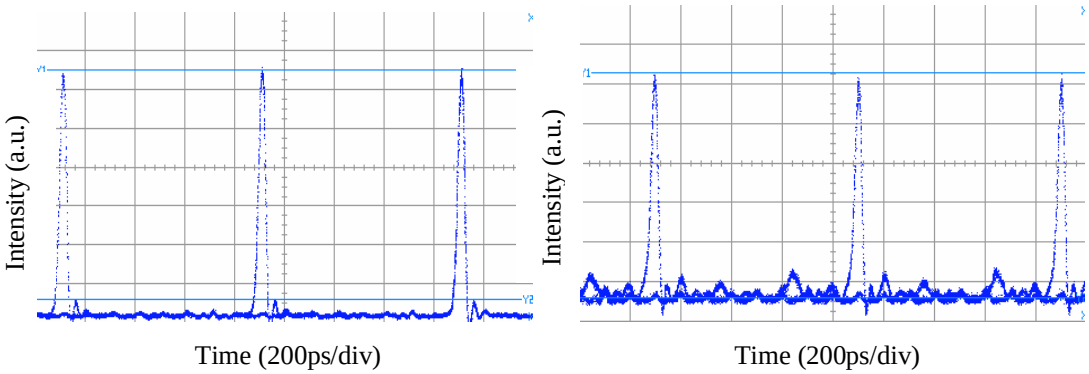

Figure 4.6 Eye diagrams at a data rate of 1.25Gbit/s. (a) input pulses (b) autocorrelation of Q1:Q1.*

Theoretically, either one of the pair of gratings can be used as the encoder and the other one as the decoder, since their code profiles are exactly time-reversed. This is verified by swapping the position of Q1 and Q1* in the experimental setup, e.g. firstly, using Q1 as the encoding grating while Q1* is the decoding grating, afterwards using Q1* as the encoding grating while Q1 is the decoding grating. Figure 4.7 shows the oscilloscope traces of the autocorrelations for the two cases. Nearly identical autocorrelation features are observed, as expected.

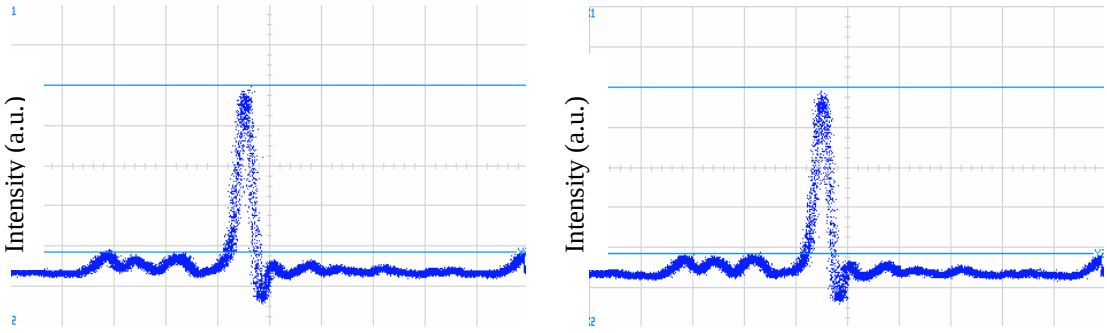

Figure 4.7 Oscilloscope traces of the autocorrelation for (a) Q1:Q1 and 2) Q1*:Q1 (100ps/div)*

4.2.2 Correlation properties of discrete phase-shift SSFBG encoder and code-reconfigurable decoder with 25ps input pulse

Although the reconfigurablity of both encoder and decoder are desired to maximise the flexibility of the optical coding related systems, considering the limited stability of the reconfigurable grating, the combination of a fixed-coded SSFBG and a reconfigurable grating is an easier and more practical implementation with our current laboratory setup. Hence the performance of the discrete phase-shift SSFBG encoder and code-reconfigurable decoder was studied with 25ps input pulses.

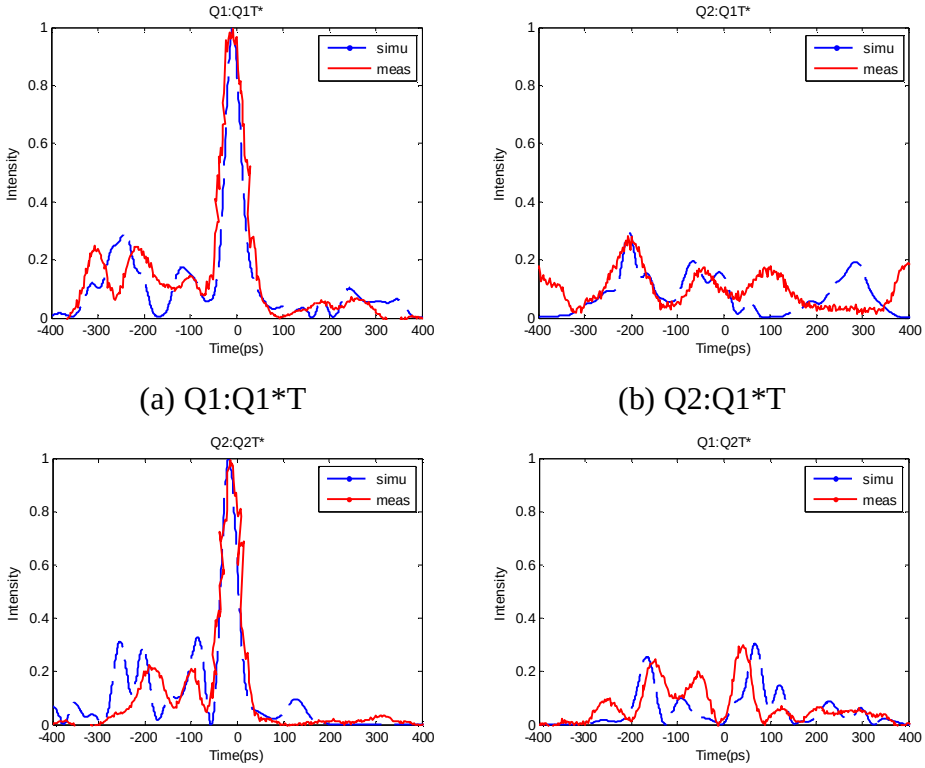

(a) Q1:Q1*T (b) Q2:Q1*T

(c) Q2:Q2*T (d) Q1:Q2*T

Figure 4.8 Measured and simulated autocorrelation and cross-correlation of the discrete phase-shift SSFBG encoder and code-reconfigurable decoder

The experimental setup is the same as the one in Figure 4.2, except that the decoding SSFBG is replaced by a reconfigurable grating. The reconfigurable grating has been described in Section 3.3. In this setup, the 15-chip reconfigurable decoder can be programmed to match either one of the fixed encoding SSFBGs. The code-reconfigurable grating is demonstrated to be compatible with the discrete phase-shift SSFBG. Good autocorrelation and cross-correlation have been obtained for both sets of codes Q1 and Q2. The measured and simulated autocorrelation and cross-correlation are plotted in Figure 4.8. Note that the roughness on the measured traces is

due to the digital sampling on the original low definition oscilloscope traces. The measured autocorrelation pulse width is about 40ps for both codes, in good agreement with the simulations. The contrast ratio between the cross-correlation and autocorrelation peaks is about 28% for both cases.

Figure 4.9 illustrates the relative spectral position of the input short pulse and the reflectivity spectra of the matched encoding SSFBG and decoding reconfigurable grating when the experimental system is working with the best autocorrelation performance. Just as in the fixed to fixed system, the input pulse is centred to match the spectrum of the fixed encoding SSFBG. The obvious difference from the fixed to fixed case is the spectrum of the reconfigurable grating. The measured reflectivity spectrum of the reconfigurable grating is much narrower than that of the fixed SSFBG. The measured 20dB bandwidths for the reconfigurable grating with codes Q1*T and Q2*T are ~0.40nm, in comparison with the ~0.55nm 20dB bandwidth for the fixed discrete phase-shift SSFBGs with codes Q1 and Q2. The narrower bandwidth is due to the distributed thermally-induced phase shift along the grating. The unique features of the reconfigurable grating attracted our attention because of their potential to improve the spectral efficiency. Although the correlation properties are slightly degraded relative to the fixed SSFBG to fixed SSFBG setup.

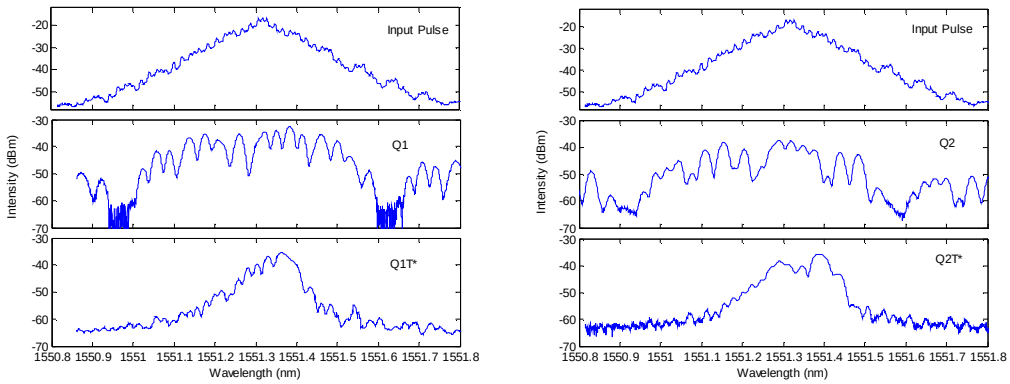

(a) *(b)*

Figure 4.9 the spectra of input short pulse and the reflectivity spectra of the encoding SSFBG and decoding reconfigurable grating when the experimental system is working with the best autocorrelation performance. (a) Q1:Q1T, (b) Q2:Q2T*.*

In order to assess the code recognition performance of the fixed discrete phase-shift SSFBG as well as the code-reconfigurable grating, and to evaluate the compatibility of the two different types of gratings, BER measurements were taken

for the two different codes. The measurements were taken with a PRBS 2^7-1 at a bit rate of 1.25Gb/s. The BER measurement results in Figure 4.10 show a moderate power penalty of 1dB compared to the laser back-to-back case when both the encoder and decoder are fixed discrete phase-shift SSFBGs. For the fixed encoding and reconfigurable decoding case, the power penalty is about 3.5dB compared to the laser back-to-back case. The extra power penalty is due to the distributed thermally-induced phase shift in the reconfigurable grating, as well as the instability associated with the electrical heating and package. However, the BER results still confirm the code recognition capability of both the fixed SSFBG and the reconfigurable grating.

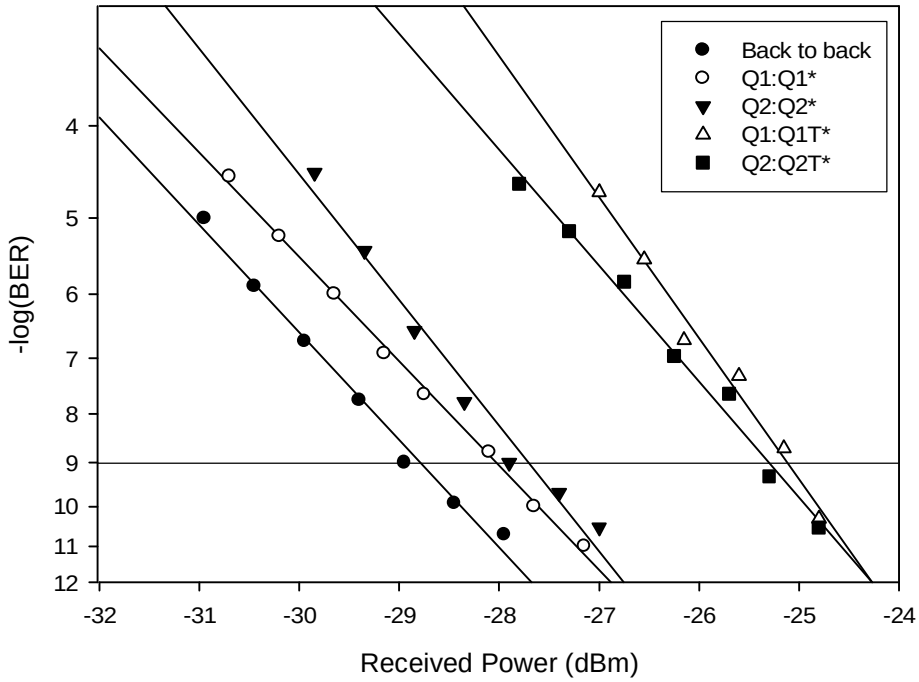

Figure 4.10 BER test results for fixed encoding fixed decoding case and fixed encoding reconfigurable decoding case with 25ps input pulses.

4.2.3 Correlation properties of code-reconfigurable encoder and code-reconfigurable decoder with 6ps input pulse

In the previous fixed to reconfigurable system experiment, the compatibility of the traditional fixed-coded SSFBGs with discrete phase shift and the reconfigurable grating with distributed phase shift was confirmed. The system also shows a certain flexibility compared to the all fixed-coded system. However, to maximise the flexibility of the system based on optical codes, both the encoding and decoding

facility need to be reconfigurable. In the following section, the performance of an all-reconfigurable optical coding/decoding system was investigated, for which two identical code-reconfigurable gratings have been made, and used, as the encoder and decoder separately (Figure 4.11).

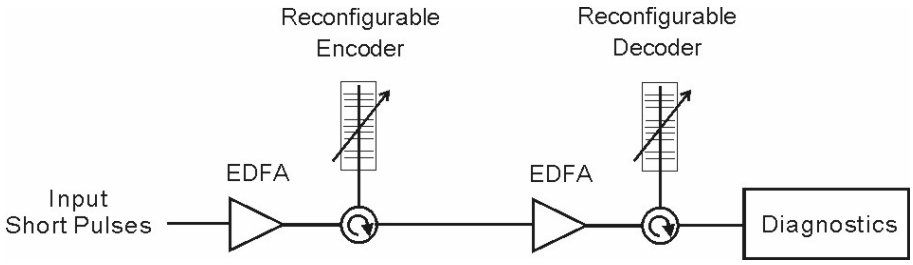

Figure 4.11 All reconfigurable OCDMA coding/decoding system

Thanks to the reconfigurablity provided by the reconfigurable coder and decoder, it is possible to investigate the performance of any different code conveniently. Four different 15-chip quaternary phase shift codes, selected randomly from Family A sequences, are used in the experiments. The four codes are marked as Q1-Q4 separately, among which Q1 and Q2 are the same codes as I used in the previous section, Q3 and Q4 and their corresponding conjugated codes Q3* and Q4* are listed as following:

Q3 = [2 1 1 3 1 2 0 2 1 2 0 3 1 0 1]

Q3*=[1 0 1 3 0 2 1 2 0 2 1 3 1 1 2]

Q4 = [1 1 2 1 0 3 3 1 1 2 0 0 1 2 2]

Q4*=[2 2 1 0 0 2 1 1 3 3 0 1 2 1 1]

Figure 4.12 shows the reflectivity spectra of the encoder and decoder when they are configured with code Q1-Q4, Q1*-Q4* respectively. The measured results generally agree with the simulated ones. To avoid overlapping for a clear view, the spectra of the conjugated codes are shifted by 20dB. The measured 20dB bandwidth for the four codes are about 0.45nm. As expected, each pair of conjugated codes have a highly similar spectral shape, confirming the reconfigurablity of the device.

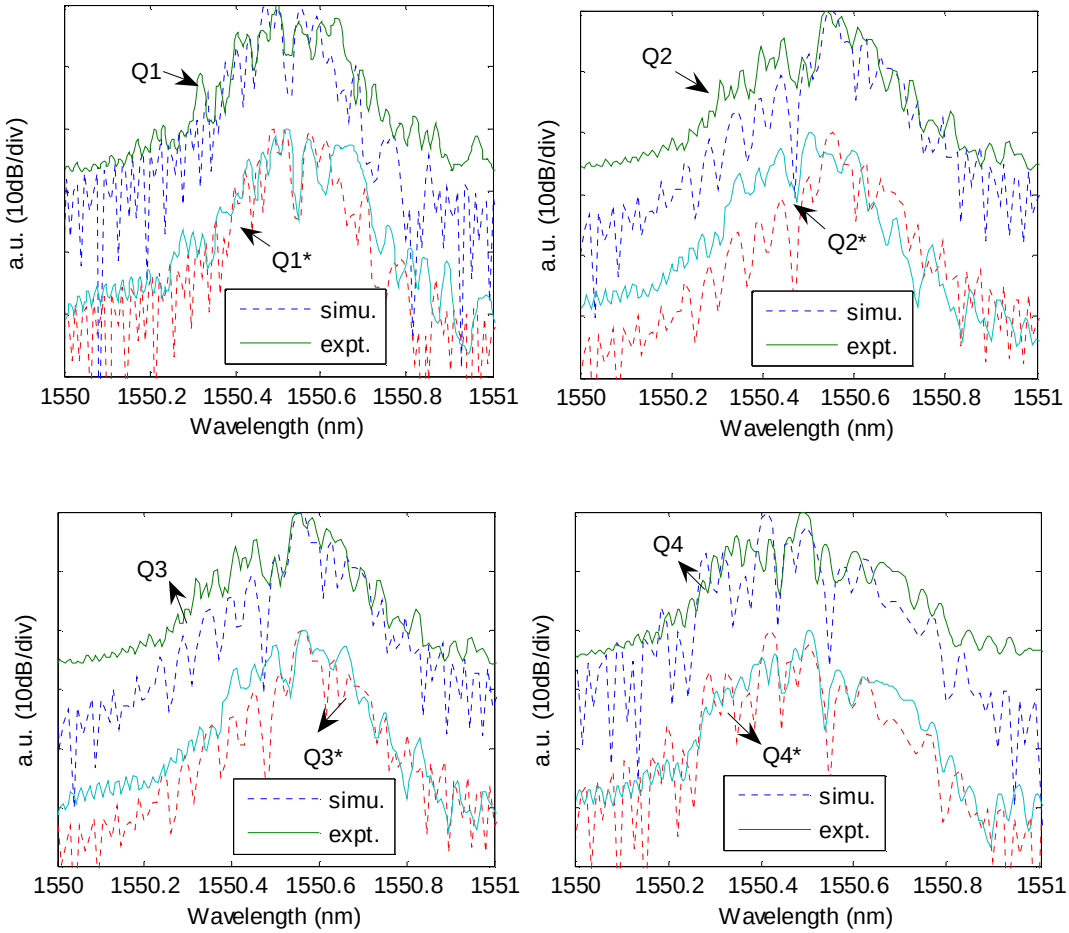

Figure 4.12 Simulated and measured reflectivity spectra of the encoder and decoder when they are configured with code Q1-Q4, Q1-Q4* respectively. The spectra of the conjugated codes are shifted by 20dB to avoid overlapping and to facilitate comparison.*

Figure 4.13 compares the spectra of the 25ps input pulse, 6ps input pulse, and reflectivity spectra of fixed SSFBG Q1, reconfigurable grating with code Q1. As shown in the figure, 25ps input pulse generated by the EAM modulator has 'just enough' spectral coverage for the grating spectra. Although the 25ps input pulse is a good compromise between performance and cost, in order to have a better investigation on the performance of the reconfigurable grating, 6ps pulse generated by the gain switched laser was employed as the short input pulse, which has a wider spectrum and thus can present better correlation results than the 25ps pulse.

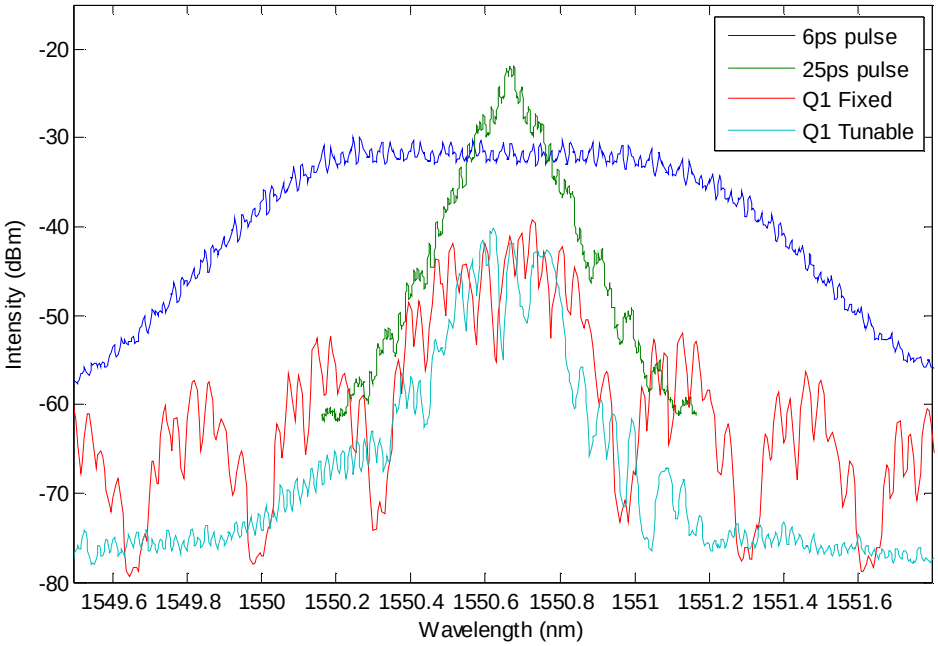

Figure 4.13 Spectra of the 25ps input pulse, 6ps input pulse, and reflectivity spectra of fixed SSFBG Q1, reconfigurable grating with code Q1

Figure 4.14 shows the spectra for the encoded signal after reflecting from the reconfigurable grating with the codes Q1-Q4 respectively. For Q1 and Q2, the encoded signal using fixed SSFBGs Q1 and Q2 was imposed for comparison. As can be seen from the spectra, the encoded signal using the reconfigurable grating has a narrower bandwidth without obvious sidelobes, in agreement with the reflectivity spectra of the reconfigurable grating which has shown the suppression of the sidelobes. The narrower spectra have the potential to improve the spectral efficiency and reduce the inter-channel interference under DWDM operation.

Excellent autocorrelation results have been achieved for all the four different codes when both the encoder and decoder are reconfigurable gratings. The oscilloscope traces are shown in Figure 4.15. The measured autocorrelation pulsewidth is about 30ps.

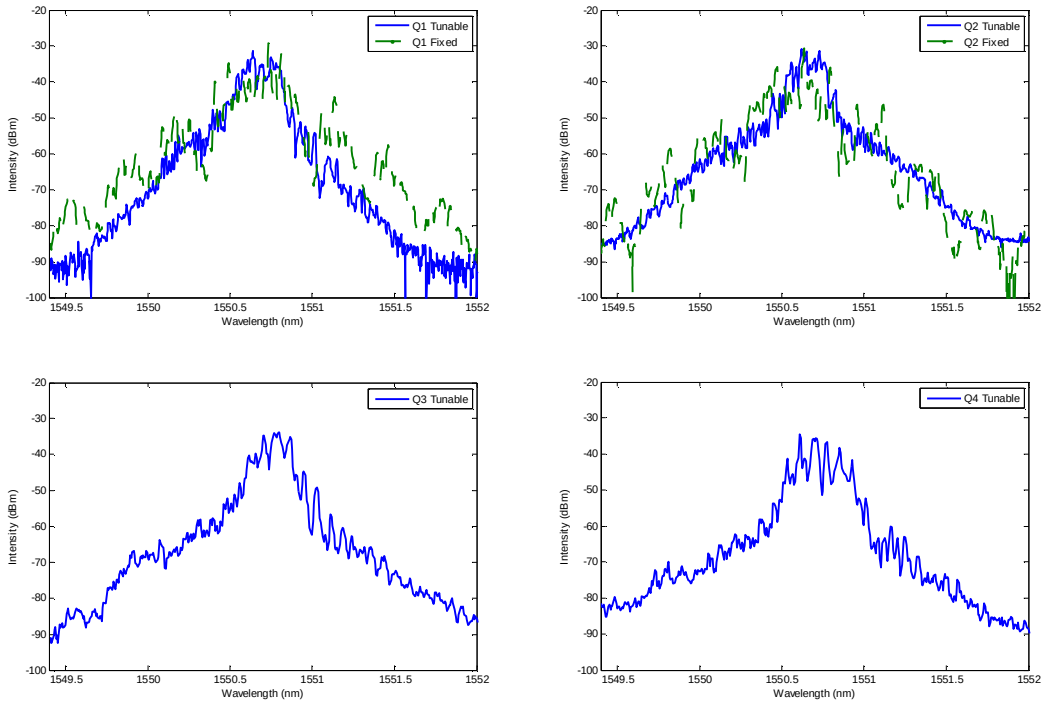

Figure 4.14 Spectra for the encoded signal after reflecting from the reconfigurable grating with the codes Q1-Q4 respectively

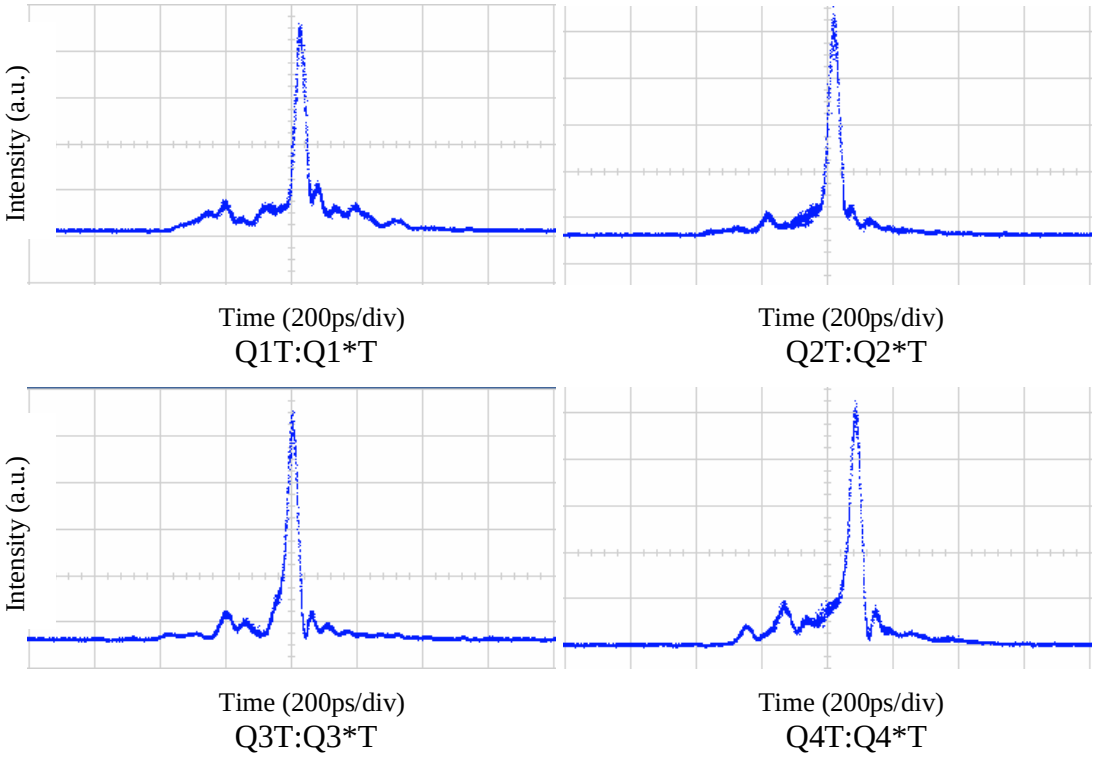

Figure 4.15 Oscilloscope traces (200ps/div) of autocorrelations with reconfigurable codes Q1-Q4 respectively

The above experiments demonstrated the code recognition capability as well as the flexibility of the all reconfigurable system. Without changing the system setup, just by changing the code configuration on the coding/decoding devices, excellent correlation performance for different codes can be achieved conveniently.
The 15-chip code-reconfigurable grating can also be used to implement 7-chip quaternary phase-shift codes by applying heating current to tungsten wires 2, 4, 6, 8, 10, 12, 14 only. The resulting chip length is 5mm instead of 2.5mm. And the corresponding chip duration is ~50ps. 2 sets of 7-chip quaternary phase-shift codes were experimentally demonstrated:

R1 = [3 0 2 3 0 3 1]

R1*= [1 3 0 3 2 0 3]

R2 = [1 0 1 3 1 0 2]

R2*= [2 0 1 3 1 0 1]

Figure 4.16 shows the oscilloscope traces of the encoded signal after the input pulse is reflected from the code-reconfigurable grating. Different temporal responses are observed for the different code configurations.

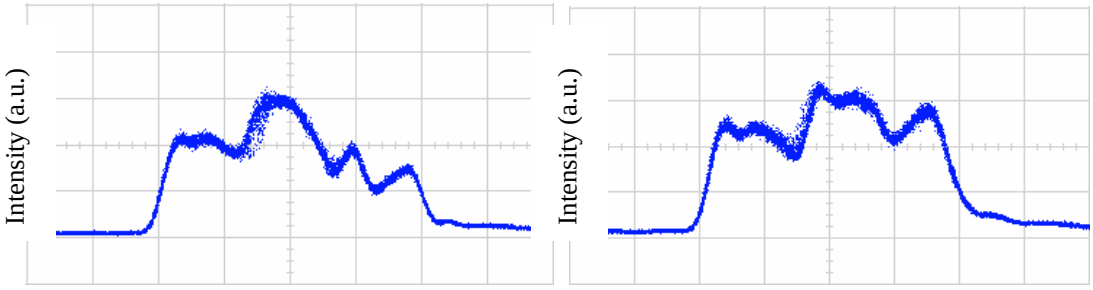

Figure 4.16 oscilloscope traces (100ps/div) of the encoded signal (a) R1 and (b) R2

Figure 4.17 shows the reflectivity spectra when the grating is configured with code R1, R1*, R2, R2* respectively, and the corresponding spectra of the decoded signal when autocorrelation is achieved.

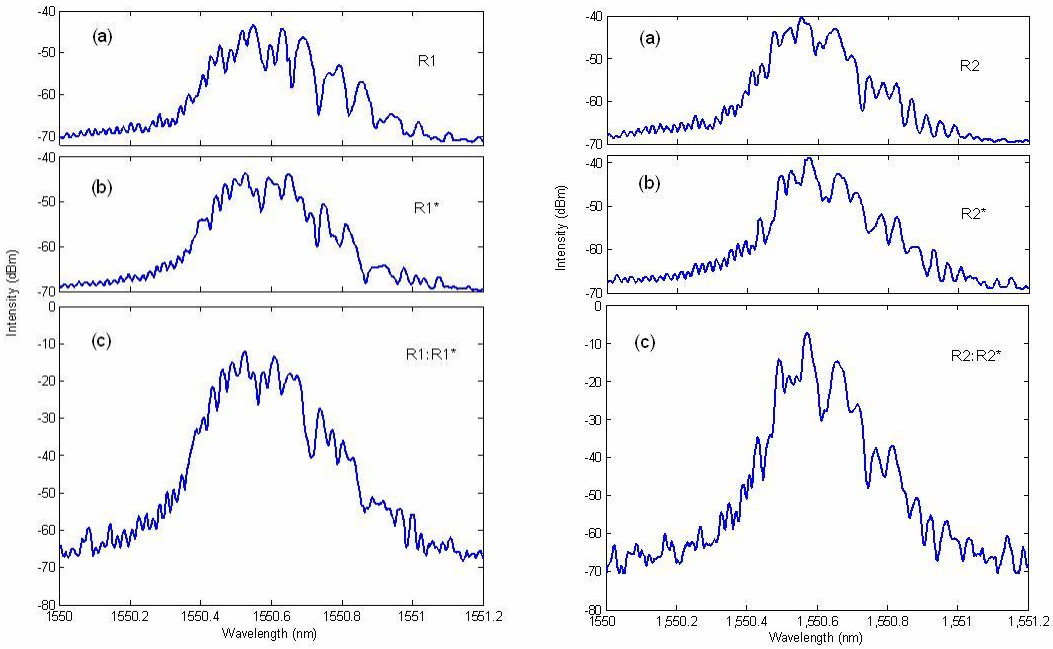

Figure 4.17 Reflectivity spectra when the grating is configured with code R1, R1, R2, R2* respectively, and the corresponding spectra of the decoded signal when autocorrelation is achieved*

By simply changing the configured codes, the autocorrelation and cross-correlation for the two sets of codes were obtained conveniently. Figure 4.18 shows the oscilloscope traces for the decoded signal. A distinctive autocorrelation peak is still achieved with these relatively short codes. The contrast ratio between the crosscorrelation peak to the autocorrelation peak is 27.6% and 26.7% for R1 and R2 respectively. The viability of the reconfigurable grating is verified again. Basically it is feasible to implement other types of code, e.g. the bipolar orthogonal codes, within the code length range of the reconfigurable grating.

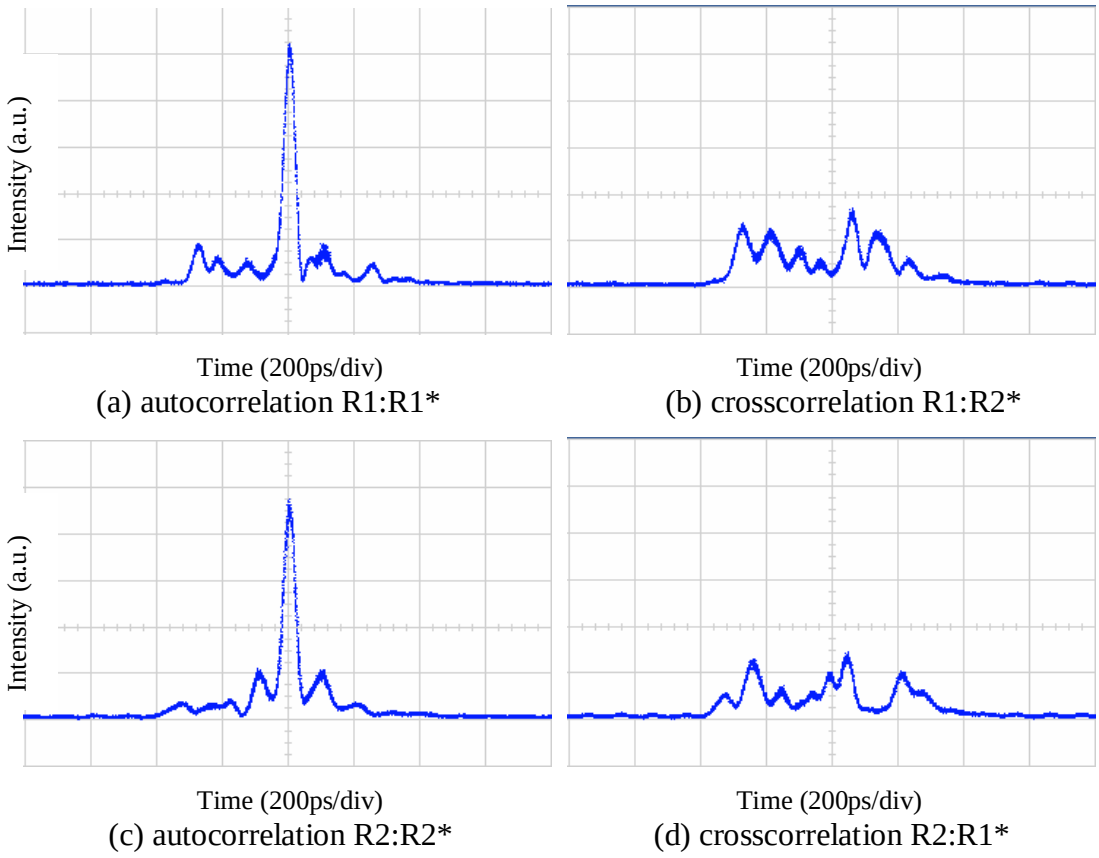

Figure 4.18 Oscilloscope traces (200ps/div) for (a) autocorrelation R1:R1, (b) crosscorrelation R1:R2*, (c) autocorrelation R2:R2*, (d) crosscorrelation R2:R1**

4.2.4 Correlation properties comparison of the discrete phase-shift SSFBG and code-reconfigurable grating with 6ps input pulses

In section 4.2.1 and 4.2.2, 25ps input pulses were preliminarily used to investigate the correlation properties of fixed: fixed, and fixed: reconfigurable OCDMA system. In this section, the performance of the all-reconfigurable coding/decoding system is compared with fixed: fixed, and fixed: reconfigurable system using the same 6ps input pulses generated by the GSL. Figure 4.19 displays the simulated autocorrelation and cross-correlation of code Q1 for the three system cases. As can be seen from the simulation, for the same input pulse, the fixed: fixed setup displays the best correlation properties in terms of both autocorrelation and cross-correlation. The all-reconfigurable setup (tunable:tunable) has a slightly degraded performance. However it is still comparable to the fixed: fixed case. The worst performance is associated with the fixed encoding and tunable decoding setup. This is believed to be due to the mismatch between the fixed-coded abrupt phase shift

in the SSFBGs and the thermally induced distributed phase shift in the reconfigurable gratings.

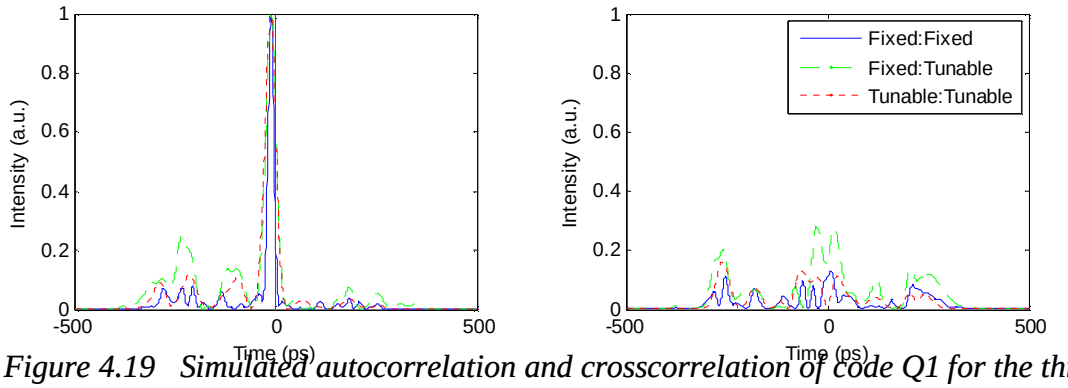

Figure 4.19 Simulated autocorrelation and crosscorrelation of code Q1 for the three different system cases

The experimental oscilloscope traces in Figure 4.20 verified the simulation results. The fixed: fixed system has the best correlation properties, the tunable: tunable system has a similar performance, while the fixed: tunable system displays somehow degraded properties.

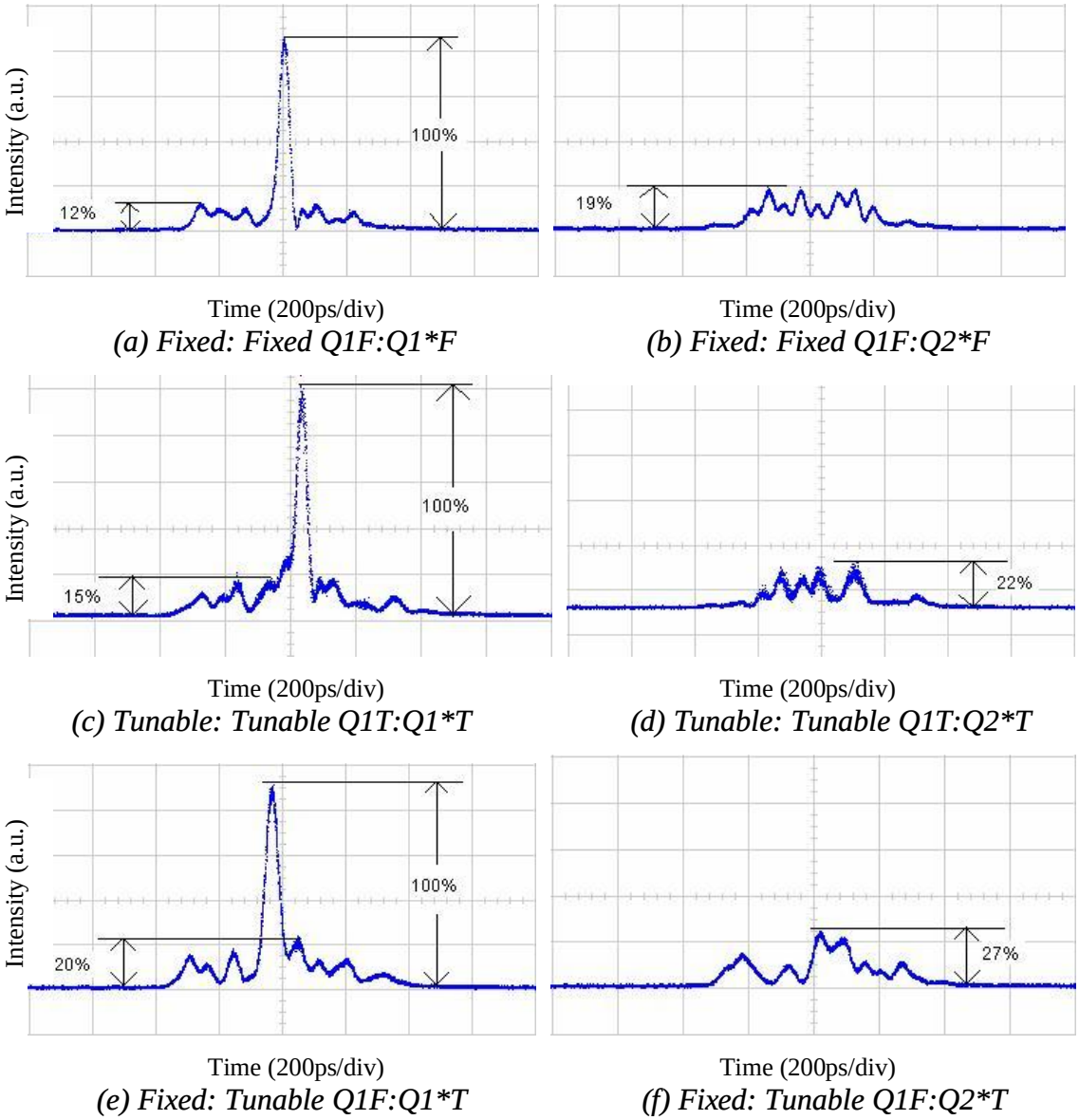

*(a) Fixed: Fixed Q1F:Q1*F* *(b) Fixed: Fixed Q1F:Q2*F*

*(c) Tunable: Tunable Q1T:Q1*T* *(d) Tunable: Tunable Q1T:Q2*T*

*(e) Fixed: Tunable Q1F:Q1*T* *(f) Fixed: Tunable Q1F:Q2*T*

Figure 4.20 oscilloscope traces for the autocorrelation and cross-correlation (a,b): Fixed: Fixed case, (c,d): Tunable: Tunable case, (e,f) Fixed: Tunable case.

Table 4.1 summarises the simulated and measured contrast ratio (defined as sidelobe or cross-correlation peak to the autocorrelation peak) for codes Q1 and Q2. Note that the contrast ratio is originally determined by the correlation properties of individual codes.

Table 4.1 Summary of the simulated and measured contrast ratio

	F:F				F:T				T:T			
	A/C		X/C		A/C		X/C		A/C		X/C	
	Simu.	Expm.	Simu.	Expm.	Simu.	Expm.	Simu.	Expm.	Simu.	Expm.	Simu.	Expm.
Q1	Q1FQ1F		Q1FQ2F		Q1FQ1T		Q1FQ2T		Q1TQ1T		Q1TQ2T	
	8%	12%	13%	19%	24%	20%	28%	27%	12%	15%	16%	22%
Q2	Q2FQ2F		Q2FQ1F		Q2FQ2T		Q2FQ1T		Q2TQ2T		Q2TQ1T	
	15%	19%	12%	25%	22%	20%	30%	28%	7.5%	11%	14%	20%

The system performances of the three different setups are confirmed again by the bit-error-rate (BER) test at 1.25Gb/s. the results are shown in Figure 4.21. A power penalty of ~1.5dB relative to the laser back to back case is observed for the all-reconfigurable system. It is slightly more degraded than the fixed: fixed case, but better than the fixed: tunable case.

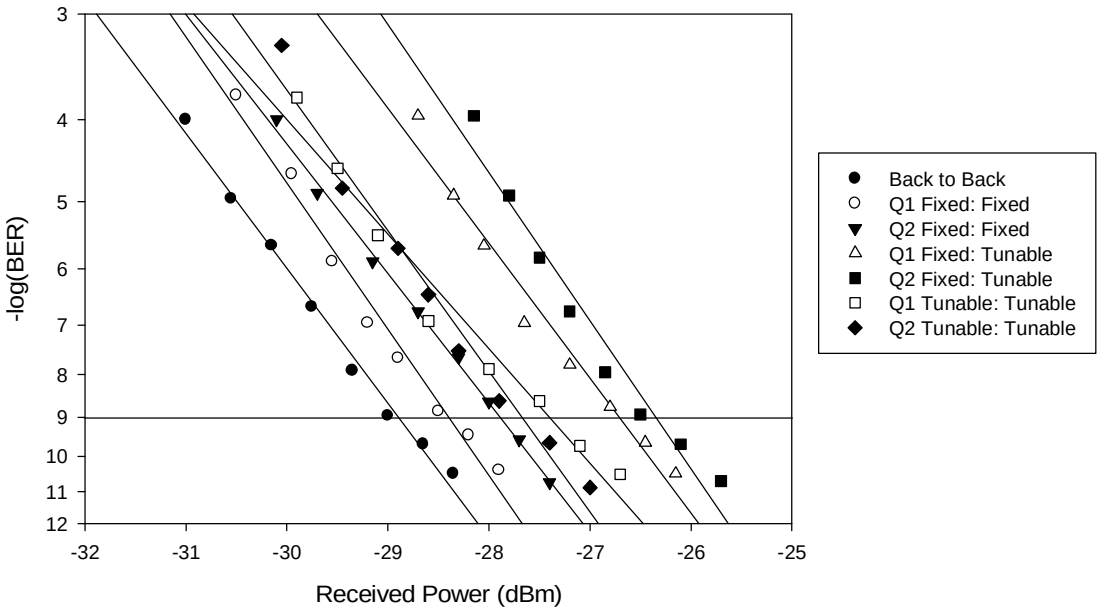

Figure 4.21 BER test results for the three different OCDMA systems

4.3 15-chip Continuous phase-shift SSFBGs

In the reconfigurable grating experiments, a noticeable feature is the narrowed reflectivity spectrum which is inherently due to the thermally induced distributed phase-shift along the grating. Another feature is that, due to the phase mis-match between the reconfigurable grating and fixed-coded SSFBGs, although they are compatible to each other to perform the coding/decoding process, the correlation performances are degraded compared to the all fixed to fixed case and all reconfigurable to reconfigurable case. In this section, we proposed a novel fixed-coded continuous phase-shift SSFBG which basically mimics the thermally induced phase distribution in the reconfigurable grating in order to achieve a similarly narrower spectrum with improved stability[4-6].

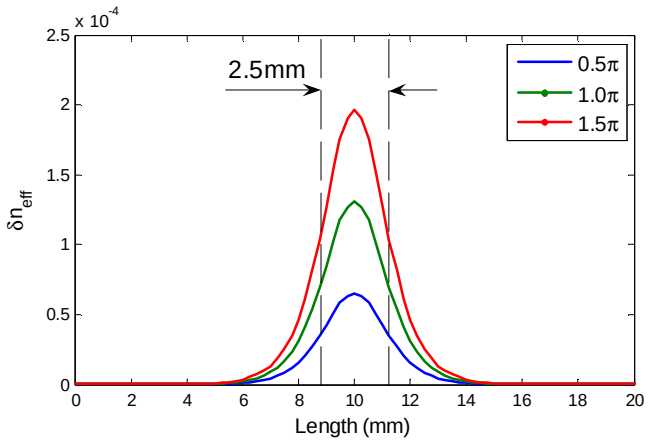

(a) the single phase distribution design

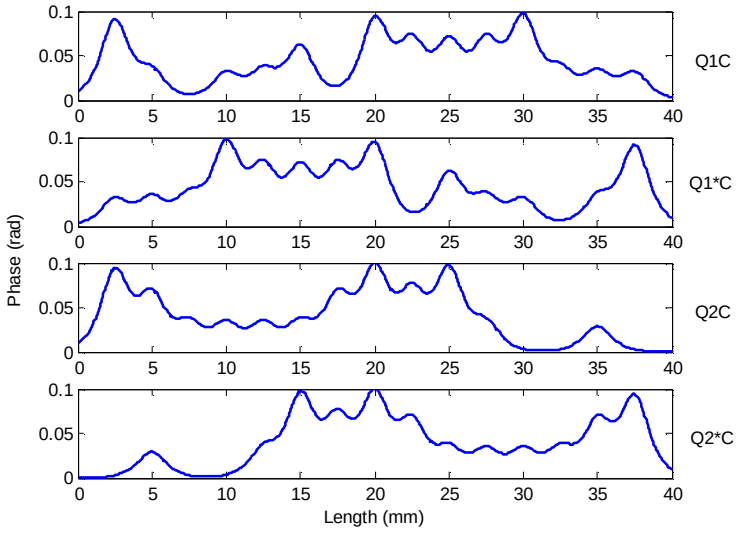

(b) the phase profile design for the four different codes

Figure 4.22 phase profile design for the continuous phase-shift SSFBGs.

As the phase distribution in the reconfigurable grating has been investigated, we designed a similar phase profile for the continuous phase-shift SSFBG[4-7, 8]. The phase distribution has a hyperbolic distribution shape with FWHM= 2.5mm, as shown in Figure 4.22(a). The same 15-bit quaternary codes Q1 and Q2 from the Family A sequences as used in the previous experiments have been chosen for the continuous phase-shift gratings, denoted as Q1C, Q1*C, Q2C, Q2*C respectively. The designed phase profiles for these gratings are illustrated in Figure 4.22(b).

Note that the designed phase profiles for the continuous phase-shift SSFBGs is similar to the one of the code-reconfigurable grating. Thus the reflectivity spectra and temporal responses are also similar to those have been obtained for the code-reconfigurable gratings. Figure 4.23 shows the measured reflectivity spectra for the continuous phase-shift SSFBGs. The spectra of the conjugated codes pair, e.g. Q1C

and Q1*C, Q2C and Q2*C exhibit high similarity, which indicates good phase matching and correlation performance in the coding/decoding process. In addition, the reflectivity spectra of the reconfigurable grating with codes Q1*R and Q2*R were superposed onto the continuous SSFBGs Q1*C and Q1*C respectively. As expected, the spectra for the two different types of gratings show similar features, which confirms that the phase profile in the gratings are comparable.

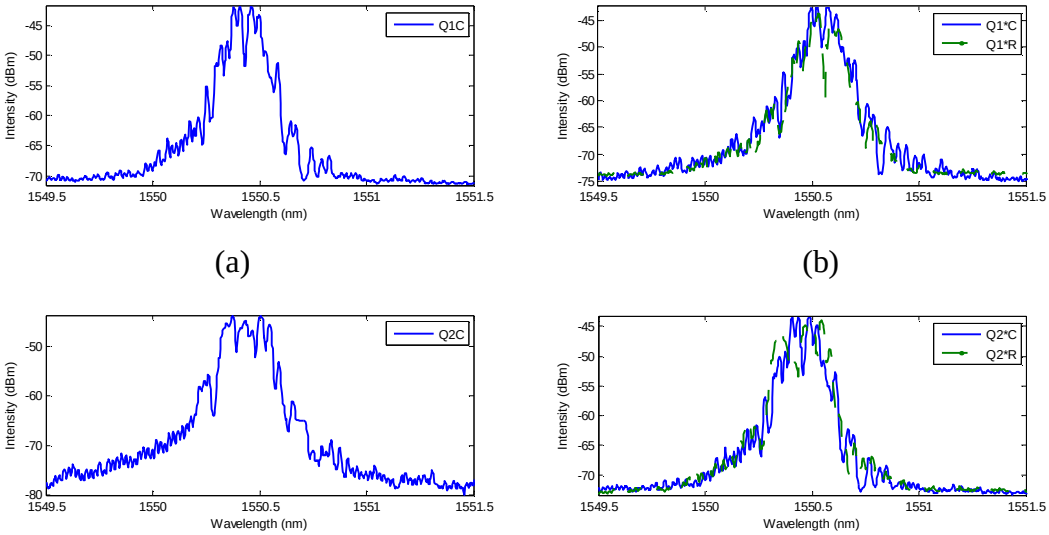

*Figure 4.23 measured reflectivity spectra for the continuous phase-shift SSFBGs: (a) Q1C, (b) Q1*C and Q1*R, (c) Q2C, (d) Q2*C and Q2*R*

The same setup for the coding/decoding system experiment as described in Figure 4.2 is also used to evaluate the performance of the continuous phase-shift SSFBGs with 6ps input pulses.

Figure 4.24 shows the oscilloscope traces of the encoded signal and the corresponding optical spectra.

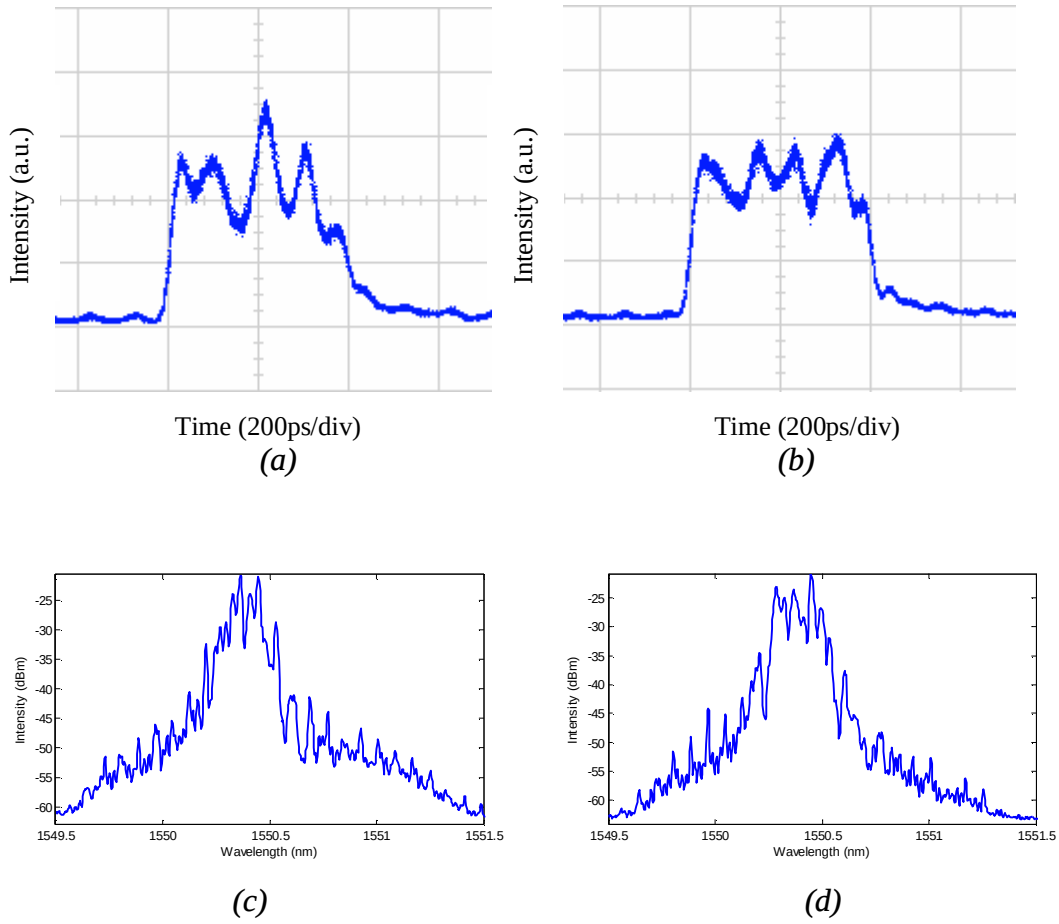

Figure 4.24 oscilloscope traces of the encoded signal (a) Q1C, (b) Q2C and the corresponding optical spectra (c) Q1C, (d) Q2C.

Figure 4.25 shows the oscilloscope traces for the autocorrelations and cross-correlations obtained by using the continuous SSFBGs as both the encoder and decoder. For Q1C, the autocorrelation contrast ratio is 14%, the cross-correlation contrast ratio is 22%. For Q2C, the contrast ratio is 12% and 21% respectively. Note that the correlation performance is highly comparable to the results I obtained for the system setup using reconfigurable gratings as both the encoder and decoder. The result is reasonable since the two types of gratings have similar phase profiles, making them totally compatible. To verify this point, the code-reconfigurable grating was used as the encoder and the continuous phase-shift SSFBG as the decoder to inspect the correlation performance again. As expected, comparable performance, even down to the sidelobe features of the correlation properties has been obtained. The oscilloscope traces are shown in Figure 4.26.

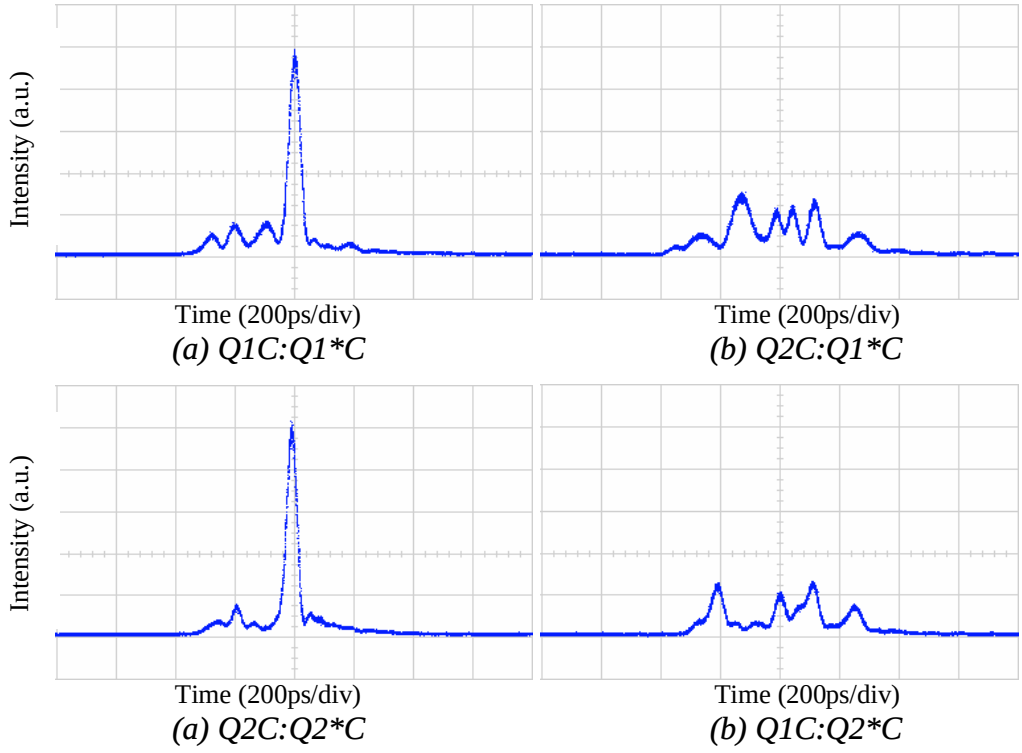

Figure 4.25 oscilloscope traces for the autocorrelations and crosscorrelations when both the encoder and decoder use continuous phase-shift SSFBGs.

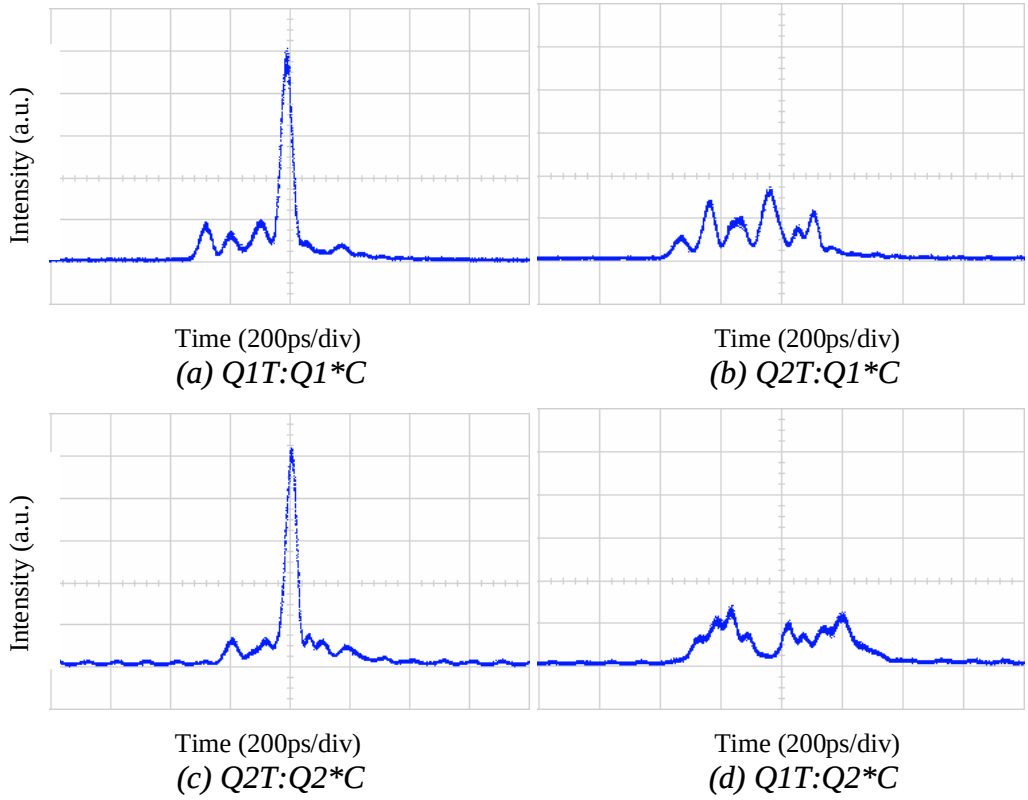

Figure 4.26 oscilloscope traces for the autocorrelations and crosscorrelations when use code-reconfigurable grating as the encoder and continuous phase-shift SSFBG as the decoder.

Again, the BER measurements have been taken to evaluate the system performance of the continuous phase-shift SSFBGs. Two sets of BER tests have been taken, one for the system setup using continuous phase-shift SSFBGs as both the encoder and the decoder. Another set of tests was for the system setup using the code-reconfigurable grating as the encoder with the continuous phase-shift SSFBGs as the decoder. The BER test results are shown in Figure 4.27. As can be seen from the results, both sets of system setup offer similar performance. The less than 0.5dB power penalty between the continuous to continuous system and reconfigurable to continuous system is believed to be associated with the instability of the code reconfigurable grating and the not exact matching of the reconfigurable codes and continuous codes. These experiments have demonstrated the feasibility of continuous phase-shift SSFBGs in the applications of OCDMA coding/decoding system.

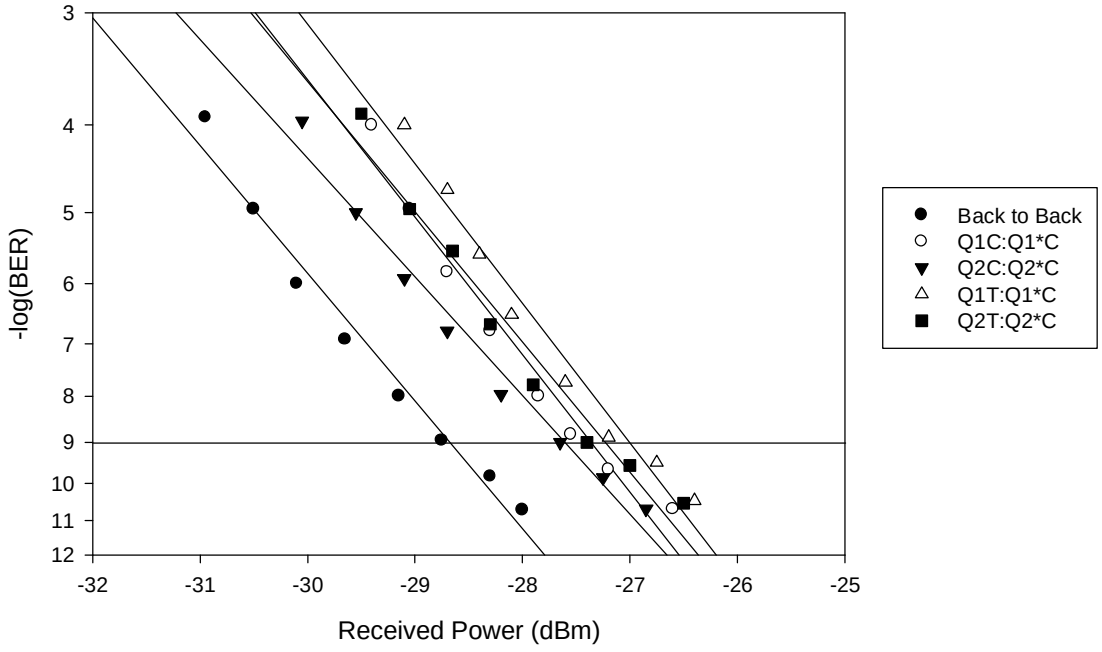

Figure 4.27 BER test results for the continuous phase-shift SSFBGs.

4.4 Conclusions

The performance of optical coding/decoding based on several different fiber Bragg grating types have been investigated in this chapter, including discrete phase-shift SSFBGs, code-reconfigurable gratings and continuous phase-shift SSFBGs.

Different combinations of these gratings in the OCDMA system have also been comparatively studied. Generally, excellent code recognition results have been obtained and error free operation have been achieved for all the different types of gratings. By comparing the correlation performance of the different gratings, it is found that the combination of a discrete phase-shift encoder with a discrete phase-shift decoder has the best correlation performance, the combination of code-reconfigurable encoder and code-reconfigurable decoder has a slightly degraded performance, while the combination of discrete phase-shift encoder and code-reconfigurable decoder offers the worse but still acceptable performance due to the mis-match of the two different types of gratings. Among these results, the code-reconfigurable grating displays several attractive features, e.g. flexible code reconfigurability, narrower spectrum, and a tolerance to wider input pulses. These features enable our further demonstration of reconfigurable systems in the following chapters. Meanwhile, inspired by the unique features of code-reconfigurable gratings, a novel continuous phase-shift SSFBG was proposed, which presents similar features to the code-reconfigurable gratings, with higher stability but no reconfigurability due to the nature of fixed-coded SSFBGs. These experiments highlight the advances of optical coding/decoding based on improved FBG techniques in the application of OCDMA system.

References

[4-1] P. C. Teh, P. Petropoulos, M. Ibsen, and D. J. Richardson, "Phase encoding and decoding of short pulses at 10 Gb/s using superstructured fiber Bragg gratings," *IEEE Photonics Technology Letters*, vol. 13, pp. 154-156, Feb 2001.

[4-2] P. C. Teh, P. Petropoulos, M. Ibsen, and D. J. Richardson, "A comparative study of the performance of seven- and 63-chip optical code-division multiple-access encoders and decoders based on superstructured fiber Bragg gratings," *Journal Of Lightwave Technology*, vol. 19, pp. 1352-1365, Sep 2001.

[4-3] P. C. Teh, P. Petropoulos, M. Ibsen, and D. J. Richardson, "160 GBit/s, 64-bit all-optical code generation and recognition using superstructured fibre Bragg gratings," in *ECOC 2000. 26th European Conference on Optical Communication*, Munich, Germany, 2000, pp. 15-16.

[4-4] S. Boztas, R. Hammons, and P. Y. Kumar, "4-phase sequences with near-optimum correlation properties," *IEEE Transactions on Information Theory* , vol. 38, pp. 1101-1113, 1992.

[4-5] T. Erdogan, "Fiber grating spectra," *Lightwave Technology, Journal of*, vol. 15, pp. 1277-1294, 1997.

[4-6] Z. Zhang, C. Tian, P. Petropoulos, D. J. Richardson, and M. Ibsen, "Distributed-phase OCDMA encoder-decoders based on fiber Bragg gratings," *IEEE Photonics Technology Letters*, vol. 19, pp. 574-6, 2007.

[4-7] Z. Zhang, C. Tian, M. A. F. Roelens, M. R. Mokhtar, P. Petropoulos, D. J. Richardson, and M. Ibsen, "Direct characterization of the spatial effective refractive index profile in Bragg gratings," *IEEE Photonics Technology Letters*, vol. 17, pp. 2685-2687, Dec 2005.

[4-8] Z. Zhang, C. Tian, M. R. Mokhtar, P. Petropoulos, D. J. Richardson, and M. Ibsen, "Rapidly reconfigurable optical phase encoder-decoders based on fiber Bragg gratings," *IEEE Photonics Technology Letters*, vol. 18, pp. 1216-1218, 2006.

Chapter 5

Multiple access interference (MAI) reduction based on Two-Photon Absorption (TPA) process

5.1 Multiple access interference (MAI) reduction

Multiple access interference (MAI) refers to the interference between a signal channel and other coded channels which are transmitted simultaneously in the OCDMA system over the same bandwidth. It occurs in the region of temporal overlap of the different coded bits. MAI can severely degrade a user's ability to identify the intended coded bits and thus limits the number of simultaneous users within the system. MAI is a major noise source in OCDMA systems. In addition to the basic idea of choosing optimum codes and longer code sequences, several approaches to reduce MAI in OCDMA systems have been proposed.

For the unipolar (amplitude-modulated) codes, an optical hard limiter (OHL) can be employed to ensure that all arriving pulses have an equal light intensity after the limiter and hence this eliminates the effect of the addition of coinciding pulses of different codes[5-1,2]. Some more complex and more efficient techniques, such as parallel interference cancellation[5-3,4], have also been studied in incoherent systems. Within coherent systems, balanced detection [5-5,6] can be utilised to suppress the residual signals induced by the interfering codes. Time gating [5-7] also can effectively suppress the interference outside of the time slot of the autocorrelation peak. However, these schemes require fast and complicated electronics to ensure a synchronous process to the decoded signal, which thereby increases the complexity and cost of the system. Several optical thresholding techniques based on various nonlinear effects have also been proposed, such as second harmonic generation (SHG) in periodically-poled lithium niobate (PPLN) [5-8], super-continuum (SC) generation

in dispersion-flattened-fiber (DFF) [5-9], nonlinear Kerr switch function in nonlinear optical loop mirror (NOLM) [5-10], as well as self-phase-modulation (SPM) in high nonlinear holey fiber[5-11]. These methods do work but rely on the use of a separate optical thresholder followed by an optical detector to convert the optical signal into electrical form, making for a complex system.

5.2 Nonlinear thresholding based on Two-Photon Absorption (TPA) process

In this chapter, an alternative approach based on the nonlinear optical to electrical conversion process of Two-Photon Absorption (TPA) in a semiconductor micro-cavity is demonstrated. Using this approach one can carry out simultaneous optical thresholding and detection.

TPA is a nonlinear process where two photons are absorbed and result in the generation of a single electron-hole pair [5-12]. The generated photocurrent is proportional to the square of the intensity, and it is this nonlinear response that enables the use of TPA for various optical signal processing applications including optical demultiplexing, optical sampling and optical thresholding. For OCDMA thresholding, the nonlinear response of TPA should permit a clearer differentiation between a correctly decoded autocorrelation peak and residual MAI noise interference, as the intensity of correctly decoded pulses is much higher than that of the MAI. The theoretical analysis of TPA in semiconductor microcavities is introduced in [5-12]. The feasibility of using TPA for optical thresholding has been demonstrated before[5-13]. The application of TPA optical thresholder in the OCDMA networks is investigated in this chapter.

This work was done in collaboration with Dr. P.J.Maguire and Prof. L.P.Barry from Dublin City University, who provided the TPA devices and collaborated in the experiments.

5.2.1 TPA device using a semiconductor microcavity with a bandwidth of ~100MHz

A simple 2-channel OCDMA system, as shown in Figure 5.1, was set up for the MAI reduction demonstration. A gain switched laser and a section of DCF are used to

generate 6ps input pulses. The 10GHz short pulse train is then gated down to an appropriate repetition rate by a $LiNbO_3$ modulator, before being split into two paths and fed into two different encoding SSFBGs. The delay stage in one path can be used to adjust the relative timing position of the two encoded signals. A 150m length of SMF is used in one path to break the coherence between the two encoded signals before they are combined together for the decoding process. Due to the high peak power required for the TPA process, several EDFAs were used at appropriate places within the system to boost the optical power. A 3nm band-pass filter is used after the first EDFA to suppress ASE noise. After the decoding process, the decoded signal is fed into the TPA detector. The resulting photocurrent generated from the TPA device is then electrically amplified with a low noise RF amplifier, before being displayed on an oscilloscope. For this experiment, we deployed 63-chip bipolar SSFBGs which have a chip-length of 0.66mm, resulting in a total grating length of 41.58mm. The performance of these gratings has been investigated and described in detail in[5-14]. We chose these SSFBGs because their central wavelength (1553.1nm) was within the range of the resonant wavelength (1559nm) of the TPA device. The decoding SSFBG3 was written with code B2* which is the conjugate of the code of encoding SSFBG2 (B2), while the other encoding grating SSFBG4 (B4) acts as the interference source. Figure 5.2 displays a trace of both the autocorrelation (B2:B2*) and cross-correlation (B4:B2*), captured by an oscilloscope with an overall detection bandwidth of 20GHz.

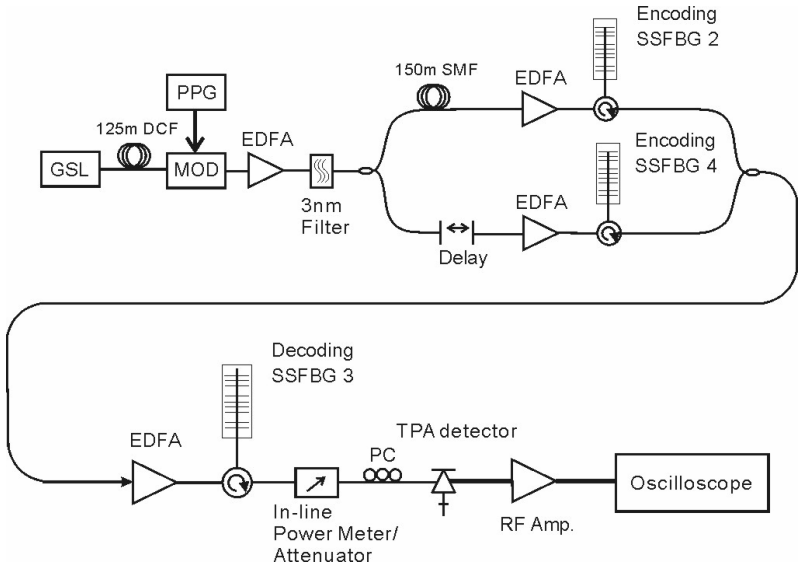

Figure 5.1 Experimental setup for TPA thresholding and detection in a 2-channel OCDMA system

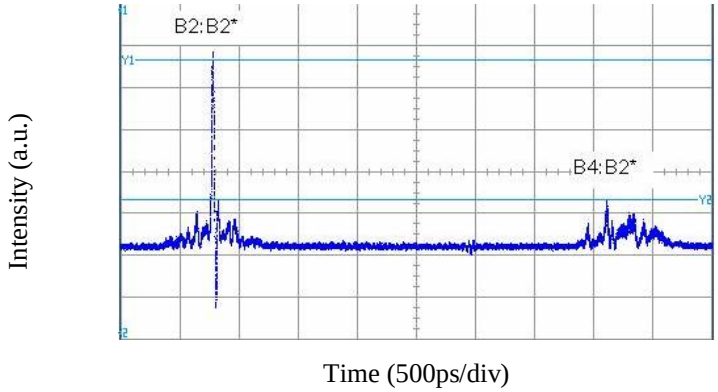

Figure 5.2 Linear detection (oscilloscope trace) of the decoded signal

The TPA device used in our first experiment was a semiconductor micro cavity consists of two GaAs/AlAs Distributed Gragg Reflector mirrors surrounding an undoped GaAs active region. The Active region is 460nm thick. The device length is designed to have a resonant wavelength of 1553.5 nm and electrical bandwidth of ~100MHz. The photocurrent was characterised as a function of input optical power for the TPA device before carrying out the thresholding experiments. The P-I curve is shown in Figure 5.3. As is clear from the curve, the nonlinear TPA process happens when the input peak power exceeds ~10W, showing a square dependence of the photocurrent on the incident optical peak power.

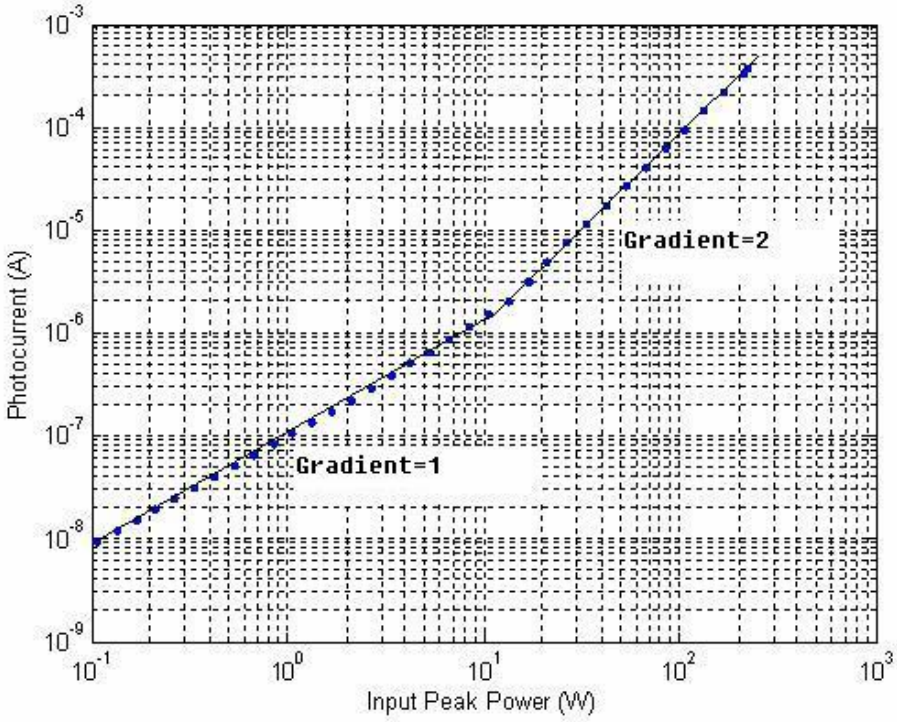

Figure 5.3 Photocurrent as a function of incident optical signal for the semiconductor micro cavity.

Firstly the enhanced code recognition quality by the TPA thresholding effect is demonstrated when the two encoded signal are separated in the time domain. Considering the bandwidth of the TPA device is about 100MHz, to make the results comparable, an oscilloscope with 100MHz bandwidth was used to observe the linear detection results. Figure 5.4(a) shows the detected signal when the repetition rate of the encoded signal is 12.5MHz and the average input power to the TPA device is 3.2dBm (equivalent optical peak power of 27.8W). As can be seen from the results, the cross-correlation has been suppressed considerably by the TPA detection. The contrast ratio (autocorrelation peak to cross-correlation peak) is 2.16 (3.34dB) for the linear detection. While for the TPA detection, the contrast ratio is improved to 6.41 (8.07dB). Figure 5.4(b) shows the results when the repetition rate of the encoded signal is 25MHz and the input power to the TPA device is 6.1 dBm (equivalent optical peak power of 32.6W). Compared to the detection results achieved with 12.5MHz pulses, the linear detection result displays obvious MAI degradation. The contrast ratio for the linear detection is 1.78 (2.49dB) only. The degradation is due to the closer temporal separation of the autocorrelation and cross-correlation signals than for the 12.5MHz case, as well as the linear detector's bandwidth limitation. However, great crosscorrelation suppression has been achieved by the TPA detection, for which the contrast ratio is only 8.93 (8.07dB). The improvement is mainly due to the higher input peak power for the TPA detector than the 12.5MHz case. This experiment confirms the potential of the TPA device to improve the overall system performance relative to the linear detector.

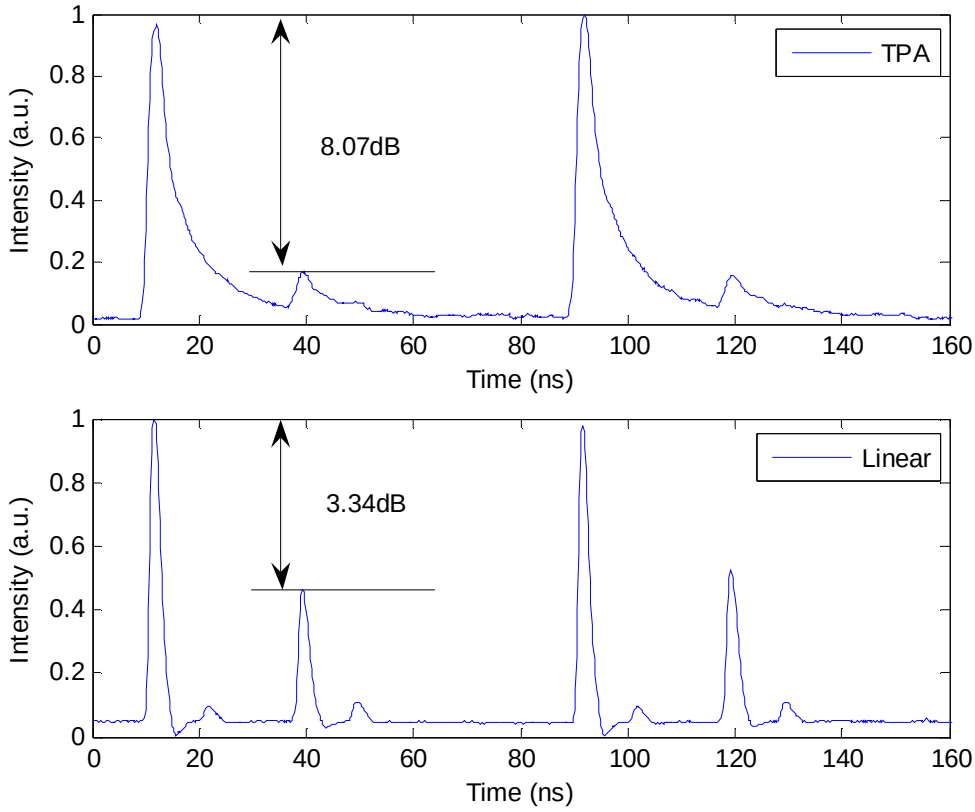

(a) Repetition rate = 12.5MHz

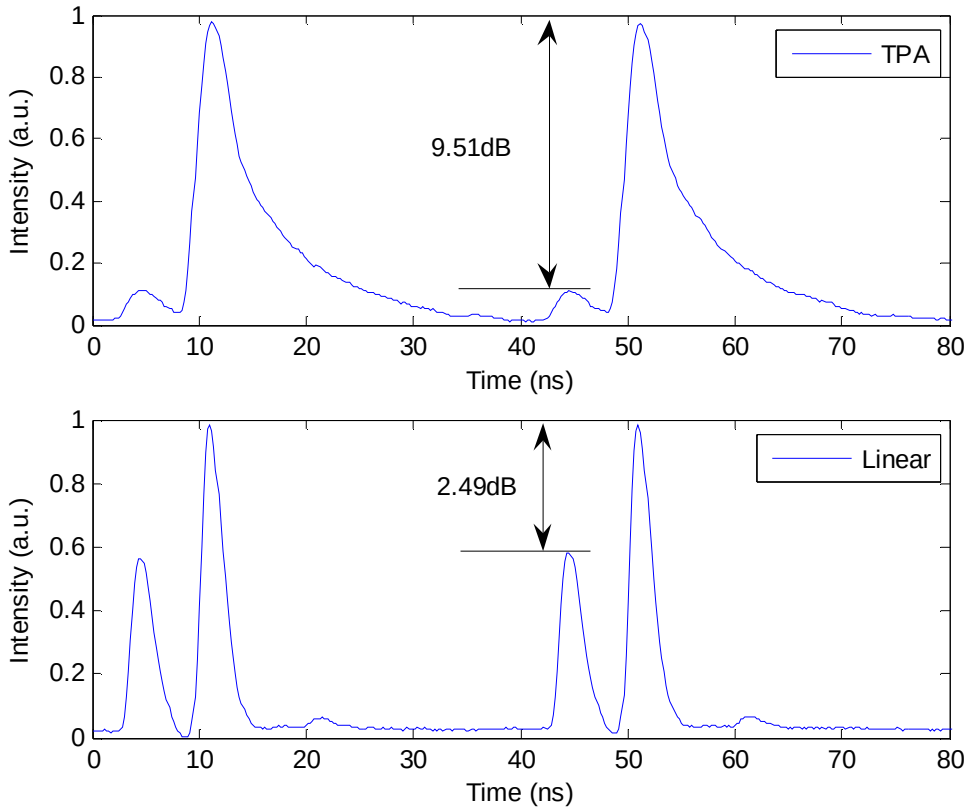

(b) Repetition rate = 25MHz

Figure 5.4 The linear detection and TPA detection results.

Next, the suppression of MAI noise using the same TPA device in the 2-channel OCDMA system was demonstrated, in which the two different encoded signals are completely overlapped (as shown in Figure 5.5(a)). Figure 5.5(b) shows the eye diagram of the decoded signal captured by the 20GHz oscilloscope (linear detector) when the data is modulated with a PRBS sequence at a bit rate of 16.47Mb/s. the overlapping of the two codes has induced severe interference at the decoded signal. Note that due to the generic code-distinguishing capability of OCDMA, and the sufficient oscilloscope bandwidth, the eye diagram in Figure 5.5(b) still keeps well open. We try to achieve further suppression of MAI noise by deploying the TPA device.

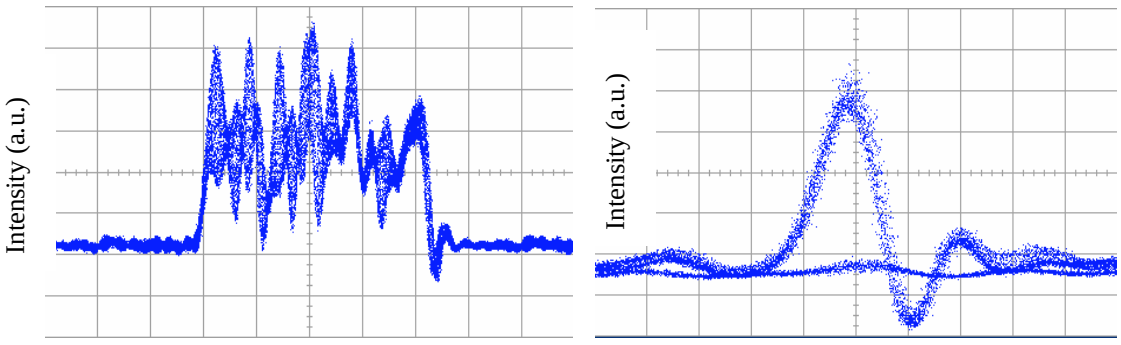

(a) 100ps/div (b) 20ps/div

Figure 5.5 (a) the overlapped two encoded signal, (b) the decoded eye diagram.

Prior to the experimental measurements, a simulation has been done of the detected contrast ratio (autocorrelation peak to cross-correlation peak) of both the TPA device and the linear detector as a function of input optical power. The simulation is based on the measured P-I curve of the TPA device and the correlation properties of the gratings used in the experiments. The simulation results are plotted in Figure 5.6, together with the experimental results. The results are presented as the autocorrelation peak to cross-correlation peak contrast ratio, which means that higher contrast ratio indicates better performance. As can be seen in Figure 5.6, for the linear detector, the contrast ratio is not affected by the input power, while the contrast ratio for the TPA detector increases as the input power is increasing. Generally, for input average power below 4dBm (equivalent autocorrelation peak power is about 12W), the contrast ratio is worse than that of the linear detector, and the change of contrast ratio is relatively small. The deviation between the experimental and simulation results might be due to the low optical power, which has induced large measurement

uncertainty. While for the input average power above 5dBm, the contrast ratio for the TPA device starts to overperform the linear detector. The contrast ratio for the TPA device increases rapidly when the input power keeps increasing.

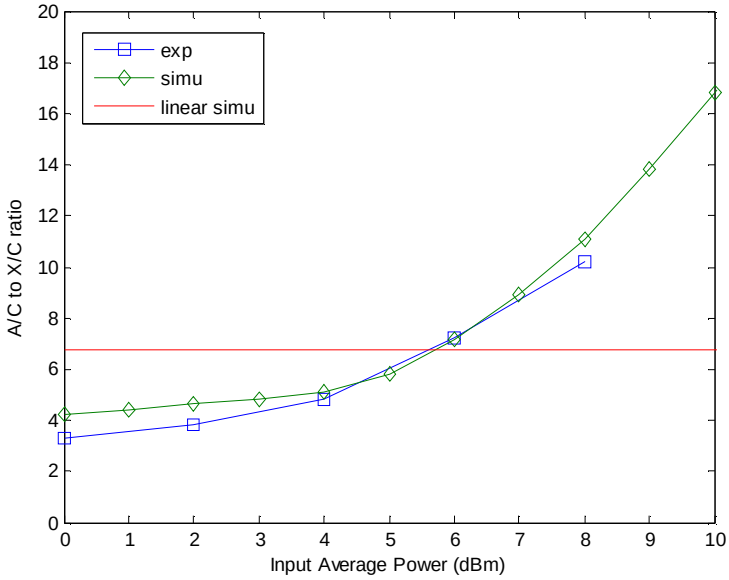

Figure 5.6 Detected contrast ratio (autocorrelation peak to cross-correlation peak) of both the TPA device and linear detector as a function of input optical power

Table 5.1 lists the equivalent optical peak power for the different average input power when the pulses' repetition rate is 16.47MHz:

Table 5.1 Corresponding autocorrelation and crosscorrelation peak power for the different average input power

Avg. (dBm)	0	1	2	3	4	5	6	7	8	9	10
AC Peak (W)	5.12	6.45	8.11	10.22	12.86	16.20	20.39	25.67	32.31	40.68	51.21
XC Peak (W)	0.36	0.46	0.58	0.72	0.91	1.15	1.45	1.82	2.30	2.89	3.64

As can be seen from the table, when the input average power is between 0dBm and 4dBm, both the autocorrelation peak power and cross-correlation peak power are located in the single photon absorption region. When the input average power is above 5dbm, the autocorrelation peak power falls into the TPA region, while the corresponding cross-correlation peak power is still located in the single photon absorption region. This explains why the contrast ratio increases (MAI reduces) when the input average power exceeds 4dBm.

Table 5.2 compares the eye diagrams detected by the TPA device and the normal 2GHz and 20GHz linear detector at different optical power levels. As can be

seen, with increasing power, the TPA output has an increasingly clear open eye, while the eye diagram obtained by the 2GHz linear detector remains the same, other than the overall increased power level. The nonlinear TPA process is thus shown to suppress the interference noise significantly. The effect of the different detectors' bandwidth is also presented in these eye diagrams. Because the initial input pulses were driven by a 10GHz clock signal, the narrow 100MHz bandwidth can only produce an eye diagram with a long trailing. The linear 2GHz and 20GHz detectors have a better presentation of the signal, although the 2GHz detector exhibits wider traces than the 20GHz detector does.

Table 5.2 Comparison of the detection results by the TPA device and the normal linear detector at different optical power level

Input Power	Simu. BW=100MHz	TPA BW=100MHz (500ps/div)	Linear BW=2GHz (200ps/div)	Linear BW=20GHz (50ps/div *)
0dBm	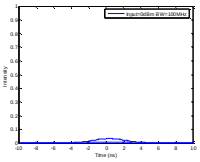	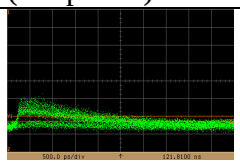	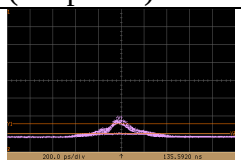	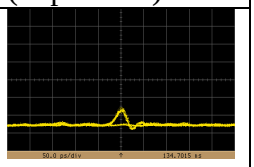
2dBm	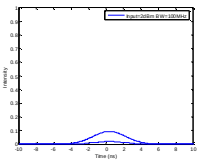	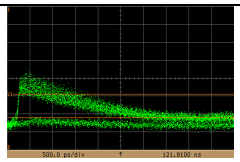	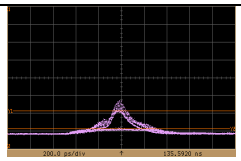	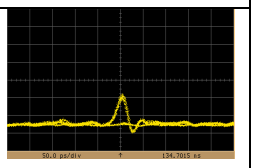
4dBm	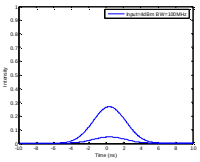	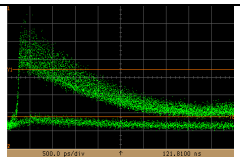	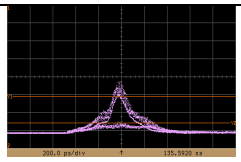	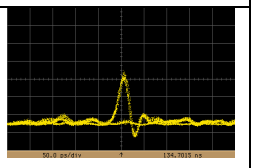
6dBm	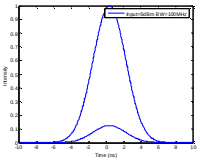	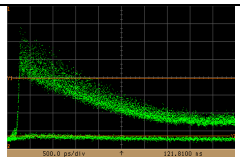	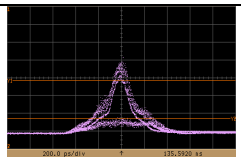	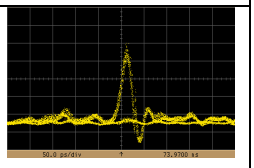
8dBm	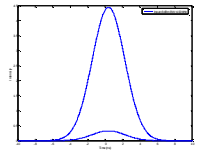	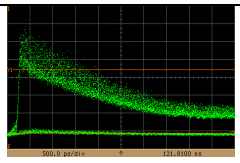	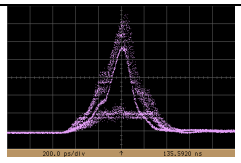	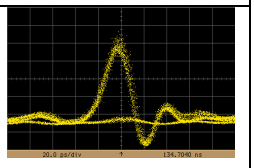

* The last one is 20ps/div

5.2.2 TPA device using a 1310nm laser diode with a bandwidth of 1GHz

After the success of the experiment with the first TPA device, further experiments were carried out with another TPA device, a commercially available 1310nm FP laser diode with a detection bandwidth of ~1GHz. The experimental setup is shown in Figure 5.7, which is similar to Figure 5.1 except that we deploy EAM-carved 25ps short pulses as the input pulses, and a set of 31-chip quaternary continuous phase-shift SSFBGs working at 1561.6nm, which have been used in the OCDMA system. As we know, the use of wider input pulses and the continuous phase-shift SSFBGs will degrade the correlation properties slightly, making the use of the optical thresholder increasingly desirable.

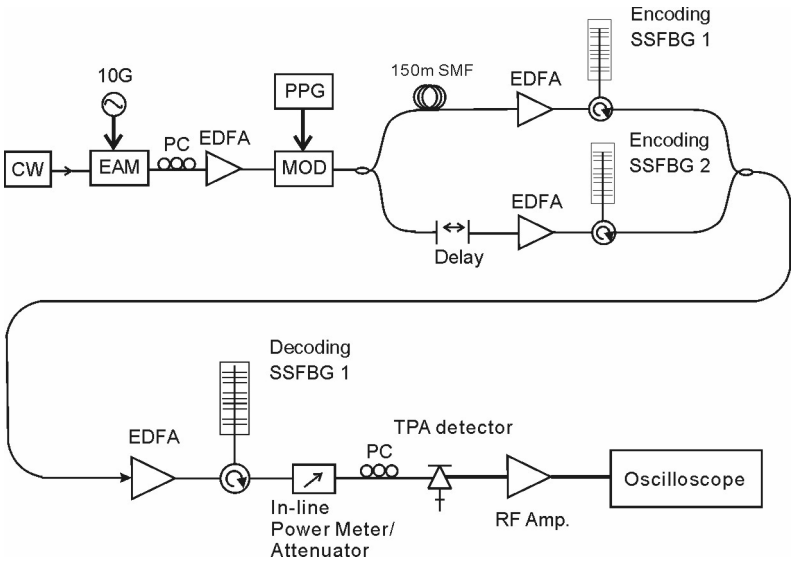

Figure 5.7 Experimental setup for the 1310nm laser diode TPA thresholding and detection in a 2-channel OCDMA system.

The photocurrent as a function of incident optical peak power was also measured for the 1310nm laser diode; the results are plotted in Figure 5.8. This device shows high sensitivity to the TPA process, as the approximate square dependence of the photocurrent on the incident optical intensity starts at very low input power.

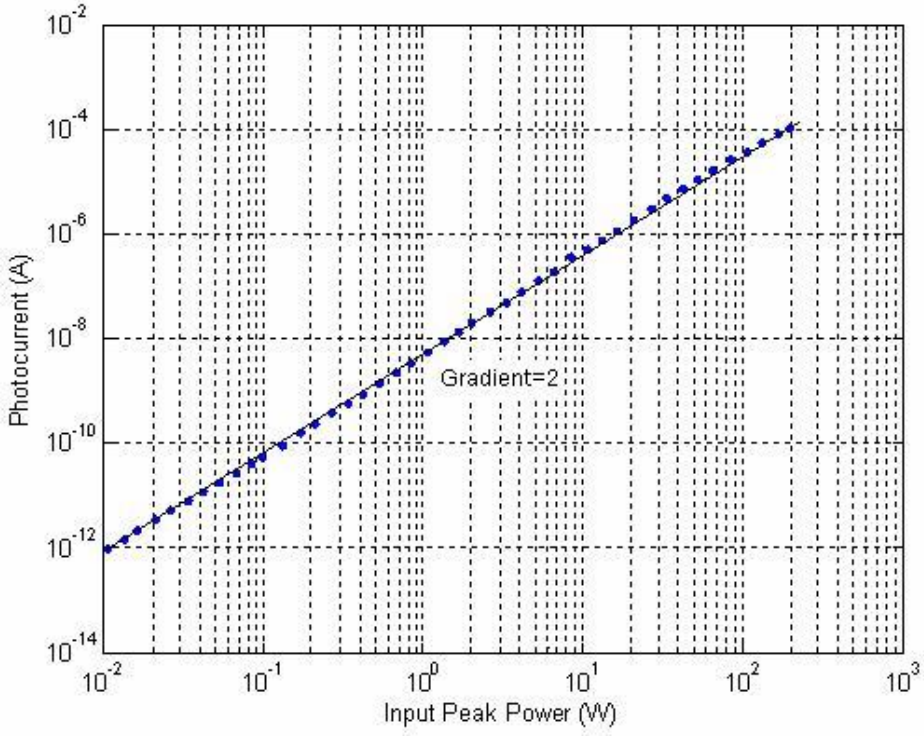

Figure 5.8 Photocurrent as a function of incident optical peak power for the 1310nm laser diode

Figure 5.9 displays the eye diagram obtained by both the linear detector and TPA device when the two-channel OCDMA system is operating at an individual channel rate of 155Mb/s. To make the results comparable, the results of both the linear detector and the TPA device are displayed on an oscilloscope with a bandwidth of 622MHz. The thresholding effect of the TPA device can be seen clearly with the absence of cross-correlation. The extinction ratio for the linear detection is ~5.3dB. With the TPA device, the extinction ratio is improved by more than 10dB. Note that, because of the relative low bandwidth of the two detectors compared to the chip rate of the codes, the fine features of the correlation signals are not resolved. However, the feasibility of using the TPA process for simultaneous optical thresholding and detection in OCDMA networks has been confirmed. With a properly fabricated TPA device, improved performance in such systems should be achievable.

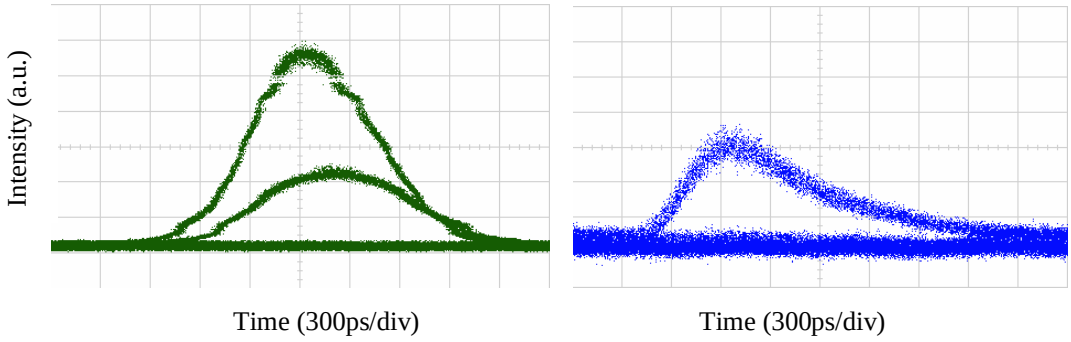

Figure 5.9 Eye diagram obtained by (a) the linear detector and (b) the TPA device

5.3 Conculsions

Using a TPA process to simultaneously perform nonlinear optical thresholding and detection has been proposed and experimentally demonstrated. Multiple access interference (MAI) reduction in the multi-user OCDMA system has been achieved by using the TPA-based nonlinear detector, thereby improving system performance. Due to the bandwidth limit of the available TPA devices, we could not go further with measurements such as BER characterization. However, the feasibility of using TPA process for MAI reduction in the OCDMA system has been clearly demonstrated. While TPA detector still requires high optical intensity due to its inherent inefficiencies, it is being improved. Provided with an appropriate TPA device, distinguished performance improvement can be expected. Future work is needed to

optimise the TPA detector in terms of resonant wavelength, efficiency, detecting bandwidth, to make it suitable for the applications in the telecommunications system.

References

[5-1] T. Ohtsuki, "Performance analysis of direct-detection optical asynchronous CDMA systems with double optical hard-limiters," *Journal of Lightwave Technology*, vol. 15, pp. 452-7, 1997.

[5-2] L. Che-Li and W. Jingshown, "A synchronous fiber-optic CDMA system using adaptive optical hardlimiter," *Journal of Lightwave Technology*, vol. 16, pp. 1393-403, 1998.

[5-3] C. Goursaud, A. Julien-Vergonjanne, C. Aupetit-Berthelemot, J. P. Cances, and J. M. Dumas, "DS-OCDMA receivers based on parallel interference cancellation and hard limiters," *IEEE Transactions on Communications*, vol. 54, pp. 1663-71, 2006.

[5-4] H. M. H. Shalaby, "Synchronous fiber-optic CDMA systems with interference estimators," *Journal of Lightwave Technology*, vol. 17, pp. 2268-75, 1999.

[5-5] R. Adams, J. Faucher, L. Thomas, D. V. Plant, and L. R. Chen, "Demonstration of encoding and decoding 2-D wavelength-time bipolar codes for OCDMA systems with differential detection," *IEEE Photonics Technology Letters*, vol. 17, pp. 2490-2492, 2005.

[5-6] X. Wang, N. Wada, T. Miyazaki, and K. Kitayama, "Coherent OCDMA system using DPSK data format with balanced detection," *IEEE Photonics Technology Letters*, vol. 18, pp. 826-828, 2006.

[5-7] P. Petropoulos, N. Wada, P. C. Teh, M. Ibsen, W. Chujo, K. I. Kitayama, and D. J. Richardson, "Demonstration of a 64-chip OCDMA system using superstructured fiber gratings and time-gating detection," *IEEE Photonics Technology Letters*, vol. 13, pp. 1239-1241, 2001.

[5-8] Z. Jiang, D. Seo, S. Yang, D. E. Leaird, R. V. Roussev, C. Langrock, M. M. Fejer, and A. M. Weiner, "Four-user 10-Gb/s spectrally phase-coded O-CDMA system operating at 30 fJ/bit," *IEEE Photonics Technology Letters*, vol. 17, pp. 705-707, 2005.

[5-9] X. Wang, T. Hamanaka, N. Wada, and K.-I. Kitayama, "Dispersion-flattened-fiber based optical thresholder for multiple-access-interference suppression in OCDMA system," *Optics Express*, vol. 13, pp. 5499-5505, 2005.

[5-10] P. C. Teh, M. Ibsen, J. H. Lee, P. Petropoulos, and D. J. Richardson, "A 4-channel WDM/OCDMA system incorporating 255-chip 320 Gchip/s quaternary phase coding and decoding gratings," *Optical Fiber Communication (OFC 2001)*, vol. Postdeadline, 2001.

[5-11] J. H. Lee, P. C. Teh, Z. Yusoff, M. Ibsen, W. Belardi, T. M. Monro, and D. J. Richardson, "A holey fiber-based nonlinear thresholding device for optical CDMA receiver performance enhancement," *IEEE Photonics Technology Letters*, vol. 14, pp. 876-8, 2002.

[5-12] H. Folliot, M. Lynch, A. L. Bradley, T. Krug, L. A. Dunbar, J. Hegarty, J. F. Donegan, and L. P. Barry, "Two-photon-induced photoconductivity enhancement in semiconductor microcavities: a theoretical investigation," *Journal of the Optical Society of America B (Optical Physics)*, vol. 19, pp. 2396-402, 2002.

[5-13] L. P. Barry, B. C. Thomsen, J. M. Dudley, and J. D. Harvey, "Autocorrelation and ultrafast optical thresholding at 1.5 μm using a commercial InGaAsP 1.3 μm laser diode," *Electronics Letters*, vol. 34, pp. 358-60, 1998.

[5-14] P.C.Teh, P.Petropoulos, M.Ibsen, and D.J.Richardson, "160 Gbit/s, 64-bit all-optical code generation and recognition using superstructured fibre Bragg gratings," presented at ECOC 2000, Munich, 2000.

Chapter 6

Reconfigurable Optical packet processing system

6.1 Introduction

The explosive data traffic demands imposed by the internet require telecommunication networks to provide higher speed, subscriber-oriented services. Optical packet switching [6-1,2] is a promising solution to support the continuous growth of transmission capacity demand. It offers great advantages in terms of flexibility, functionality, and granularity. By adopting all-optical approaches, optical packet switching may overcome the bottleneck associated with electronic processing, providing higher bandwidth utilization as well as payload transparency.

Among the other functions within a switch node, such as routing[6-3,4], switching [6-5,6] and buffering[6-7,8], a critical function in any optical packet-based network is the reliable generation and processing of headers, since this function is responsible for the generation of the control signal which determines how the packets are routed.

A packet is composed of a data payload which contains user data and a packet header which holds the packet routing information. Several schemes for tagging the optical header to the data payload have been proposed and demonstrated. In general, the header can either be allocated in a different spectral region, in which the header and payload overlap in the time domain, or it can be allocated serially in time with the payload, as in the normal implementation of an electrical router. In the first case, there is no strict timing or synchronization requirement at the bit level between the label and the payload, while the latter case is more spectrally efficient and the interference between the header and payload can be kept at a minimum level.

The multiwavelength labeling scheme [6-9,10] employs separate wavelength channels for the payload and header. Header extraction and processing is simple but the spectral efficiency of the scheme is low. Moreover, different wavelengths have different phase velocities when propagating in a dispersive fiber, resulting in a walk off between the header and the payload.

Both the header and the data payload can also be accommodated on the same optical wavelength with optical subcarrier multiplexing (SCM), by treating the payload as a baseband signal and modulating the header on the subcarrier[6-11,12]. However, some crosstalk between the header and payload is unavoidable. It also places stringent requirements on the modulator and the receiver. Orthogonal modulation [6-13,14] is another labelling technique, in which differential phase shift keying (DPSK) or frequency shift keying (FSK) labels are modulated on the intensity modulated (IM) payload. However, the extinction ratio of the header and payload has to be compromised to ensure they can be separated efficiently.

There are various bit-serial time-domain labelling techniques. The main challenges facing these systems are how to discriminate the header from the packet, as well as how to process the information included in the header, which in this case has to be a fast waveform, in order to ensure that efficiency is not compromised. Both Refs. [6-15]and [6-16] relied on the application of different types of modulation for the header and the payload, and subsequently used nonlinear effects in a semiconductor optical amplifier to discriminate one type of data from the other.

In the previous chapters we have extensively studied the feasibility of optical coding/decoding using FBG based techniques. Whereas these techniques have been applied directly for the all-optical implementation of OCDMA systems, they can also offer the unique potential to process the labels of packet switched systems in an all-optical and linear fashion. Figure 6.1 illustrates the principle of packet generation and header recognition using SSFBGs. The packet header is a specific sequence of individual pulses, generated from the reflection of an input pulse from a single encoding SSFBG. Similar to the decoding process in OCDMA systems, header recognition is performed by a decoding SSFBG which has the time-reversed profile of the encoding grating. A strong autocorrelation peak appears when the header is injected into the corresponding decoding SSFBG, while low intensity noise-like cross-correlation appears both for the payload and headers that do not match the

decoder. The autocorrelation peak can be easily detected using threshold detection and used to control the routing actions of a suitable fast optical switch.

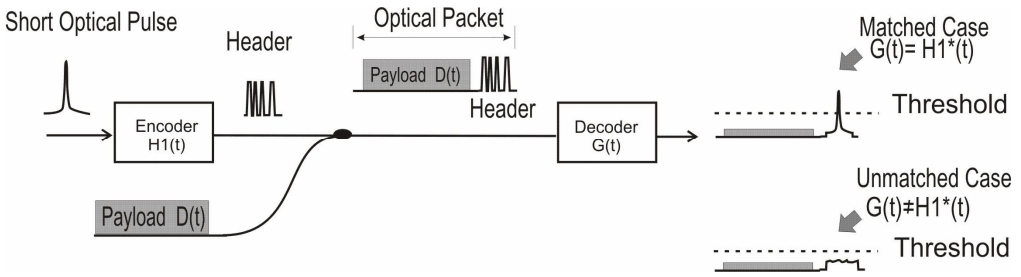

Figure 6.1 Principle of packet assembly and header recognition using SSFBGs

Compared to other bit-serial labeling techniques, SSFBG-based all optical header generation and recognition offers the additional advantages of all-fiber low cost operation and passive generation of the codes with the capability to accommodate large address spaces. All header processing is performed optically and in one step. In addition, there is no restriction on the modulation format used for the payload, making the system totally transparent. However, from a systems point of view, a dynamic header recognition function, i.e. the capability to program the decoder to "read" different labels, is highly desirable in an optical switching node in order to maximize network flexibility.

In this chapter, an experimental demonstration of a reconfigurable optical header processing system based on a code-reconfigurable grating is described. The system performance is characterized and the relative factors that affect the system performance is investigated.

6.2 Demonstration of reconfigurable packet processing system

6.2.1 Experimental setup

The experimental setup we used to demonstrate the operation of our packet processing scheme is shown in Figure 6.2, which incorporates a packet transmitter and a reconfigurable packet processing node. The packet transmitter uses a single CW laser source, tuned to match the wavelength of the encoding SSFBGs. The laser light is split into two paths to generate the headers and payload respectively. For the header generation, the CW beam is EAM-carved into a 10 GHz pulse train and then gated

down to 78 MHz using a $LiNbO_3$ modulator. The generated 20 ps pulses are split again to generate two 400ps long headers (H1 and H2) from two different 15-chip, 40 Gchip/s quaternary phase-shift keyed fixed-coded SSFBGs. Light in the second path is intensity modulated by a $LiNbO_3$ modulator with NRZ data sequences at 10 Gb/s which represents the payloads for both types of packets (P1 and P2). The relative delay between each header and associated payload is adjusted to allocate them sequential time slots before they are combined together.

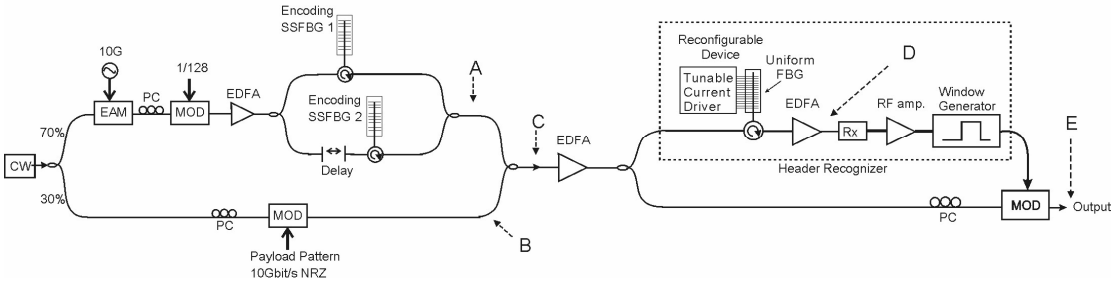

Figure 6.2 Experimental setup for the all-optical packet switching system.

At the packet processing node, optical header recognition is performed to control the switching of the payload. The incoming packet stream is split by a 3dB fiber coupler. One part of the signal is input to a $LiNbO_3$ modulator which acted as an optical switch. The other part of the signal is injected into the 15-chip code-reconfigurable grating, which was described in Section 4.2. Dynamic assignment of a phase-shift keyed code on the FBG superstructure could be achieved by appropriate control of the current flowing through each of the wires due to the induced localized heating. It should be noted that the wavelength-selective nature of the FBG means that no other filter is required for header processing, even when more than one channel is included in the system. The resulting autocorrelation peak reflected off the decoding grating is detected by a photodetector and used to trigger an electrical pulse generator, which generated an electrical pulse of a suitable window width to drive the $LiNbO_3$ switch. By simply changing the code configuration of the decoding device we were able to detect either header H1 or H2 and to switch out either payload P1 or P2 accordingly.

6.2.2 Experimental results

Figure 6.3(a) shows the generated packet waveforms at point C in Figure 6.1. Each packet is 6.4 ns long, which comprises the 0.4 ns header, the 5.2 ns payload, and 0.4 ns guard bands both before and after the header. Two different packets are transmitted alternately. Figure 6.3(b) shows the corresponding optical spectra at point A (the generated headers), B (the generated payload), C (the generated packet) in Figure 6.1 respectively. Due to the higher average power of the payload, the payload dominates the generated packet spectrum. It is possible to increase the intensity of the headers to improve the header recognition performance. This is discussed later.

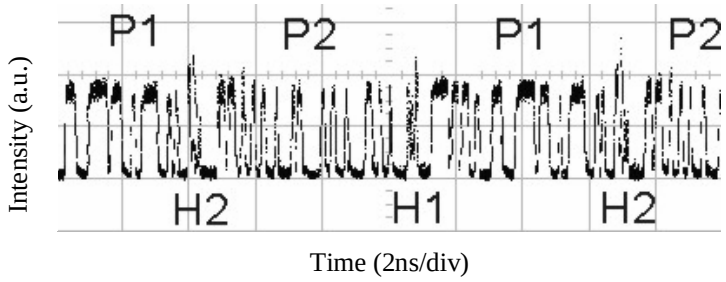

(a) Oscilloscope trace of the generated packets

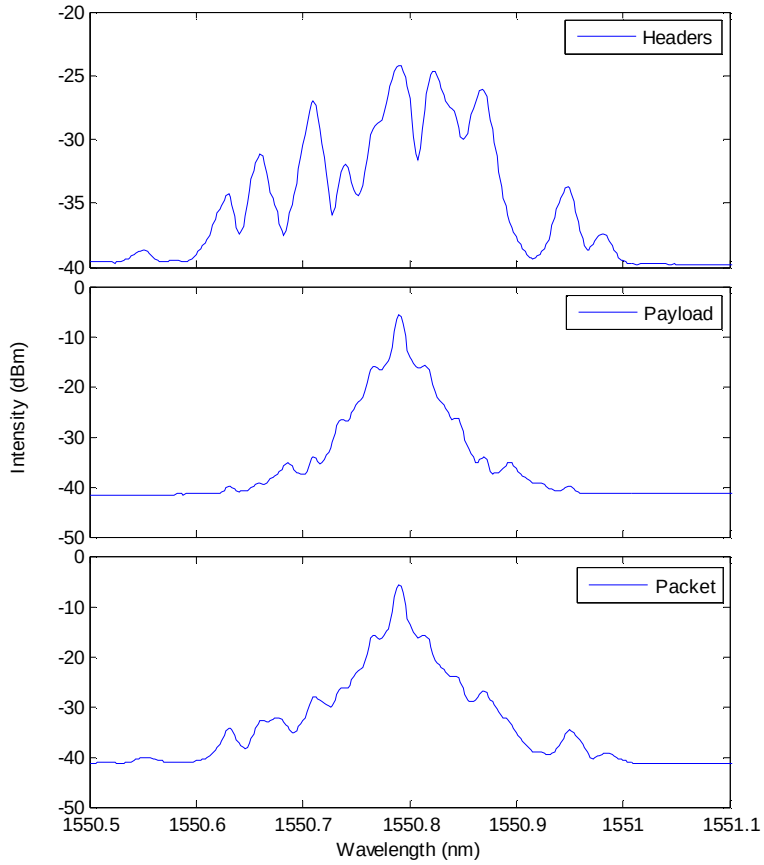

(b) spectra for the generated headers, payload, and packet respectively.

Figure 6.3 Packet components

Figure 6.4 shows the reflectivity spectra of the header encoding SSFBGs and the reconfigurable header decoder when it is configured to recognise header H1 and H2 respectively. These spectra were taken when the gratings were tuned to the working status, that is with either header H1 or H2 being recognised. Figure 6.5 shows the output of the reconfigurable decoder at point D in Figure 6.2, when the reconfigurable device is programmed to decode header H1 or H2 respectively. As we expect, the corresponding header is decoded correctly as denoted by the distinct autocorrelation peak, while for both the unmatched header and payload, low intensity cross-correlations are observed. The distinct autocorrelation peak is used to control the switching actions.

Figure 6.6 shows the corresponding dropped payload at point E in Figure 5.2 when the reconfigurable device is programmed to decode header H1 or H2 respectively. The corresponding packet payload is switched out correctly. Note that in this experiment, a $LiNbO_3$ modulator was used as the switch. However, a multi-port switch could readily be incorporated to fulfil the real switching functions.

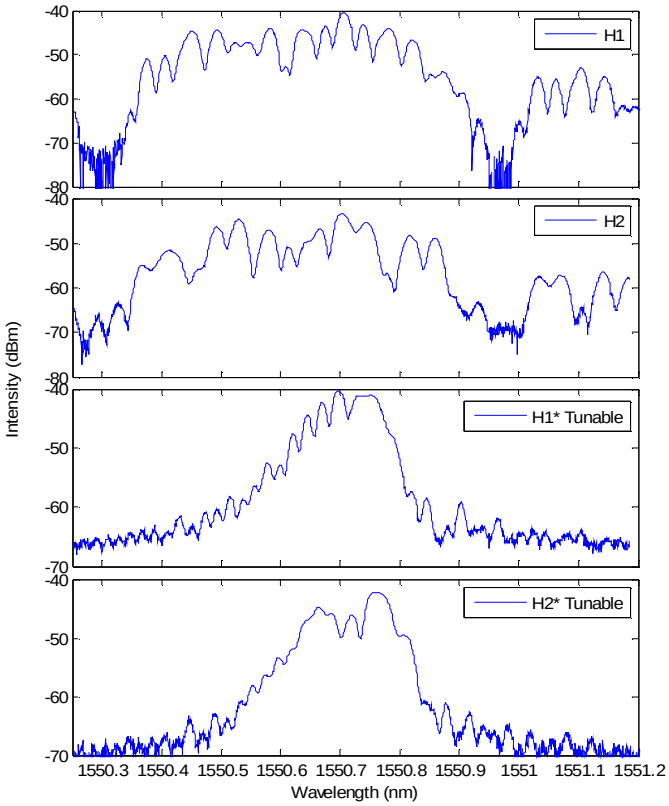

Figure 6.4 Reflectivity spectra of the header encoding SSFBGs and the reconfigurable header decoder

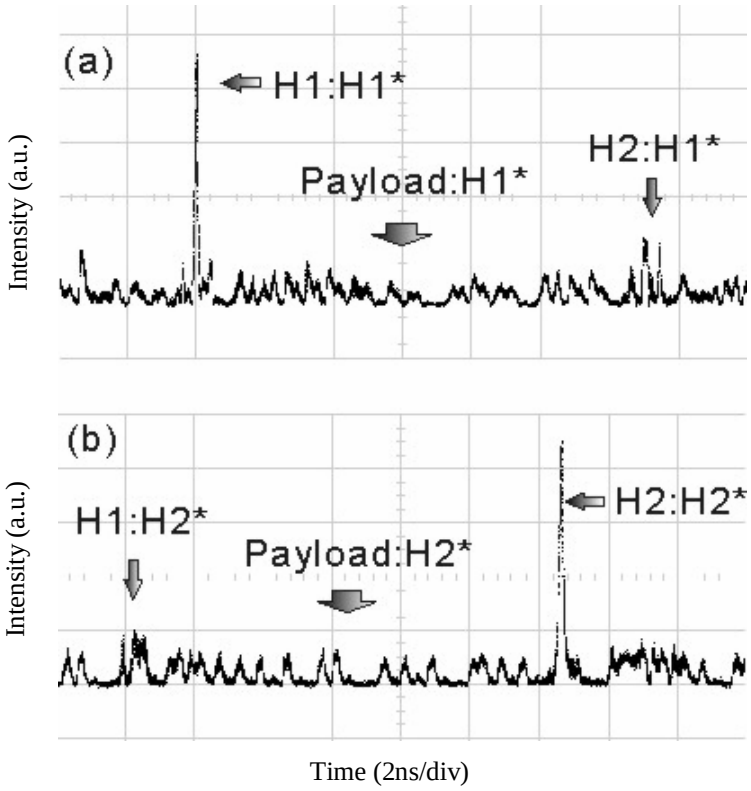

Figure 6.5 Output of header recognition when the reconfigurable grating is set to decode H1 and H2 respectively.

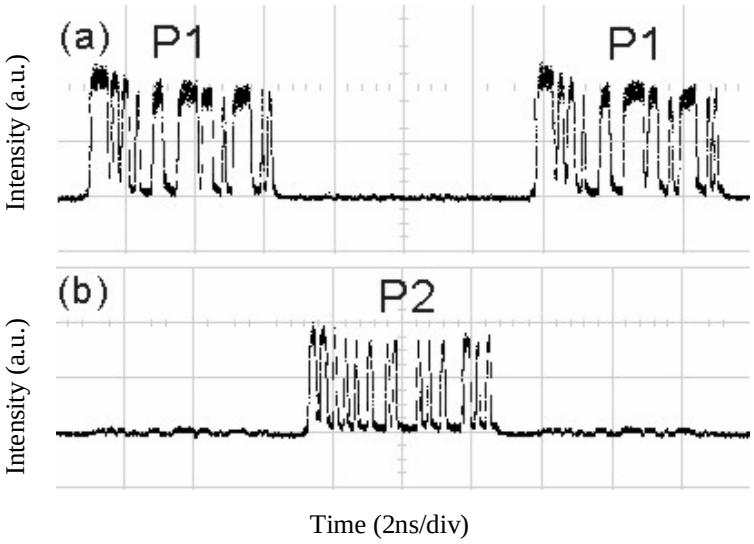

Figure 6.6 Dropped out payload when the reconfigurable grating is set to decode H1 and H2 respectively.

The above experiment has demonstrated the feasibility of all-optical packet processing systems based on SSFBGs and code-reconfigurable grating. In order to evaluate the system performance in terms of the packets that cannot be detected and switched correctly by mis-detecting the correct header autocorrelation, which is determined by successfully detecting the header of the packet, the packet error-rate

(PER) was measured at point B of the experimental set-up. For comparison, the back-to-back case (which contained no header encoding), the one header autocorrelation case (in which only one type of packet contained an encoded header, and the header of the other type of packet is empty), the cases when only headers are presented in the packet (without data payload) and the case when both header and payload were present in the packet, were also tested. The PER results are plotted in Figure 6.7. When there is no data payload in the packet, the power penalty due to the encoding process is ~3dB. Error-free performance is also achieved when the payload is switched on, however the remaining power of the cross-correlation signal between the FBG code and the payload reaches the receiver, resulting in an additional "power penalty" of ~7 dB.

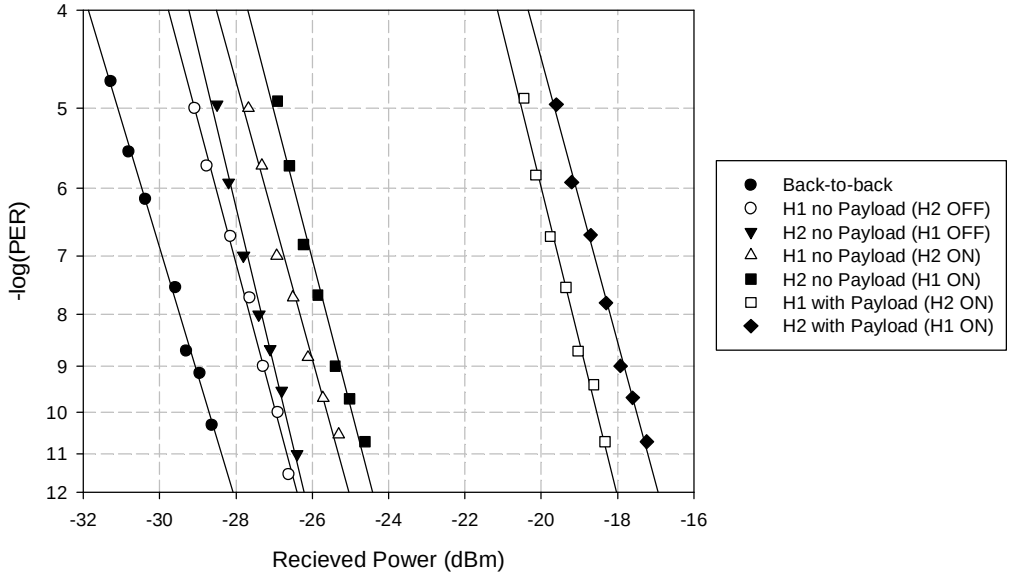

Figure 6.7 PER results.

6.3 Investigation to improve the header recognition performance

In the previous section, the feasibility of our proposed all-optical packet processing system based on SSFBGs and code-reconfigurable grating has been verified. Due to the extra optical power brought by the cross-correlation of payload during the header recognition process, the header recognition sensitivity seemingly degraded, although it is appreciated that at least a component of the apparent penalty is simply due to the increased average power reaching the receiver outside of the header time window. In order to improve the header recognition performance, that is mainly to minimise the effect of payload cross-correlation, several possibilities to

enhance the system performance are investigated.

6.3.1 Increasing header intensity

In the previous experiment, the intensity of the headers was maintained at the same level as the payload on the oscilloscope. It has been noticed that when the payload is added into the packet, the spectrum of the payload dominates the spectrum shape of the packet, due to the much higher average power of the payload than the short headers. the average power change at point C in Figure 6.2 was measured when the payload was added on or cut off the packet stream. When the payload is off, the measured average power is －24.98 dBm, when the payload is added on, the measured average power is －13.42dBm. Since the correlation properties are determined by the codes and the gratings, it is impracticable to change the available gratings. Considering the extra power penalty that is induced by the cross-correlation of the payload, I tried to increase the average power of the headers, relative to the payload, to improve the header recognition performance. Figure 6.8 shows the spectral change of the generated packets when the headers intensity is increased from the 'normal' status (same as the payload intensity level) to 'double' status (roughly twice the payload intensity) by adjusting the EDFA in the header generating path. When the header intensity is increased, the packet spectrum shows more details of the encoded headers than the normal case and thus broadens the spectrum. However, the broadening of the spectrum happens at a very low intensity level (<-30dB), still making little effect on the total packet spectrum.

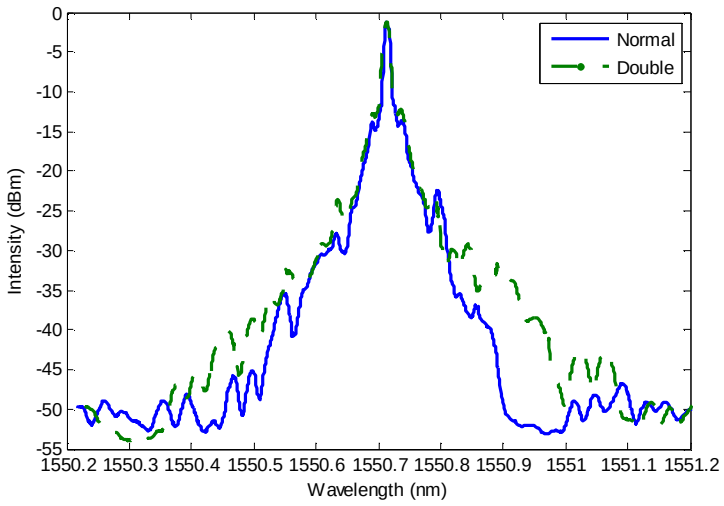

Figure 6.8 Spectrum change of the generated packets when the headers' intensity is increased

Figure 6.9(a) shows the oscilloscope trace of the normal packet stream, as we demonstrated in the previous section. Figure 6.9(b) shows the oscilloscope trace of the packet stream when the headers intensity was increased to about twice than the normal case by adjusting the EDFA in the header generating path. Figure 6.9(c) and (d) show the corresponding output of the header recognition grating (point D in Figure 6.2) when the reconfigurable grating is set to decode header H1. As can be seen from the figures, when the headers' intensity is increased, the shape of autocorrelation and cross-correlation remain unchanged, but the contrast ratio between the autocorrelation peak and the payload cross-correlation is increased accordingly. It reduces the interference of payload cross-correlation at the detection point and thus improves the header recognition performance.

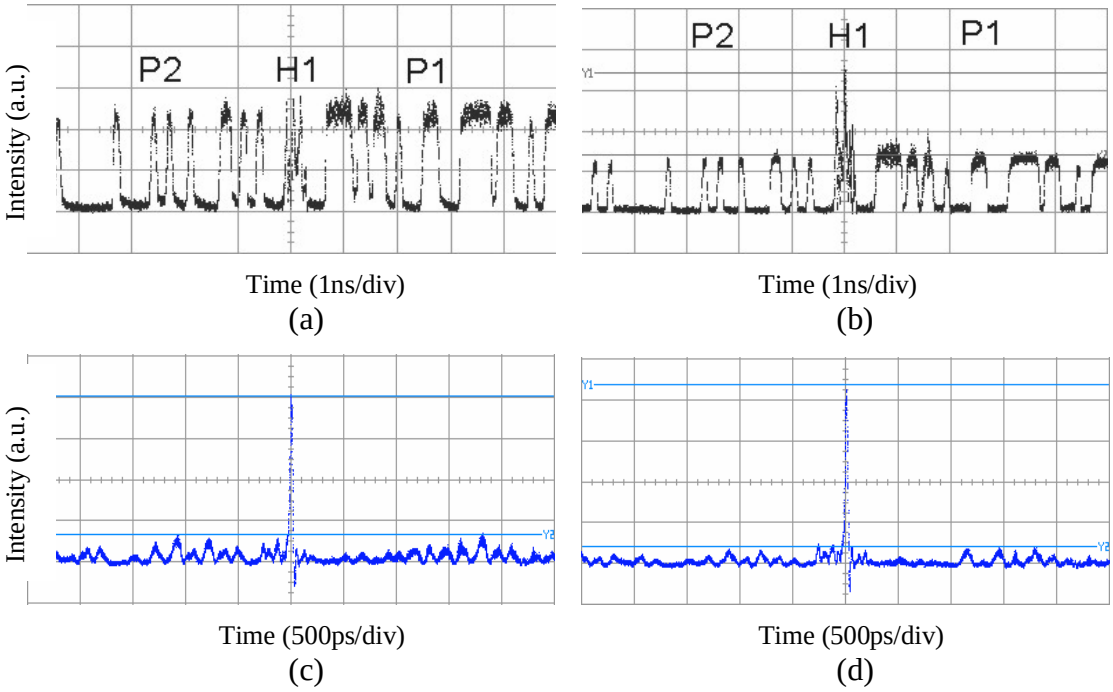

Figure 6.9 Oscilloscope traces for comparison of changing the headers intensity. (a) normal packet stream, (b) packet stream with increased header intensity, (c)decoded (H1) output for the normal packet, (d) decoded (H1) output for the increased header intensity.

The effect of adjusting the headers' intensity can be seen more clearly in Figure 6.10, in which the reconfigurable grating was set to decode header H2, while all the autocorrelation, cross-correlation of unmatched header H1, and cross-correlation of the payload are displayed on the same screen. As can be seen, when the headers' intensity is increased, the contrast ratio between the autocorrelation peak and the

cross-correlation of unmatched header H1 remains constant, while the contrast ratio between the autocorrelation peak and the cross-correlation of the payload is increased.

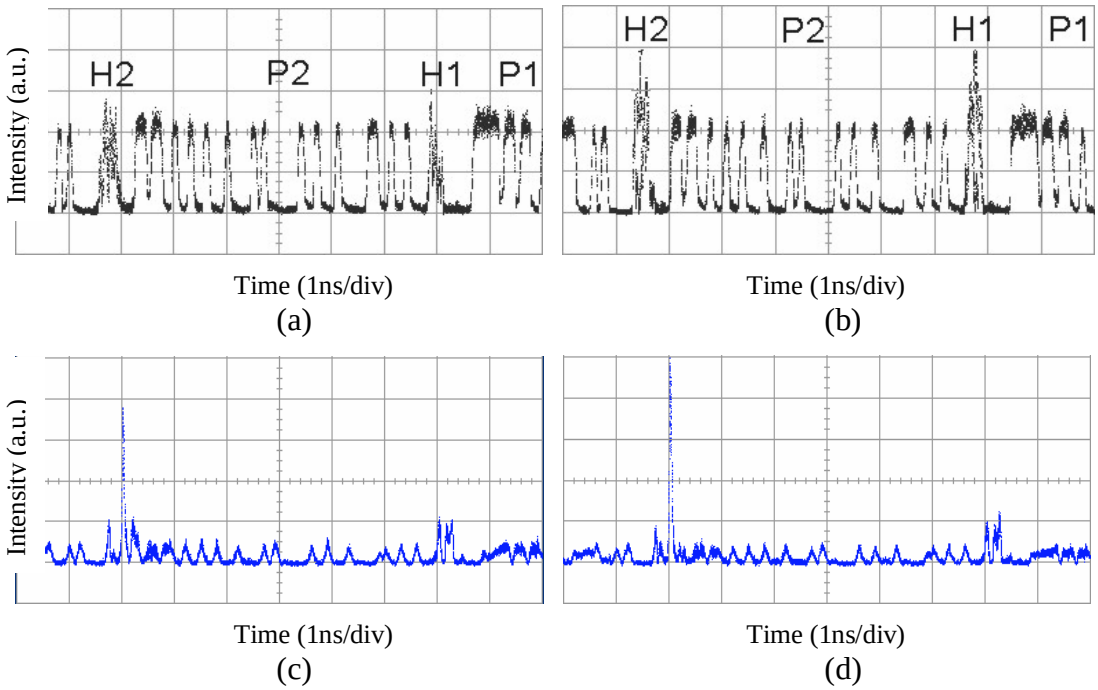

Figure 6.10 Oscilloscope traces for comparison of changing the headers intensity. (a) normal packet stream, (b) packet stream with increased header intensity, (c)decoded (H2) output for the normal packet, (d) decoded (H2) output for the increased header intensity.

The above oscilloscope traces indicate that with the same optical power arriving at the photodetector, for the increased headers' intensity case, there is more power concentrated in the autocorrelation peak, thereby improving the header recognition sensitivity and reducing the extra power penalty induced by the payload cross-correlation. This is verified by the PER measurement. Figure 6.11 shows the PER results for the increased header intensity, in comparison with the 'normal' case. Considering the original ~3dB power penalty due to the header coding/decoding process, the extra power penalty brought by the payload cross-correlation is reduced from ~7dB to ~3dB. The results verify that this is an effective method to improve the header recognition sensitivity by increasing the headers' intensity.

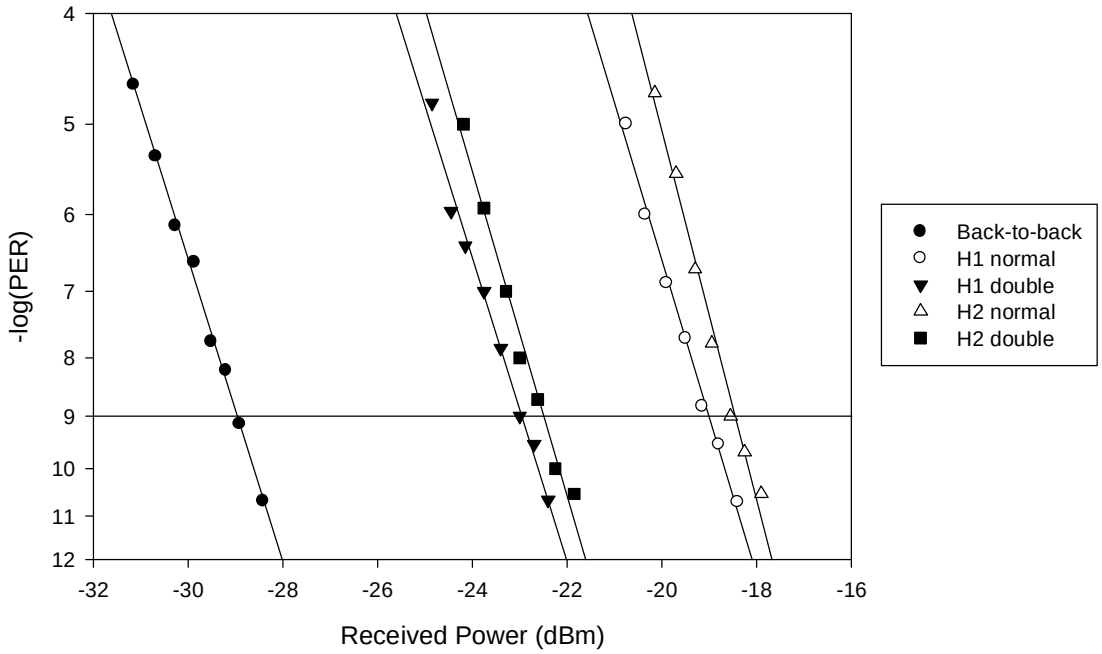

Figure 6.11 PER results for the increased headers' intensity, in comparison with the 'normal' case.

6.3.2 Wavelength shifting of payload

During the investigation of the correlation properties of the SSFBGs, it was noticed that the correlation properties are mainly determined by the selected codes and the characteristics of the fabricated gratings. As long as the encoding and decoding gratings are tuned to the matching status, the autocorrelation shape remains the same regardless of the wavelength of the input short pulse, although the intensity will change accordingly. Considering the small contribution of the headers to the spectrum of the generated packet, and inspired by the idea of optical subcarrier multiplexing (SCM), the effect of shifting the wavelength of the payload away from the gratings' central wavelength was investigated.

This was done by simply shifting the wavelength of the CW source of the system setup (Figure 6.2). The centre wavelength of both the payload and the input short pulses for the header generation are moved accordingly since they are modulated directly on the CW source. However, as both the encoding and the decoding gratings were not touched, they still work at the original wavelength. After the header encoding process, the encoded header spectrum still remains at the original wavelength (λ1), although the intensity is reduced since it does not utilize the spectral

peak of the input pulses. The decreased optical power of the headers can be compensated conveniently by the EDFA in the optical encoding path. As the payload is shifted away from the working wavelength (λ1) of the header recognition grating (to λ2), it is partly filtered out by the inherent wavelength selectivity of the gratings, thereby reducing the cross-correlation between payload data and header.

This idea was demonstrated experimentally. The gratings were tuned to 1550.77nm and set to recognize header H1. The CW source was originally centered at 1550.77nm, and then shifted towards 1551.10nm. Figure 6.12 shows the observed change of header recognition output during this process. The figures display some dramatic changes when the CW source is shifted towards the longer wavelength. Figure 6.12(a) shows the decoded output for the normal operation. When Δλ=+0.05nm and +0.15nm, (b) and (c) show that the intensity of both the autocorrelation of the matched header (H1) and the cross-correlation of the unmatched header (H2) is decreased, while the intensity of payload cross-correlation is increased, making the decoded header in the whole output difficult to be recognized. When Δλ is tuned to around +0.24nm, (d) and (e) show that the autocorrelation becomes distinguishable again as the payload cross-correlation is suppressed, making the overall output better than the 'normal' case. When Δλ is shifted further to longer wavelengths, beyond +0.28nm, the intensity of the decoded output decreases quickly to become indiscernible on the oscilloscope.

It is demonstrated that Δλ around 0.20nm- 0.26 is the ideal range to improve the decoded header recognition performance by shifting the payload wavelength. The detailed measurement of the contrast ratio as a function of Δλ verifies this point. Figure 6.13(a) shows the contrast ratio between the decoded autocorrelation peak of the matched header (H1) and the cross-correlation of the unmatched header (H2). Figure 6.13(b) shows the contrast ratio between the decoded autocorrelation peak of the matched header (H1) and the payload cross-correlation. The CW source wavelength is tuned from 1550.67nm to 1551.10nm (Δλ from -0.10nm to +0.33nm), at various steps from 0.005nm to 0.05nm. The results confirm what we observed on the oscilloscope. The contrast ratio between the decoded autocorrelation peak of the matched header (H1) and the cross-correlation of the unmatched header (H2) remains roughly constant between 2 and 4, showing that the correlation properties of the gratings are not particularly dependent on the wavelength of the input short pulse. However for the contrast ratio between the decoded autocorrelation peak of the

matched header (H1) and the payload cross-correlation, there are two wavelength regions in which good decoded performance can be achieved. One is a narrow area around the 'original' wavelength, the other is a wider zone Δλ running from 0.2nm to 0.3nm. The latter one also allows improved header recognition performance.

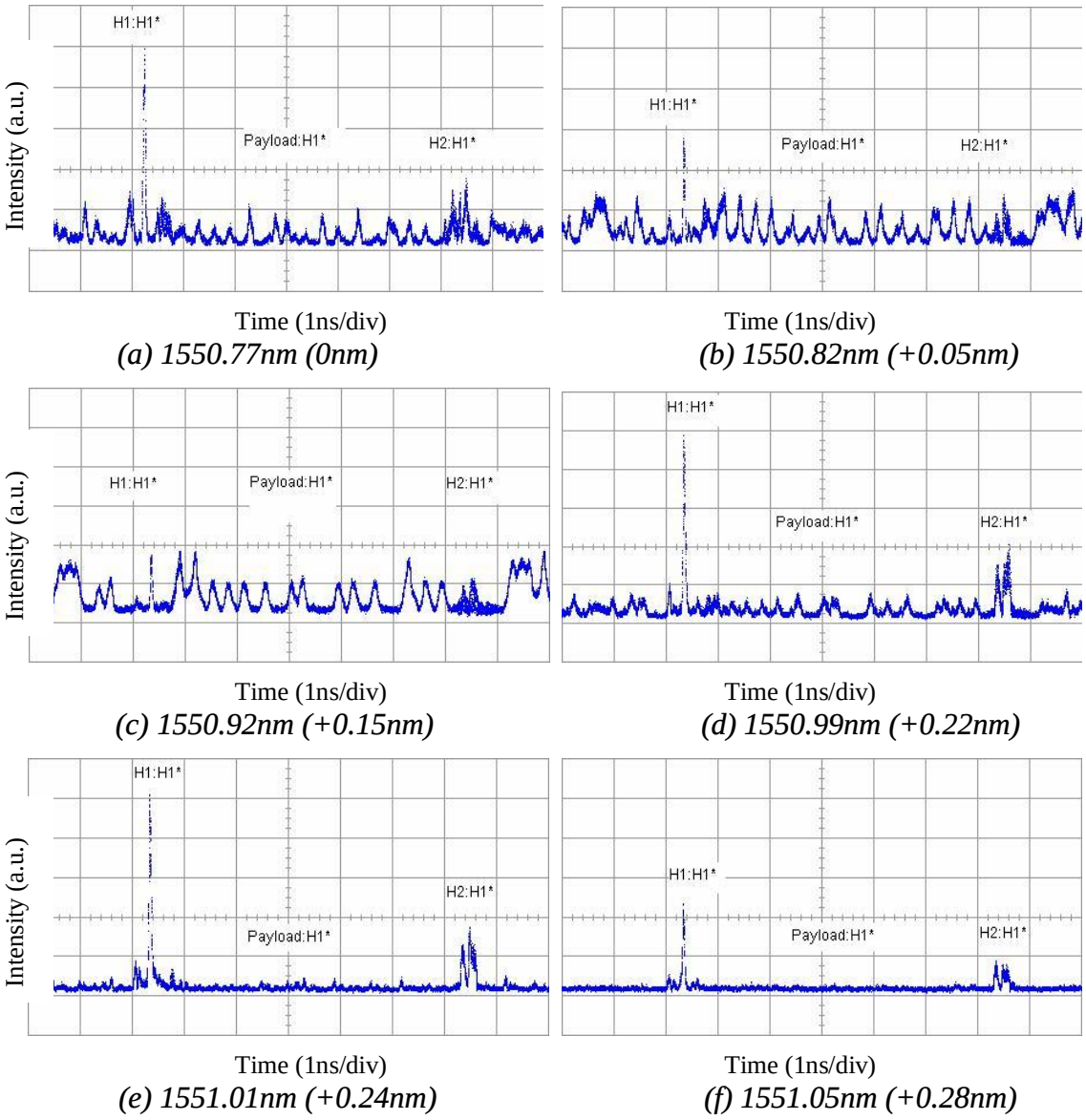

Figure 6.12 Oscilloscope traces of header recognition output when the CW source wavelength is shifting from 1550.77nm to 1551.10nm.

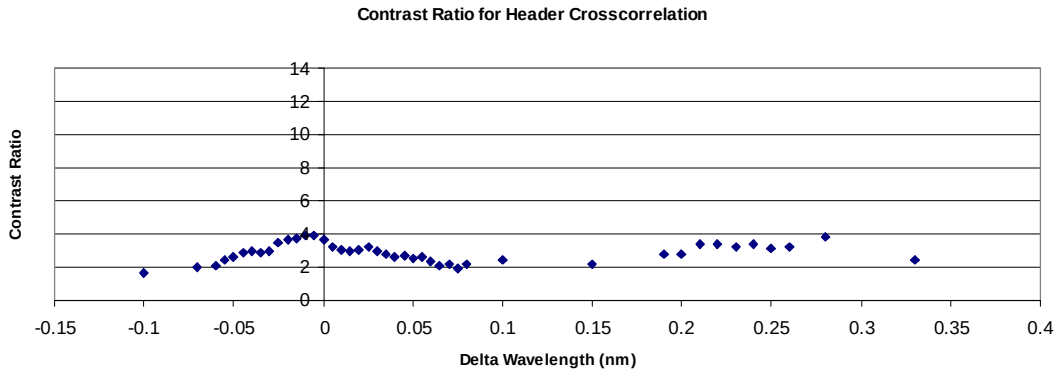

(a)

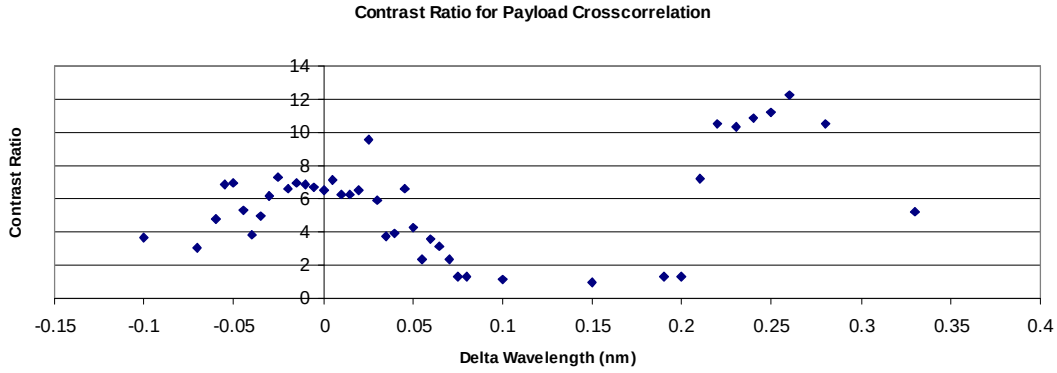

(b)

Figure 6.13(a) Contrast ratio between decoded autocorrelation peak of the matched header (H1) and the cross-correlation of the unmatched header (H2), (b) contrast ratio between decoded autocorrelation peak of the matched header (H1) and the payload cross-correlation.

PER measurements for selected wavelengths have been taken: 1550.77nm (original wavelength), 1550.97nm ($\Delta\lambda$=+0.2nm), 1551.01nm ($\Delta\lambda$=+0.24nm). The results are plotted in Figure 6.14. A large power penalty reduction is achieved by shifting the payload wavelength around $\Delta\lambda$=+0.24nm area. Considering the inherent power penalty of ~3dB due to the correlation properties of the coding/decoding gratings, it shows that most of the additional power from the payload cross-correlation has been filtered out by the decoding grating's wavelength selectivity.

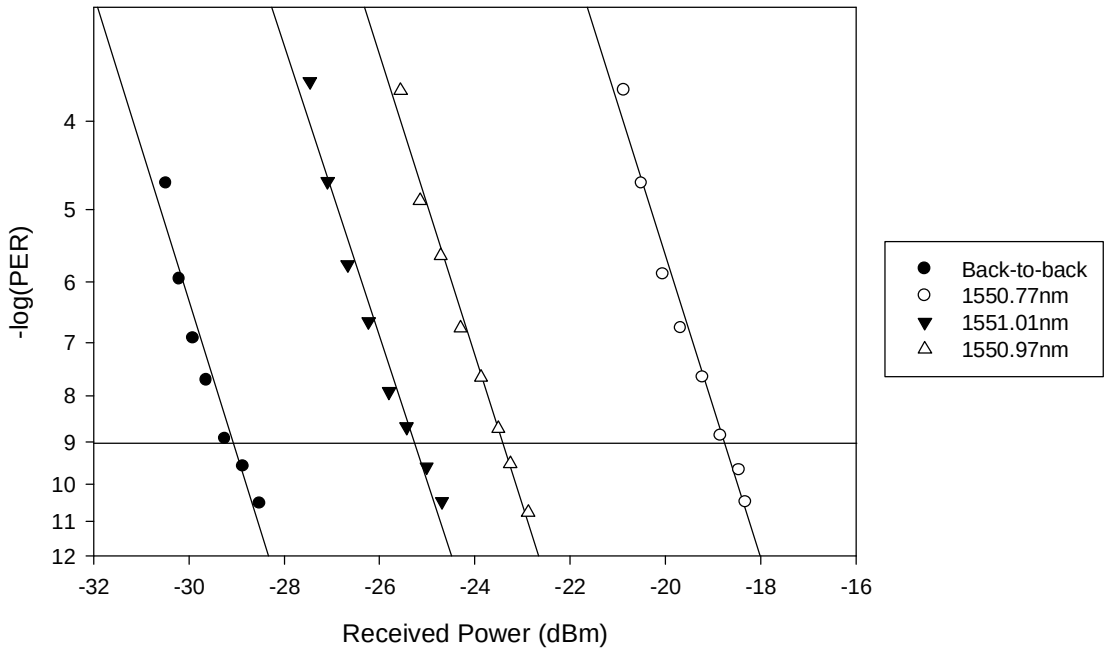

Figure 6.14 PER results for different payload wavelength.

Obviously, the improvement of header recognition performance leads to some compromise in the spectral efficiency. Figure 6.15 records the spectra of the generated packet stream at two typical wavelengths, superposed with the spectrum of the decoding grating, (a) is the original wavelength when the system is in 'normal' status, (b) is at 1551.01nm ($\Delta\lambda$=+0.24nm) where the best header recognition improvement is achieved. Figure 6.15(a) shows a generally symmetric spectrum since both the gratings and payloads are aligned. The bandwidth of the mainlobe is ~0.65nm. In Figure 6.15(b), it can be seen clearly that the shifting of the payload wavelength in the spectrum, which has broadened the bandwidth of the mainlobe to ~0.95nm. Part of the spectrum associated with the encoded header is revealed due to the shift of the payload. Note that this approach is different from the multiwavelength labeling scheme, since the header and payload are not totally separated in the spectral domain. It is also different from the subcarrier multiplexing because no complex modulation is needed. However, it has been demonstrated as a simple and effective method to improve the header recognition performance in our optical packet process system.

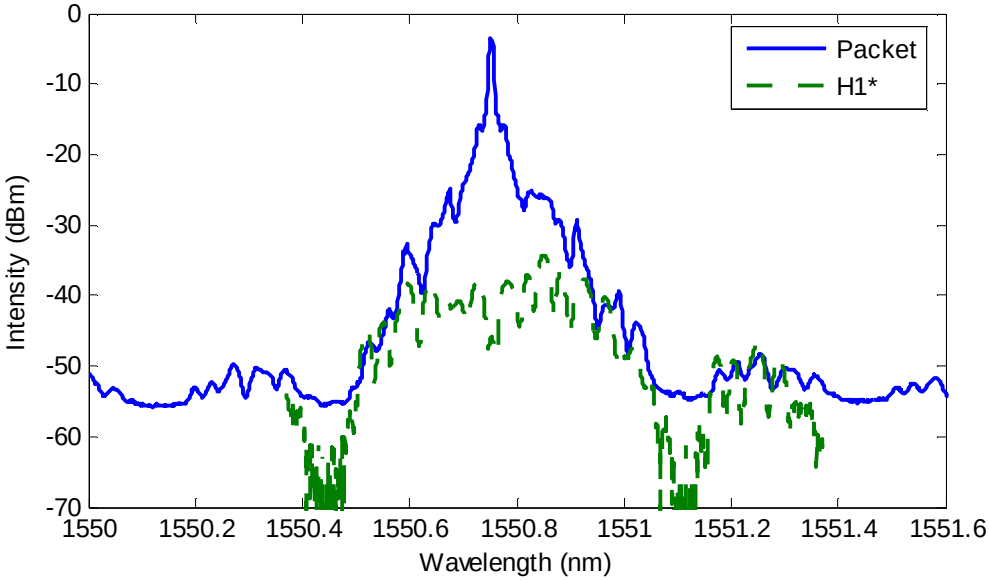

(a) 1550.77nm (original)

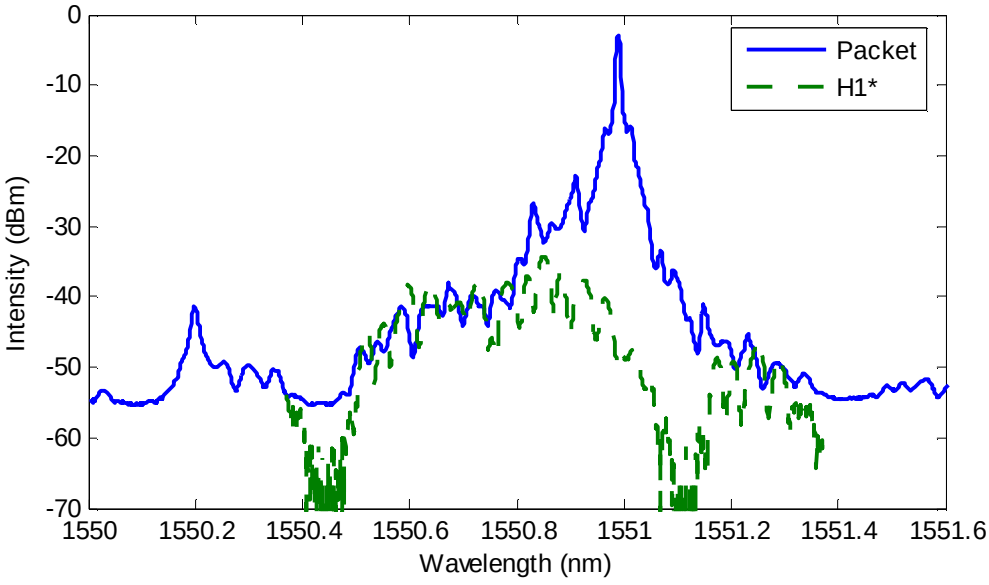

(b)1551.01nm ($\Delta\lambda$=+0.24nm)

Figure 6.15 Optical spectra of generated packet stream at two typical wavelengths

6.4 Reconfiguration speed of the reconfigurable device

Except for the requirement for recognizing the headers reliably, another key parameter in the optical packet processing system is the routing speed. In our proposed system, the routing speed is determined by the reconfiguration speed of the reconfigurable decoding grating. The reconfiguration speed was investigated using the

setup in Figure 6.16, which is a two-channel OCDMA coding/decoding system as discussed in Chapter 4. A CW laser tuned at 1550.7nm is EAM carved into a 20ps pulse train. The 10GHz pulse train is then gated down to 625MHz to avoid overlapping after the coding/decoding process. This pulse train is split by a 3dB coupler into two parts, then reflected from two different encoders respectively. The encoding gratings employ the fixed coded SSFBGs H1 and H2. The encoded signals are then combined by another 3dB coupler. A delay line is used to make sure that the combined encoded signals are separated properly in the time domain. Then the combined signal is reflected from the reconfigurable decoding grating. The reconfigurable grating can be quickly configured, or switched, from one code to the other. A photon detector and oscilloscope are used to monitor the decoded signal from the reconfigurable grating. The oscilloscope has an effective detection bandwidth of 100MHz which is enough to monitor the optical power change of the decoded signal.

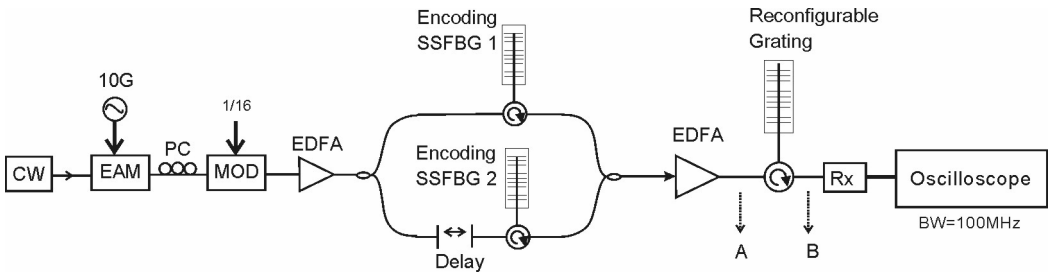

Figure 6.16 Experimental setup to investigate the Reconfiguration speed of the reconfigurable grating

Figure 6.17(a) shows the combined signal with two different codes at point A in the setup. The encoded signal repetition period is 1.6ns. Figure 6.17(b) shows the decoded output when the reconfigurable decoding grating is configured with code H1*. A distinct autocorrelation peak, at the corresponding position of H1, is observed. Meanwhile at the position corresponding to code H2, the low intensity cross-correlation between H2 and H1* is produced. Figure 6.17(c) shows the decoded output when the reconfigurable decoding grating is switched to code H2*. The distinct autocorrelation peak and low intensity cross-correlation are observed at the corresponding position of H2 and H1 respectively. Note that the delay time between the encoded H1 and H2 is only about 200ps. It is not enough to separate the two codes completely in the decoding process and thus will introduce some interference between

the two codes and degrade the correlation performance. However, since the reconfiguration speed is measured by monitoring the optical power change, the interference does not affect the measurement result.

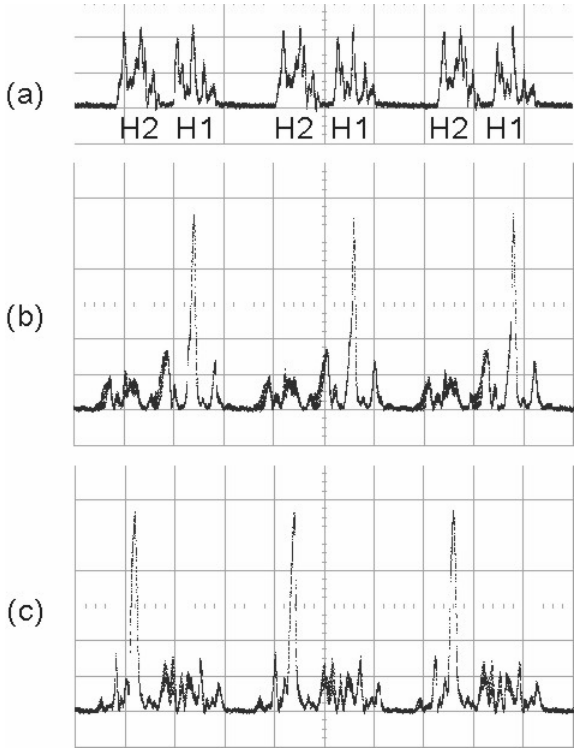

Figure 6.17 Oscilloscope traces for (a) the encoded signal, (b) the decoded signal by code H1, (c) the decoded signal by code H2*.*

Figure 6.18 shows the measured results from the oscilloscope when the reconfigurable decoding grating is switched from H1* to H2*, and then back to H1*. The overall power generally remains constant except at the switching point. Note that the slight power difference when decoding H1 and H2 is due to the different correlation properties of the two codes. The measured response time of the switching process is ~1.75 seconds.

The reconfiguration speed is also confirmed by simply switching off and on the controlling currents of the reconfigurable decoding grating with code H1. The observed output power change is shown in Figure 6.19. From a working status to the 'off' status, the switching time is ~0.88 seconds. From an 'off' status to configuring the grating and decoding the code H1 stably, the switching time is ~1.86 seconds.

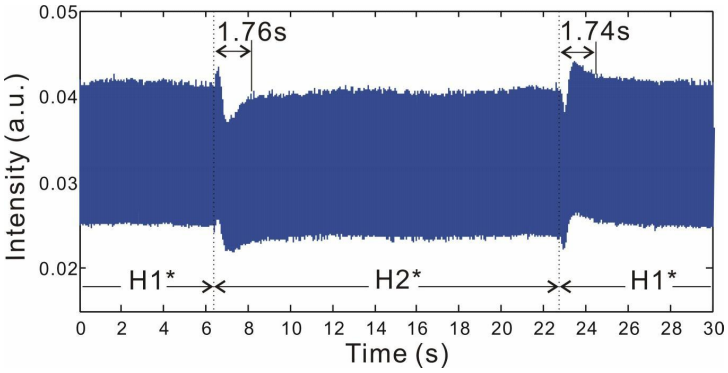

Figure 6.18 Measurement of the reconfiguration speed when the reconfigurable grating is switched between code H1 and H2**

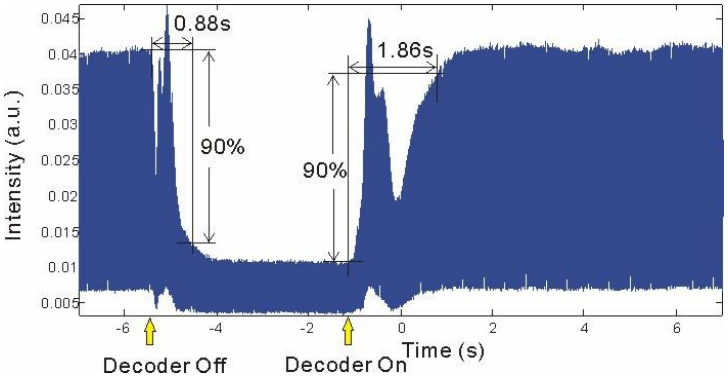

Figure 6.19 Measurement of the reconfiguration speed when the reconfigurable grating is switched off and on.

The reconfiguration speed measurements demonstrate that the reconfigurable grating has a reasonably fast tuning ability of less than 2 seconds. A faster response time should be possible by using smaller diameter grating fibers and more sensitive temperature control methods.

6.5 Conclusion

This chapter introduces the demonstration of an all-optical packet processing system based on optical header recognition through matched filtering in a dynamically reconfigurable FBG device. The decoding device used in our experiments utilized the 15-chip 40 Gchip/s SSFBGs and code-reconfigurable gratings, as described previously in Chapter 4. The possibility to improve the header recognition performance by some simple method is also discussed. The reconfiguration speed of the reconfigurable grating has been measured. These experiments demonstrate a

particular application of the FBG-based optical coding/decoding techniques. It highlights the capability of fast dynamic reconfiguration, which is essential to improve the functionality and flexibility of future OCDMA and all-optical packet switching networks.

Although the 2 second switching time is not fast enough for real time packet switching applications. Faster switching time can be achieved by using thinner grating fibers and proper packaging technique. Such reconfigurable code recognition device can find its application in the semi-fixed routing system. It is also of significant interest for use in reconfigurable OCDMA systems where code tuning speed is a lesser concern.

References

[6-1] M. J. O'Mahony, D. Simeonidou, D. K. Hunter, and A. Tzanakaki, "The application of optical packet switching in future communication networks," *IEEE Communications Magazine*, vol. 39, pp. 128-135, 2001.

[6-2] A. Jourdan, D. Chiaroni, E. Dotaro, G. J. Eilenberger, F. Masetti, and M. Renaud, "The perspective of optical packet switching in IP-dominant backbone and metropolitan networks," *IEEE Communications Magazine*, vol. 39, pp. 136-141, 2001.

[6-3] L. Stampoulidis, E. Kehayas, K. Vyrsokinos, D. Apostolopoulos, and H. Avramopoulos, "Design of all-optical contention detection and resolution for 40-gb/s label-switched routers," *IEEE Photonics Technology Letters*, vol. 18, pp. 2478-80, 2006.

[6-4] D. T. Neilson, "Photonics for switching and routing," *IEEE Journal of Selected Topics in Quantum Electronics*, vol. 12, pp. 669-78, 2006.

[6-5] L. Dittmann, C. Develder, D. Chiaroni, F. Neri, F. Callegati, W. Koerber, A. Stavdas, M. Renaud, A. Rafel, J. Sole-Pareta, W. Cerroni, N. Leligou, L. Dembeck, B. Mortensen, M. Pickavet, N. Le Sauze, M. Mahony, B. Berde, and G. Eilenberger, "The European IST project DAVID: a viable approach toward optical packet switching," *IEEE Journal on Selected Areas in Communications*, vol. 21, pp. 1026-40, 2003.

[6-6] L. Sheng-Chyan, R. Varrazza, O. Ansell, and Y. Siyuan, "Highly flexible 4X4 optical crosspoint packet switch matrix for optical multicast operations," *IEEE Photonics Technology Letters*, vol. 17, pp. 911-13, 2005.

[6-7] D. K. Hunter, M. C. Chia, and I. Andonovic, "Buffering in optical packet switches," *Journal of Lightwave Technology*, vol. 16, pp. 2081-94, 1998.

[6-8] S. J. B. Yoo, "Optical packet and burst switching technologies for the future photonic Internet," *Journal of Lightwave Technology*, vol. 24, pp. 4468-92, 2006.

[6-9] A. Okada, "All optical packet routing in AWG based wavelength routing networks using an out of band filter," presented at OFC, Washington, DC, 2002.

[6-10] S. L. Xiao, Q. J. Zeng, J. X. Wang, J. Xu, and Y. Wang, "Realization of multiwavelength label optical packet switching," *IEEE Photonics Technology Letters*, vol. 15, pp. 605-607, 2003.

[6-11] M. Y. Jeon, Z. Pan, J. Cao, Y. Bansal, J. Taylor, Z. Wang, V. Akella, K. Okamoto, S. Kamei, J. Pan, and S. J. B. Yoo, "Demonstration of all-optical packet switching routers with optical label swapping and 2R regeneration for scalable optical label switching network applications," *Journal of Lightwave Technology*, vol. 21, pp. 2723-2733, 2003.

[6-12] H. J. Lee, S. J. B. Yoo, V. K. Tsui, and S. K. H. Fong, "A simple all-optical label detection and swapping technique incorporating a fiber Bragg grating filter," *IEEE Photonics Technology Letters*, vol. 13, pp. 635-637, 2001.

[6-13] E. N. Lallas, N. Skarmoutsos, and D. Syvridis, "An optical FSK-based label coding technique for the realization of the all-optical label swapping," *IEEE Photonics Technology Letters*, vol. 14, pp. 1472-1474, 2002.

[6-14] J. J. V. Olmos, I. T. Monroy, M. G. Larrode, and A. M. J. Koonen, "All-optical processing of time-serial IM/DPSK encoded label and payload packets," *IEEE Journal of Selected Topics in Quantum Electronics*, vol. 12, pp. 679-85, 2006.

[6-15] J. J. V. Olmos, I. T. Monroy, Y.Liu, and A.M.J.Koonen, "Self_controlled All-Optical label and payload separator for variable length bursts in a Time-Serial IM/DPSK Scheme," presented at OFC, Anaheim, USA, 2005.

[6-16] A. Srivatsa, H. de Waardt, M. T. Hill, G. D. Khoe, and H. J. S. Dorren, "All-optical serial header processing based on two-pulse correlation," *Electronics Letters*, vol. 37, pp. 234-235, 2001.

Chapter 7

16-channel OCDMA/DWDM system

7.1 Overview

With the rapidly growing desire for information and communication, the requirements of transmission capacity and service categories are increasingly challenging the telecommunications industry. The WDM technique emerges as a quick, economical, and now mature method to increase network capacity multiple times. The advantages of WDM include media transparency, long haul and high capacity transmission, use of existing optical fibres and easy upgrading. The overlay of WDM techniques in the OCDMA applications is a natural trend and thereby attracts lots of research interest. However, many other OCDMA/WDM approaches [7-1] still rely on the use of a conventional WDM DEMUX to drop off the desired wavelength channel.

The use of Superstructured Fiber Bragg Grating (SSFBG) technology represents an attractive means to perform the phase encoding/decoding in OCDMA systems. Relative to other coding approaches, SSFBGs offer advantages in terms of fiber compatibility, ease and cost of manufacture, the ability to support long phase and amplitude code sequences, and the inherent wavelength selectivity which make the devices highly suitable for use within WDM systems. To demonstrate these benefits, a 4-channel (2 OCDM×2 WDM at 4nm interval) system has been demonstrated previously, using both 63-chip 160Gchip/s BPSK SSFBGs and 255-chip 320Gchip/s QPSK SSFBGs[7-2]. After the decoding process, 15dB suppression ratio of the out-band wavelength channel was achieved by the decoding gratings. Although this preliminary experiment operated at a wavelength interval of 4nm, it demonstrated that

the inherent wavelength selectivity of the gratings can be utilised to provide both wavelength channel filtering and the decoding function for the 'in-band' signals, eliminating the requirement for additional wavelength channel filtering elements. A 4 OCDM×4 WDM×311Mbit/s OCDMA system operating on a 100GHz grid using fixed 16-chip, 20Gchip/s, quaternary phase coding SSFBGs was also demonstrated [7-3]. Up to 25dB of extinction between adjacent 100GHz channels was achieved. This experiment verified that SSFBGs offer a practical and flexible approach to multi-user operation with different coding schemes, data rates and wavelength channels. As described in the previous chapters, one limitation of the basic SSFBG approach is that the codes are fixed during the writing process, and cannot be readily changed by the user. Consequently, to address this issue a code-reconfigurable grating device has been developed and substantially investigated the device's behaviour in Chapters 3 and 4 [7- 4-8]. An important feature of the reconfigurable grating is that it has a narrower spectrum compared to the normal discrete phase-shift SSFBGs. Despite the thermally-induced distributed phase-shift, the code-reconfigurable device has proven to be compatible with the use of normal discrete phase-shift SSFBGs in Chapter 4. Furthermore, a fixed-code continuous phase-shift SSFBG was recently proposed [7-9]. This novel grating is designed to have a similar distributed phase distribution to the reconfigurable grating, thereby achieving a similarly narrow spectral bandwidth and a better match to the reconfigurable grating. The preliminary study, based on 15-chip gratings in Chapter 4, indicated that the continuous phase-shift SSFBGs are more tolerant to broader input coding pulses than discrete phase-shift SSFBGs thereby having the potential to reduce the overall system bandwidth, complexity and associated cost.

In this chapter, the work on incorporating the new techniques, mentioned above, to demonstrate a spectrally efficient 16-channel reconfigurable OCDMA/DWDM system operating on a 50GHz DWDM-compatible grid is introduced. The investigations began with 15-chip continuous phase-shift SSFBGs and the discrete phase-shift SSFBGs since they were available for immediate use. After the system design parameters being obtained, 31-chip continuous phase-shift SSFBGs and 31-chip code-reconfigurable gratings which have longer codes to accommodate more simultaneous code-division channels in the experiments were fabricated. Obviously, before launching system experiments, further experiments were conducted to optimise and understand the experimental setup parameters. The correlation performance for each

of the new gratings was characterised before I undertook the 16-channel OCDMA/DWDM systems.

7.2 Investigation of OCDMA/DWDM system design

In order to obtain the correct system design parameters for the 16-channel OCDMA/DWDM experiment, The wavelength selectivity of the continuous phase-shift SSFBGs, the possible system setup, and the suitable transmitter design were investigated.

7.2.1 Wavelength selectivity based on 15-chip SSFBGs

Firstly, the wavelength selecting capability of the two different types of gratings were compared, 15-chip continuous phase-shift SSFBGs (denoted as Q1C and Q2C) and 15-chip discrete phase-shift SSFBGs (denoted as Q1F and Q2F). The correlation performance of these gratings has been studied in detail in Chapter 4. In this section their wavelength selecting capability was particularly investigated. The study was based on a simple 2-WDM channel OCDMA system as shown in Figure 7.1. Encoding Grating 1 (Q1F or Q1C) was tuned to 1550.5nm (λ_1) and the working wavelength was fixed. Decoding Grating 3 (Q1*F or Q1*C) was tuned to decode Grating 1. Encoding Grating 2 (Q2F or Q2C) acted as the interference source and the wavelength (λ_2) was shifted from 1549.9nm to 1551.1nm in order to observe the effect on the decoded output. For simplicity of the experiment, a single wavelength input pulse was used, since the spectrum of the 6ps pulses is wide enough to cover the two wavelengths. Figure 7.2 illutrates the spectrum of the input pulse and the reflectivity spectra of the continuous phase-shift SSFBGs and discrete phase-shift SSFBGs. The spectrum of the input pulse is shown to be wide enough for the experiment.

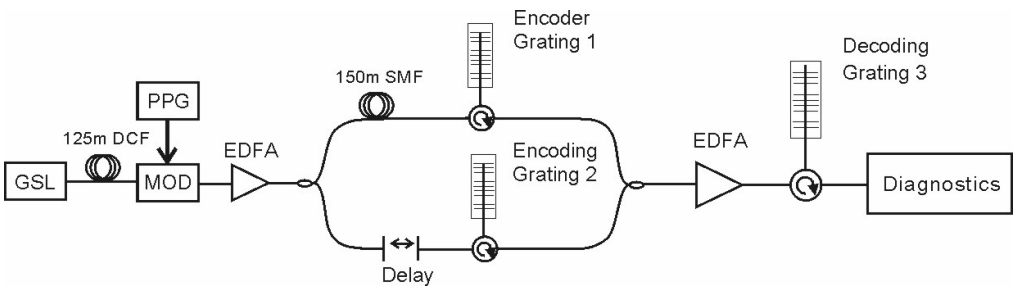

Figure 7.1 Experimental setup of a simple 2-channel OCDMA system

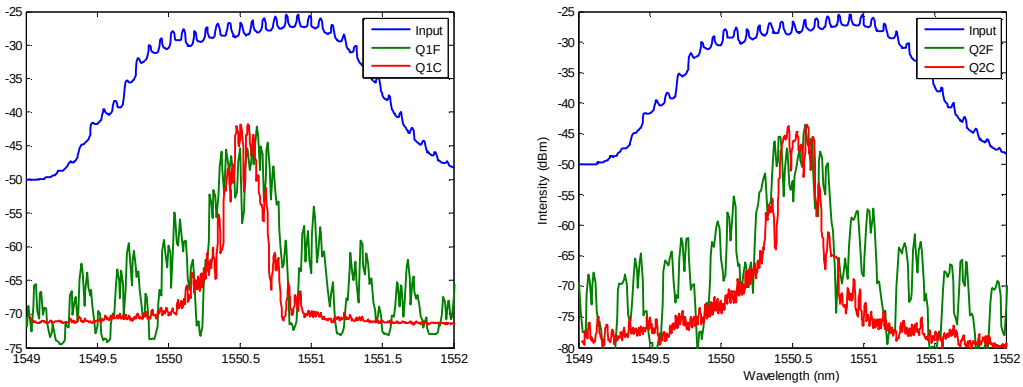

Figure 7.2 Spectrum of input pulse and the reflectivity spectra of continuous phase-shift SSFBGs (Q1F, Q2F) and discrete phase-shift SSFBGs (Q1C, Q2C)

Table 7.1 and Table 7.2 record the spectra and oscilloscope traces of the encoded signal and the decoded output for the continuous phase-shift SSDFBGs and discrete phase-shift SSFBGs respectively, when the interference channel (Q2) is shifted from 1549.9nm to 1551.1nm, while keeping the two codes overlapped in the time domain. The results show a general trend such that, when the two channels are separated well enough in the spectral domain, there is little interference between the two channels even when they are overlapped in the time domain. While as the two channels are moved closer to each other, there is increasing interference which deteriorates the decoded autocorrelation. When the two channels are tuned to the same wavelength, a similar interference level is presented in the encoded signal and decoded output for both the continuous phase-shift SSFBGs and discrete phase-shift SSFBGs. The little difference is when Q2 is tuned 0.3nm apart from Q1, for the discrete phase-shift SSFBGs, there is still obvious interference between the channels. While much less interference is observed for the continuous phase-shift SSFBGs. When the two channels are tuned further apart, to 0.6nm, for the continuous phase-shift SSFBGs, very clean traces are obtained. While for the discrete phase-shift SSFBGs, there is still some interference, although it is less severe than before. The results make sense if we look at the detailed spectra. The narrower spectrum of the continuous phase-shift SSFBGs determines that the two adjacent encoded signals are less overlapped in the spectral domain than the discrete phase-shift SSFBGs. It thus reduces the inter-channel interference in the encoded signal. On the decoded side, better suppression of the 'out of band' signal is also achieved by the narrower spectra of the continuous phase-shift SSFBGs. It can be claimed that the continuous phase-

shift SSFBG has better wavelength selection capability than the discrete phase-shift SSFBG and is an ideal candidate for dense OCDMA/DWDM system.

Table 7.1 Spectrum and oscilloscope (200ps/div) records of the encoded and decoded signal for the continuous phase-shift SSFBGs.

λ_2(nm)	2 input codes	output	2 overlapped codes	A/C output
1549.9 Δλ=-0.6	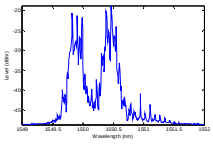	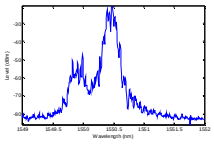	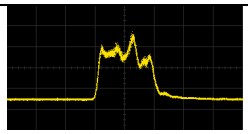	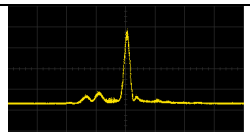
1550.2 Δλ=-0.3	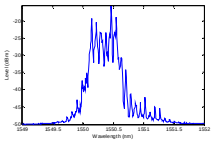	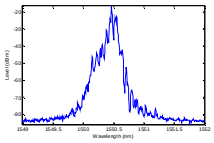	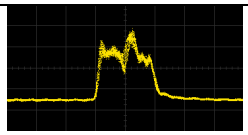	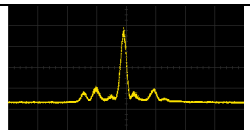
1550.5 Δλ=0	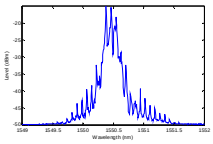	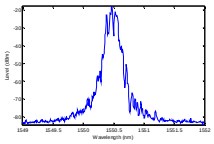	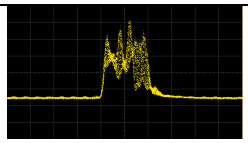	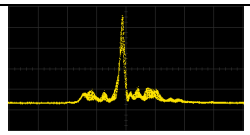
1550.8 Δλ=0.3	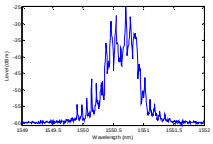	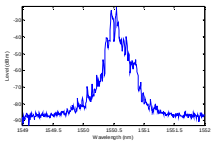	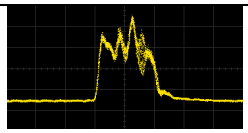	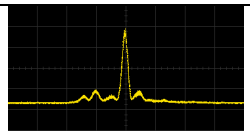
1551.1 Δλ=0.6	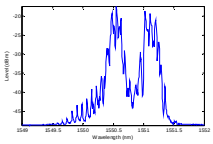	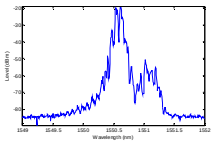	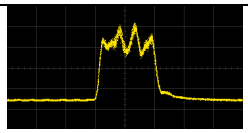	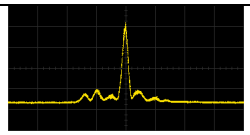

The high wavelength selectivity of the continuous phase-shift SSFBGs is confirmed again by another simple experiment. The experimental setup is the same as shown in Figure 7.1. Q1C is tuned at 1550.55nm and Q2C at 1550.15nm, that is a 0.4nm interval, decoding grating Q1*C is tuned to decode Q1C correctly. By adding on and cutting off Q2C in the combined encoded signal, the effect on the decoded autocorrelation signal can be observed. Figure 7.3(a) shows spectra of the encoded signal with the Q2C at 0.4nm interval both on and off, which shows that the addition of another WDM channel has little effect on the existing channel. The distinction between the two adjacent channels (at a 0.4nm interval) is about 20dB. Figure 7.3(b) shows the decoded signal when Q2C is present at a 0.4nm interval. Figure 7.3(c) shows the decoded signal when there is only Q1C in the encoded signal. As we can see from the results, there is no obvious difference between the decoded signals whenever the interference code Q2C is added on or not at 0.4nm interval. This

experiment confirms the excellent wavelength selection capability down to 0.4nm of the continuous phase-shift SSFBGs.

Table 7.2 Spectrum and oscilloscope (200ps/div) records of the encoded and decoded signal for the discrete phase-shift SSFBGs.

λ_2(nm)	2 input codes	output	2 overlapped codes	A/C output
1549.9 Δλ=-0.6	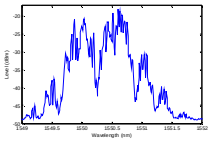	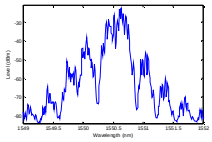	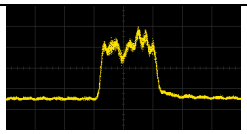	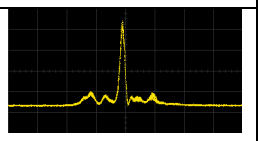
1550.2 Δλ=-0.3	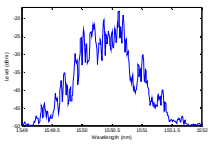	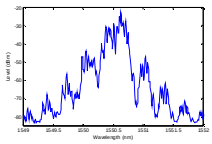	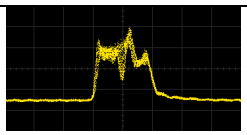	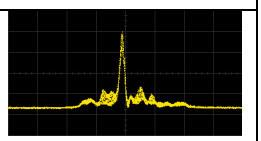
1550.5 Δλ=0	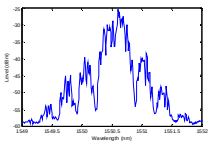	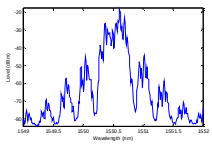	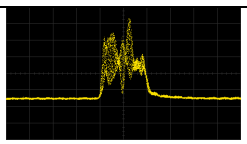	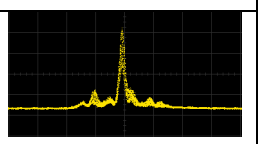
1550.8 Δλ=0.3	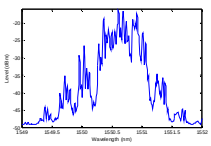	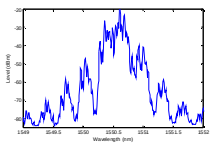	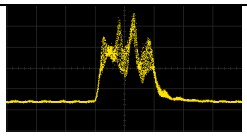	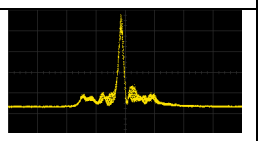
1551.1 Δλ=0.6	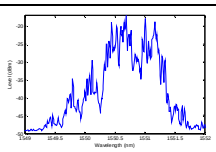	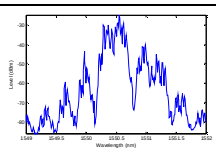	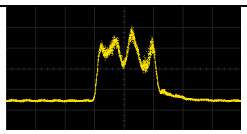	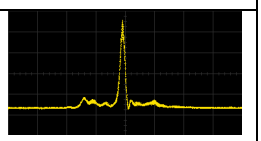

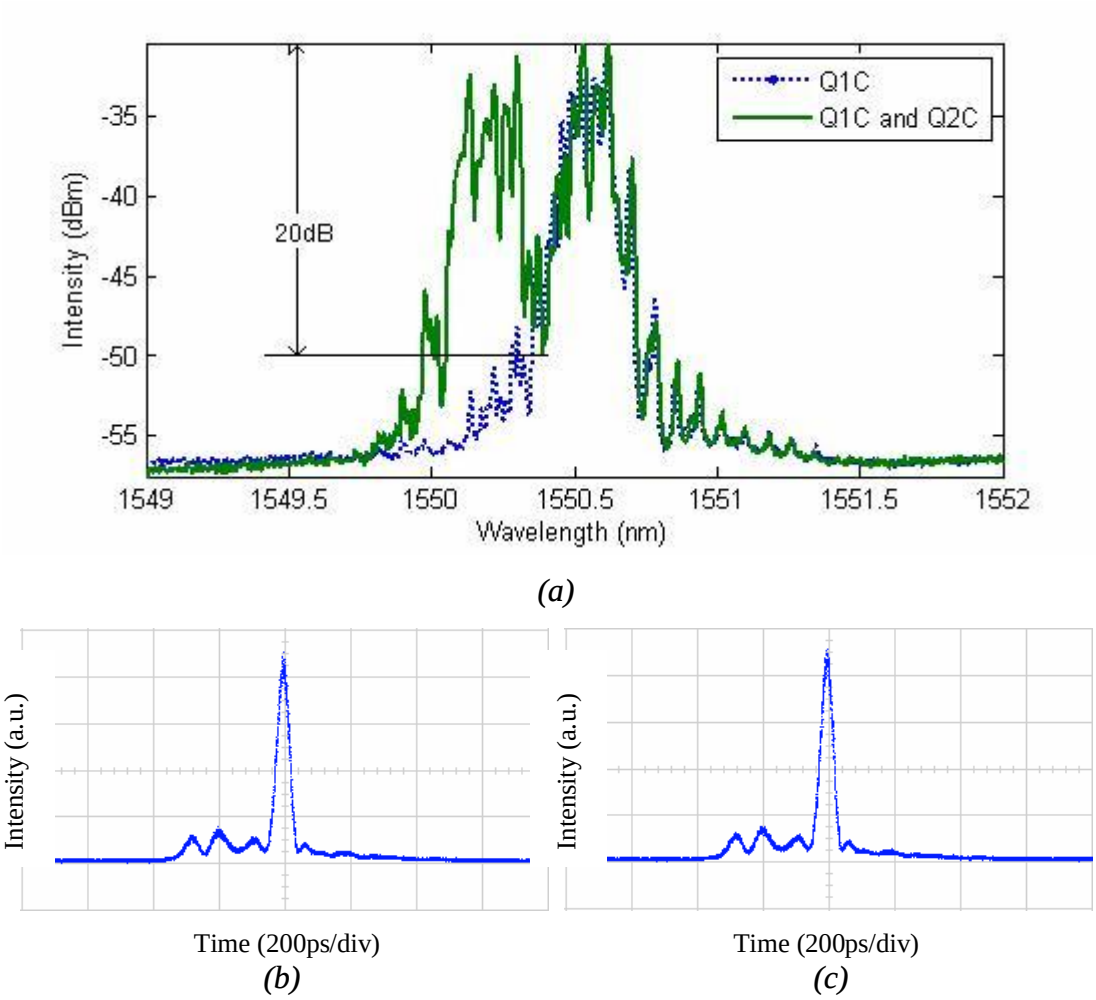

Figure 7.3 (a) Spectra of the encoded signal with and without presence of Q2C at 0.4nm interval, (b) oscilloscope trace for the decoded signal when Q2C is present at a 0.4nm interval. (c) oscilloscope trace for the decoded signal when there is only Q1C in the encoded signal.

To find out the effect of the different adjacent wavelength channel intervals, the received optical power was measured, while keeping the BER at 1e-9, and compared the results with the single wavelength channel case. Similar to the previous experiments, Q1 was used as the probe channel and kept at a fixed wavelength. Q2 acted as the interference channel and was shifted from 1549.9nm to 1551.1nm. The input data was set as a 2^7-1 PRBS at 277Mb/s, which was chosen to ensure that the encoded signal of the two different channels are overlapped in the time domain. The results are plotted in Figure 7.4 (a) and (b) for the discrete phase-shift SSFBGs and continuous phase-shift SSFBGs respectively. For the same wavelength interval, the discrete phase-shift SSFBGs lead to more interference on the adjacent channel than

the continuous SSFBGS. When the two channels are aligned in the spectral domain, the power penalty relative to the single channel case, for the discrete phase-shift SSFBGs to keep BER at 1e-9, is 3dB. For the continuous phase-shift SSFBGs, the power penalty is 2dB. Meanwhile, we can see that, for the discrete phase-shift SSFBGs, there is no obvious interference when the two channels are separated by 0.6nm in the spectral domain. While for the continuous phase-shift SSFBGs, 0.4nm is enough to minimise the interference.

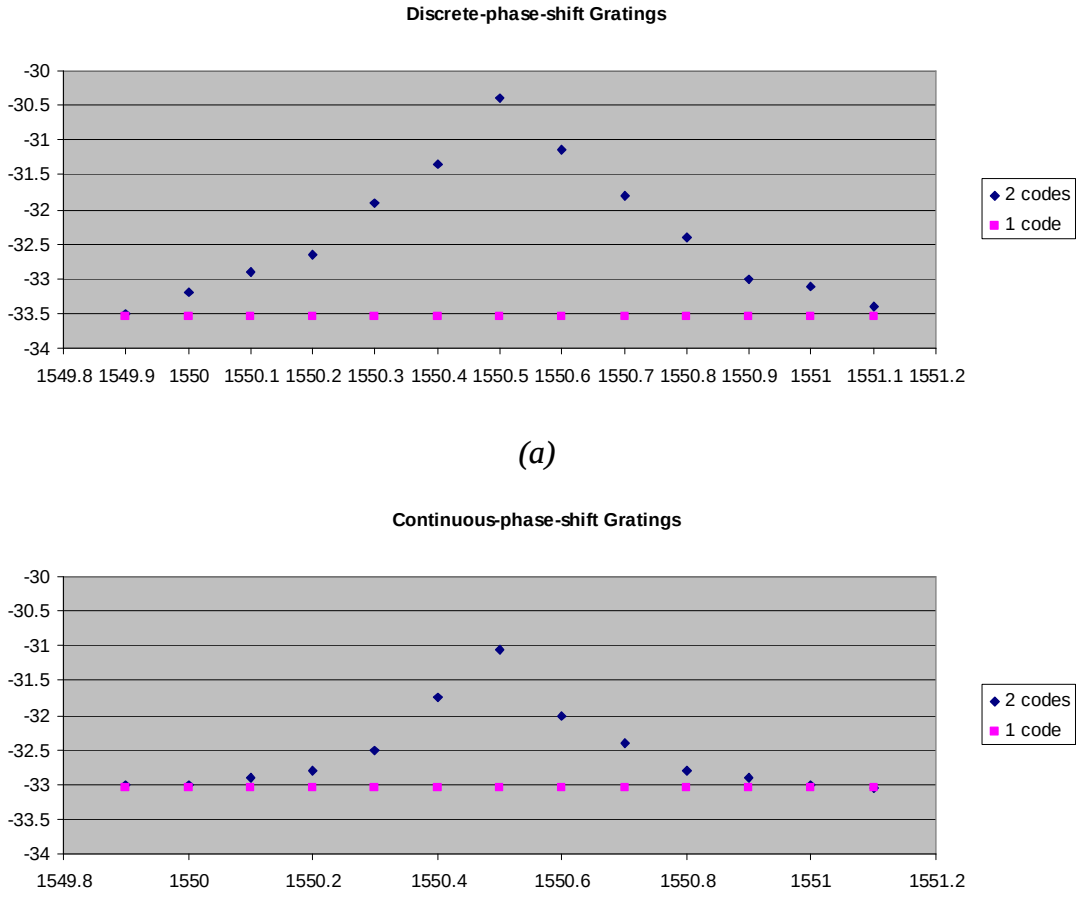

Figure 7.4 Effect of the different adjacent wavelength channel intervals (a) discrete phase-shift SSFBGs, (b) continuous phase-shift SSFBGs.

7.2.2 Consideration of the system setup

The effect of three different setup configurations on the system performance was also evaluated in order to choose the appropriate system configuration for the OCDMA/DWDM experiment. The first case (A) is the one I have described in Figure7.1. The second case (B) is similar to the first one, except that there is no 150m

SMF in one encoding path. The 150m SMF is used to reduce the temporal coherence of the input pulses in the two paths. The third case (C) is a genuine asynchronous encoding system, as shown in Figure 7.5, which deploys two short pulse sources for the two different channels. One of the short pulse sources is the 6ps pulses generated by the gain switched laser. The other is the 2ps pulses generated by a commercial mode-locked fiber ring laser. They are driven by independent clock signals, making the system genuinely asynchronous.

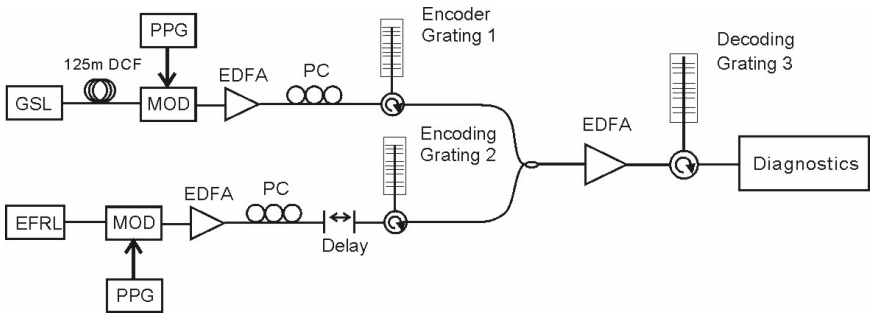

Figure 7.5 Asynchronous two channel OCDMA system.

The experiment is carried out with the continuous phase-shift SSFBGs, of which Q1C and Q1*C perform the coding/decoding process, Q2C in the 2ps pulse channel acts as the interfering channel and is adjusted to overlap with Q1C in both the time and spectral domains. Table 7.3 compares the decoded signal for the three cases with, and without, interfering code.

Table 7.3 Oscilloscope traces (200ps/div) of the decoded signal for the three different system configurations with, and without, interfering code

	Q1C only	Q1C+Q2C
Case A	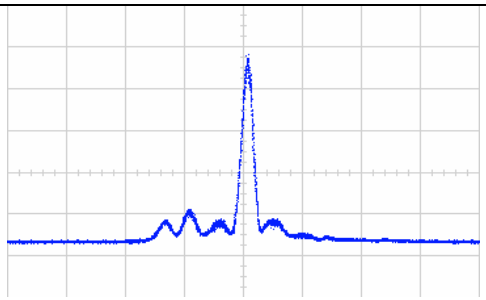	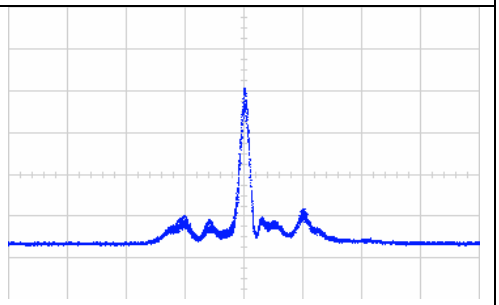
Case B	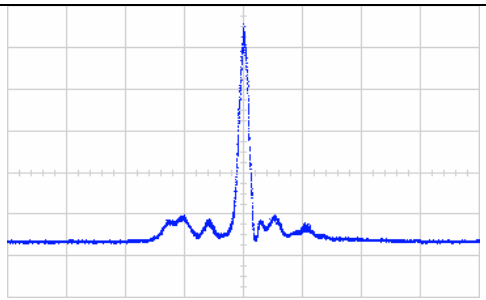	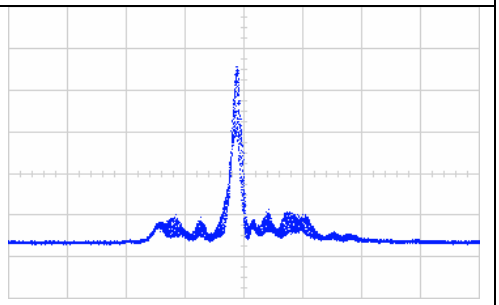
Case C	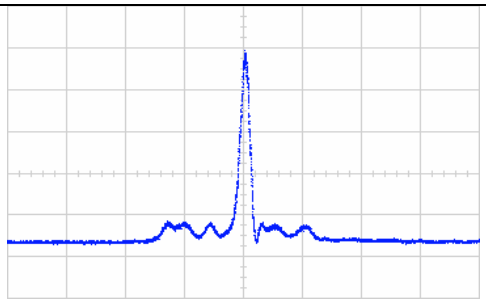	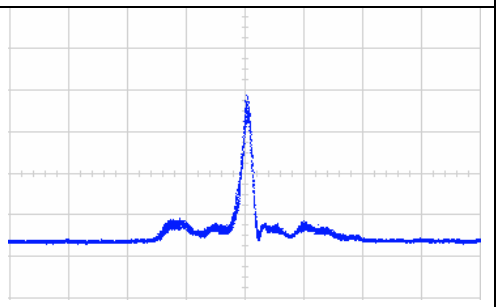

Basically, when there is only a single channel (Q1C) in the system, the decoded signals for the three cases are the same, since there is no difference in the input pulse and the coding/decoding gratings. While, when there are two channels in the system, case A and C have a similar performance, and case B displays more severe interference. This phenomenum is confirmed by the BER measurements for the three configurations. The BER results are plotted in Figure 7.6. Based on these experiments, we conclude that the extra length of fiber can effectively break the laser coherence from the same source. It provides a convenient and cheap way to simulate an asynchronous environment in the optical communication system.

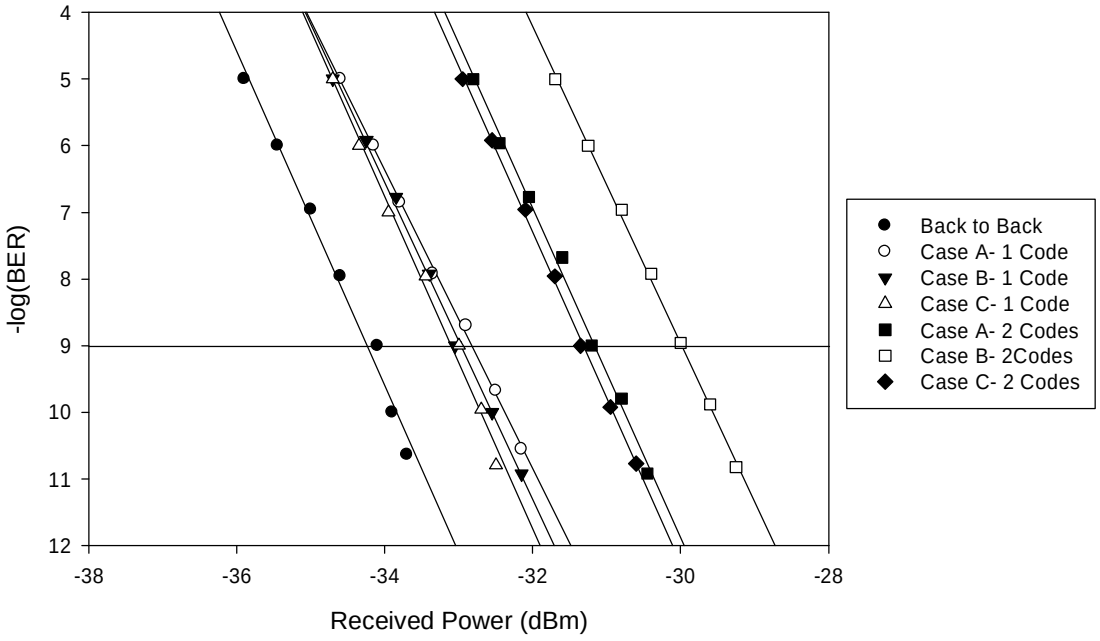

Figure 7.6 BER test results for the three different system configurations with, and without, interfering code.

7.2.3 Transmitter design

In our OCDM/DWDM experiments, the pulsed signal was generated by coupling continuous wave WDM sources into a pulse carving electro-absorption modulator (EAM), driven by a high frequency RF signal, as shown in Fig. 7.7. The generated pulse width could be modified by adjusting the frequency of the RF signal and the bias voltage applied to the EAM. The short pulse trains were then modulated using a $LiNbO_3$ intensity modulator to gate down the repetition rate and/or generate a data pattern.

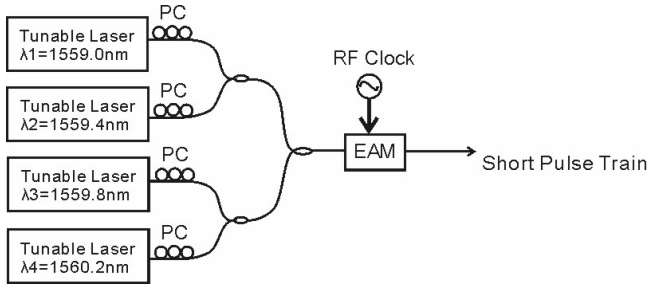

Figure 7.7 Experimental setup for DWDM short pulse generation.

Thus, by driving the EAM with a 10 GHz RF signal we are able to generate 25 ps pulses, which presents a good match with the chip duration (25ps) of the encoding SSFBGs. However, it was noticed that the optical spectrum of the 25ps pulses was too broad to allow DWDM operation on 50 GHz channel spacing. As shown in Fig. 7.8(b), the extinction ratio between adjacent channels on a 50GHz grid was just ~15 dB, implying that there would be significant interchannel crosstalk introduced during the encoding process. This was also confirmed through measurements of the relative power penalty introduced when detecting one OCDMA signal (P4 at wavelength λ_2) in the presence of two adjacent interfering encoded WDM channels (at wavelengths λ_1 and λ_3) as a function of the channel spacing from 0.4nm to 0.8nm. The experimental setup is shown in Figure 7.9. A cluster of 4 continuous phase-shift SSFBGs with the same code (P4), but which can be tuned around different central wavelength (λ_1=1559.0nm, λ_2=1559.4nm, λ_3=1559.8nm, λ_4=1560.2nm), was used as the encoding gratings. The decoding grating was chosen to decode P4 at wavelength λ_2. The CW source λ_4 in the transmitter was turned off so that encoded signals at only λ_1 to λ_3 were generated Figure. 7.10 presents the measured results for the relative power penalty (compared to the single wavelength channel) for 25ps and 50ps input pulses, when the decoding BER was maintained at 1e-9, while the WDM channel spacing was changed from 0.4nm to 0.8nm. The result shows that, for the 25ps input pulses, it is not possible to reduce the channel spacing below 0.6 nm without introducing a significant power penalty. Note that in the previous section it was found out that the continuous phase-shift SSFBG has a wavelength selection capability down to 0.4nm. However in this instance, the dominant factor is the 25ps DWDM input pulse which induces the initial inter-channel interference.

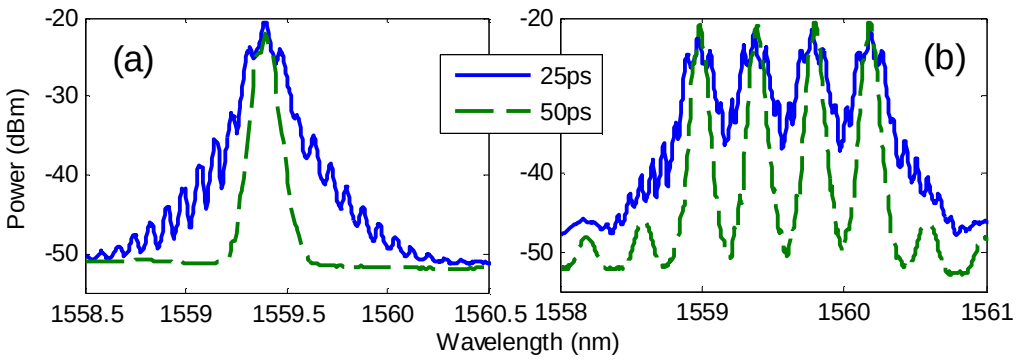

Figure 7.8 Measured optical spectra for the 25ps and 50ps pulses, (a) single

wavelength channel. (b) 4 DWDM channels.

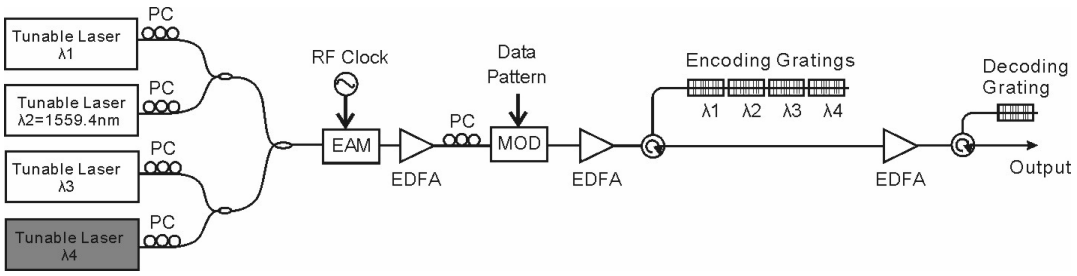

Figure 7.9 Experimental setup for a simple DWDM/OCDMA system

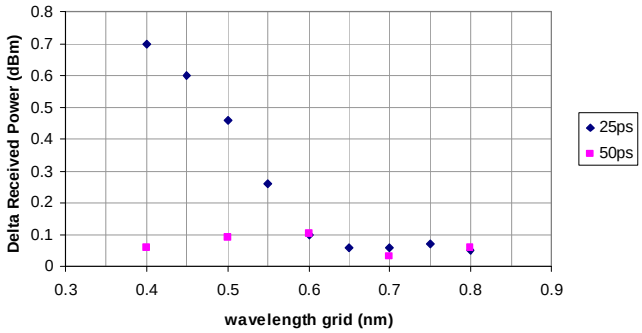

Figure 7.10 Received optical power penalty compared to single channel (λ_2 1559.4nm) decoding as a function of the wavelength spacing between adjacent channels in the presence of two interfering WDM channels (λ_1 1559.0nm and λ_3 1559.8nm).

Therefore the option of using broader pulses at the output of the EAM was investigated. By driving the EAM with a 5 GHz signal, 50 ps pulses were generated with a spectrum as shown in Figure 6.8 (dashed lines). An extinction ratio of ~30 dB between adjacent channels was now achieved, and no additional power penalty was introduced when reducing the WDM channel spacing to 0.4 nm (i.e. 50 GHz), as show in Figure 7.10. This result indicates that the 50ps input pulse is an appropriate choice for the DWDM/OCDMA experiments considering our available laboratory equipment.

7.3 31-chip Continuous Phase-shift SSFBGs and Code-reconfigurable Grating

In the OCDMA/DWDM experiments described in this chapter, we have employed encoding/decoding devices based on two different fiber grating technologies, fixed-coded continuous phase-shift SSFBG and code-reconfigurable gratings. All gratings carry 31-chip, 40Gchip/s quaternary phase codes chosen from the *FamilyA* code sequences [7-10]. These longer sequences allow for a better correlation performance and more simultaneous users. The chip-length for these gratings is 2.5 mm (25ps chip duration), resulting in a total grating length of 77.5 mm. The four codes used in this experiment are listed below, where 1 unit stands for 0.5π phase-shift:

F1= [3 2 0 2 3 3 0 3 3 1 2 1 2 3 2 2 0 2 1 2 0 1 2 1 3 0 2 3 3 1 3]

F2= [3 1 2 1 1 3 2 1 2 1 0 2 2 0 3 2 2 1 0 1 3 0 2 1 3 1 1 3 0 2 2]

F3= [2 3 2 3 0 2 2 0 1 2 2 3 0 3 1 0 2 3 1 3 3 1 0 2 2 1 3 2 3 3 1]

F4= [3 3 1 2 2 2 3 3 0 1 3 1 0 1 0 1 2 2 2 0 3 0 2 1 2 1 1 2 2 1 1]

In this chapter the individual gratings used are labeled according to the following rules: The first letter defines the grating type; ‘F’ stands for a fixed-coded continuous phase-shift SSFBG, ‘R’ stands for the reconfigurable grating. The first number (1 to 4) identifies the four different codes. The second number (1 to 4) indicates the wavelength. * is used to indicate whether the grating is for decoding, rather than coding, a particular channel. For example, ‘F32’ means fixed-coded grating with code 3, at λ2, and R32* is the corresponding reconfigurable decoder grating.

A description of the different types of gratings is presented in the following paragraphs. The code-reconfigurable grating is described first, since its characteristics were used as the basis for the design of the continuous phase-shift SSFBGs.

7.3.1 Code-reconfigurable grating

The structure of the reconfigurable grating is the same as described in Chapter 3, except this is a longer grating and has more tungsten wires to accommodate the 31-chip codes. A 77.5 mm uniform FBG is mounted on a fiber stretcher to allow tuning of the grating Bragg wavelength. There are 30 tungsten wires distributed at 2.5 mm intervals along the FBG. Each of the wires can be individually temperature-tuned to

induce the desired phase code distribution along the grating length. The operation of this device is described in Chapter 3, where it is shown that it is possible to tune from one code to another by simple re-assignment of the current flowing through each of the tungsten wires (and hence their temperatures). Figure 7.11 shows the reflectivity spectra of the device when it is configured with four different codes (R13*, R23*, R33*, R43* respectively) and tuned to wavelength λ_3 (1559.80 nm).

Based on the characterization information we obtained using the EAM-FROG technique, as described in Section 3.3, and the experience of our first 15-chip continuous phase-shift SSFBG in Section 4.3. The 31-chip continuous phase-shift SSFBGs were designed to ensure an optimal matching performance between the two types of gratings.

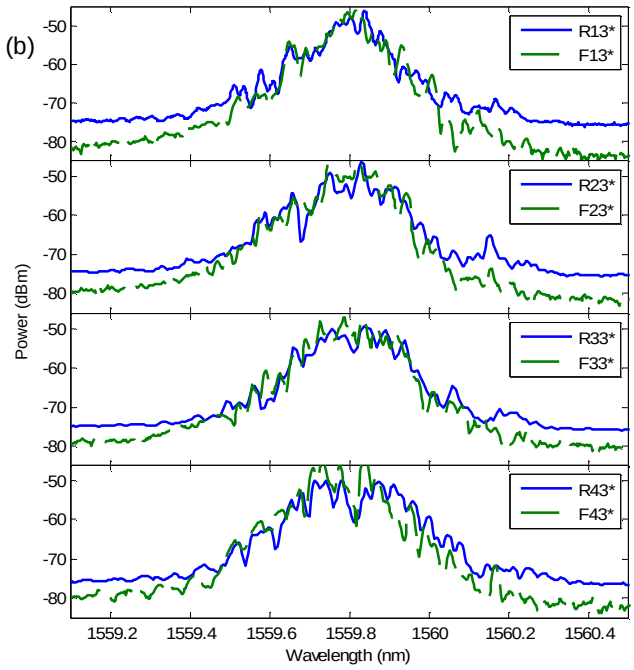

Figure 7.11 Measured reflectivity spectra of the reconfigurable grating (solid line) and the continuous phase-shift SSFBGs (dash line) for 4 different codes.

7.3.2 Continuous phase-shift SSFBGs

Figure 7.12(a) shows the effective refractive index distributions corresponding to a single phase-shift 0.5π, 1.0π, 1.5π in the quaternary OCDMA codes of the fixed continuous phase-shift SSFBGs. The matched continuous phase distribution profiles have been shown to provide a better correlation performance than the combination of discrete and continuous phase-shift codes. The use of continuous phase shifts in the

SSFBG structure also allows the grating bandwidth to be reduced, which was critical in our OCDMA/DWDM experiments in order to ensure high efficient bandwidth utilization. The phase distribution profiles for the discrete phase-shift SSFBG and the continuous phase-shift SSFBG with the same code F2 are illustrated in Figure 7.12(b). Figure 7.13 shows the measured and simulated reflectivity spectrum of grating F22. For comparison, we also plot the simulated spectrum of a grating with the same code and strength as grating F22 but with a discrete, rather than continuous, chip-phase transition. It can be readily seen that the continuous phase-shift SSFBG has a narrower 20dB bandwidth (~0.45nm) and no unwanted side-lobes, allowing for much closer wavelength channel spacings than were previously possible using discrete phase shift gratings.

In order to allow a comparison between the performance of the continuous phase-shift SSFBG and the code-reconfigurable grating, the reflectivity spectra of the two devices are superimposed in Figure 7.11. The good agreement between the reflectivity spectra of the continuous fixed phase-shift SSFBGs and that of the reconfigurable grating confirms the results of our previous measurements of the thermally induced phase distributions within the reconfigurable grating, and shows that the reconfigurable grating works as expected.

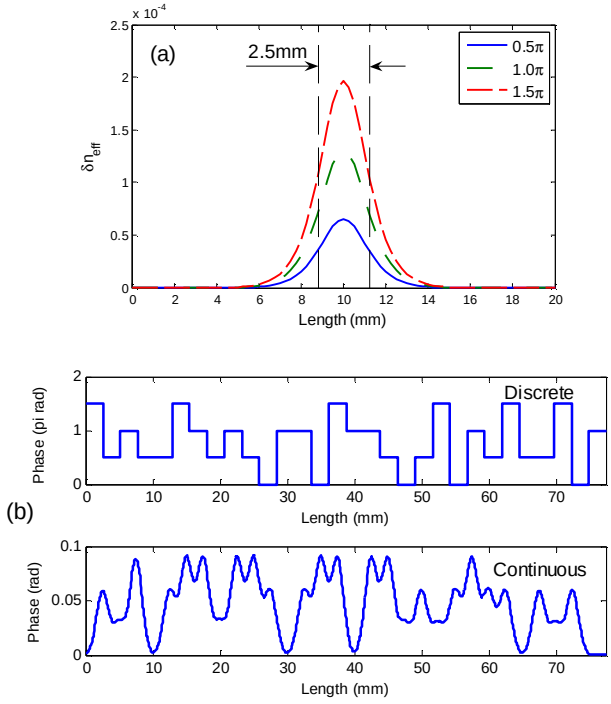

Figure 7.12 (a) Effective refractive index distributions of a single phase-shift within the continuous phase-shift SSFBGs. (b) Phase distribution profile for the discrete

phase-shift SSFBG and the continuous phase-shift SSFBG with the same code F2.

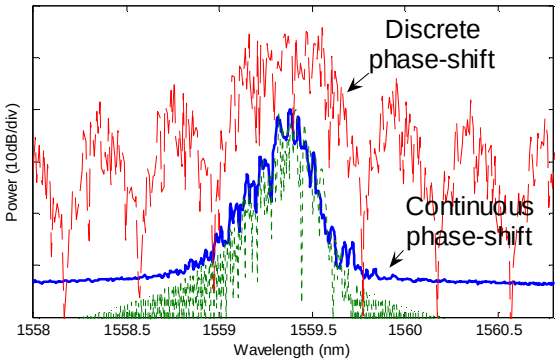

Figure 7.13 Reflectivity spectra of grating F22 (solid line: measurement, dotted line: simulation, dashed line: simulation of a discrete phase-shift grating, up-shifted by 15dB to avoid overlap with the continuous phase-shift data).

7.3.3 Correlation Properties

The correlation properties for each individual grating were tested before undertaking the system experiments. In order to ensure that all features of the encoded sequences were presented reliably after reflection off the gratings; firstly 25ps input pulses were used, of which the pulse width is comparable to the chip length of the codes.

Figure 7.14 shows example oscilloscope traces of the autocorrelation and cross-correlation, for both the continuous phase-shift and the code-reconfigurable gratings. For all the grating pairs, distinctive autocorrelation pulses and relatively low level cross-correlation pulses between codes were successfully achieved. As shown, both types of gratings display similar correlation properties due to the excellent match of the phase distribution within the gratings. In both cases, the width of the autocorrelation is ~50ps.

After confirming the correlation properties of the fabricated gratings, using 25ps input pulses, I moved on to measure the correlation properties of these gratings using 50ps input pulses. Table 7.4 summarises the autocorrelation traces for all the 16 continuous phase-shift SSFBGs. Distinctive autocorrelation peaks have been achieved for all the gratings. The autocorrelation pulse width varies between 51ps and 78ps. This is because, when the input pulse width is wider than the grating chip duration, its spectral width is narrower than that of the SSFBG, thus the spectral width of the autocorrelation pulse will mainly follow the bandwidth of the input pulse. In the time

domain, the autocorrelation pulse width will be comparable to the input pulse width [7-11]. Table 7.5 summarises the autocorrelations and cross-correlations between the four codes at 1559.4nm (λ2). Similar results are obtained for the code-reonfigurable grating decoding cases, which are summarised in Table 7.6 and Table 7.7.

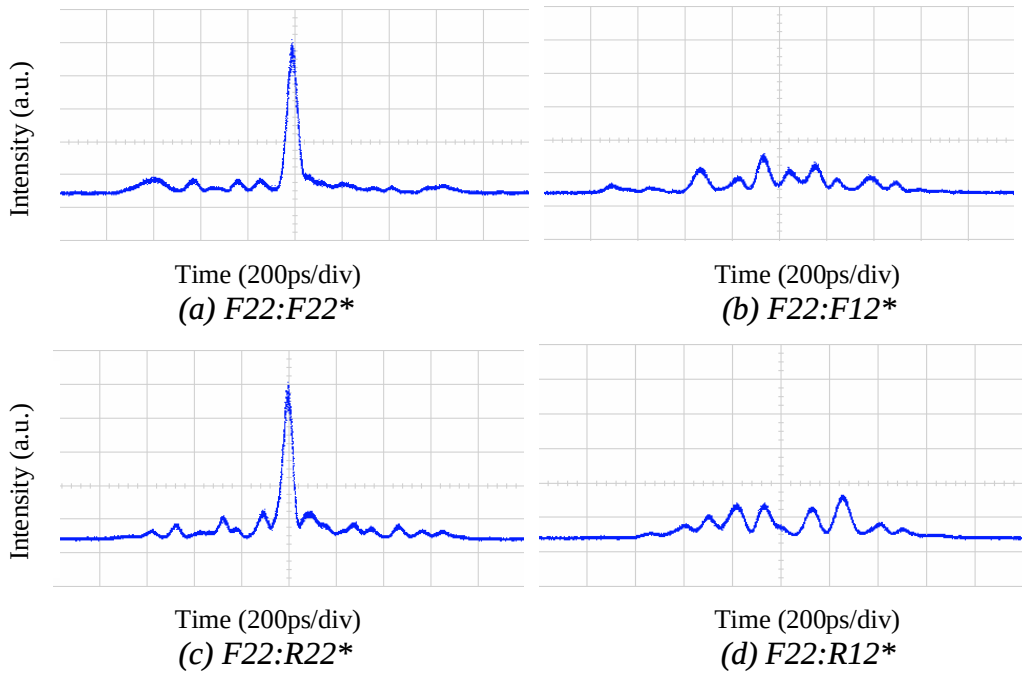

Figure 7.14 Oscilloscope traces when using 25ps input pulses for (a) autocorrelation: F22:F22. (b) cross-correlation: F22:F12*. (c) autocorrelation: F22:R22*. (d) cross-correlation: F22:R12*. (Timescale: 200ps/div)*

	λ1	λ2	λ3	λ4
F1	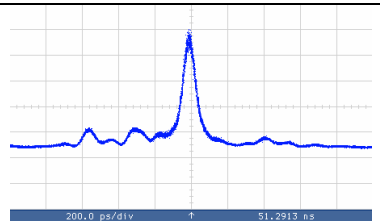	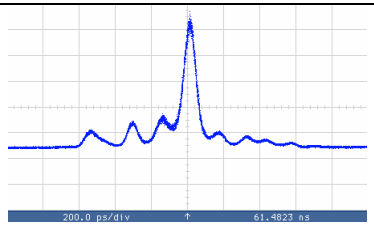	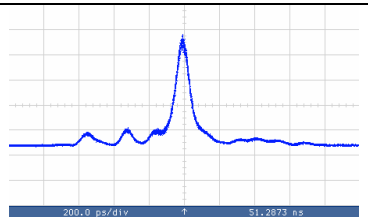	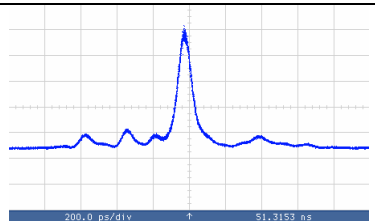
F2	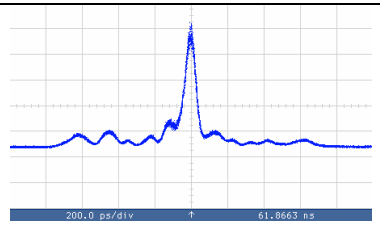	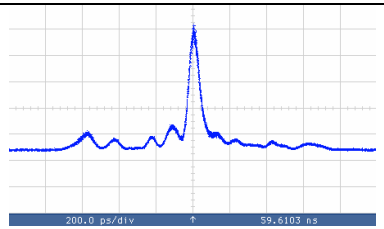	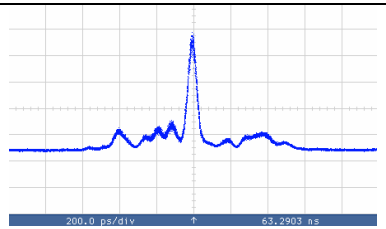	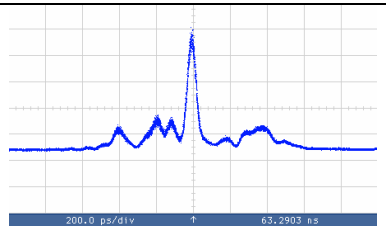
F3	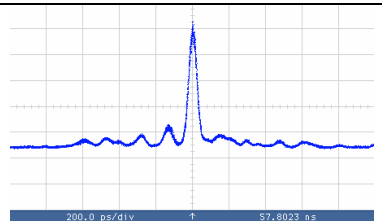	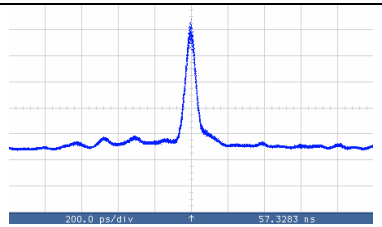	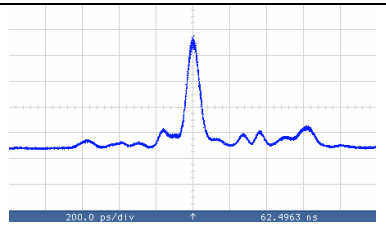	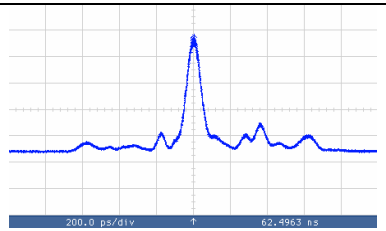
F4	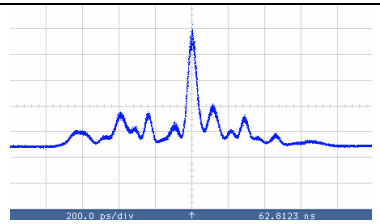	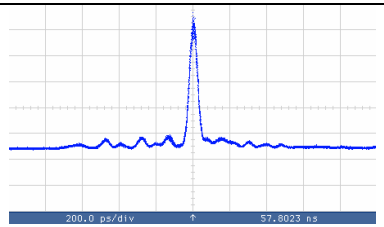	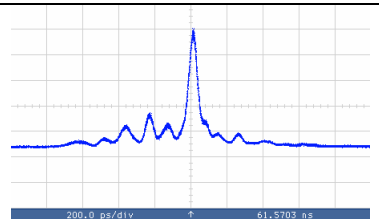	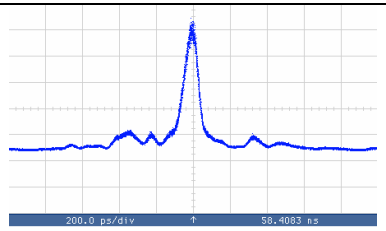

Table 7.4 Autocorrelation of the continuous phase-shift SSFBGs with 50ps input pulse (Timescale: 200ps/div)

	F1	F2	F3	F4
F1*	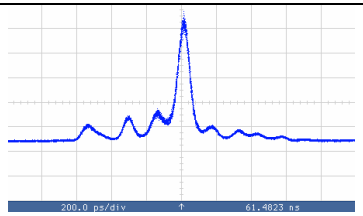	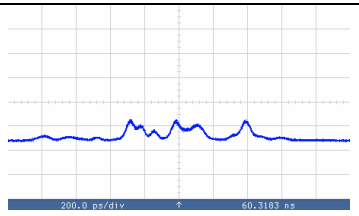	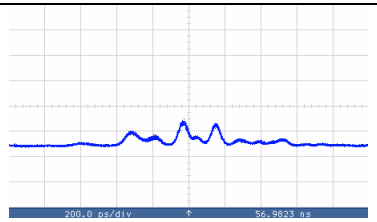	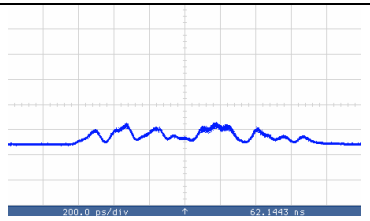
F2*	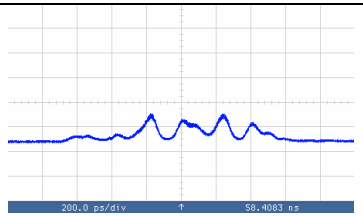	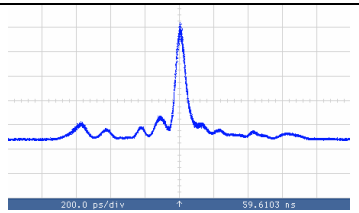	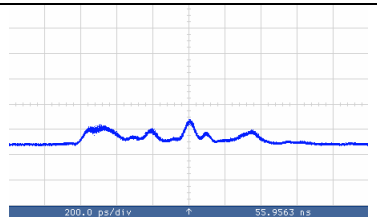	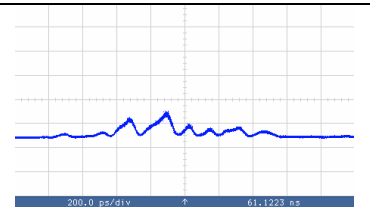
F3*	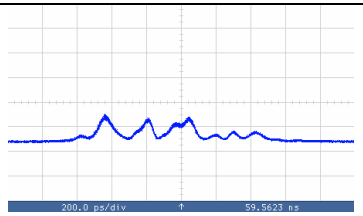	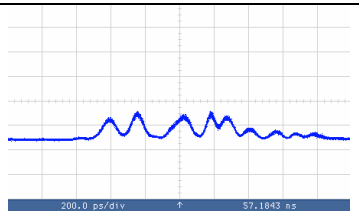	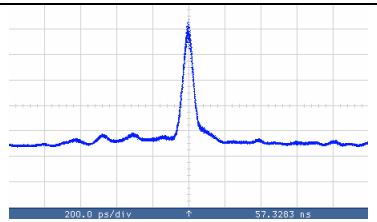	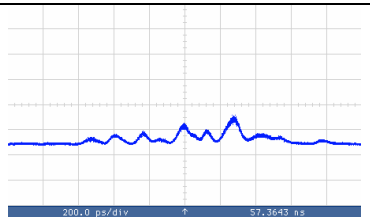
F4*	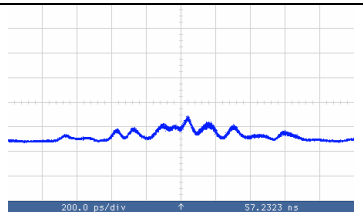	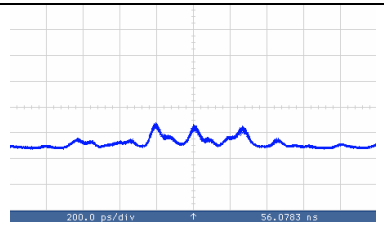	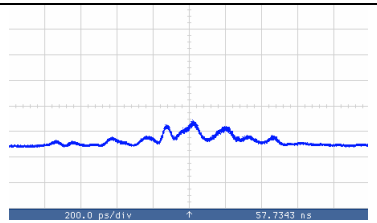	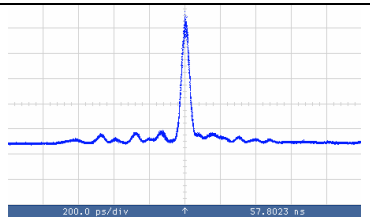

Table 7.5 Correlation properties of continuous phase-shift SSFBGs at λ2= 1559.4nm with 50ps input pulse (Timescale: 200ps/div)

	λ1	λ2	λ3	λ4
R1	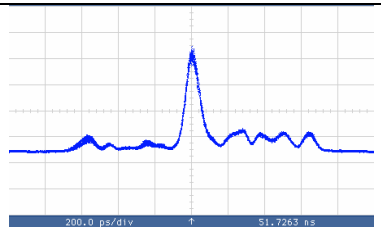	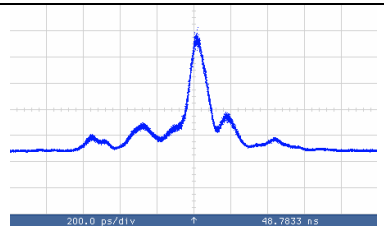	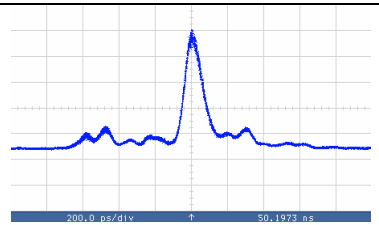	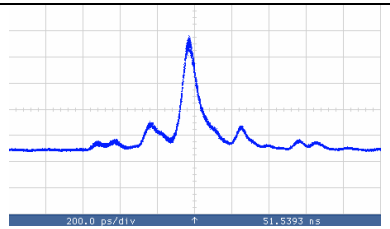
R2	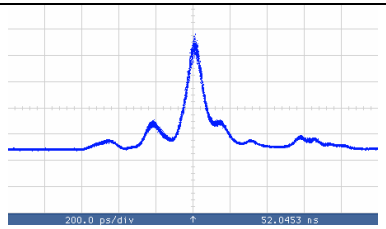	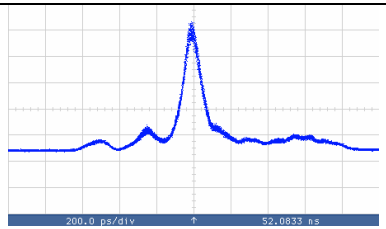	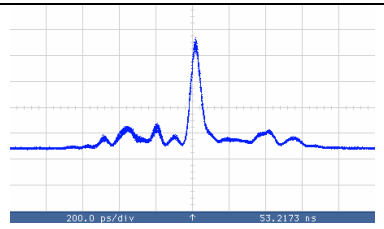	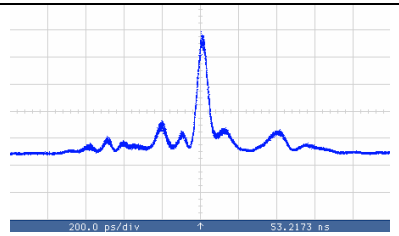
R3	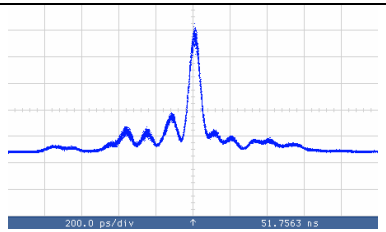	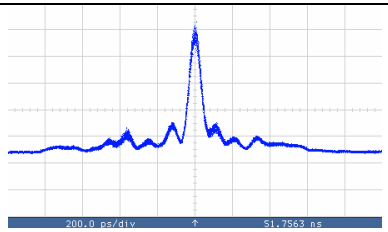	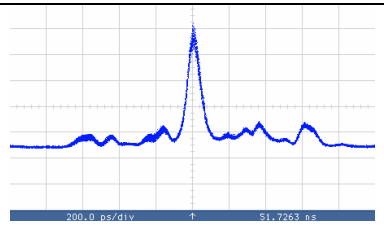	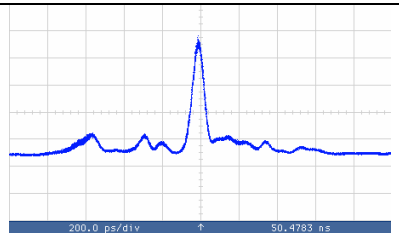
R4	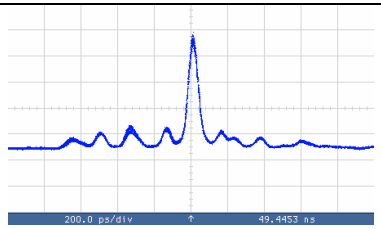	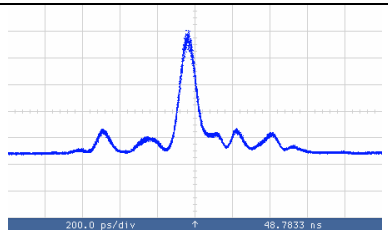	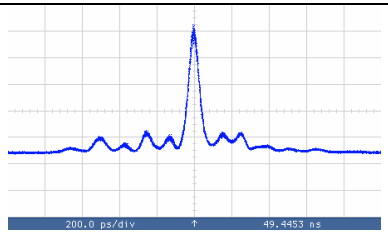	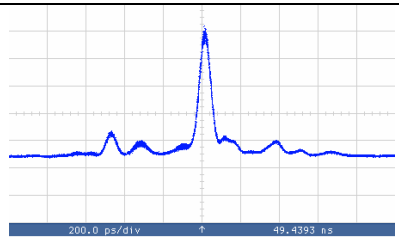

Table 7.6 Autocorrelation of the code-reconfigurable gratings with 50ps input pulse (Timescale: 200ps/div)

	F1	F2	F3	F4
R1*	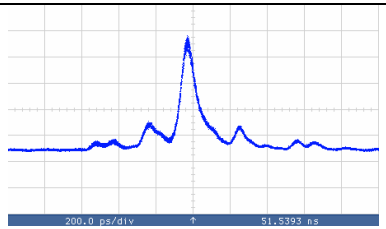	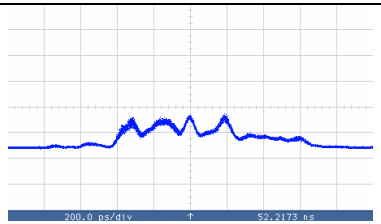	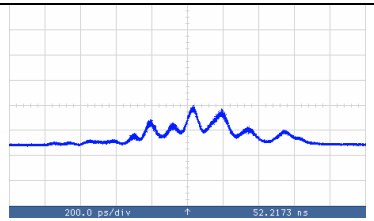	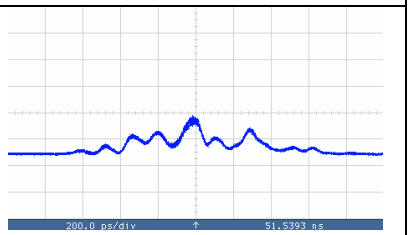
R2*	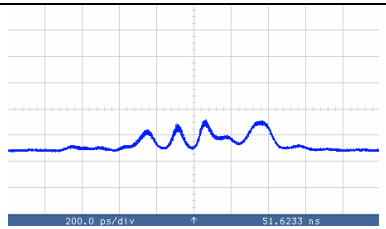	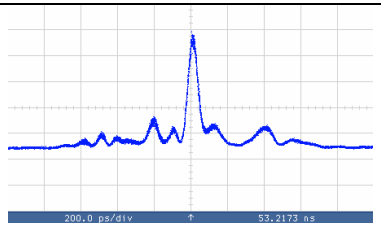	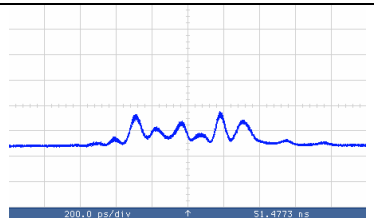	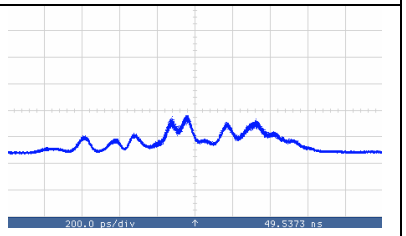
R3*	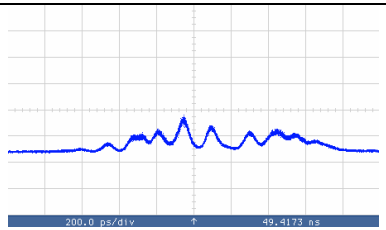	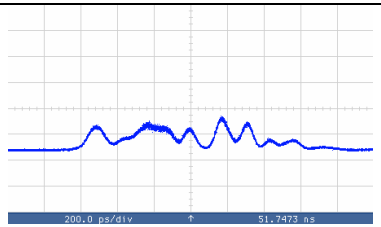	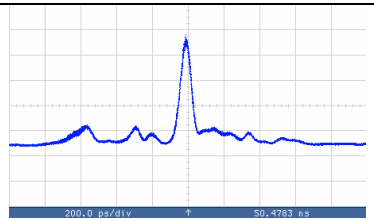	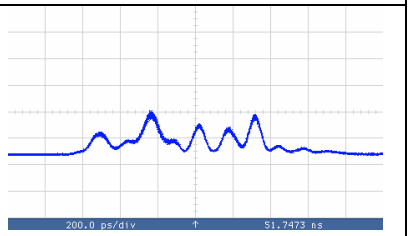
R4*	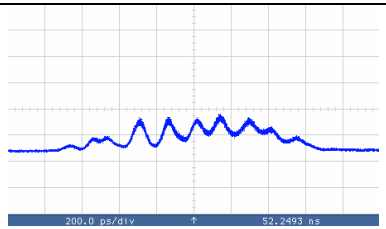	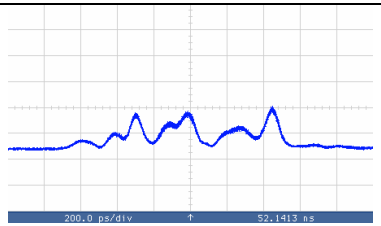	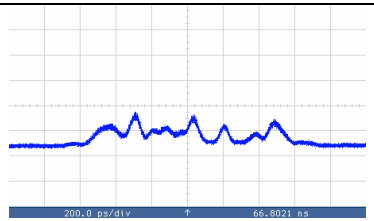	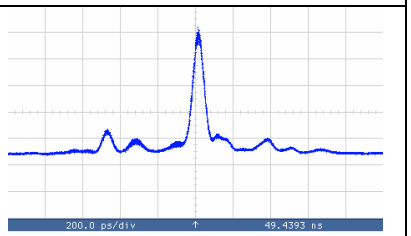

Table 7.7 Correlation properties of reconfigurable gratings at λ4= 1560.2nm with 50ps input pulse (Timescale: 200ps/div)

7.4 OCDMA/DWDM System Experiment

The schematic in Figure 7.15(a) shows the experimental configuration of the 16-channel OCDMA/DWDM system. The incoming signal was generated, as described in the previous Section. A $LiNbO_3$ intensity modulator is used to modulate the multiwavelength pulse trains to generate a 2^7-1 PRBS at 625 Mbit/s at each of the four wavelengths. The modulated pulses are fed to an array of 16 continuous phase-shift SSFBGs to generate data representing an effective 16 users. The grating array is composed of four different codes (F1-F4), each code being repeated on each of four different central wavelengths (λ_1 to λ_4). The SSFBGs are grouped together by their code, thus forming the four branches shown in Figure 7.15(a). Different lengths of single-mode fiber (SMF) were included in each branch to ensure that the recombined signals at the output of the encoding system were not mutually coherent. Note that there was no active control over the temporal positioning of the various encoded waveforms. However, the duty cycle of the encoded signals at 625 Mbit/s was around 1:2, implying that there was significant overlap between the coded signals at the output of the transmitter. Figure 7.15(b) shows the spectrum of the 16-channel encoded signal after being combined into a single fiber. At the receiver end, either a (fixed) continuous phase-shift SSFBG or a code-reconfigurable grating was used to decode a particular target data channel. The inherent wavelength selectivity of the grating is used to filter out the twelve out-of-band channels (four codes at each wavelength). Of the remaining four in-band channels, only the code matched to the decoding grating generates a distinct autocorrelation peak, while the other three unmatched channels produce relatively low level cross-correlation signals.

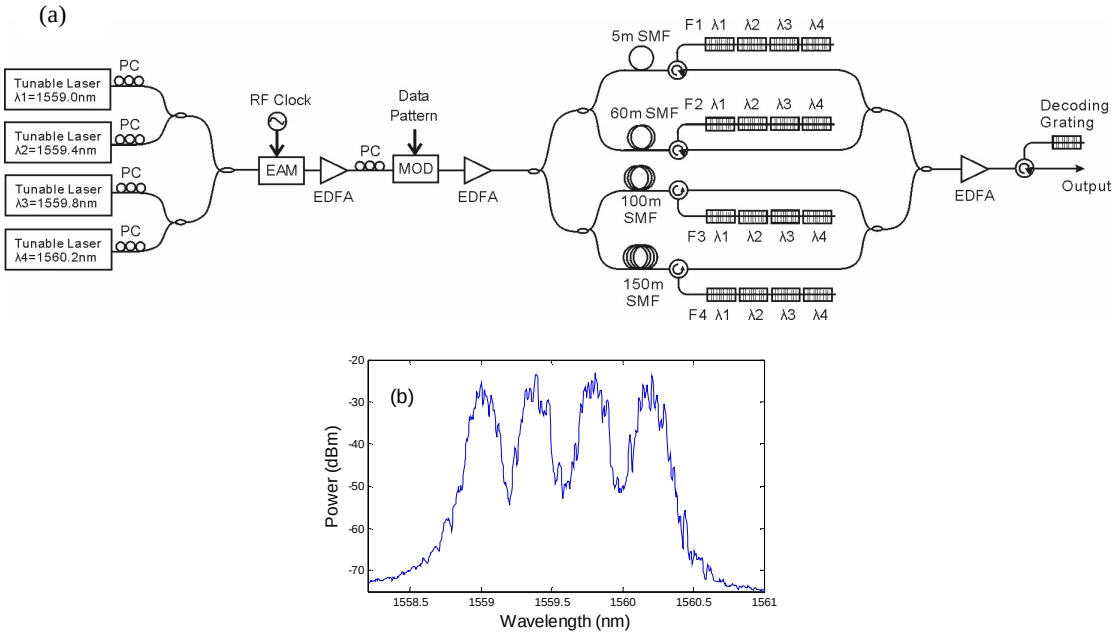

Figure 7.15 (a) Experimental 16-channel OCDMA/DWDM system setup. (b) Measured optical spectrum for the encoded 16-channel OCDMA/DWDM signal.

Figure 7.16 (a, c) show the result of decoding F33 by using fixed-coded SSFBG F33* and reconfigurable grating R33* respectively, when only code F3 (at all 4 wavelengths) was present in the incoming signal. The clear eye diagrams highlight the excellent wavelength discrimination provided by the continuous phase-shift decoders. Figure 7.16 (b, d) show the results of decoding input channel F33, using fixed-coded grating F33* and reconfigurable grating R33* respectively, when all 16 channels were incident on the receiver. The eye diagrams in Figure 7.16 (b, d) are somewhat degraded relative to those in Figure 7.16 (a, c) due to Multiple Access Interference (MAI) noise from the other in-band channels. However, an open eye is still achieved and the performance of both fixed and reconfigurable gratings is seen to be comparable. The corresponding received optical spectra are shown in Figure 7.17. The inter-channel spectral extinction ratio is better than -25dB in all cases.

Time (200ps/div)
Time (200ps/div)

Time (200ps/div)
Time (200ps/div)

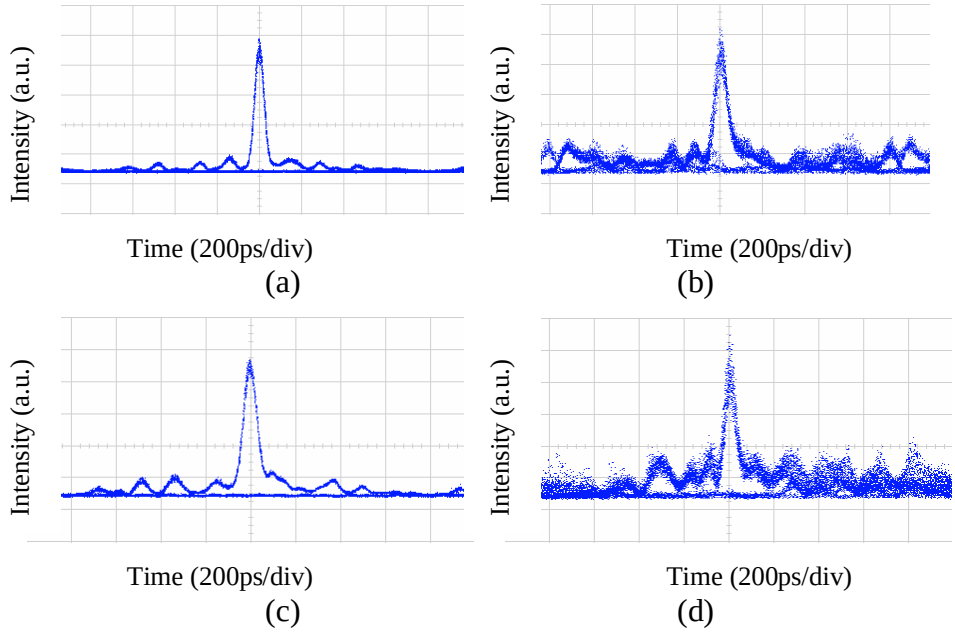

Figure 7.16 Oscilloscope traces for (a) using F33 and (c) using R33* to decode F33 when only F3 at four wavelengths were present in the incoming signal, (b) using F33* and (d) using R33*to decode F33 when all 16 channels were present.*

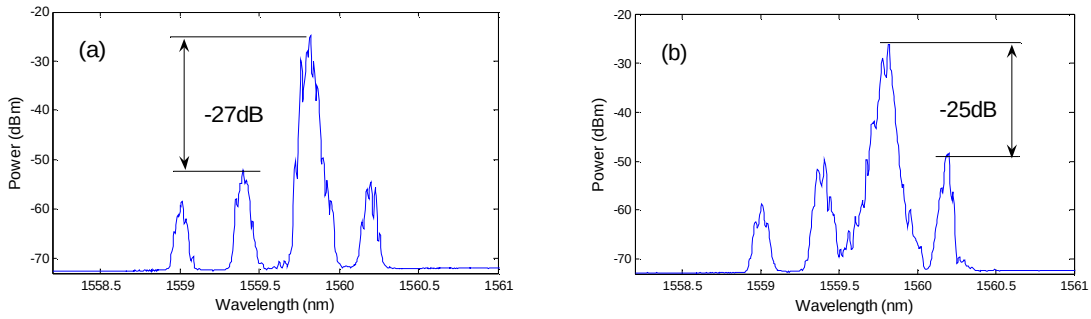

Figure 7.17 (a) and (b) are the corresponding optical spectra for Figure 6.16 (b) and (d) respectively.

The system performance was evaluated through a series of bit error rate (BER) measurements, which are summarized in Figure 7.18. In Figure 7.18(a), it plots the BER curves obtained using decoder grating F33*. First, code F33 was transmitted alone, and then in the presence of other wavelength channels (each transmitting the same OCDMA code F3). Finally, more OCDMA codes were progressively added into the system (codes F1, F2 and F4 respectively). The figure shows that, when there is only one OCDMA code (F33) in the incoming signal, the effect of the out-of band channels is negligible. A power penalty of ~2.1 dB is associated with the OCDMA decoding of this signal, whereas the presence of the remaining DWDM channels

introduces no further penalty when used at 50GHz grid spacing. With all four DWDM wavelengths turned on, the additional codes are added, resulting in a corresponding rise in the power penalty due to the increasing MAI. ~1.5dB power penalty for each additional in-band code was measured at a BER of 10^{-9}, however error-free performance was achieved in all instances.

Figure 7.18(b) is shown to facilitate a comparison between the fixed and reconfigurable decoders. In this case, the performance of four different channels, namely F22, F23, F32, F33, were studied. For the assessment of the fixed decoders, a different SSFBG is used to decode each of the channels, whereas obviously for the reconfigurable decoder, the same device was tuned to decode the various incoming signals. Firstly the noise performance of the system was measured when just one OCDMA code per wavelength channel was transmitted, and then the measurements were repeated in the presence of all 16 channels. As before, the noise degradation is predominantly associated with the inclusion of more OCDMA codes. However, error-free performance is achieved for all channels tested. In agreement with the trend shown in Figure 7.18(a), inclusion of 4 in-band codes (16 channels in total) is associated with an additional ~4.5 dB power penalty (at BER=10-9) relative to the case when only one OCDMA code is present (4 wavelength channels). The performance of the reconfigurable decoder is seen to be only slightly worse than that of the fixed code decoder. Note that some form of nonlinear thresholding technique at the receiver could be used to improve the performance albeit at an additional cost as discussed in Section 4.4.

(a)

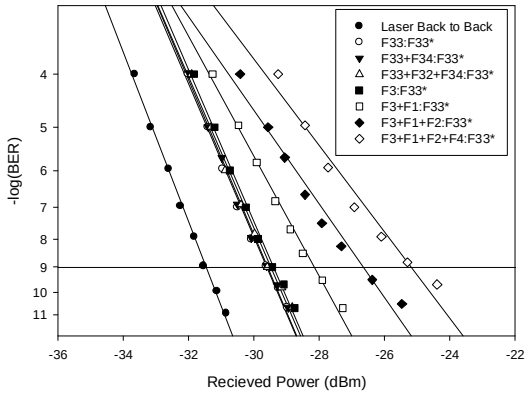

(b)

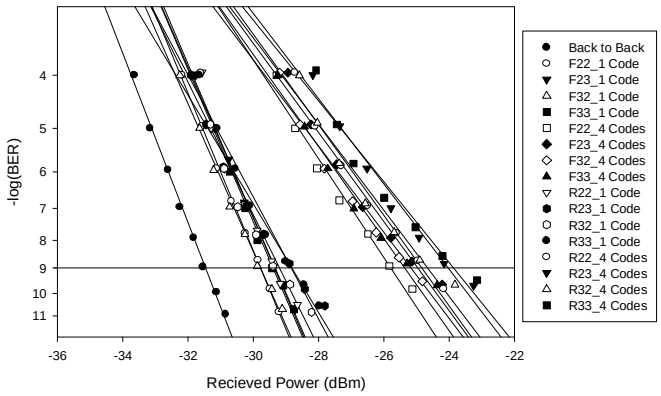

(c)

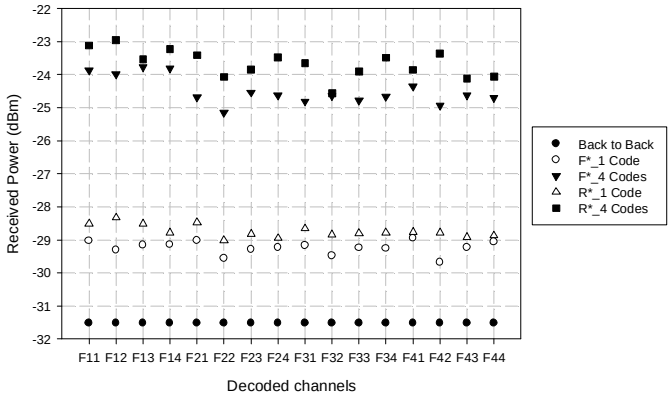

Figure 7.18 (a) BER results for decoding F33, with increasing interference channels. (b) BER results for decoding F22, F23, F32, F33, with 1 and 4 in-band codes × 4 DWDM channels. (c) Received optical power for decoding each of the 16 channel at a BER=10^{-9}.

Only detailed BER measurements at λ_2 and λ_3 have been presented since these are the most vulnerable to inter-channel crosstalk. However, a summary of the performance of all codes, both in absence of any OCDMA-induced MAI and under

full 16-channel operation is presented in Figure 7.18 (c). This figure shows the power level required at the receiver in order to achieve a 10^{-9} BER, and highlights that uniform performance could be achieved for all 16 channels. In agreement to the results shown in Figure 7.18 (b), the power penalty between the fixed-coded decoder and the reconfigurable decoder is ~0.5 dB when only one OCDMA channel is present, which increases to ~1 dB in the presence of all four OCDMA channels. It is believed that improvements in the thermal stability of the reconfigurable device will help improve its performance relative to the fixed decoders. Finally, the small variations in the received power required to achieve error-free operation for the various codes, is attributed to be primarily due to slight differences in the correlation properties of the coding sequences. However, the relative timing of the various transmitted OCDMA code sequences (which was set arbitrarily in this experiment) might also contribute to this variation.

7.5 Conclusions

A 16-channel OCDMA/DWDM system based on new SSFBG-based coding/decoding approaches have been experimentally demonstrated. The narrow bandwidth of continuous phase-shift SSFBGs allows the DWDM grid spacing to be reduced down to 50 GHz. Considering the spectrum-spreading essence of OCDMA technology, our system highlights the spectral efficiency of our proposed OCDMA system based on advanced SSFBGs. The reconfigurability at the receiver have been demonstrated by employing a dynamically code-reconfigurable decoder, and have shown that no significant additional power penalty is associated with its use relative to the decoder based on fixed-coded continuous SSFBGs. Relatively wide input pulses of ~50 ps duration (twice the chip duration) were employed in the system to allow the use of 50 GHz DWDM channel spacing, confirming the capability of both the continuous phase-shift SSFBG and reconfigurable grating technologies to tolerate wider input pulses without significant degradation in their correlation properties. Error-free performance was achieved for all 16 channels. Furthermore, it was shown that most significant power penalties were introduced from the correlation process when decoding OCDMA signals at a given wavelength, whereas wavelength filtering of the DWDM channels did not introduce any significant additional penalty. One can therefore envisage that a system like the one described herein can be directly scaled

by extending its wavelength dimension. It is also clear that DS-OCDMA based on SSFBG coding techniques is fully compatible with WDM technologies, allowing for example, OCDMA channels to co-exist with other WDM channels carrying conventionally encoded data.

The demonstrated OCDMA/DWDM system has a spectral efficiency of 0.05(bit/s)/Hz, which is 4 times higher than the previous 4 OCDM×4 WDM×311Mbit/s OCDMA system operating on a 100GHz grid. The state of the art DWDM system using complex modulation format can achieve as high spectral efficiency as 4.2(bit/s)/Hz [7-12]. Given the spectrum spreading nature and the flexibility offered by OCDMA technique, it is more suitable for the access network rather than the transmission system.

References

[7-1] X. Wang, N. Wada, T. Miyazaki, G. Cincotti, and K. Kitayama, "Field trial of 3-WDM ×10-OCDMA × 10.71-Gb/s asynchronous WDM/DPSK-OCDMA using hybrid E/D without FEC and optical thresholding," *Journal of Lightwave Technology*, vol. 25, pp. 207-15, 2007.

[7-2] P. C. Teh, M. Ibsen, J. H. Lee, P. Petropoulos, and D. J. Richardson, "A 4-channel WDM/OCDMA system incorporating 255-chip 320 Gchip/s quaternary phase coding and decoding gratings," *Optical Fiber Communication (OFC 2001)*, vol. Postdeadline, 2001.

[7-3] P. C. Teh, M. Ibsen, L. B. Fu, J. H. Lee, Z. Yusoff, and D. J. Richardson, "A 16-channel OCDMA system (4 OCDM X 4 WDM) based on 16-chip, 20 Gchip/s superstructure fibre Bragg gratings and DFB fibre laser transmitters," presented at OFC 2002, Anaheim, 2002.

[7-4] M. R. Mokhtar, M. Ibsen, P. C. Teh, and D. J. Richardson, "Reconfigurable multilevel phase-shift keying encoder-decoder for all-optical networks," *IEEE Photonics Technology Letters*, vol. 15, pp. 431-433, 2003.

[7-5] Z. Zhang, C. Tian, M. R. Mokhtar, P. Petropoulos, D. J. Richardson, and M. Ibsen, "Rapidly reconfigurable optical phase encoder-decoders based on fiber Bragg gratings," *IEEE Photonics Technology Letters*, vol. 18, pp. 1216-1218, 2006.

[7-6] C. Dorrer and I. Kang, "Simultaneous temporal characterization of telecommunication optical pulses and modulators by use of spectrograms," *Optics Letters*, vol. 27, pp. 1315-1317, 2002.

[7-7] Z. Zhang, C. Tian, M. A. F. Roelens, M. R. Mokhtar, P. Petropoulos, D. J. Richardson, and M. Ibsen, "Direct characterization of the spatial effective refractive index profile in Bragg gratings," *IEEE Photonics Technology Letters*, vol. 17, pp. 2685-2687, 2005.

[7-8] C. Tian, Z. Zhang, M. A. F. Roelens, P. Petropoulos, M. Ibsen, and D. J. Richardson, "Full characterisation of the temporal response of phase-shifted SSFBGs using electroabsorption modulator based frequency resolved optical gating," presented at BGPP/ACOFT 2005 Sydney, Australia, 2005.

[7-9] Z. Zhang, C. Tian, P. Petropoulos, D. J. Richardson, and M. Ibsen, "Distributed-phase OCDMA encoder-decoders based on fiber Bragg gratings," *IEEE Photonics Technology Letters*, vol. 19, pp. 574-6, 2007.

[7-10] S. Boztas, R. Hammons, and P. Y. Kumar, "4-phase sequences with near-optimum correlation properties," *IEEE Transactions on Information Theory* , vol. 38, pp. 1101-1113, 1992.

[7-11] Z. Zhang, "Passive and active Bragg gratings for optical networks," *Thesis submitted for the degree of Doctor of Philosophy*, University of Southampton, chapter 4, 2007.

[7-12] X. Zhou, J. Yu, D. Qian, T. Wang, G. Zhang, and P. Magill, "8x114 Gb/s, 25-GHz-Spaced, PolMux-RZ-8PSK Transmission over 640 km of SSMF Employing Digital Coherent Detection and EDFA-Only Amplification," in *OFC2008*, San Diego, USA, paper PDP1.

Chapter 8

Conclusions and Future Work

This thesis is devoted to the development and applications of FBG-based optical coding/decoding techniques.

Firstly a linear spectrogram technique EAM-FROG has been employed to characterize the complex code profile of the various FBGs used in the work. This technique can provide direct and accurate information about both amplitude and phase distribution profile along the grating and thus provided a powerful method to investigate the behaviour of our thermally-induced code-reconfigurable grating.

Three different types of FBG-based optical encoder/decoder have been investigated: (a) fixed-coded discreet phase-shift SSFBGs, (b) code-reconfigurable FBG gratings, (c) fixed-coded continuous phase-shift SSFBGs. All the gratings are designed with shorter chip duration (25ps), higher reflectivity (~50%) than the gratings demonstrated before, to enable higher chip rates, higher spectral efficiencies and more flexible OCDMA and optical packer processing systems. The system performance of three different OCDMA system configurations using the different gratings have been compared: (a) discrete phase-shift encoding SSFBG and discrete phase-shift decoding SSFBG, (b) discrete phase-shift encoding SSFBG and continuous phase-shift decoding SSFBG or reconfigurable grating, (c) continuous phase-shift encoding SSFBG or reconfigurable grating and continuous phase-shift decoding SSFBGs or reconfigurable gratings. The study reveals that the continuous phase-shift gratings (either fixed-coded SSFBGs or reconfigurable grating) display satisfactory correlation performance with narrower bandwidth compared with conventional discrete phase-shift SSFBGs.

The improvement in the grating design enabled a 16-channel reconfigurable OCDMA/DWDM system (4OCDMA×4DWDM×625Mbit/s) operating with higher bit rate and improved spectral efficiency on a 50GHz DWDM-compatible grid. An

all-optical packet processing system based on our dynamically reconfigurable FBG device was also demonstrated. All of the experiments were carried out with common, readily available telecommunication devices, showing the ready integrability of FBG-based optical coding/decoding techniques.

However, there are some future research possibilities for the FBG-based optical coding/decoding techniques:

Reconfigurable grating

The thermally-induced code-reconfigurable grating could be improved further in terms of stability and tuning speed. More work could be carried out to provide a more stable control of the environmental temperature, higher localization of the thermally-induced phase-shifts, and more flexible controlling mechanisms. The effect of different distribution of the thermally-induced phase-shifts (continuous phase-shift) also needs further investigation.

OCDMA codes and system structure

Various optical codes have been designed for OCDMA applications, but not all of them are suitable for FBG implementations. However, it is possible to employ some new codes such as higher order phase levels (8- and 16- phase level) and two-dimensional codes to improve the correlation performance and reduce the multiple access interference (MAI). Some new coding and detection schemes such as differential phase-shift keying (DPSK) data format and balanced detection could also be considered with our FBG techniques.

Optical Packet Switching Networks

We have demonstrated the feasibility of a dynamically reconfigurable optical packet processing system. Provided the improvement of reconfiguration speed and laboratory equipments resource, more complex system structure and packet switching functions are expected. For example, the packet header generation with more than one optical code, to provide more header information.

Further work to reduce MAI using TPA device

We have preliminarily demonstrated the feasibility of using TPA process to simultaneously perform nonlinear optical thresholding and detection in the OCDMA system. Due to the breakdown of TPA device, the work was not continued. However, it is worthwhile to carry out further work on this topic, e.g. to increase TPA bandwidth to meet the telecommunication requirement, to investigate the performance in a complicated DWDM-OCDMA scenario.

List of Publications

Journal Papers

[1] **C. Tian**, Z. Zhang, M. Ibsen, P. Petropoulos, and D. J. Richardson, "A 16-channel OCDMA/DWDM system using continuous phase-shift SSFBGs and reconfigurable grating," *IEEE Journal of Selected Topics in Quantum Electronics*, vol. 13, pp.1480 – 1486, 2007.

[2] Z. Zhang, **C. Tian**, P. Petropoulos, D. J. Richardson, and M. Ibsen, "Distributed-phase OCDMA encoder-decoders based on fiber Bragg gratings," *IEEE Photonics Technology Letters*, Vol. 19, pp.574 – 576, 2007.

[3] **C. Tian**, Z. Zhang, M. Ibsen, P. Petropoulos, and D. J. Richardson, "A reconfigurable optical header recognition system for optical packet routing applications," *IEEE Photonics Technology Letters*, vol.18, pp. 2395-2397, 2006.

[4] Z. Zhang, **C. Tian**, M. R. Mokhtar, P. Petropoulos, D. J. Richardson, and M. Ibsen, "Rapidly reconfigurable optical phase encoder-decoders based on fiber Bragg gratings," *IEEE Photonics Technology Letters*, vol. 18, pp. 1216-1218, 2006.

[5] Z. Zhang, **C. Tian**, M. A. F. Roelens, M. R. Mokhtar, P. Petropoulos, D. J. Richardson, and M. Ibsen, " Direct characterization of the spatial effective refractive index profile in Bragg gratings ," *IEEE Photonics Technology Letters*, vol. 17, pp. 2685-2687, 2005.

Conference Presentations

[6] **C. Tian**, Z. Zhang, M. Ibsen, P. Petropoulos, and D. J. Richardson, "Demonstration of a 16-channel code-reconfigurable OCDMA/DWDM system," *OFC 2007*, Anaheim, 25-29 Mar 2007.

[7] Z. Zhang, **C. Tian**, P. Petropoulos, D. J. Richardson, and M. Ibsen, "Fibre Bragg grating based continuous-phase encoder-decoders for OCDMA networks," *ECOC 2006*, Cannes, 24-28 Sep 2006.

[8] **C. Tian**, Z. Zhang, M. Ibsen, M.R.Mokhtar, P. Petropoulos, and D. J. Richardson, "Reconfigurable all-optical packet switching based on fiber Bragg gratings," *OFC 2006* Anaheim, 5-10 Mar 2006.

[9] Z. Zhang, **C. Tian**, M.R.Mokhtar, P.Petropoulos, D.J.Richardson, and M.Ibsen, "Rapidly reconfigurable phase code generation and recognition using fiber Bragg gratings," *OFC 2006,* Anaheim, 5-10 Mar 2006.

[10] M. A. F. Roelens, **C. Tian**, Z. Zhang, P. Petropoulos, M. Ibsen, and D. J. Richardson, "Full characterisation of the temporal response of complex phase shifted Bragg gratings for OCDMA using frequency resolved optical gating," ECOC 2005, Glasgow, 25-29 Sep 2005.

[11] D.J.Richardson, P.C.Teh, M.R.Mokhtar, M.A.F.Roelens, B.C.Thomsen, C.Tian, Z.Zhang, P.Petropoulos and M.Ibsen, "Direct sequence OCDMA systems based on fibre grating technology," ECOC 2005, Glasgow, 25-29 Sep 2005 (Invited)

[12] P. Petropoulos, **C. Tian**, Z. Zhang, M. Ibsen, M. A. F. Roelens, P. C. Teh, and D. J. Richardson, "Applications of superstructured fibre Bragg gratings in OCDMA systems," *NOC 2005,* London, 5-7 Jul 2005 (Invited).

[13] **C. Tian**, Z. Zhang, M. A. F. Roelens, P. Petropoulos, , M. Ibsen, and D. J. Richardson, "Full characterisation of the temporal response of phase-shifted SSFBGs using electro-absorption modulator based frequency resolved optical gating," *BGPP/ACOFT 2005,* Sydney, 4-8 Jul 2005.

[14] Z. Zhang, **C. Tian**, M. A. F. Roelens, M. R. Mokhtar, P. Petropoulos, D. J. Richardson, and M. Ibsen, "Direct accurate determination of the spatial refractive index profile in Bragg gratings," *BGPP/ACOFT 2005,* Sydney, 4-8 Jul 2005.